UAB
Universitat Autònoma de Barcelona

Synthesis and characterization of giant porous molecules

Alba Cortés Martínez

UAB
Universitat Autònoma
de Barcelona

Synthesis and characterization of giant porous molecules

Alba Cortés Martínez

Doctoral Thesis

PhD in Chemistry

Supervisors

Prof. Daniel Maspoch

Dr. Arnau Carné

Catalan Institute of Nanoscience and Nanotechnology (ICN2)

Department of Chemistry – Faculty of Science

2025

Memòria presentada per aspirar al Grau de Doctora

per Alba Cortés Martínez

Alba Cortés Martínez

vist-i-plau

Prof. Dr. Daniel Maspoch

ICREA Research Professor & Group Leader

Supramolecular NanoChemistry & Materials Group

Catalan Institute of Nanoscience and Nanotechnology

Dr. Arnau Carné

RyC Researcher

Chemistry Department

Autonomous University of Barcelona

Supramolecular NanoChemistry & Materials Group

Catalan Institute of Nanoscience and Nanotechnology

Bellaterra, 17 de juliol de 2025

Table of contents

Abstract v

Resum vii

Resumen xi

Acknowledgements xv

1. Introduction 21

1.1. The start of supramolecular chemistry 21

1.2. Self-assembly of metallacycles 24

1.3. Self-assembly of three-dimensional structures: Synthesis of metal-organic cages 30

1.3.1. Metal-pyridyl based structures 30

1.3.2. Subcomponent self-assembly: Chelate effect 34

1.3.3. Carboxylate-metal based structures 37

1.3.4. Diversity in the metallic nodes: Increasing the stability 40

1.4. Porous properties of MOCs/MOPs 44

1.4.1. Porosity in solution 45

1.4.2. Porosity in solid state 47

1.5. Giant assemblies 48

1.5.1. Mesoporous cages 50

1.5.2. Oligomeric supramolecules 55

1.6. References 58

2. Objectives 73

3. Experimental section 79

3.1. Materials and methods 79

3.2. Synthetic procedures of Chapter 4: Giant oligomeric porous cage-based molecules 85

3.3. Synthetic procedures of Chapter 5: Isoreticular synthesis of mesoporous metal-organic polyhedra with permanent porosity to gas and water 95

3.4. References 105

4. Giant oligomeric porous cage-based molecules 111
4.1. Introduction 111
4.2. Results and discussion 114
4.2.1. Synthesis of 1-connected Rh-MOPs 114
4.2.2. Synthesis of dimeric MOP-based supramolecule 129
4.2.3. Increasing the connectivity in the synthesis of oligomeric MOP-based supramolecules 135
4.2.4. Study of the adsorption capabilities of oligomeric molecules in solid state 148
4.3. Conclusions 150
4.4. References 152
5. Isoreticular synthesis of mesoporous metal-organic polyhedra with permanent porosity to gas and water 161
5.1. Introduction 161
5.2. Results and discussion 165
5.2.1. Synthesis of parent microporous Rh(II)-based octahedral MOP 165
5.2.2. First isoreticular expansion of the Rh(II)-based octahedral MOP 169
5.2.3. Geometry mismatch in discrete metal-organic assemblies 184
5.2.4. Second isoreticular expansion of the Rh(II)-based octahedral MOP 187
5.2.5. Solid-state properties of isoreticular octahedral Rh(II)-based MOPs 191
5.3. Conclusions 197
5.4. References 199
5.5. Crystallographic data 206
6. General conclusions 215
7. Glossary 221
8. List of publications 227

Abstract

This PhD Thesis focuses on the assembly of metal-organic giant structures, specifically targeting mesoporous cages and oligomeric supramolecules, defined as structures with an internal cavity larger than 2 nm or an overall diameter exceeding 5 nm, respectively. The aim of this work is to explore strategies for obtaining permanently porous giant cage-based molecules. Special emphasis is placed on understanding the design principles and synthetic pathways required to construct such large, porous architectures, either through direct synthesis or post-synthetic modification. Ultimately, this study seeks to contribute to the development of robust, permanently porous giant molecules, expanding their potential for applications in areas such as molecular separation, catalysis, or storage.

Chapter 1 provides an overview of the fundamentals of discrete metal-organic materials, including the self-assembly of metallacycles and the formation of three-dimensional metal-organic cages. This chapter reviews the synthetic approaches developed to date and introduces the key concepts underlying their design and synthesis. Particular emphasis is placed on the strategies used to construct giant assemblies and the progress achieved in this field so far.

Chapter 2 specifies the general and specific objectives of this PhD Thesis.

Chapter 3 presents the formation of the first family of oligomeric supramolecules synthesised via a stepwise approach. Specifically, it demonstrates how the connectivity of metal-organic polyhedra (MOPs) can be precisely controlled through a protection-deprotection strategy, enabling the formation of 1-connected cages. These cages serve as monomeric building blocks for the construction of oligomeric, cage-based supramolecules, including a dimer, a tetramer, and a satellite-like architecture. Finally, the permanent porosity of this new family of supramolecules is evaluated through CO_2 adsorption studies.

Chapter 4 focuses on the synthesis of mesoporous MOPs capable of withstanding the desolvation process, enabling their application as solid-state adsorbents. To achieve this, an isoreticular expansion strategy was applied to a Rh(II)-based parent microporous MOP, leading to the formation of two novel mesoporous cages. This study highlights the critical influence of linker planarity on structural control. In particular, the use of a non-planar linker led to the formation of three unexpected architectures: a trigonal prism, a pentagonal macrocycle, and a hexagonal macrocycle. Finally, the permanent porosity of the isoreticularly expanded cages was confirmed through N_2, CO_2, and H_2O adsorption studies.

Finally, Chapter 5 summarizes the key findings and main conclusions of this Thesis.

Resum

La present Tesi Doctoral està dedicada a l'autoensamblatge d'estructures metal·loorgàniques gegants. En concret, en materials metal·loorgànics discrets o caixes de caràcter mesoporós i en supramolècules oligomèriques. Aquestes entitats es defineixen per tenir una cavitat interior amb un diàmetre superior als 2 nm o per tenir un diàmetre total major als 5 nm, respectivament. L'objectiu d'aquest treball és explorar les estratègies per a obtenir molècules gegants formades per caixes que tinguin porositat permanent. Particularment, emfatitzant en la comprensió dels principis de disseny i de rutes sintètiques necessaris per a construir dites estructures grans i poroses, ja sigui mitjançant síntesi directa o modificacions post-sintètiques. Per últim, aquest estudi busca contribuir en el desenvolupament de molècules gegants i robustes que tinguin porositat permanent, expandint el potencial d'aplicacions en àrees com la separació molecular, la catàlisis o l'emmagatzematge.

Al Capítol 1 es proporciona una visió sobre els fonaments dels materials metal·loorgànics discrets, incloent-hi l'autoensamblatge de metal·lacicles i la formació de caixes metal·loorgàniques tridimensionals. Aquest capítol repassa les aproximacions sintètiques desenvolupades fins al moment i introdueix els conceptes claus per el seu disseny i síntesi. Particularment, s'enfoca en les estratègies utilitzades per a la construcció

d'ensamblatges gegants i el progres que s'ha donat en aquest camp.

Al Capítol 2 s'especifiquen els objectius generals i específics d'aquest Tesi Doctoral.

Al Capítol 3 es presenta la formació de la primera família de supramolècules oligomèriques sintetitzades a partir d'una ruta amb diferents passos. Concretament, es demostra com la connectivitats dels poliedres metal·loorgànics (del seu acrònim en anglès, MOPs) es pot controlar mitjançant una estratègia de protecció-desprotecció, podent obtenir caixes 1-conectades. Aquestes caixes serveixen com a unitat monomèrica per a la construcció de supramolècules oligomèriques, incloent un dímer, un tetràmer i una estructura tipus satèl·lit. Per últim, la porositat permanent d'aquesta nova família de supramolècules es avaluada a partir de l'estudi d'adsorció de CO_2.

El Capítol 4 es centra en la síntesi de MOPs mesoporosos capaços d'aguantar el procés de desolvatació, el que permet el seu ús com a materials adsorbents en estat sòlid. Amb aquesta finalitat, s'ha seguit una estratègia d'expansió isoreticular d'un MOP model de Rh(II) microporós, el que ha donat lloc a la formació de dues caixes mesoporosas noves. En aquest estudi es ressalta la crítica influencia que té la planaritat del lligand en el control estructural. En particular, l'ús d'un lligand que no es pla dona lloc a la formació de tres estructures inesperades: un prisma trigonal, un macrocicle

pentagonal i un macrocicle hexagonal. Finalment, la porositat permanent de les caixes expandides isoreticularment es va confirmar amb l'estudi d'adsorció de N_2, CO_2, i H_2O.

Finalment, el Capítol 5 resumeix els resultats clau i les conclusions principals d'aquesta Tesi Doctoral.

Resumen

La presente Tesis Doctoral está dedicada al autoensamblaje de estructuras metal-orgánicas gigantes. En concreto, a materiales metal-orgánicos discretos o cajas de carácter mesoporoso y en supramoléculas oligoméricas. Estas entidades se definen por tener una cavidad interior con diámetro superior a los 2 nm o por tener un diámetro total mayor a los 5 nm, respectivamente. El objetivo de este trabajo es explorar estrategias para obtener moléculas gigantes formadas por cajas que tengan porosidad permanente. Particularmente, haciendo especial énfasis en la comprensión de los principios de diseño y rutas sintéticas necesarias para construir dichas estructuras grandes y porosas, ya sea mediante síntesis directa o a través de modificaciones post-sintéticas. Por último, este estudio busca contribuir en el desarrollo de moléculas gigantes robustas y con porosidad permanente, expandiendo el potencial de aplicaciones en áreas como la separación molecular, la catálisis o el almacenamiento.

En el Capítulo 1 se proporciona una visión sobre los fundamentos de los materiales metal-orgánicos discretos, incluyendo el autoensamblaje de metalocíclos y la formación de cajas metal-orgánicas tridimensionales. Este capítulo repasa las aproximaciones sintéticas desarrolladas hasta la fecha e introduce los conceptos clave para su diseño y síntesis. Particularmente, se enfoca en las estrategias usadas para la construcción de

ensamblajes gigantes y el progreso que se ha desarrollado en este campo hasta el momento.

En el Capítulo 2 se especifican los objetivos generales y específicos de esta Tesis Doctoral.

En el Capítulo 3 se presenta la formación de la primera familia de supramoléculas oligoméricas sintetizadas mediante una ruta con diferentes pasos. Concretamente, se demuestra cómo la conectividad de los poliedros metal-orgánicos (de su acrónimo en inglés, MOPs) se puede controlar mediante una estrategia de protección-desprotección, permitiendo la formación de cajas 1-connectadas. Estas cajas sirven como unidad monomérica para la construcción de supramoléculas oligoméricas, incluyendo un dímero, un tetrámero y una estructura tipo satélite. Por último, la porosidad permanente de esta nueva familia de supramoléculas es evaluada mediante el estudio de adsorción de CO_2.

El Capítulo 4 se centra en la síntesis de MOPs mesoporosos capaces de aguantar el proceso de desolvatación, lo que permite su uso como adsorbentes en estado sólido. Con este fin, se ha seguido una estrategia de expansión isoreticular de un MOP modelo de Rh(II) microporoso, lo que ha llevado a la formación de dos cajas mesoporosas nuevas. En este estudio se resalta la crítica influencia que tiene la planaridad del ligando en el control estructural. En particular, el uso de un ligando que no es plano lleva a la formación de tres estructuras inesperadas: un prisma trigonal, un macrociclo

pentagonal y un macrociclo hexagonal. Por último, la porosidad permanente de las cajas expandidas isoreticularmente se confirmó mediante el estudio de adsorción de N_2, CO_2 i H_2O.

Finalmente, el Capítulo 5 resume los resultados clave y las conclusiones principales de esta Tesis Doctoral.

Acknowledgements

La meva arribada a NanoUp va ser, si no record malament, al Novembre del 2019. En aquell moment jo era una estudiant de TFG i no creia que pogués aconseguir tot el que ha passat en aquests anys, tant científica com personalment, i aquests agraïments van per totes aquelles persones que han estat donant-me suport i ajudant-me a aconseguir tot això.

Primer de tot vull donar les gràcies tant al Prof. Daniel Maspoch com al Dr. Arnau Carné per donar-me l'oportunitat de començar com a TFG i deixar que seguis formant-me científicament fins a arribar a fer una Tesi Doctoral. Gràcies per confiar en mi en tot moment i donar-me el suport per poder-ho fer. He pogut aprendre molt de vosaltres i de la passió que li fiqueu a la ciència, que és molt inspiradora. Gràcies Arnau per sempre tenir una estona per poder fer una mica de discussió científica, per sempre dir-me les coses amb claredat i per donar-me la oportunitat de poder fer tantes coses diferents en diversos projectes, he aprés molt gràcies a tu.

Durant tots aquests anys he pogut conèixer a molta gent a NanoUp, i he pogut arribar fins aquí gràcies a tots vosaltres, des de les persones que hi eren quan jo era TFG i em van inspirar per a fer un Máster i un Doctorat, fins a les que hi han sigut durant aquests anys compartint tantes hores al meu costat. Gràcies Jordi, Mateusz, Yang, Xu, Inhar, Thais, Sonia, Mary, Funda, Anna, Michele, Sofia, Mateo, Javier, Susana, Marcel, Akim, Kornel, Jorge, José, Marta Sara, Roberto, Dongsik, Partha, Carlos, Fran, Sahel, Benedetta, Lingxin, Xiang, Gerard, Amir, Lorena, Caterina, Chen, Yuto, Chuanqi and Olga. I would like to do a special acknowledgement to Laura, Borja, Sara, Gerard and Yunhui, since the first moment you made me feel as one more, and you made me feel like in a group of friends. Thanks to

many conversations I discovered that doing a PhD could be very enriching (and funny). Seguidamente, a Xulián, con quien compartimos poco tiempo, pero que a todos nos marcó mucho, gracias por toda la energía fresca i divertida que nos trajiste. I would like to express my infinite gratitude to the *PEGgy team*, Laura and Cornelia, I learned a lot next to you, and I had the most amazing time in the laboratory with you. I will never forget those moments of laugh, and I will always remember to go big or go home. Gracias también a Marta y a José, por siempre estar ahí para ayudar en todo lo que necesitamos y darnos una solución. Quiero dar las gracias también a Pilar, aunque (o gracias a que) trabajemos en campos distintos he aprendido mucho a tu lado, me has hecho ver cosas desde otra perspectiva. Gracias por compartir todas tus ideas (normales o de bombero) conmigo, espero poder siempre tener discusiones científicas contigo, son las mejores. Per últim, vull tornar a agrair a la Laura (si, ja és la tercera vegada en aquest paràgraf, només això demostra tot el que has fet), gràcies per ajudar-me a créixer científica i personalment, sense tu, segurament, no estaria on estic ara. Ser el *teu Minion* ha sigut un gran plaer.

M'agradaria donar les gràcies també a la Dr. Judith Juanhuix, amb qui coincidint només algunes hores al mes (i a vegades, a deshores) al Sincrotró, m'ha ajudat a entendre una mica la cristal·lografia. Gràcies per sempre explicar-nos-ho tot fins assegurar-te que ho entenem i per ajudar-nos a poder fer qualsevol experiment. Vull fer també un especial agraïment a la Dr. Irene Fernandez, amb qui també he pogut compartir algunes hores al mes durant tota la Tesis, has fet que el MALDI em sembli una tècnica extraordinària, gràcies també per totes les converses del futur i donar-me sempre la teva ajuda i punt de vista.

He d'agrair també el suport de les meves amigues, gràcies Sílvia, Laies, Núries i Élia per tot. Perqué tot i que sempre estigui al lab i no tingui massa temps, sempre sou al meu costat. Heu fet que el camí sigui una mica més fàcil gràcies a les birres, sopars o viatges. Gràcies també per valorar sempre el que faig i per interessar-vos per aquestes grans caixetes (tot i que no tinguin forma de caixa).

No puedo no dar las gracias a las de la uni, sin vosotras estoy segura que no apreciaría la química tanto como lo hago. Porque pensar en la química es recordar muchas cosas vuestro lado. Gracias Cristina, Sara, Sara Parrón, Sandra, Ylenia, María y Judith.

Me queda dar las gracias a mi familia, siempre confiáis en mí y me hacéis sentir que valgo mucho. Gracias mama y papa, estos años han sido de muchos cambios y os agradezco el apoyo y sobre todo los tuppers. Gracias tata por cuidarme siempre, por haberme dado un segundo hogar y siempre estar a mi lado. Gràcies Eloi, sé que tu ets un dels qui més "ha patit" aquesta Tesi, per tots els dies que hem estat junts i jo t'he dit que no podia jugar i havia de treballar, i tu ho has respectat. Ets un gran exemple per a mi i veure't créixer és meravellós. Por último, aunque ya no estéis, gracias iaios, porque sé que seguís a mi lado y me dais mucho apoyo.

Para el final dejo la persona mas importante de todas, Pilar. Tu llegaste en mitad de este viaje, y seguramente en los momentos mas difíciles. Lo has hecho todo fácil, has dado luz a todo. Gracias por ayudarme siempre y hacer que disfrute aun mas de todo. Compartir esto contigo ha sido único. Gracias.

01

INTRODUCTION

1. Introduction

1.1. The start of supramolecular chemistry

Scientists have long been fascinated by Nature's ability to construct well-defined, large, and functional structures. However, the synthesis of such complex molecules remains a significant challenge in covalent chemistry, despite the extensive catalogue of reagents and reactions available through this approach. In light of these limitations, alternative synthetic strategies have been explored to access structurally intricate systems.

Within this context, Prof. D. S. Lawrence drew an analogy to cellular synthesis, where multiple components are assembled to form a unique and complex entity, an outcome that cannot be achieved

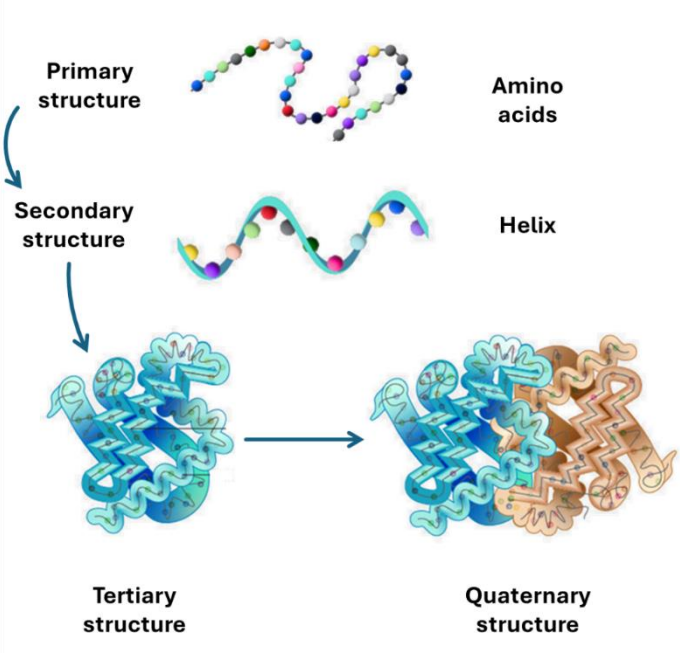

Figure 1.1. Schematic of the formation of a protein through the spontaneous assembly of its parts.

through conventional linear synthesis. As Prof. G. Wald further proposed, individual components of the cell are capable of assembling with high specificity through mutual recognition, thus enabling the spontaneous formation of complex systems.[1] This phenomenon can also be compared to protein folding, where the final three-dimensional structure arises from independently formed subunits that associate in a precise and hierarchical manner (Figure 1.1). Based on these principles, supramolecular chemistry emerged as "the chemistry beyond the molecule", a field concerned with the organization of two or more chemical entities held together by non-covalent intermolecular interactions, ultimately leading to the construction of higher-order structures.

The foundations of this emerging area of chemistry were established in the 1960s through the pioneering work of Prof. C. J. Pedersen, Prof. D. J. Cram, and Prof. J. M. Lehn, who investigated the interactions of crown ethers, cryptands, and cyclodextrins with alkali metal cations, leading to the formation of structures termed “supermolecules”.[2–6] These seminal studies laid the groundwork for the development of supramolecular chemistry, a field that later shifted its focus toward the study of self-assembly processes, defined as the spontaneous organization of well-defined, discrete or infinite architectures from precisely designed molecular components via non-covalent interactions.

In the early stages of self-assembly research, various types of non-covalent interactions were systematically explored, including

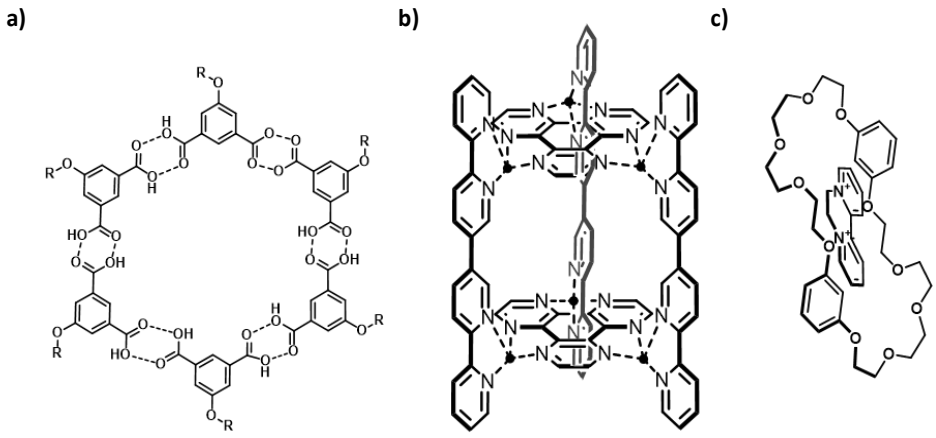

Figure 1.2. Self-assembled molecules obtained through hydrogen-bonding (***a***), coordination (***b***) and π-π (***c***) interactions.

hydrogen bonding, π–π stacking, and metal coordination (Figure 1.2). These interactions not only directed the selective formation of target structures but also played a crucial role in stabilizing the integrity of the resulting assemblies.

This approach has enabled the synthesis of a wide range of molecules and materials, including metal complexes and supramolecular polymers.[7–11] In the present Thesis, the focus is placed on how supramolecular chemistry has been employed to tackle the challenge of constructing defined voids that give rise to functional porous materials. At first glance, the use of inherently weak and reversible supramolecular interactions to stabilize empty spaces may appear counterintuitive. However, the incorporation of coordination bonds, characterized by their strength and directionality, has been critical in facilitating the formation of such stable porous materials.

1.2. Self-assembly of metallacycles

The first deliberate construction of empty space via coordination chemistry was achieved through the synthesis of metallacycles. Coordination bonds form spontaneously between a Lewis base donor, typically an organic ligand bearing donor atoms, and a Lewis acid acceptor, usually a metal center. The geometry of the metal coordination sphere, along with the spatial arrangement of donor atoms within the ligand, dictates the resulting complex's shape and size. Although early examples of metallocycles had been previously reported in the literature,[12,13] Prof. M. Fujita and Prof. P. J. Stang exploited the directional and predictable nature of metal-ligand (M-L) interactions to establish a rational design strategy for the self-assembly of discrete supramolecular architectures. Their contributions defined a new paradigm in coordination-driven self-assembly, enabling the systematic construction of well-defined molecular structures.

Their studies were done using Pd(II) and Pt(II) as metallic centres. These ions adopt square planar geometries, and thus, when combined with bidentate ligands, they tend to generate extended, potentially infinite coordination networks. Nevertheless, the uncontrolled nature of such assemblies can be circumvented by strategically protecting the metal's coordination sites. Instead of using a "naked" metal centre, the introduction of *cis*-blocking ligands restricts the number and orientation of accessible coordination positions, effectively enforcing a 90° angle between

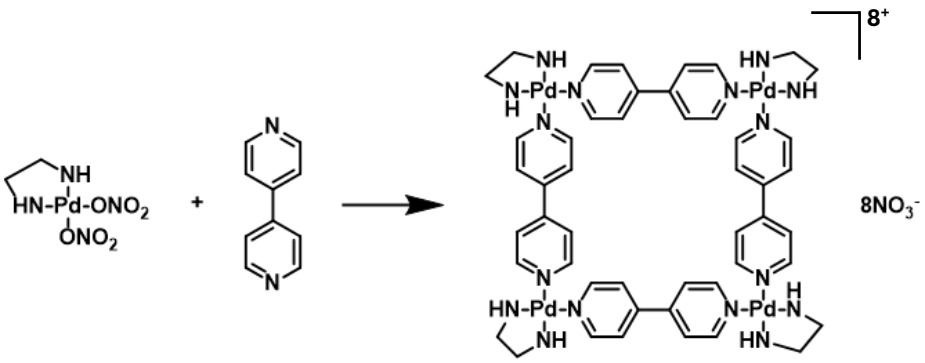

Figure 1.3. Schematic of the reaction for the synthesis of Pd-based macrocycle.

two incoming donor ligands. This strategy shifts the assembly behaviour from extended frameworks to discrete, well-defined supramolecular entities.

The first demonstration of this approach was reported in 1990 by Prof. M. Fujita, who employed a *cis*-protected Pd(II) complex as a coordination building block.[14] In this work, the reaction of the protected Pd(II) center with a linear ditopic ligand, 4,4'-bipyridine, led to the formation of a discrete tetranuclear square-shaped metallacycle (Figure 1.3). Notably, the internal cavity, approximately 8 Å in diameter, was shown to be suitable for the molecular recognition of guest species in aqueous solution. The ease of synthesis, high yields, and functional potential of this self-assembly approach, particularly in host–guest chemistry, motivated extensive studies involving a variety of metals and ligands. These efforts

aimed to establish a broader library of self-assembled architectures featuring well-defined and functional internal voids.

In the following year, Prof. M. Fujita further demonstrated the generality of the protected-cluster strategy by assembling a tetranuclear square metallacycle using the same linear bidentate ligand, but with Pt(II) as the metal centre.[15] In this case, the formation of the target architecture proved to be more challenging, due to the higher coordination strength of the Pt(II)-N bond relative to Pd(II)-N. As a result, reactions conducted at room temperature yielded a mixture of oligomeric species. By contrast, when the self-assembly was carried out at 100 °C, the desired discrete square complex was successfully obtained. This temperature-dependent outcome was attributed to the preferential formation of kinetically favored intermediates under mild conditions, whereas elevated temperatures promoted the generation of the thermodynamically most stable product.

Building on the early development of macrocyclic assemblies, Prof. P. J. Stang further demonstrated the versatility of coordination-driven self-assembly through the use of cluster-protected metal centers. In his work, a series of square metallacycles were synthesized by varying both the protecting groups on the metal centers and the nature of the organic ligands employed.[16,17] These studies highlighted how rigid linkers with well-defined 90° bite angles effectively direct the formation of tetranuclear architectures. Moreover, by tuning the structural components, it was possible to

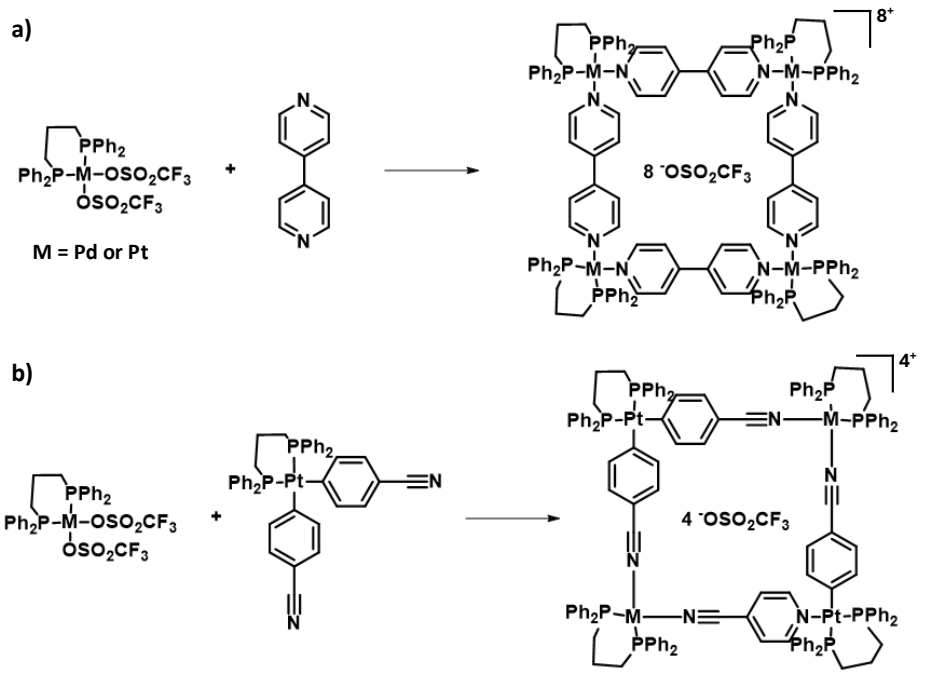

Figure 1.4. Examples of tetranuclear macrocycles with different protecting group (***a***) and organic linker (***b***).

access assemblies with different physicochemical characteristics, for example, generating neutral instead of cationic complexes (Figure 1.4).

A few years later, in 1996, Prof. M. Fujita investigated the synthesis of metallacycles with larger internal cavities by modulating ligand length through the incorporation of various spacers between two aromatic rings.[18] With this work it was demonstrated the feasibility of making tetranuclear square metallacycles with different sizes. Interestingly, the study revealed that, when ligands longer than 4,4'-bipyridyl were employed, a competing self-assembled specie emerged: a trinuclear triangular metallacycle. Although this

triangular structure is less favourable from an enthalpic standpoint, it is entropically preferred due to its formation from fewer components.

The ratio between the triangular and square assemblies was shown to depend on the concentration of the precursors, indicating a thermodynamically controlled equilibrium. Moreover, modifying the cluster's protecting group with bulkier substituents shifted the product distribution, highlighting the influence of steric hindrance. The formation of this mixture illustrated the synthetic challenges associated with constructing such supramolecular complexes, even when using rigid and directional building blocks.

The unexpected discovery of a trinuclear macrocycle sparked scientific interest in exploring new structures with alternative geometries. As a result, various strategies were employed, such as modifying the ligand's bite angle or altering the directionality of the metal cluster, to broaden the scope of the self-assembly process and assess its limitations.[19–22]

In an initial attempt to use flexible ligands, Prof. M. Fujita designed three 4,4'-bipyridyl-based ligands by inserting a carbon atom between the two heterocycles. This structural modification caused a significant reduction in the bite angle, from 180° in the original linear ligand to approximately 109° or 120° in the new derivatives. The altered angle promoted the formation of dimeric species, composed of two metal centers and two organic ligands. This

outcome further demonstrated the role of entropy in favoring the formation of closed, discrete assemblies with fewer components over extended polymeric structures (Figure 1.5a).

In another attempt to control the geometry of the final assembly, several studies demonstrated that the use of rigid ligands with an appropriate bite angle and/or bulky protecting groups on the metal center can direct the formation of trimeric macrocycles, composed of three metal centers and three organic ligands (Figure 1.5b).

Simultaneously, Prof. P. J. Stang showed that the final geometry of the assembly can be carefully programmed to yield alternative architectures, such as an hexagon.[23] To achieve this, it was rationalized that 120° coordination angles at the corners, combined with suitable linkers, were required. For this purpose, two types of

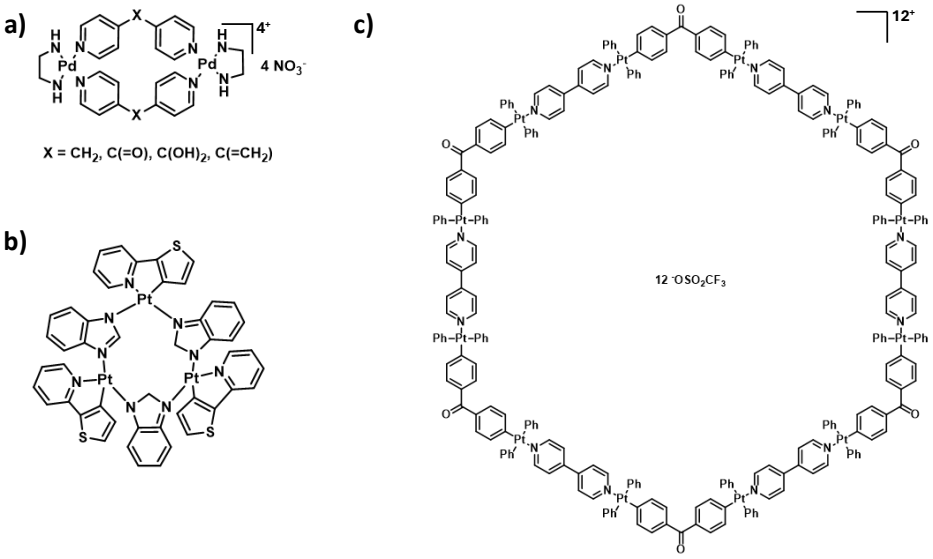

Figure 1.5. Dinuclear (***a***), trinuclear (***b***) and hexanuclear (***c***) macrocycles.

ligands were employed: one with a 120° bite angle (a bispyridyl ketone) and another linear ligand with a 180° bite angle (4,4'-bipyridyl). Additionally, a new Pt(II) complex with 180° directionality was introduced by replacing its bidentate ligands with monodentate ones, enabling its use as a linear metallic connector. The reaction of these components, the two ligands and the Pt(II) center, resulted in the formation of the expected hexagonal macrocycle (Figure 1.5c).

These findings collectively demonstrated that the directional nature of coordination bonds enables the rational design of supramolecular structures with defined internal cavities through geometric control of the molecular building blocks.

1.3. Self-assembly of three-dimensional structures: Synthesis of metal-organic cages

After successfully forming polygonal structures through the self-assembly of metal nodes and organic linkers, researchers confirmed the feasibility of creating molecules with different shapes, sizes, and functions. The next step was to move beyond two-dimensional (2D) assemblies and construct three-dimensional (3D) discrete metal–organic cages (MOCs).

1.3.1. Metal-pyridyl based structures

The first reported example of a self-assembled molecular cage was developed by Prof. M. Fujita. He followed the same strategy of using cluster protection to control the directionality of the metal centre, along with a carefully designed organic linker. To obtain a 3D

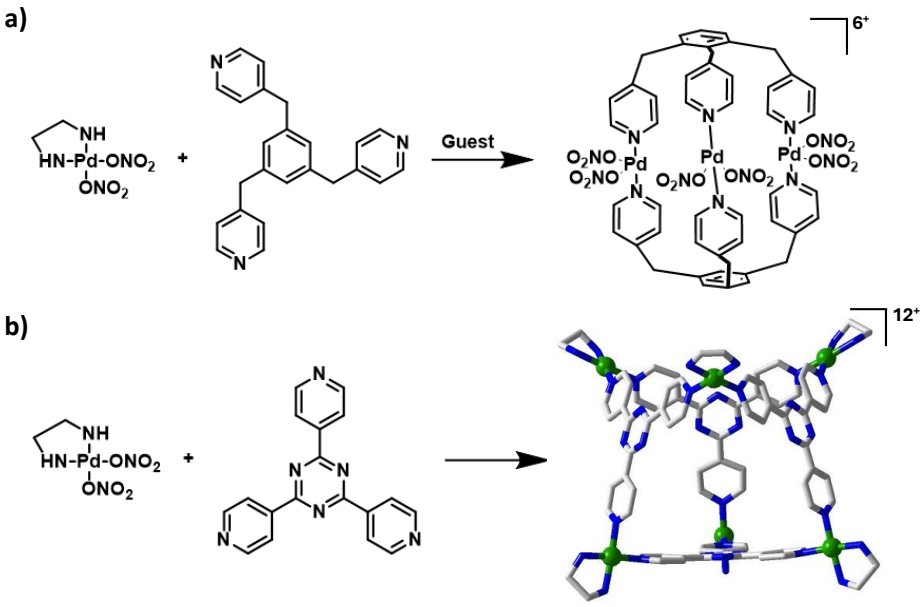

Figure 1.6. ***a)*** Synthesis of 3D MOC with a flexible ligand. Note that in the final MOC the guest is inside the cage, and it has NO_3^- as counter anion, however they have been omitted for clarity. ***b)*** Synthesis of 3D MOC with a rigid ligand and the crystal structure of the final product.

structure, a tridentate ligand, 1,3,5-tris(4-pyridylmethyl)benzene, was used instead of a bidentate pyridyl moiety.[24] Despite this, the design was not sufficient to prevent the formation of oligomeric byproducts instead of the desired MOC.

Interestingly, it was shown that the presence of a molecular guest during the assembly directed the formation of the cage host. This finding demonstrated the feasibility of obtaining MOCs through self-assembly (Figure 1.6a).

That same year, Prof. M. Fujita demonstrated that using a rigid ligand, rather than the more flexible one used in the previous

example, directs the formation of a MOC without the need for an additional guest during synthesis (Figure 1.6b). He further validated the approach by introducing one or two phenyl rings into the rigid ligands. In all cases, the same MOC structure was obtained. As a result, the cavity size increased, yielding assemblies with internal diameters ranging from 2 to 5 nm, thus reaching the nanometre scale.[25]

Later, in 2004, Prof. M. Fujita introduced the possibility of obtaining discrete MOCs using bidentate ligands and naked Pd(II) ions. This strategy took advantage of all available coordination sites of the metal centre.[26] It was reasoned that combining a square-planar metal centre with a linear ligand (180° angle) would result in an infinite 2D network. In contrast, using a bent ligand with an angle of approximately 120° would led to the formation of a spherical, finite assembly with a constant radius of curvature.

This concept was confirmed by reacting $Pd(NO_3)_2$ with 1,3-di(pyridin-4-yl)benzene. The system self-assembled into a cuboctahedron with a diameter of approximately 3.4 nm and in high yield. The strategy's versatility was further demonstrated using alternative ligands. In one case, the central benzene ring was replaced by a furan ring (Figure 1.7a). In another, two phenyl rings were inserted between the central core and the terminal pyridines. In both cases, the self-assembly yielded cuboctahedral MOCs in high yields.

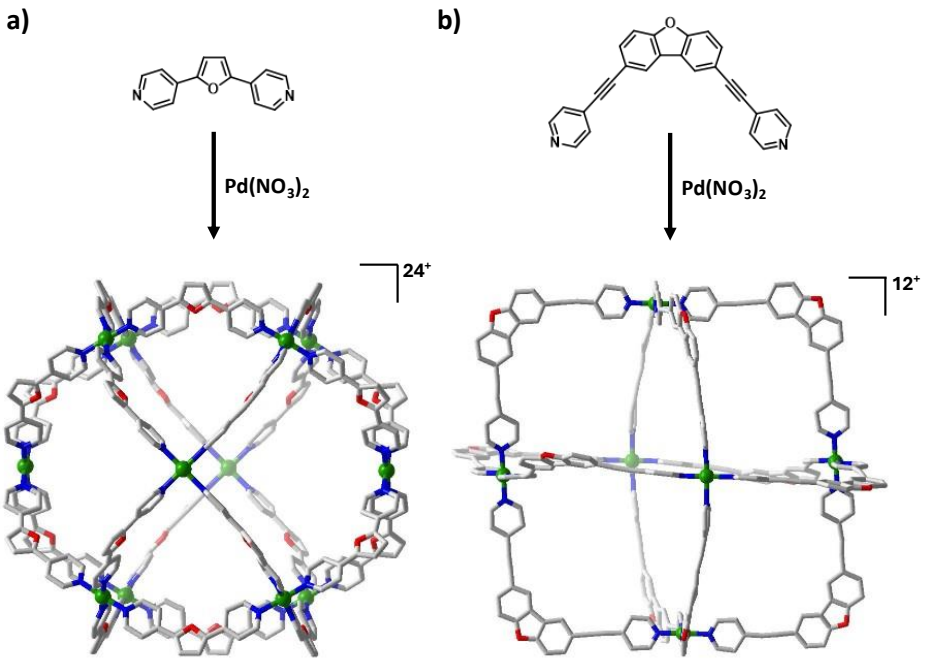

Figure 1.7. Single crystal structures of a cuboctahedral (***a***) and an octahedral (***b***) MOC.

Finally, the approach also enabled peripheral functionalization. This was exemplified by modifying the initial bent ligand with fullerene and porphyrin groups, resulting in cuboctahedral MOCs bearing different functional units on their surface.

The synthesis of this family of $M_{12}L_{24}$ 3D finite spheres helped clarify how the assembly of metal ions and bridging ligands leads to the formation of discrete, highly symmetrical molecules. These structures often correspond to Platonic or Archimedean solids. Platonic solids are composed of identical regular polygons, while Archimedean solids combine different types of regular faces. This insight suggested the possibility of obtaining other geometries

beyond the cuboctahedron. In principle, structures with the general formula M_nL_{2n} could be synthesized for n = 6, 12, 24, 30, and 60.

To demonstrate this, Prof. M. Fujita designed a ligand with a 90° bite angle. Its self-assembly with $Pd(NO_3)_2$ produced a smaller MOC with molecular formula M_6L_{12} and octahedral geometry (Figure 1.7b).[27] Building on this concept, Prof. Fujita began synthesizing a broader family of M_nL_{2n} 3D finite spheres with varying shapes, sizes, and functionalities. A few years later, the strategy was extended to the use of Pt(II) instead of Pd(II). As previously observed in macrocyclic systems, Pt(II)-based MOCs showed enhanced stability.[28]

1.3.2. Subcomponent self-assembly: Chelate effect

In parallel with the development of self-assembly processes involving square-planar Pd(II) and Pt(II) metal centres and rigid ligands, an alternative strategy known as subcomponent self-assembly has also been investigated.[29] This approach relies on the simultaneous formation of dynamic covalent bonds, specifically, imine bonds, and coordination bonds between nitrogen donor atoms and metal centres during the self-assembly process. The strategy capitalizes on the *in-situ* formation of imine bonds, which generate ligands bearing nitrogen donor atoms. In combination with pyridine units within the same ligand structure, also acting as nitrogen donors, this results in organic components capable of forming chelating complexes (Figure 1.8).[30]

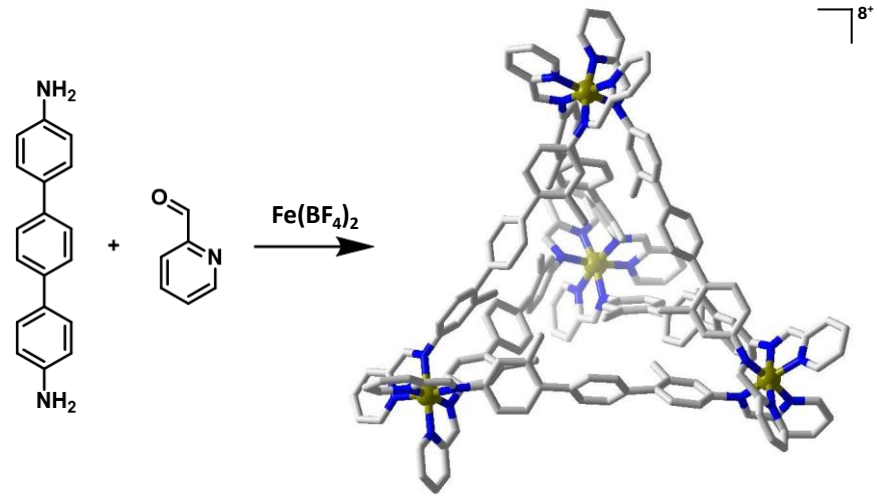

Figure 1.8. Synthesis of tetrahedral cage through subcomponent self-assembly strategy.

The formation of a chelated structure eliminates the need for capping ligands and has been shown to enhance the stability of the final complex through a cooperative effect. This has enabled, for example, the synthesis of water-soluble cages using Cu(I) centres and imine-based linkers, despite the fact that both, the metal centre and the imine bond, are typically known to be hydrolytically unstable.[31,32]

This strategy also employs a symmetry-adapted approach to enable the construction of the target structure. In this methodology, the symmetry elements of the desired architecture are first identified to guide the selection of appropriate building blocks for both the self-assembly process and the synthons involved in the imine condensation reaction. The resulting ligands typically exhibit a significant degree of internal twisting, which imparts the necessary

directionality for the coordination bonds to occupy all available coordination sites of the metal centres.

This field has been extensively developed by Prof. J. Nitschke, who has demonstrated the feasibility of this approach through the synthesis of a wide variety of Cu(I), Co(II), Ni(II), and Fe(II)-based cages in combination with diverse ligands, varying in size, functionality, and directionality.[33–36] By taking advantage of the *in situ* formation of chelating ligands from simple synthons (amines and aldehydes), complex architectures with Platonic and Archimedean symmetries have been achieved, for example, M_8L_6

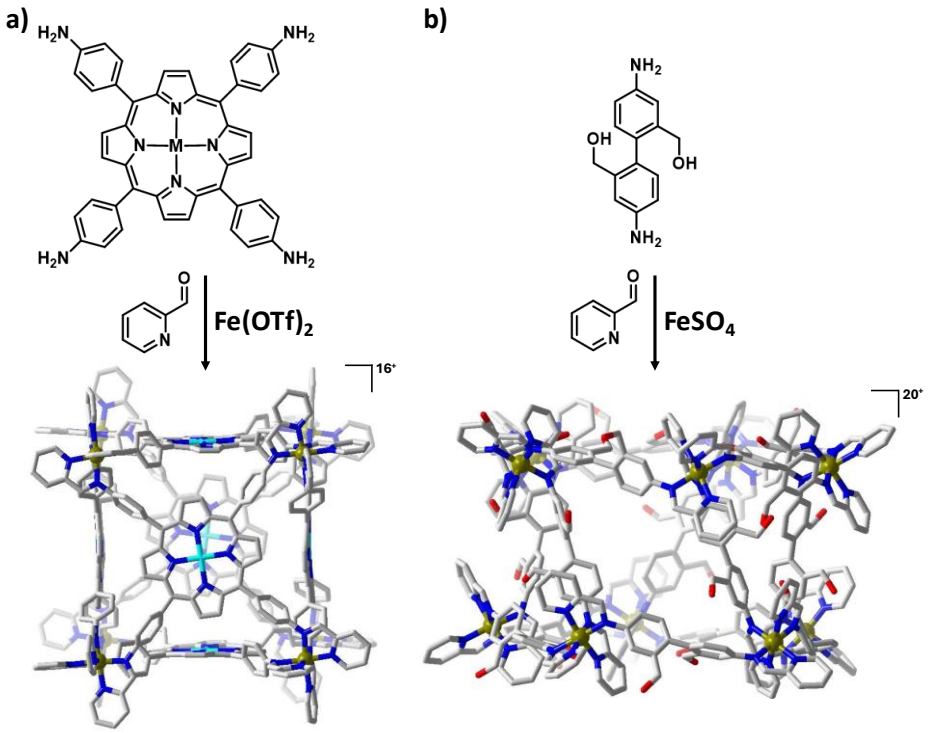

Figure 1.9. Single crystal structures of a cubic (***a***) and a pentagonal prismatic (***b***) MOC.

cubes, M_4L_4 tetrahedra, and other types of assemblies such as pentagonal $M_{10}L_{15}$ prisms (Figure 1.9).[37,38] These results highlight the potential for constructing highly complex and robust structures from relatively simple starting components in a one-step reaction.

1.3.3. Carboxylate-metal based structures

Almost simultaneously with the development of N-donor ligand chemistry for cage construction, another type of coordination bond was explored for the same purpose. In this case, metal nodes were connected by O-donor ligands, forming carboxylate-metal (COO–M) coordination bonds. The first implementation of this strategy was reported simultaneously by Prof. O. Yaghi and Prof. M. J. Zaworotko in 2001.[39,40] These studies built upon the previously established stability of metal–organic frameworks (MOFs), enabled by the use of rigid carboxylate ligands and metal ions or clusters. The synthesis of extended MOFs typically involves linear linkers that propagate the network infinitely. It was therefore hypothesized that replacing a linear ligand with an angular one, specifically, with a bite angle of 120°, could result in the formation of a discrete molecule. This was demonstrated by the reaction of copper(II) acetate with 1,3-benzenedicarboxylate (BDC), leading to the synthesis of a cuboctahedral structure composed of 12 Cu(II)–Cu(II) paddlewheel units and 24 ligands, designated as MOP-1 (Figure 1.10a). This structure exhibits enhanced stability compared to the previously described Pd(II)/Pt(II) cages, as evidenced by its resistance to harsh

conditions, such as solubilization in DMF under reflux. Furthermore, thermogravimetric analysis (TGA) showed that it possesses thermal stability comparable to that of extended paddlewheel-based porous frameworks. Interestingly, although individual paddlewheel complexes are not inherently stable, a positive chelate cooperativity effect emerges upon formation of finite cages or infinite frameworks.[41] The synthesis of MOP-1 thus opened the door to a new class of neutral metal–organic polyhedra (MOPs), which are soluble in common organic solvents, stable under harsh conditions, and possess large accessible internal cavities.

However, the solubility of MOP-1 was very limited, which was attributed to the absence of pendant functional groups on its surface, restricting its solubility to DMF under reflux conditions. Nevertheless, the incorporation of non-bridging pendant functional

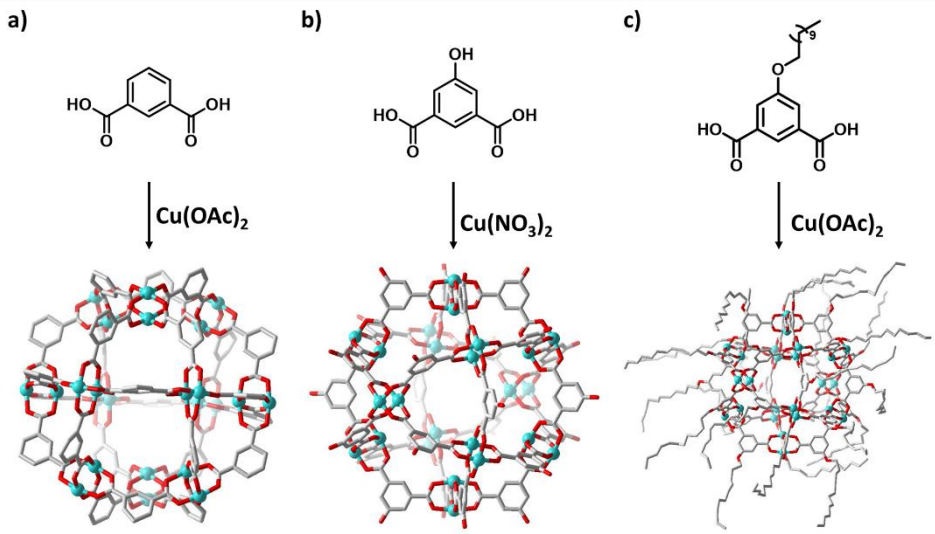

Figure 1.10. Single crystal structure of cuboctahedral Cu(II)-based MOPs with no surface functionality (***a***) and with hydroxyl groups (***b***) and alkoxy chains (***c***) as pendant surface groups.

groups onto the surface of the cage significantly enhances solubility. Thus, solubility is largely dictated by the nature of these pendant groups. This principle was first demonstrated by Prof. M. J. Zaworotko, who self-assembled 5-hydroxy-1,3-benzenedicarboxylate with Cu(II) paddlewheel units to yield a cuboctahedral cage decorated with 24 hydroxyl groups on its surface (Figure 1.10b).[42] Remarkably, this MOP was soluble in various alcohols (e.g., methanol and ethanol) as well as in DMF. Some years later, this concept was further exemplified by Prof. O. Yaghi, who employed a BDC-derivative ligand functionalized with a dodecoxy chain for the synthesis of MOP-18. This structure featured alkyne moieties as pendant groups, imparting solubility in common organic solvents such as chloroform, toluene, and tetrahydrofuran, among others (Figure 1.10c).[43] Subsequently, Prof. H. C. Zhou advanced this approach by reporting a Cu(II)-based cuboctahedral MOP synthesized using 5-sulfono-1,3-benzenedicarboxylate. The presence of sulfonate pendant groups on the surface rendered the cage water-soluble. However, due to the hydrolytic instability of Cu–carboxylate coordination bonds, the cage underwent decomposition within minutes of solubilization in aqueous media.[44]

These results demonstrate that MOPs can be regarded as soluble molecular entities, which facilitates their use in a variety of applications, such as host–guest chemistry or their incorporation into more processable materials, such as membranes.

Nonetheless, the Cu(II)–Cu(II) paddlewheel unit lacks of sufficient stability for its use in aqueous environments, which significantly limits its applicability, as water, particularly moisture, is ubiquitous across many application domains.

1.3.4. Diversity in the metallic nodes: Increasing stability

Apart from employing different ligands to increase structural diversity, a wide range of metal nodes has been explored in the case of MOPs to enhance their structural stability. Numerous metals have been successfully utilized in the self-assembly process; paddlewheel-based nodes have been obtained from Cu(II), Mo(II), Rh(II), Cr(II), Ni(II), Rh(II/III), Zn(II), and Ru(II).[45–50]

In 2005, Prof. H. C. Zhou reported the first synthesis of a cuboctahedral MOP based on a Mo(II)–Mo(II) paddlewheel cluster. This cluster features a quadruply bonded Mo(II)–Mo(II) interaction, which involves direct metal–metal bonding. Its use broadens the set of available building blocks for MOP construction. It also introduces new electrochemical and spectroscopic functionalities. At the same time, it enhances the structural stability of the resulting cages.[51] Indeed, the modified electrochemical properties allow for the investigation of these cages in solution using techniques such as ultraviolet-visible (UV-Vis) spectroscopy, nuclear magnetic resonance (NMR), and cyclic voltammetry (CV).

In 2010, Prof. Zhou demonstrated that Mo(II)-based MOPs exhibit excellent porosity in the solid state, as confirmed by nitrogen adsorption measurements (Figure 1.11a). The enhanced porosity of Mo(II)-based MOPs compared to their Cu(II) analogues was attributed to the presence of metal–metal bonds in the Mo(II) paddlewheel clusters. However, despite the improved solid-state stability, the Mo(II)-Mo(II) paddlewheel does not impart water stability to the structure.

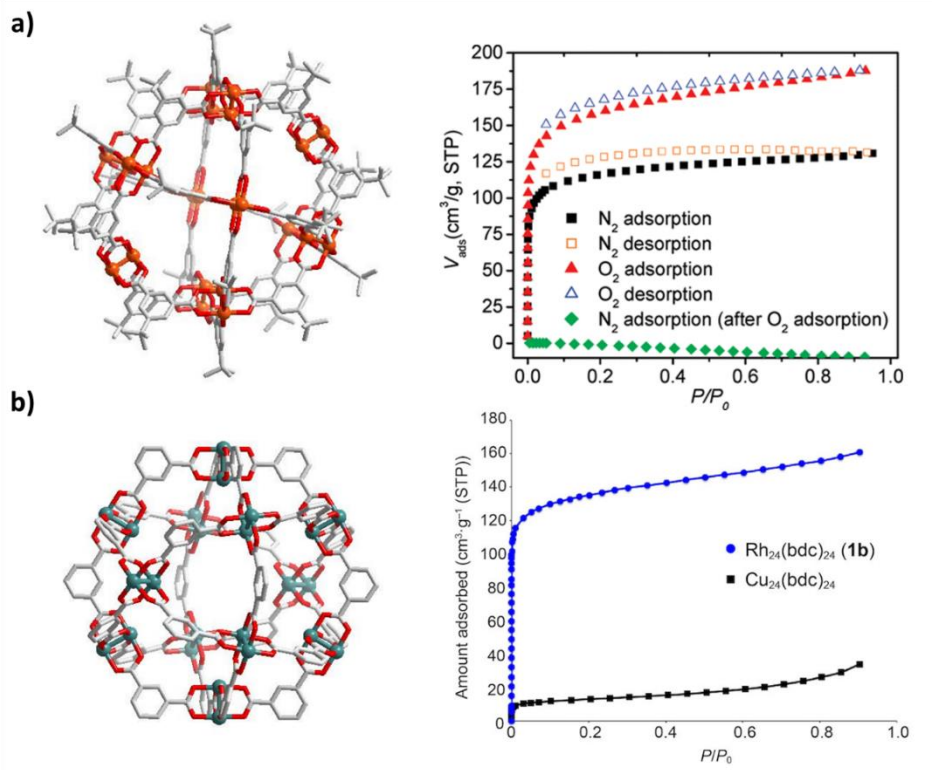

Figure 1.11. ***a)*** Single crystal structure of a Mo(II)-based MOP (left) and its O_2 and N_2 adsoprtion isotherms (right). ***b)*** Single crystal structure of a Rh(II)-based MOP (left) and its N_2 adsoprtion isotherm in comparison with the one from its Cu(II) analogue (right).

Subsequently, in 2016, Prof. S. Kitagawa and Prof. S. Furukawa reported the use of a more robust Rh(II) paddlewheel to construct a cuboctahedral MOP (Figure 1.11b).[52,53] Similar to previous findings, the Rh(II)-based structure exhibited superior adsorption properties compared to its Cu(II) counterpart, further confirming its enhanced solid-state stability. Notably, the material could be activated under vacuum at 100 °C while retaining its porosity. Moreover, TGA revealed a decomposition temperature of approximately 300 ^{0}C. Both findings support the superior thermal stability of the Rh(II)-based structure. Additionally, the paramagnetic nature of the Rh(II) paddlewheel enables solution-state studies.

In subsequent years, the chemical stability of Rh(II)-based MOPs was further investigated under various challenging conditions, including exposure to coordinating ligands, elevated temperatures, and aqueous media at high pH. These studies demonstrated that the Rh(II) paddlewheel cluster not only provides exceptional structural robustness but also remarkable chemical stability.[54–56]

Another strategy to improve the robustness of MOPs is to increase the bond strength between the metal and the ligand. This can be achieved by using metal ions with high valence states. Such ions can form high-nuclearity clusters with strong M-L nodes. Alternatively, metals with high charge density, known as hard acids, can form strong bonds with carboxylates, which are hard bases. This follows Pearson's hard and soft acid–base (HSAB) principle.[57] In this context, Zr^{4+} has been used to synthesize Zr(IV)-based MOPs.

These materials are self-assembled from trinuclear, ligand-bridged ((C_5H_5)Zr-cation clusters and ditopic or tritopic ligands (Figure 1.12). This synthetic approach was first reported by Prof. M. Hong. The resulting Zr(IV)-MOPs showed high stability as solid adsorbents retaining their structure after desolvation.[58]

Later, Prof. S. Q. Zhang demonstrated the exceptional chemical stability of these structures, with the synthesis of a Zr(IV)-MOP functionalized with SO_3^{2-} groups on its surface. This material could be dispersed in water across a wide pH range (from pH 3 to pH 11)

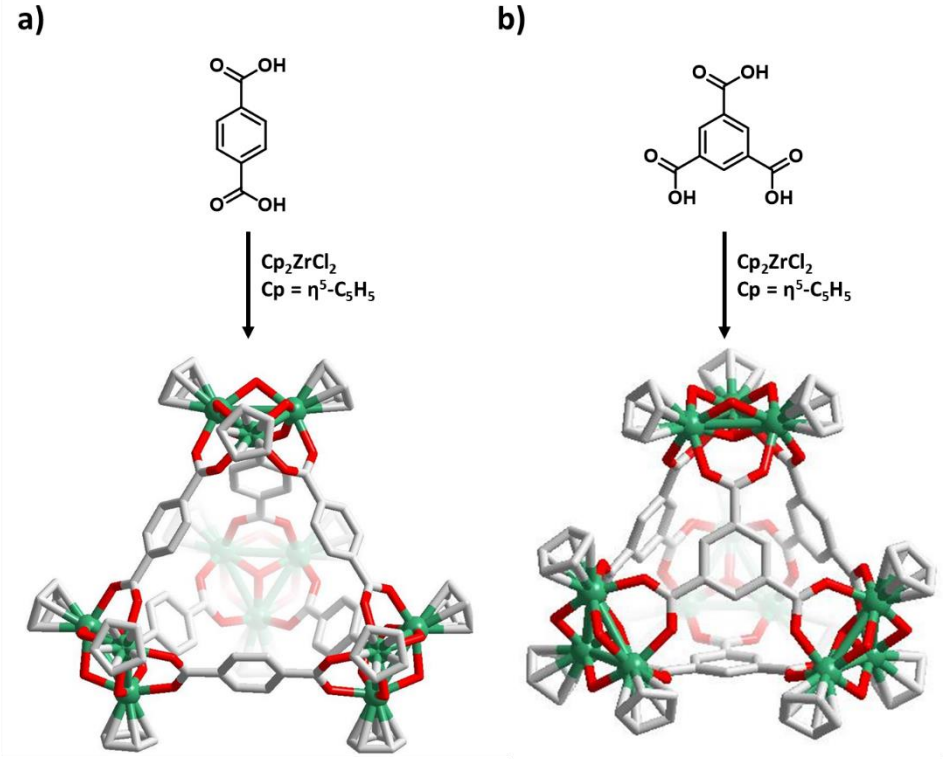

Figure 1.12. Single crystal structure of Zr(IV)-based MOPs synthesized with ditopic (***a***) and tritopic ligands (***b***).

without losing its structural integrity.[59]

1.4. Porous properties of MOCs/MOPs

The discrete assemblies described in the previous sections share similar structural features, where MOPs have been postulated a sub-class of MOCs. The main characteristic of MOPs is their permanent porosity in the solid state. This is achieved thanks to their increased stability in comparison to other type of MOCs, which comes from their carboxylate-metal coordination bond.[60,61] The porosity of MOCs and MOPs arises from an internal cavity that is accessible and capable of hosting guest molecules. Both have been used to exploit this cavity for various applications, including catalysis, molecular stabilization, separation, and storage.[50,62–66]

In this scenario, their use can be divided in solution or in solid state, depending on the use of the cage dissolved or in dispersion (solution state), or if the cavity is free of solvent (solid state). These two modes define distinct research approaches. MOCs have been more frequently studied in solution compared to MOPs. This may be due to their frequent use of diamagnetic metal ions (e.g., Pd(II), Pt(II), Fe(II)) and the presence of aromatic panels oriented toward the internal cavity. These features enhance host–guest interactions.[67–72] In contrast, the greater structural stability of MOPs makes them better suited for studies in the solid state. MOCs, on the other hand, are rarely used in solid-state applications due to their limited stability.[73–78]

1.4.1. Porosity in solution

Interest in the porous properties of MOCs through host–guest interactions emerged with the synthesis of the first cages. Many examples of guest inclusion in MOCs have since been reported. These systems can be studied in solution using techniques such as UV-Vis spectroscopy, ^{1}H-NMR, and even single-crystal X-ray diffraction (SC-XRD), which confirm strong binding between host and guest.[79] These studies also revealed that the cavity's microenvironment can alter the physical and chemical properties of the guest molecules. As a result, MOCs have been used in solution to carry out reactions that are otherwise inaccessible. This may be due to the guest's insolubility or because the confined space inside the cavity promotes selective product formation via steric effects.[5,80]

A notable example was reported by Prof. M. Fujita in 2006. His group used a Pd(II)-based cage as a water-soluble host to perform a Diels–Alder cycloaddition. The reaction took place in aqueous media and led to an unusual product, highlighting the green chemistry potential of the system and the confinement effect.[81] Normally, Diels–Alder reactions with anthracenes produce an adduct via the 9,10-positions of the central ring. However, when confined inside the cage, the reactivity shifts, and the product arises from the 1,4-positions instead (Figure 1.13a).

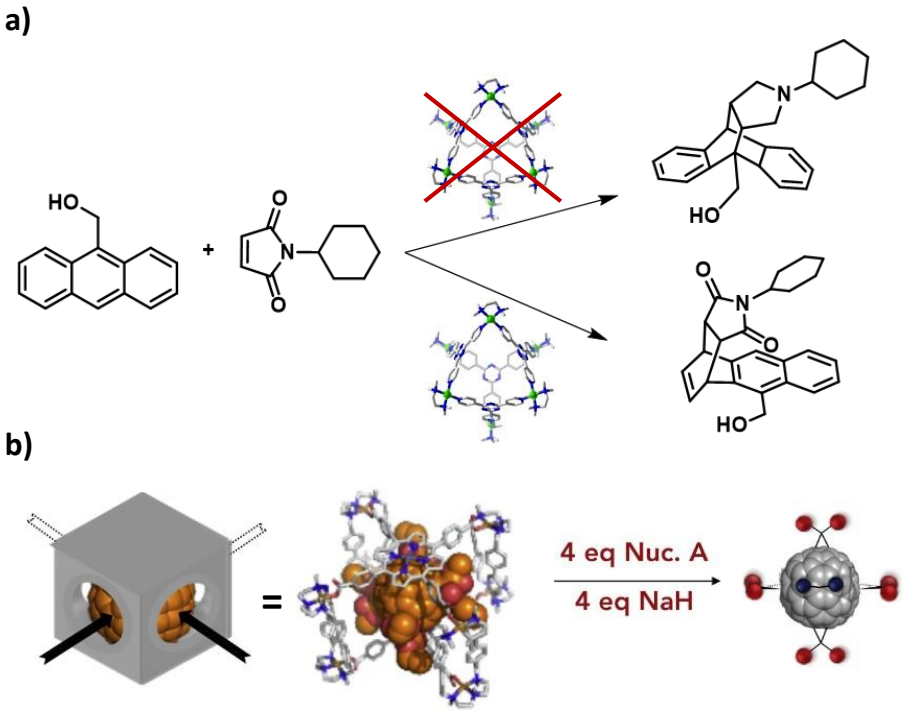

Figure 1.13*. *a) Diels-Alder reaction in the absence (top) and in the presence (bottom) of the catalytic Pd-based MOC. ***b)*** MOC used to mark selected positions of a C_{60} and the product obtained.

Guest encapsulation within MOCs can also be used to direct or protect specific reactive sites. This strategy was applied by Prof. X. Ribas, who controlled the regioselectivity of fullerene functionalization by encapsulating it within a MOC (Figure 1.13b).[82]

In addition, the possibility of precisely controlling the shape and size of the cavity, as well as the orientation of internal functional groups, allows for the design of structurally and chemically tailored cavities. These features make MOCs highly suitable for separation processes.[65,83,84]

1.4.2. Porosity in solid state

As previously explained, MOPs emerged from the challenge of isolating discrete cages rigid enough to maintain their structure in the absence of guest molecules. Achieving structural integrity with an empty internal cavity was essential to enable porosity in the solid state. Since the synthesis of the first MOP nearly 25 years ago, approximately 130 surface areas have been reported. A significant increase has occurred in the last five years, reflecting growing scientific interest in developing MOPs with high adsorption capabilities.[73]

Prof. O. Yaghi was the first to report a Brunauer–Emmett–Teller (BET) surface area for a MOP, demonstrating the permanent porosity of MOP-28. This Cu(II)-based truncated octahedron exhibited a remarkable surface area of 914 $m^2 g^{-1}$.[85] Following this, more robust assemblies were developed through the use of paddlewheel nodes featuring metal–metal bonds. These designs led to larger surface areas, culminating in a key milestone in 2019. That year, Prof. E. D. Bloch synthesized a Mo(II)-based MOP assembled from 5-*tert*-butyl-1,3-benzenedicarboxylate, which reached a surface area of 1320 $m^2 g^{-1}$.[86] Even so, these values remain well below those of MOFs, which can exceed 7000 $m^2 g^{-1}$. This difference is mainly due to two factors: (i) the less efficient packing of molecular assemblies in the solid state, and (ii) the partial loss of structural order upon desolvation.[87]

The solid-state porosity of MOPs has opened new possibilities for gas storage and separation. In addition, the processability of the ligands facilitates their integration into functional materials such as membranes and monoliths.

1.5. Giant assemblies

Given the wide range of structures that can be designed by combining different metal centers and organic ligands, the synthesis of giant molecular cages has attracted considerable attention. This interest stems from the complexity involved in assembling large structures with distinct molecular weights and dimensions. In this context, the concept of “giant molecules” can be viewed from two perspectives. The first refers to a single large cage formed by metal nodes and organic linkers, creating one central cavity. These are typically defined as mesoporous cages. The second refers to oligomeric supramolecules, where multiple smaller molecular units assemble into a large structure without forming a confined space, similar to a protein built from various subunits (Figure 1.14). Despite the growing interest and the publication of several examples, no clear definition of what qualifies as “giant” has been established. For the purposes of this discussion, only MOCs will be considered. Structures with an internal cavity larger than 2 nm, or a total diameter greater than 5 nm, will be classified as giant. This definition is based on two criteria: (i) an internal diameter above 2 nm marks the transition

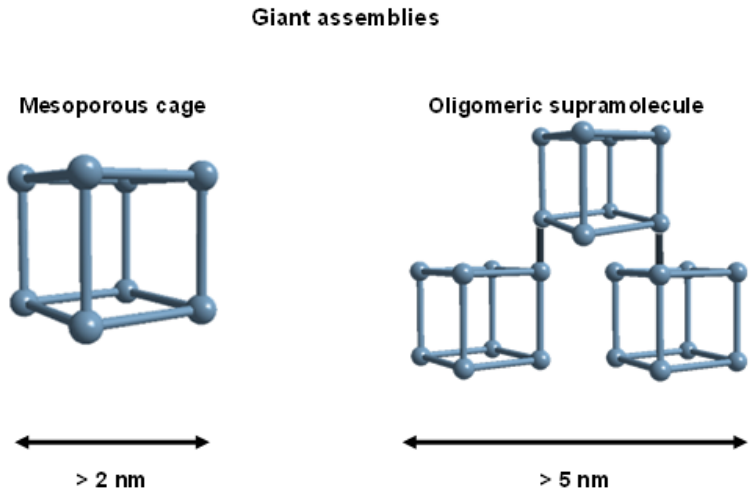

Figure 1.14. Schematic of the two types of giant assemblies.

from microporous to mesoporous systems, according to IUPAC,[88] and (ii) most metal-organic assemblies are smaller than 5 nm in total size.[89,90]

The synthesis of giant molecular cages is not trivial. Compared to smaller assemblies, these systems present greater challenges. This is due to the reversible nature of the interactions involved in self-assembly, which must reach thermodynamic equilibrium. As the number of building blocks increases, their rotational and translational freedom become more restricted. As a result, larger assemblies are entropically less favorable than smaller ones. Nonetheless, giant assemblies are clearly feasible in Nature, as seen in virus capsids and protein complexes. This suggests that general principles guiding the self-assembly of complex, multicomponent systems do exist.

Beyond their structural complexity, giant molecular cages are also of interest due to the new properties they can exhibit. These include the ability to encapsulate large guest molecules and their potential applications in gas storage.

1.5.1. Mesoporous cages

The previous sections of this introduction have focused on the synthesis of molecular cages. These studies have enabled the development of a wide catalogue of metallic nodes and organic ligands, resulting in a variety of final shapes and sizes.

In supramolecular chemistry, the final structure of a cage is determined by two key factors: the coordination geometry of the metal node, and the directionality and bite angle of the ligand. Based on these principles, there are two main strategies to self-assemble giant hollow supramolecules: (i) isoreticular expansion of the ligand, or (ii) enlargement of the bite angle.

1.5.1.1. Isoreticular expansion

The term isoreticular expansion was first introduced by Prof. O. Yaghi in 2002. He demonstrated that the structure of a parent MOF could be enlarged to form larger pores while preserving the original topology. This was achieved by maintaining the key structural attributes of the building blocks: the coordination geometry of the metal nodes and the bite angle of the ligands.[91] This concept was validated through the synthesis of a family of MOF-5 materials using ligands of increasing length, which led to progressively larger pore

sizes. Since then, isoreticular expansion has been widely applied not only in the field of MOFs, but also in the synthesis of giant cages.[92–94]

During the same decade, the use of extended ligands was also explored in the self-assembly of paddlewheel-based cages. Prof. O. Yaghi showed that isoreticular expansion could be applied to MOPs by replacing the standard BDC ligand with longer analogues, such as 2,7-naphthalenedicarboxylate or 1,1'-binaphthyl-4,4'-dicarboxylate. In all cases, the cuboctahedral geometry of the resulting MOPs was preserved, while the inner diameter increased accordingly (Figure 1.15).[95] These MOPs reached maximum internal and external diameters of 2.4 nm and 2.9 nm, respectively.

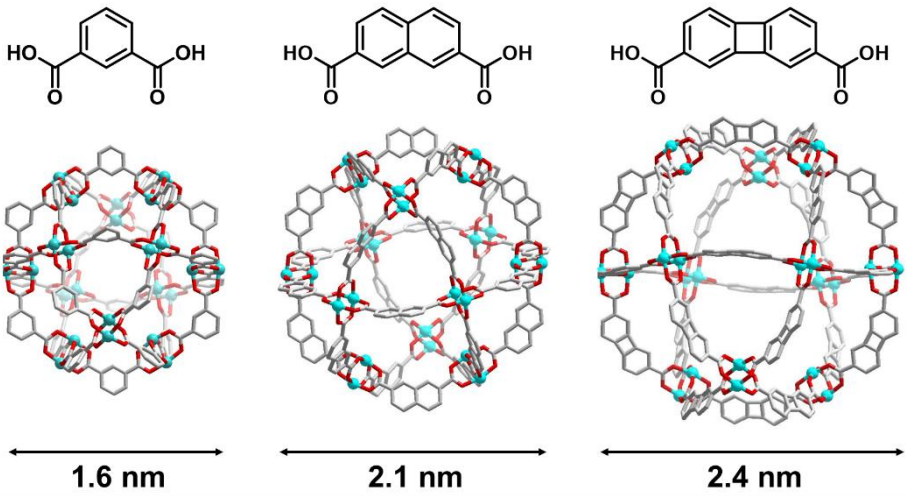

Figure 1.15. Single crystal structures of the isoreticular expansion of Cu(II)-based MOPs. Inner diameter measured from Cu(II) of opposite vertices.

Despite these advances, no permanently porous MOPs with internal diameters of 2 nm or greater have yet been reported in the solid state. This limitation arises from the tendency of large, empty cages to collapse upon solvent removal.

Prof. M. Fujita later demonstrated that isoreticular expansion could also be extended to the synthesis of MOCs. In 2012, he modified the common organic linker 1,3-bis(pyridin-4-ylethynyl)benzene by adding two additional benzene rings. The resulting Pd(II)-based cage exhibited a diameter of 5.0 nm. The large cavity enabled the encapsulation of macromolecules such as proteins, thus opening the field of host-guest chemistry with (macro)molecules (Figure 1.16).[96–98]

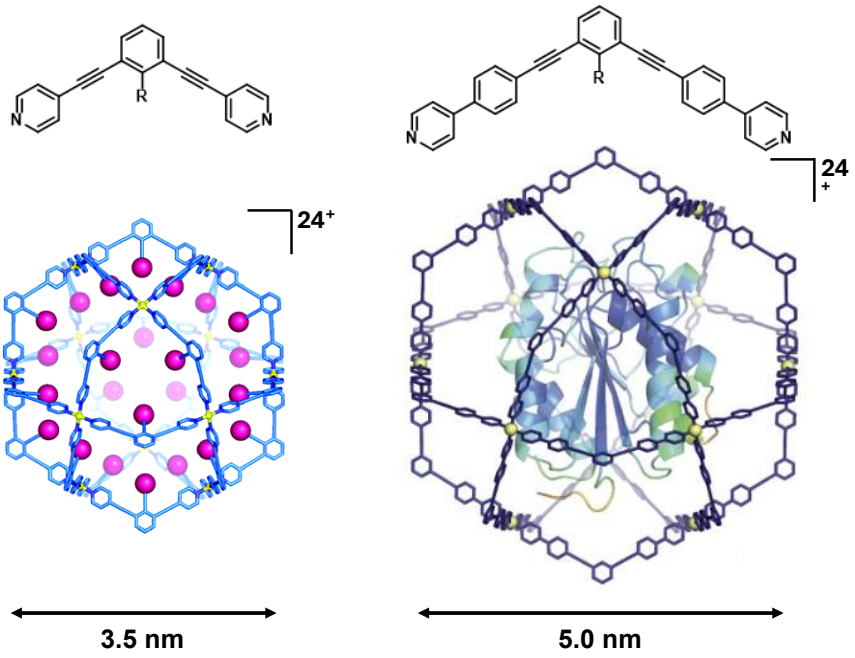

Figure 1.16. Schematic of the isoreticular expansion of Pd(II) MOCs. Inner diameter measured from Pd(II) of opposite vertices.

1.5.1.2. Widening of the bite angle

Up to this point, all the structures discussed have geometries corresponding to Platonic or Archimedean solids, typically following a general formula of M_nL_{2n}. Among them, several geometries have been described (e.g. lanterns, octahedra, and cuboctahedra) and how they can be predicted based on the bite angle of the ligand used.

However, the synthesis of structures with n > 24 is significantly more challenging. Prof. M. Fujita reported the first example of such a case with the synthesis of an icosidodecahedron having the formula $M_{30}L_{60}$.[99] The increased difficulty arises from kinetic trapping effects during self-assembly. These effects are negligible in smaller systems, but as the number of components increases, the likelihood of forming metastable intermediates also increases. Some of these intermediates can become kinetically trapped products. It was demonstrated that, even when using a ligand with a bite angle very close to the ideal value for forming an icosidodecahedron (149º vs. the ideal 150º), the resulting structure had the formula $M_{24}L_{48}$. This suggested that the system had become trapped in a local minimum, forming a thermodynamically disfavoured product. After careful ligand design, introducing some flexibility to favor the formation of the pentagonal faces required for an icosidodecahedron, but avoiding excessive flexibility that could favor smaller structures, the target $M_{30}L_{60}$ cage was successfully

synthesized. This MOC, with a diameter of 7.4 nm, remains the largest molecular cage reported to date (Figure 1.17a).

Another relevant class of polyhedra is the Goldberg polyhedra, which are composed solely of pentagonal and hexagonal faces, as observed in fullerenes. The synthesis of a molecular cage with a Goldberg-type geometry was also achieved by Prof. M. Fujita.[100] This new class of structures first appeared in 2016, when the use of a ligand with a bite angle of 152º led to the formation of a cage with formula $M_{48}L_{96}$ (Figure 1.17b). This cage represents the largest discrete self-assembled structure reported to date in terms of

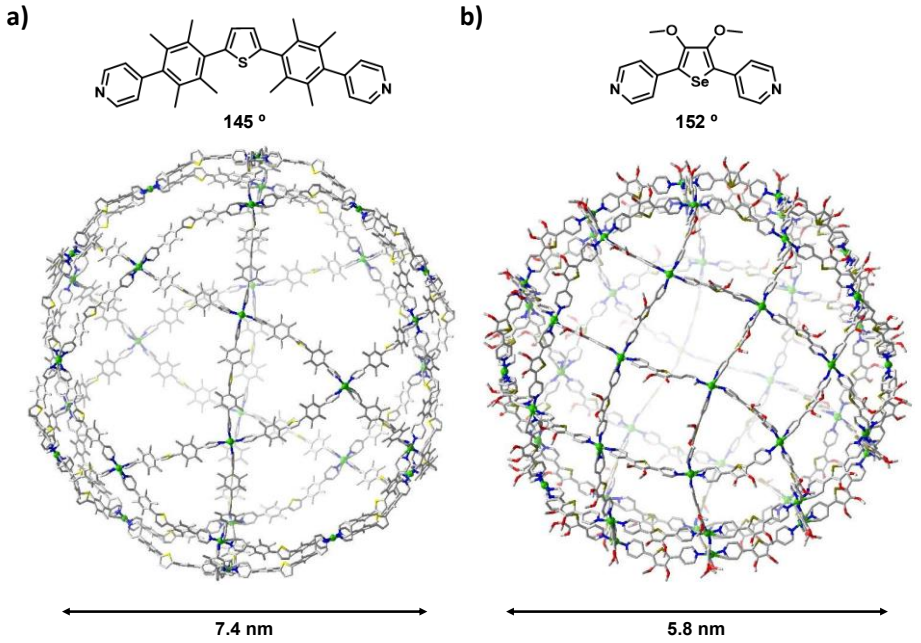

Figure 1.17. ***a)*** Single crystal structure of $Pd_{30}L_{60}$ icosidodecahedron (bottom) and the ligand used for the synthesis (top). Diameter calculated from Pd of opposite vertices. ***b)*** Single crystal structure of $Pd_{48}L_{96}$ Goldberg polyhedra (bottom) and the ligand used for the synthesis (top). Diameter calculated from Pd of opposite vertices.

number of components. Unlike previous structures, this assembly lacked mirror symmetry and consisted only of pentagonal and hexagonal faces.

Despite these remarkable achievements, paddlewheel-based MOPs with such large chemical formulas (e.g., $M_{30}L_{60}$ or $M_{48}L_{96}$) have not yet been reported. This is likely due to the geometric and coordination constraints imposed by the paddlewheel node, which are more restrictive than those of single metal centers.

1.5.2. Oligomeric supramolecules

Oligomeric supramolecules are formed by linking mono- or polynuclear units through spacer groups to generate a single, discrete entity. The formation of giant assemblies, those with diameters larger than 5 nm, can be conceptualized by connecting already large building blocks, such as MOPs. The use of MOPs as

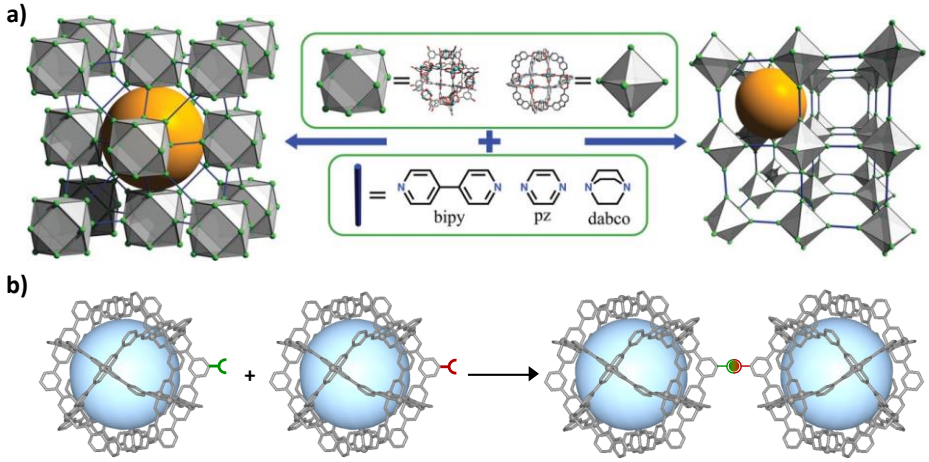

Figure 1.18. ***a)*** Use of MOPs as building blocks to form MOFs. ***b)*** Schematic of the use of metal-organic polyedra for the synthesis of oligomeric supramolecules.

building blocks for the construction of new materials has already been explored. Notably, they have been employed in the synthesis of cage-based MOFs and gels.[101–105] In these cases, the final material is obtained through post-synthetic modification of the MOPs, using either coordinative or covalent linkages (Figure 1.18a).

Based on these precedents, MOPs can also be rationally used for the synthesis of oligomeric supramolecules. In this approach, the cage functions as a monomeric unit that can be reacted to form a finite assembly, for example, a dimer formed by the linkage of two MOPs (Figure 1.18b).

Another strategy for obtaining oligomeric supramolecules is through direct self-assembly. Prof. Y. Wang demonstrated that, by using a ligand pre-functionalized with a cage, the final MOP can be

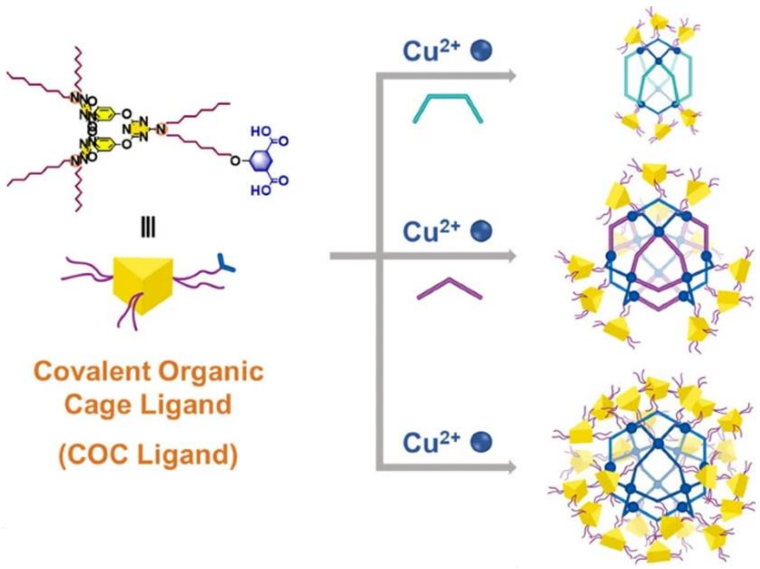

Figure 1.19. Ligand decorated with a cage (left) and its coordination to achieve satellite-like oligomeric supramolecules (right).

decorated with peripheral cages, resulting in a satellite-like architecture (Figure 1.19).[106] Nevertheless, steric hindrance caused by the incorporation of bulky substituents around the ligand periphery limits the size and complexity of the attached cages, thus restricting further structural expansion.

1.6. References

[1] George Wald, *Proc. Natl. Acad. Sci. U. S. A.* **1964**, *52*, 595–611.

[2] J. Lehn, *Angew. Chem. Int. Ed. English* **1988**, *27*, 89–112.

[3] C. J. Pedersen, *Angew. Chem. Int. Ed. English* **1988**, *27*, 1021–1027.

[4] C. G. Claessens, J. F. Stoddart, *J. Phys. Org. Chem.* **1997**, *10*, 254–272.

[5] M. Yoshizawa, J. K. Klosterman, M. Fujita, *Angew. Chem. Int. Ed.* **2009**, *48*, 3418–3438.

[6] B. L. Allwood, H. Shahriari-Zavareh, J. F. Stoddart, D. J. Williams, *J. Chem. Soc. Chem. Commun.* **1987**, 1058.

[7] O. Ikkala, G. ten Brinke, *Science* **2002**, *295*, 2407–2409.

[8] D. L. Caulder, K. N. Raymond, *Acc. Chem. Res.* **1999**, *32*, 975–982.

[9] P. Stricklen, J. Verkade, *J. Am. Chem. Soc.* **1983**, *105*, 2494–2495.

[10] B. Hasenknopf, J.-M. Lehn, N. Boumediene, A. Dupont-Gervais, A. Van Dorsselaer, B. Kneisel, D. Fenske, *J. Am. Chem. Soc.* **1997**, *119*, 10956–10962.

[11] P. N. W. Baxter, J.-M. Lehn, G. Baum, D. Fenske, *Chem. Eur. J.* **1999**, *5*, 102–112.

[12] A. J. Pryde, B. L. Shaw, B. Weeks, *J. Chem. Soc. Chem. Commun*. **1973**, 947.

[13] N. A. Al-Salem, H. D. Empsall, R. Markham, B. L. Shaw, B. Weeks, *J. Chem. Soc., Dalt. Trans*. **1979**, 1972–1982.

[14] M. Fujita, J. Yazaki, K. Ogura, *J. Am. Chem. Soc*. **1990**, *112*, 5645–5647.

[15] M. Fujita, J. Yazaki, K. Ogura, *Chem. Lett*. **1991**, *20*, 1031–1032.

[16] P. J. Stang, J. A. Whiteford, *Organometallics* **1994**, *13*, 3776–3777.

[17] P. J. Stang, D. H. Cao, *J. Am. Chem. Soc*. **1994**, *116*, 4981–4982.

[18] M. Fujita, O. Sasaki, T. Mitsuhashi, T. Fujita, J. Yazaki, K. Yamaguchi, K. Ogura, *Chem. Commun*. **1996**, 1535.

[19] R.-D. Schnebeck, L. Randaccio, E. Zangrando, B. Lippert, *Angew. Chem. Int. Ed*. **1998**, *37*, 119–121.

[20] S.-W. Lai, M. C.-W. Chan, S.-M. Peng, C.-M. Che, *Angew. Chem. Int. Ed*. **1999**, *38*, 669–671.

[21] J. R. Hall, S. J. Loeb, G. K. H. Shimizu, G. P. A. Yap, *Angew. Chem. Int. Ed*. **1998**, *37*, 121–123.

[22] M. Fujita, M. Aoyagi, K. Ogura, *Inorg. Chim. Acta* **1996**, *246*, 53–57.

[23] P. J. Stang, N. E. Persky, J. Manna, *J. Am. Chem. Soc.* **1997**, *119*, 4777–4778.

[24] M. Fujita, S. Nagao, K. Ogura, *J. Am. Chem. Soc.* **1995**, *117*, 1649–1650.

[25] M. Fujita, D. Oguro, M. Miyazawa, H. Oka, K. Yamaguchi, K. Ogura, *Nature* **1995**, *378*, 469–471.

[26] M. Tominaga, K. Suzuki, M. Kawano, T. Kusukawa, T. Ozeki, S. Sakamoto, K. Yamaguchi, M. Fujita, *Angew. Chem. Int. Ed.* **2004**, *43*, 5621–5625.

[27] K. Suzuki, M. Tominaga, M. Kawano, M. Fujita, *Chem. Commun.* **2009**, 1638.

[28] D. Fujita, A. Takahashi, S. Sato, M. Fujita, *J. Am. Chem. Soc.* **2011**, *133*, 13317–13319.

[29] T. K. Ronson, S. Zarra, S. P. Black, J. R. Nitschke, *Chem. Commun.* **2013**, *49*, 2476.

[30] W. Meng, J. K. Clegg, J. D. Thoburn, J. R. Nitschke, *J. Am. Chem. Soc.* **2011**, *133*, 13652–13660.

[31] T. R. Cook, P. J. Stang, *Chem. Rev.* **2015**, *115*, 7001–7045.

[32] V. Campbell, J. Nitschke, *Synlett* **2008**, *2008*, 3077–3090.

[33] H. Zhu, N. M. A. Speakman, T. K. Ronson, J. R. Nitschke, *Acc. Chem. Res.* **2025**, *58*, 1296–1307.

[34] M. Kieffer, R. A. Bilbeisi, J. D. Thoburn, J. K. Clegg, J. R. Nitschke, *Angew. Chem. Int. Ed.* **2020**, *59*, 11369–11373.

[35] J. L. Bolliger, T. K. Ronson, M. Ogawa, J. R. Nitschke, *J. Am. Chem. Soc.* **2014**, *136*, 14545–14553.

[36] T. K. Ronson, W. Meng, J. R. Nitschke, *J. Am. Chem. Soc.* **2017**, *139*, 9698–9707.

[37] W. Meng, B. Breiner, K. Rissanen, J. D. Thoburn, J. K. Clegg, J. R. Nitschke, *Angew. Chem. Int. Ed.* **2011**, *50*, 3479–3483.

[38] S. Zarra, J. K. Clegg, J. R. Nitschke, *Angew. Chem. Int. Ed.* **2013**, *52*, 4837–4840.

[39] M. Eddaoudi, J. Kim, J. B. Wachter, H. K. Chae, M. O'Keeffe, O. M. Yaghi, *J. Am. Chem. Soc.* **2001**, *123*, 4368–4369.

[40] B. Moulton, J. Lu, A. Mondal, M. J. Zaworotko, *Chem. Commun.* **2001**, 863–864.

[41] M. Tonigold, D. Volkmer, *Inorg. Chim. Acta* **2010**, *363*, 4220–4229.

[42] H. Abourahma, A. W. Coleman, B. Moulton, B. Rather, P. Shahgaldian, M. J. Zaworotko, *Chem. Commun.* **2001**, 2380–2381.

[43] H. Furukawa, J. Kim, K. E. Plass, O. M. Yaghi, *J. Am. Chem. Soc.* **2006**, *128*, 8398–8399.

[44] J.-R. Li, H.-C. Zhou, *Nat. Chem.* **2010**, *2*, 893–898.

[45] J. Park, Z. Perry, Y.-P. Chen, J. Bae, H.-C. Zhou, *ACS Appl. Mater. Interfaces* **2017**, *9*, 28064–28068.

[46] S. P. Argent, I. da Silva, A. Greenaway, M. Savage, J. Humby, A. J. Davies, H. Nowell, W. Lewis, P. Manuel, C. C. Tang, A. J. Blake, M. W. George, A. V. Markevich, E. Besley, S. Yang, N. R. Champness, M. Schröder, *Inorg. Chem.* **2020**, *59*, 15646–15658.

[47] J. M. Teo, C. J. Coghlan, J. D. Evans, E. Tsivion, M. Head-Gordon, C. J. Sumby, C. J. Doonan, *Chem. Commun.* **2016**, *52*, 276–279.

[48] J. Zhao, X. Yan, *Chem. Lett.* **2020**, *49*, 659–665.

[49] M. D. Young, Q. Zhang, H.-C. Zhou, *Inorg. Chim. Acta* **2015**, *424*, 216–220.

[50] H. Vardhan, M. Yusubov, F. Verpoort, *Coord. Chem. Rev.* **2016**, *306*, 171–194.

[51] Y. Ke, D. J. Collins, H.-C. Zhou, *Inorg. Chem.* **2005**, *44*, 4154–4156.

[52] S. Mollick, S. Fajal, S. Mukherjee, S. K. Ghosh, *Chem. – An Asian J.* **2019**, *14*, 3096–3108.

[53] S. Furukawa, N. Horike, M. Kondo, Y. Hijikata, A. Carné-Sánchez, P. Larpent, N. Louvain, S. Diring, H. Sato, R. Matsuda, R. Kawano, S. Kitagawa, *Inorg. Chem.* **2016**, *55*, 10843–10846.

[54] A. Carné-Sánchez, J. Albalad, T. Grancha, I. Imaz, J. Juanhuix, P. Larpent, S. Furukawa, D. Maspoch, *J. Am. Chem. Soc.* **2019**, *141*, 4094–4102.

[55] L. Hernández-López, A. Cortés-Martínez, T. Parella, A. Carné-Sánchez, D. Maspoch, *Chem. – A Eur. J.* **2022**, *28*, e202200357.

[56] J. Troyano, S. Horike, S. Furukawa, *J. Am. Chem. Soc.* **2022**, *144*, 19475–19484.

[57] R. G. Pearson, *J. Chem. Educ.* **1968**, *45*, 581.

[58] G. Liu, Z. Ju, D. Yuan, M. Hong, *Inorg. Chem.* **2013**, *52*, 13815–13817.

[59] W.-H. Xing, H.-Y. Li, X.-Y. Dong, S.-Q. Zang, *J. Mater. Chem. A* **2018**, *6*, 7724–7730.

[60] A. Khobotov-Bakishev, L. Hernández-López, C. von Baeckmann, J. Albalad, A. Carné-Sánchez, D. Maspoch, *Adv. Sci.* **2022**, *9*, 2104753..

[61] T. Tateishi, M. Yoshimura, S. Tokuda, F. Matsuda, D. Fujita, S. Furukawa, *Coord. Chem. Rev.* **2022**, *467*, 214612.

[62] E.-S. M. El-Sayed, Y. Di Yuan, D. Zhao, D. Yuan, *Acc. Chem. Res.* **2022**, *55*, 1546–1560.

[63] N. Ahmad, H. A. Younus, A. H. Chughtai, F. Verpoort, *Chem. Soc. Rev.* **2015**, *44*, 9–25.

[64] S. Chen, L.-J. Chen, *Chemistry (Easton).* **2022**, *4*, 494–519.

[65] D. Zhang, T. K. Ronson, Y.-Q. Zou, J. R. Nitschke, *Nat. Rev. Chem.* **2021**, *5*, 168–182.

[66] T. Grancha, A. Carné-Sánchez, L. Hernández-López, J. Albalad, I. Imaz, J. Juanhuix, D. Maspoch, *J. Am. Chem. Soc.* **2019**, *141*, 18349–18355.

[67] M. Han, R. Michel, B. He, Y. Chen, D. Stalke, M. John, G. H. Clever, *Angew. Chem. Int. Ed.* **2013**, *52*, 1319–1323.

[68] D. Preston, J. E. M. Lewis, J. D. Crowley, *J. Am. Chem. Soc.* **2017**, *139*, 2379–2386.

[69] C. G. P. Taylor, S. P. Argent, M. D. Ludden, J. R. Piper, C. Mozaceanu, S. A. Barnett, M. D. Ward, *Chem. – A Eur. J.* **2020**, *26*, 3054–3064.

[70] X. Jing, C. He, L. Zhao, C. Duan, *Acc. Chem. Res.* **2019**, *52*, 100–109.

[71] F. J. Rizzuto, L. K. S. von Krbek, J. R. Nitschke, *Nat. Rev. Chem.* **2019**, *3*, 204–222.

[72] J. L. Bolliger, A. M. Belenguer, J. R. Nitschke, *Angew. Chem. Int. Ed.* **2013**, *52*, 7958–7962.

[73] A. J. Gosselin, C. A. Rowland, E. D. Bloch, *Chem. Rev.* **2020**, *120*, 8987–9014.

[74] A. C. Sudik, A. R. Millward, N. W. Ockwig, A. P. Côté, J. Kim, O. M. Yaghi, *J. Am. Chem. Soc.* **2005**, *127*, 7110–7118.

[75] M. A. Andrés, A. Carné-Sánchez, J. Sánchez-Laínez, O. Roubeau, J. Coronas, D. Maspoch, I. Gascón, *Chem. – A Eur. J.* **2020**, *26*, 143–147.

[76] Y. Yan, I. Telepeni, S. Yang, X. Lin, W. Kockelmann, A. Dailly, A. J. Blake, W. Lewis, G. S. Walker, D. R. Allan, S. A. Barnett, N. R. Champness, M. Schröder, *J. Am. Chem. Soc.* **2010**, *132*, 4092–4094.

[77] G. R. Lorzing, B. A. Trump, C. M. Brown, E. D. Bloch, *Chem. Mater.* **2017**, *29*, 8583–8587.

[78] S. Tokuda, S. Furukawa, *Nat. Chem.* **2025**, *17*, 672–678.

[79] T. Kusukawa, M. Fujita, *J. Am. Chem. Soc.* **2002**, *124*, 13576–13582.

[80] H. Ito, T. Kusukawa, M. Fujita, *Chem. Lett.* **2000**, *29*, 598–599.

[81] M. Yoshizawa, M. Tamura, M. Fujita, *Science* **2006**, *312*, 251–254.

[82] C. Fuertes-Espinosa, C. García-Simón, M. Pujals, M. Garcia-Borràs, L. Gómez, T. Parella, J. Juanhuix, I. Imaz, D. Maspoch, M. Costas, X. Ribas, *Chem* **2020**, *6*, 169–186.

[83] C. García-Simón, M. Garcia-Borràs, L. Gómez, T. Parella, S. Osuna, J. Juanhuix, I. Imaz, D. Maspoch, M. Costas, X. Ribas, *Nat. Commun.* **2014**, *5*, 5557.

[84] A. Galan, P. Ballester, *Chem. Soc. Rev.* **2016**, *45*, 1720–1737.

[85] Z. Ni, A. Yassar, T. Antoun, O. M. Yaghi, *J. Am. Chem. Soc.* **2005**, *127*, 12752–12753.

[86] G. R. Lorzing, A. J. Gosselin, B. A. Trump, A. H. P. York, A. Sturluson, C. A. Rowland, G. P. A. Yap, C. M. Brown, C. M. Simon, E. D. Bloch, *J. Am. Chem. Soc.* **2019**, *141*, 12128–12138.

[87] H. K. Welgama, A. Avasthi, T. R. Cook, *Chem. Mater.* **2024**, *36*, 4185–4195.

[88] J. Rouquerol, D. Avnir, C. W. Fairbridge, D. H. Everett, J. M. Haynes, N. Pernicone, J. D. F. Ramsay, K. S. W. Sing, K. K. Unger, *Pure Appl. Chem.* **1994**, *66*, 1739–1758.

[89] H. Wang, Y. Li, N. Li, A. Filosa, X. Li, *Nat. Rev. Mater.* **2020**, *6*, 145–167.

[90] A. V. Virovets, E. Peresypkina, M. Scheer, *Chem. Rev.* **2021**, *121*, 14485–14554.

[91] M. Eddaoudi, J. Kim, N. Rosi, D. Vodak, J. Wachter, M. O'Keeffe, O. M. Yaghi, *Science* **2002**, *295*, 469–472.

[92] H. Deng, S. Grunder, K. E. Cordova, C. Valente, H. Furukawa, M. Hmadeh, F. Gándara, A. C. Whalley, Z. Liu, S. Asahina, H. Kazumori, M. O'Keeffe, O. Terasaki, J. F. Stoddart, O. M. Yaghi, *Science* **2012**, *336*, 1018–1023.

[93] W. Fan, X. Zhang, Z. Kang, X. Liu, D. Sun, *Coord. Chem. Rev.* **2021**, *443*, 213968.

[94] Z. Chen, K. O. Kirlikovali, L. Shi, O. K. Farha, *Mater. Horizons* **2023**, *10*, 3257–3268.

[95] H. Furukawa, J. Kim, N. W. Ockwig, M. O'Keeffe, O. M. Yaghi, *J. Am. Chem. Soc.* **2008**, *130*, 11650–11661.

[96] M. Tominaga, K. Suzuki, T. Murase, M. Fujita, *J. Am. Chem. Soc.* **2005**, *127*, 11950–11951.

[97] D. Fujita, R. Suzuki, Y. Fujii, M. Yamada, T. Nakama, A. Matsugami, F. Hayashi, J.-K. Weng, M. Yagi-Utsumi, M. Fujita, *Chem* **2021**, *7*, 2672–2683.

[98] D. Fujita, K. Suzuki, S. Sato, M. Yagi-Utsumi, E. Kurimoto, Y. Yamaguchi, K. Kato, M. Fujita, *Chem. Lett.* **2012**, *41*, 313–315.

[99] D. Fujita, Y. Ueda, S. Sato, H. Yokoyama, N. Mizuno, T. Kumasaka, M. Fujita, *Chem* **2016**, *1*, 91–101.

[100] D. Fujita, Y. Ueda, S. Sato, N. Mizuno, T. Kumasaka, M. Fujita, *Nature* **2016**, *540*, 563–566.

[101] Y. Lin, J. Lopez-Cabrelles, C. Lin, S. Furukawa, *Chem. – An Asian J.* **2025**, *20*, e202401456.

[102] L. Hernández-López, A. Khobotov-Bakishev, A. Cortés-Martínez, E. Garrido-Ribó, P. Samanta, S. Royuela, F. Zamora, D. Maspoch, A. Carné-Sánchez, *J. Am. Chem. Soc.* **2025**, *147*, 16560–16567.

[103] A. Khobotov-Bakishev, C. von Baeckmann, B. Ortín-Rubio, L. Hernández-López, A. Cortés-Martínez, J. Martínez-Esaín, F. Gándara, J. Juanhuix, A. E. Platero-Prats, J. Faraudo, A. Carné-Sánchez, D. Maspoch, *J. Am. Chem. Soc.* **2022**, *144*, 15745–15753.

[104] D. Kim, X. Liu, M. S. Lah, *Inorg. Chem. Front.* **2015**, *2*, 336–360.

[105] E. Sánchez-González, M. Y. Tsang, J. Troyano, G. A. Craig, S. Furukawa, *Chem. Soc. Rev.* **2022**, *51*, 4876–4889.

[106] C. Yu, P. Yang, X. Zhu, Y. Wang, *Sci. China Chem.* **2022**, *65*, 858–862.

02

OBJECTIVES

2. Objectives

In the previous chapter, MOCs and MOPs have been presented as highly versatile materials whose structure can be rationally designed. The extensive library of building blocks reported in the literature has demonstrated the feasibility of constructing MOCs and MOPs incorporating diverse metal centres and organic ligands, resulting in structures with a wide range of sizes, shapes, and functionalities. Among these parameters, the characteristics of the organic building block are particularly critical for directing the final structure: the bite angle determines the geometry, while pendant functional groups define the functionality.

Within this context, significant efforts have been devoted to the synthesis of giant assemblies, including mesoporous cages (with inner diameters larger than 2 nm) and oligomeric supramolecules (with total diameters exceeding 5 nm). Two main approaches have been employed to access such mesoporous cages: isoreticular expansion and bite-angle widening. The isoreticular expansion approach involves elongating the organic ligand of a known cage while preserving its bite angle, thereby yielding a larger structure that retains the parent cage geometry. In contrast, widening the bite angle enables the formation of cages composed of a greater number of building units (e.g., an $M_{30}L_{60}$ icosidodecahedron), resulting in significantly larger internal cavities.

Regarding oligomeric supramolecules, previous studies have shown that incorporating cage units as pendant groups within organic ligands can lead to the self-assembly of satellite-like supramolecular structures. However, given the well-established use of MOCs and MOPs as building blocks for extended materials, such as MOFs and gels, an appealing opportunity arises to exploit cages directly in controlled oligomerization reactions, yielding multi-cage oligomeric molecules. This approach requires precise control over the cage concatenation process to confine the system to the oligomeric regime and avoid uncontrolled polymerization.

In this context, the main objective of this Thesis is to further explore and advance these approaches for the synthesis of permanently porous giant molecules and establish the foundations for the preparation of mesoporous cages and oligomeric supramolecules. Specifically, the Thesis is structured around two key milestones:

- Demonstrating the synthesis of porous oligomeric supramolecules using MOPs as monomeric units, by precisely controlling MOP connectivity through protection-deprotection strategies, followed by post-synthetic reactions to produce a dimer, a tetramer, a and satellite-like supramolecule. A key goal is to preserve the cavity of the initial MOP within these assemblies, ensuring that the resulting structures remain permanently porous.

- Expanding the application of isoreticular expansion for the synthesis of mesoporous MOPs, with the aim of obtaining permanently porous cages within the mesoporous regime (inner diameters exceeding 2 nm). This objective includes demonstrating that giant cages can survive the desolvation process when constructed from robust building units, such as Rh(II)-paddlewheel nodes, thus enabling their study as solid-state porous materials.

03

EXPERIMENTAL SECTION

3. Experimental section

3.1. Materials and methods

Rhodium acetate, $Pd(PPh_3)_4$ and 3,6-diiodo-9*H*-carbazole were purchased from abcr. K_3PO_4, LiOH, (1,8-diazabicyclo[5.4.0]undec-7-ene) (DBU), pentane, K_2CO_3, 1-bromododecane, 4-*tert*butylpyridine, 1-heptyl-4-(4-pyridyl)pyridinium bromide, tetrabutylammonium fluoride (TBAF) 1.0 M in THF, anhydrous $MgSO_4$, NaOH, Na_2CO_3, anhydrous $CuSO_4$, sodium ascorbate, 1,3,5- benzenetricarboxylic acid, $SOCl_2$, 2-(trimethylsilyl)ethanol, NH_4Cl, 1-hydroxybenzotriazole (HOBt), hexafluorophosphate benzotriazole tetramethyl uranium (HBTU), *N,N*-diisopropylethylamine (DIPEA), isophthaloyl chloride, Cu wire and anhydrous pyridine were purchased from Sigma-Aldrich. 3,6-dibromo-9*H*-carbazole, 4-methoxycarbonylphenylboronic acid, methyl-4-ethynylbenzoate and copper(I) iodide were purchased from BLD. NH_2-PEG_{38}-N_3, NH_2-PEG_{38}-alkyne and trishydroxypropyltriazolylmethylamine (THPTA) were purchased from BroadPharm. NH_2-PEG_6-alkyne was purchased from Biopharma PEG. All deuterated solvents were purchased from Eurisotop. Solvents at HPLC grade were purchased from Fischer Chemicals.

Ultraviolet-visible (UV–Vis) spectra were measured using an Thermo Scientific™ NanoDrop 2000 at room temperature (ca. 25 °C).

Proton nuclear magnetic resonance (^{1}H-NMR) spectra were acquired using Bruker AVANCE 500 NMR spectrometer operating at 500.13 MHz and equipped with a cryoprobe z-gradient inverse probe head capable of producing gradients in the z direction with a maximum strength of 53.5 G cm^{-1} and a Bruker Ascend 300 MHz at "Servei de Resonància Magnètica Nuclear" from Autonomous University of Barcelona (UAB). Chemical shifts (δ) for ^{1}H-NMR spectra are reported in parts per million (ppm) and relative to the solvent residual peak.

Carbon nuclear magnetic resonance (^{13}C-NMR) spectra were acquired using Bruker AVANCE 500 NMR spectrometer operating at 500.13 MHz and equipped with a cryoprobe z-gradient inverse probe head capable of producing gradients in the z direction with a maximum strength of 53.5 G cm^{-1} at "Servei de Resonància Magnètica Nuclear" from Autonomous University of Barcelona (UAB).

Diffusion ordered NMR spectroscopy (DOSY) spectra were acquired using Bruker AVANCE 500 NMR spectrometer opera ng at 500.13 MHz and equipped with a cryoprobe z-gradient inverse probe head capable of producing gradients in the z direction with a maximum strength of 53.5 G cm^{-1} at "Servei de Resonància Magnètica Nuclear" from Autonomous University of Barcelona (UAB).

Homonuclear correlation spectroscopy (COSY) spectra were acquired using Bruker AVANCE 500 NMR spectrometer operating at 500.13 MHz and equipped with a cryoprobe z-gradient inverse probe head capable of producing gradients in the z direction with a maximum strength of 53.5 G cm^{-1} at "Servei de Resonància Magnètica Nuclear" from Autonomous University of Barcelona (UAB).

Heteronuclear multiple bond correlation (HMBC) spectra were acquired using Bruker AVANCE 500 NMR spectrometer operating at 500.13 MHz and equipped with a cryoprobe z-gradient inverse probe head capable of producing gradients in the z direction with a maximum strength of 53.5 G cm^{-1} at "Servei de Resonància Magnètica Nuclear" from Autonomous University of Barcelona (UAB).

Heteronuclear single quantum correlation spectroscopy (HSQC) spectra were acquired using Bruker AVANCE 500 NMR spectrometer opera ng at 500.13 MHz and equipped with a cryoprobe z-gradient inverse probe head capable of producing gradients in the z direction with a maximum strength of 53.5 G cm^{-1} and a Bruker Ascend 300 MHz at "Servei de Resonància Magnètica Nuclear" from Autonomous University of Barcelona (UAB).

Matrix assisted laser desorption ionization time-of-flight mass spectroscopy (MALDI-TOF) measurements were performed using a 4800 Plus MALDI TOF/TOF (ABSCIEX – 2010). $(COOH)_1$-RhMOP,

$(N_3)_1$-RhMOP, $(alkyne)_1$-RhMOP, $Rh_2(PEG_6\text{-}alkyne)_4$, $(alkyne)_{24}$-RhMOP, MOP-satellite, h(II)-MOP, BCN-13, BCN-14, BCN-15, BCN-16 and BCN-17 were analysed in positive mode. Deprotected $(N_3)_1$-RhMOP, deprotected $(Alkyne)_1$-RhMOP, MOP-dimer and MOP-tetramer were analysed in negative mode. Trans-2-[3-(4-*tert*-butylphenyl)-2-methyl-2-propenylidene]malononitrile (DCTB) was used as ionization matrix in the case of $(COOH)_1$-RhMOP, $(N_3)_1$-RhMOP, $(alkyne)_1$-RhMOP, $Rh_2(PEG_6\text{-}alkyne)_4$, $(alkyne)_{24}$-RhMOP, parent Rh(II)-MOP, BCN-13, BCN-14, BCN-15, BCN-16 and BCN-17. Sinapinic acid was used as a matrix in the case of deprotected $(N_3)_1$-RhMOP, deprotected $(alkyne)_1$-RhMOP, MOP-dimer, MOP-tetramer and MOP-satellite.

Volumetric CO_2 isotherms were collected at 200 K using an ASAP 2460 (Micrometrics). Temperature for CO_2 isotherms measurement was controlled by a chiller.

Volumetric N_2 isotherms were collected at 77 K using High-Resolution ASAP 2020 (Micromeritics). The temperature for N_2 isotherms measurement was controlled by using a liquid nitrogen bath. BET surface values were calculated according to the BETSI method.[1]

Gravimetric water vapor-sorption isotherms were measured using a DVS vacuum instrument (Surface Measurement System Ltd). The weight of the activated sample (≈ 10 mg) was constantly

monitored with a high-resolution microbalance (± 0.1 µg) and recorded at 25 °C (±0.2 °C) under pure water vapor pressures.

Supercritical CO_2 drying was performed using a Laboratory Supercritical Fluid Equipment SFE 15 mL (Extratex Supercritical Fluid Innovation, France).

Z-potential measurements were carried out using a Malvern Zetasizer Nano ZS. Prior to Z-potential measurements, a standard solution with a Z-potential of −42 ± 6 mV was measured to ensure correct calibration.

Dynamic light scattering (DLS) measurements were carried out using a Zetasizer Nano Zs.

Fourier-transform infrared spectroscopy (FTIR) measurements were performed using a Bruker Tensor 27.

Inductively coupled plasma mass spectrometry (ICP-MS) measurements were performed in an external company, Leitat, in an ICP-MS triple quadrupole Agilent 8900 ICP-QQQ. 5 mg of sample were digested with 4 mL of concentrated ultrapure nitric acid (HNO_3 70%) in an analytical microwave at 250 °C. Subsequently, the digestion residue obtained was suitably diluted to analyse the elements of interest by ICP-MS. The quantification was performed by interpolation on a calibration curve prepared from commercial standards of the elements of interest.

Contact angle measurements were measured using a DSA25S Drop shape analyser (KRÜSS Scientific, Hamburg, Germany), using the sessile drop technique and the ADVANCE software for analysing the contact angle of the water drops. Samples were compressed into flat films prior measurements.

Single-Crystal X-Ray Diffraction (SCXRD) data of all the single crystals were collected at 100 K at XALOC beamline at ALBA synchrotron (0.82653 Å).[2] Data were indexed, integrated and scaled using the XDS program.[3] Absorption correction was not applied. The structures were solved by direct methods and subsequently refined by correction of F^2 against all reflections, using SHELXT2018 within Olex2 package and WinGX (version 2021.3).[4,5] All nonhydrogen atoms were refined with anisotropic thermal parameters by full-matrix least-squares calculations on F2 using the program SHELXL2018.[6] We treated the presence of disordered solvent molecules in the cavities of all structures running solvent mask using Olex2 solvent mask or after location of the cage atoms.[7,8] We counted 3320, 135178.7, 41361.5, 41057.8, 12962.1, 24565 electrons per unit cell for parent Rh-MOP, BCN-13, BCN-14, BCN-15, BCN-16 and BCN-17 respectively that correspond to 61 DMA, 2503 DMA, 1034 DMF, 766 DMA, 240 DMA and 455 DMA molecules respectively. In BCN-17 due to the high disorder only first carbons of the C_{12} chains have been refined. Due to the low resolution of BCN-13 (1.18 Å), BCN-14(1.08 Å), BCN-15 (1.15 Å), BCN-16(1.30 Å and BCN-17(1.12 Å) crystals the thermal motions of

some phenyl groups were restrained using SIMU, DELU, EADP restrictions. Hydrogens atoms were inserted at calculated positions and constrained with isotropic thermal parameters.

Powder X-ray diffraction (PXRD) data collected at XALOC beamline at the ALBA synchrotron, using a monochromatic X-ray beam with a wavelength of λ = 0.82653 Å, using a capillary of 0.7 mm inner diameter. Data was collected using a PILATUS3 6M DECTRIS detector. The powder diffraction patterns were radially integrated using FIT2D program.[9]

Cavity measurements were performed using CageCavityCalc and a grid size of 1.0 Å.[10]

3.2. Synthetic procedures of Chapter 4: Giant oligomeric porous cage-based molecules

Synthesis of $(COOH)_1$-RhMOP: $COOTSE_{24}$-RhMOP was synthesised following the reported procedure.[11] Then, tetrabutylammonium fluoride in THF (1 M, 16.0 µL, 16.0 µmol) was added into a THF solution (3 mL) of the synthesized $COOTSE_{24}$-RhMOP (100.0 mg, 10.1 µmol). The resulting solution was kept under stirring overnight, leading to the formation of a green solution. $(COOH)_1$-RhMOP was precipitated by adding 3 mL of HCl 0.3 M to the green solution. The resulting green precipitate was washed twice with 2 mL HCl 0.3 M and twice with 2 mL H_2O. Finally, the green solid was lyophilized (yield = 95%). ^{1}H-NMR (500 MHz, $CDCl_3$): δ =

0.02 (s, 207 H, -CH_3); 1.07 (t, 46 H, -CH_2-); 4.27 (t, 46 H, -CH_2-); 8.59 (broad, 72 H, -CH-) ppm.

Synthesis of $(N_3)_1$-RhMOP: HOBt (0.53 mg, 4.0 µmol), HBTU (1.9 mg, 5.0 µmol) and DIPEA (0.87 µL, 5.0 µmol) were added into a DMF solution (800 µL) containing $(COOH)_1$-RhMOP (20.0 mg, 2.0 µmol) under stirring. After 30 minutes, NH_2-PEG_{38}-N_3 (7.42 mg, 4.0 µmol) was added to the solution. The resulting mixture was stirred overnight. Afterwards, 1 mL of HCl 0.3 M was added to the green solution to induce the precipitation of $(N_3)_1$-RhMOP as a green powder. This powder was washed twice with HCl 0.3 M (1 mL), twice with H_2O (1 mL) and three times with THF:Et_2O (1:2, 2 mL). Finally, the green solid (yield = 93%) was dried under air and stored at -2°C. ^{1}H-NMR (300 MHz, $CDCl_3$): δ = -0.17 (s, 207 H, -CH_3); 0.87 (broad, 46 H, -CH_2-); 3.45 (s, 156 H, -CH_2-) 4.08 (broad, 46 H, -CH_2-); 8.59 (broad, 72 H, -CH-) ppm.

Synthesis of deprotected $(N_3)_1$-RhMOP: The 23 protected carboxylic groups of $(N_3)_1$-RhMOP were deprotected by dissolving $(N_3)_1$-RhMOP (20.0 mg, 1.7 µmol) in 1 mL of THF and subsequently adding 2 molar equivalents of TBAF 1 M solution in THF (346.5 µL, 346.5 µmol). The solution was maintained under stirring overnight. Afterwards, the THF was evaporated and the resultant green solid was washed twice with HCl 0.3 M (1 mL), twice with H_2O (1 mL) and three times with THF:Et_2O (1:2, 2 mL). The obtained solid was finally dried under air (yield = 96%). ^{1}H-NMR (300 MHz, D_2O): δ = 3.35

(broad, 156 H, -CH_2-); 8.33 (broad, 48 H, -CH-); 8.70 (broad, 24 H, -CH-) ppm.

Synthesis of (alkyne)$_1$-RhMOP: HOBt (0.53 mg, 4.0 µmol), HBTU (1.9 mg, 5.0 µmol) and DIPEA (0.87 µL, 5.0 µmol) were added into a DMF solution (800 µL) containing (COOH)$_1$-RhMOP (20.0 mg, 2.0 µmol) under stirring. After 30 minutes, NH_2-PEG_{38}-alkyne (7.42 mg, 4.0 µmol) was added to this solution. The resulting mixture was stirred overnight. Afterwards, 1 mL of HCl 0.3 M was added to the green solution to induce the precipitation of (alkyne)$_1$-RhMOP as a green powder. This powder was washed twice with HCl 0.3 M (1 mL), twice with H_2O (1 mL) and three times with THF:Et_2O (1:2, 2 mL). Finally, the green solid was dried under air and kept at -2ºC (yield = 93%). ^{1}H-NMR (300 MHz, $CDCl_3$): δ = -0.17 (s, 207 H, -CH_3); 0.87 (broad, 46 H, -CH_2-); 3.45 (s, 156 H, -CH_2-) 4.08 (broad, 46 H,-CH_2-); 8.59 (broad, 72 H, -CH-) ppm.

Synthesis of deprotected (alkyne)$_1$-RhMOP: The 23 protected carboxylic groups of (alkyne)$_1$- RhMOP were deprotected by dissolving (alkyne)$_1$- RhMOP (20.0 mg, 1.7 µmol) in 1 mL of THF and subsequently adding 2 molar equivalents of TBAF 1 M solution in THF (346.5 µL, 346.5 µmol). The solution was maintained under stirring overnight. Afterwards, the THF was evaporated and the resultant green solid was washed twice with HCl 0.3 M (1 mL), twice with H_2O (1 mL) and three times with THF:Et_2O (1:2, 2 mL). The obtained solid was dried under air (yield = 94%). ^{1}HNMR (300 MHz,

D_2O): δ = 3.35 (broad, 156 H, -CH_2-); 8.33 (broad, 48 H, -CH-); 8.70 (broad, 24 H, -CH-) ppm.

Control experiments:

1) **Reaction with 5 mol. eqs. of NH_2-PEG_{38}-N_3:** HOBt (1.32 mg, 10.0 μmol), HBTU (4.75 mg, 12.5 μmol) and DIPEA (2.17 μL, 12.5 μmol) were added into a DMF solution (800 μL) containing $(COOH)_1$-RhMOP (20.0 mg, 2.0 μmol) under stirring. After 30 minutes, NH_2-PEG_{38}-N_3 (18.5 mg, 10.0 μmol) was added to the solution. The resulting mixture was stirred overnight. Afterwards, 1 mL of HCl 0.3 M was added to the green solution to induce the precipitation of $(N_3)_1$-RhMOP as a green powder. This powder was washed twice with HCl 0.3 M (1 mL), twice with H_2O (1 mL) and three times with THF:Et_2O (1:2, 2 mL). Finally, the green solid (yield ≈ 91%) was dried under air and stored at -2ºC.

2) **Synthesis of $(COOH)_2$-RhMOP:** Tetrabutylammonium fluoride in THF (1 M, 10.0 μL, 10.0 μmol) was added into a THF solution (3 mL) of the synthesized $COOTSE_{24}$-RhMOP (50.0 mg, 5.0 μmol). The resulting solution was kept under stirring overnight, leading to the formation of a green solution. $(COOH)_2$-RhMOP was precipitated by adding 3 mL of HCl 0.3 M to the green solu on. The resul ng green precipitate was washed twice with 2 mL HCl 0.3 M and twice with 2 mL H_2O. Finally, the green solid was lyophilized.

3) **Synthesis of $(COOH)_3$-RhMOP:** Tetrabutylammonium fluoride in THF (1 M, 15.0 µL, 15.0 µmol) was added into a THF solution (3 mL) of the synthesized $COOTSE_{24}$-RhMOP (50.0 mg, 5.0 µmol). The resulting solution was kept under stirring overnight, leading to the formation of a green solution. $(COOH)_3$-RhMOP was precipitated by adding 3 mL of HCl 0.3 M to the green solution. The resulting green precipitate was washed twice with 2 mL HCl 0.3 M and twice with 2 mL H_2O. Finally, the green solid was lyophilized.

4) **Synthesis of $(N_3)_x$-RhMOP:** Once the deprotected products were obtained, $(COOH)_2$-RhMOP (20.0 mg, 2.0 µmol) or $(COOH)_3$-RhMOP (20.0 mg, 2.0 µmol) was dissolved in DMF (800 µL). To this solution HOBt (1.32 mg, 10.0 µmol), HBTU (4.75 mg, 12.5 µmol) and DIPEA (2.17 µL, 12.5 µmol) were added under stirring. After 30 minutes, NH_2-PEG_{38}-N_3 (18.5 mg, 10.0 µmol) was added to the solution. The resulting mixture was stirred overnight. Afterwards, 1 mL of HCl 0.3 M was added to the green solution to induce the precipitation of $(N_3)_x$-RhMOP as a green powder. This powder was washed twice with HCl 0.3 M (1 mL), twice with H_2O (1 mL) and three times with THF:Et_2O (1:2, 2 mL). Finally, the green solid was dried under air and stored at -2ºC.

Synthesis of MOP-dimer: The synthesis of the MOP-dimer was performed in two steps. In the first step, $(N_3)_1$-RhMOP (10.0 mg, 0.9 µmol) and $(alkyne)_1$-RhMOP (10.0 mg, 0.9 µmol) were dissolved in 1

mL mixture of CH_2Cl_2:DMF (1:1). To this mixture, five consecutive additions of $CuSO_4$ (20 µL, 0.3 M in H_2O) and sodium ascorbate (20 µL, 0.9 M in H_2O) were done over a period of 1.25 hours. Once the addi tions were finished, the mixture was kept under vigorously stirring overnight. Afterwards, the mixture was extracted twice with HCl 0.3 M (1 mL) and twice with H_2O (1 mL). Finally, the organic phase was evaporated to obtain a green solid.

In the second step, the previously obtained green solid (17.5 mg) was dissolved in 1 mL of THF. Then, an excess of 1 M TBAF solution in THF (64.6 µL, 64.6 µmol) was added to the solution, which was kept under stirring overnight. Afterwards, the THF was evaporated and the obtained green solid was washed twice with HCl 0.3 M (1 mL), twice with H_2O (1 mL) and three times with MeOH (2 mL). The resultant solid was dried under open air. Finally, the product was further purified by washing it three times with basic methanol (43.0 mM NaOH in MeOH, 2 mL), twice with H_2O (1 mL) and three times with MeOH (2 mL). The final product was dried under air (yield = 74%). ^{1}H-NMR (300 MHz, D_2O): δ = 3.53 (broad, 312 H, -CH_2-); 8.39 (broad, 96 H, -CH-); 8.81 (broad, 48 H, -CH-) ppm.

Synthesis of the 4-c cluster $Rh_2(PEG_6\text{-Alkyne})_4$: Initially, $Rh_2(bdc)_4$ was synthesised following a reported procedure.[12] Then, HOBt (9.5 mg, 70 µmol), HBTU (34.1 mg, 90 µmol) and DIPEA (15.7 µL, 90 µmol) were added into a DMF solution (0.2 mL) containing the synthesized $Rh_2(bdc)_4$ (10.0 mg, 11 µmol) under stirring. After 30 minutes, NH_2-PEG_6-alkyne (28.7 mg, 90 µmol) was added into this

solution, which was stirred overnight. Afterwards, the propargyl-PEG-complex was isolated by precipitation with Et_2O and recovered through centrifugation. Subsequently, the isolated product was washed five times with Et_2O (10 mL) and dissolved in H_2O (5 mL). The solution was extracted twice with CH_2Cl_2 (5 mL). Then, CH_2Cl_2 (5 mL) and MeOH (5mL) were added to the aqueous solution. The presence of MeOH in the mixture induced the transfer of the product from the aqueous phase to the organic phase. Finally, the CH_2Cl_2 was evaporated to obtain the 4-c cluster $Rh_2(PEG_6\text{-Alkyne})$ as a green solid (yield = 63 %). ^{1}H-NMR (300 MHz, MeOD): δ = 2. 86 (t, 1 H, -CH); 2.58 (m, 24 H, $-CH_2-$); 4.17 (d, 2 H, $-CH_2-$); 7.43 (t, 1 H, -CH-); 7.87 (d, 1 H, -CH-); 8.08 (d, 1 H, -CH-); 8.36 (s, 1 H, -CH-) ppm.

Synthesis of MOP-tetramer: This synthesis was performed in two steps. Firstly, $(N_3)_1$-RhMOP (20.7 mg, 1.8 μmol) and $Rh_2(PEG\text{-alkyne})_4$ (0.1 mg, $4.8x10^{-2}$ μmol) were dissolved in 1 mL mixture of CH_2Cl_2:DMF (1:1). Then, $CuSO_4$ (18 μL, 0.3 M in H_2O) and sodium ascorbate (18 μL, 0.9 M in H_2O) were added to the resulting solution while stirring. After ten minutes of reaction, 5 pieces of copper wire of *ca*. 2 mg were added. The reaction mixture was kept under vigorous stirring for 48 hours. Afterwards, the mixture was extracted twice with HCl 0.3 M (1 mL) and twice with H_2O (1 mL). Finally, the organic phase was evaporated to obtain a green solid.

In the second step, the previously obtained green solid (19.4 mg) was dissolved in 1 mL of THF. Then, an excess of 1 M TBAF solution in THF (123.3 μL, 123.3 μmol) was added to the solution, which was

kept stirring overnight. Afterwards, the THF was evaporated and the green solid was washed twice with HCl 0.3 M (1 mL) and twice with H_2O (1 mL). Then, the green solid was dissolved in basic water (pH ≈ 12) and the solution was filtered using a centrifugal filter with a molecular weight cut-off of 30 kDa. The centrifugal process was repeated 5 times (50 mL of water used in total). The obtained concentrated solution from the filter was precipitated by adding 1 mL of HCl 0.3 M. The collected green solid was then washed twice with H_2O (2 mL) and three times with MeOH (2 mL). The obtained solid was dried under open air (yield = 75%). ^{1}H-NMR (300 MHz, D_2O): δ = 3.45 (broad, 736 H, -CH_2-); 8.39 (broad, 208 H, -CH-); 8.81 (broad, 96 H, -CH) ppm.

Synthesis of (alkyne)$_{24}$-RhMOP: $COOH_{24}$-RhMOP was synthesised following the reported procedure. Then, HOBt (8.6 mg, 63.8 μmol), HBTU (24.2 mg, 63.8 μmol) and DIPEA (11.1 μL, 63.8 μmol) were added into a DMF solution (2mL) containing (20.0 mg, 2.7 μmol) under stirring. After 30 minutes of reaction, NH_2-PEG_6-alkyne (40.8 mg, 127.9 μmol) was added into the solution, which was stirred overnight. Afterwards, Et_2O (15 mL) was added to precipitate the product. The obtained solid was solubilized in H_2O (15 mL) and filtered with a centrifugal filter with a molecular weight cut-off of 10 kDa. This process was repeated three times using in total 45 mL of H_2O. The concentrated solution obtained from the filter (ca. 1 mL) was extracted with CH_2Cl_2 (1mL). Then, CH_2Cl_2 (1 mL) and MeOH (1 mL) were added to the concentrated aqueous solution, and the

product was transferred to the chlorinated organic phase. Finally, the CH_2Cl_2 was evaporated to obtain $(alkyne)_{24}$-RhMOP as a green solid (yield = 50%). ^{1}H-NMR (300 MHz, $CDCl_3$): δ = 3.56 (broad, 576 H, -CH_2-); 4.10 (broad, 48 H, -CH_2-); 8.28 (broad, 48H, -CH-); 8.73 (broad, 24 H, -CH-) ppm.

Synthesis of MOP-satellite: This synthesis was performed in two steps. In the first step, $(N_3)_1$RhMOP (37.6 mg, 3.3 μmol) and $(alkyne)_{24}$-RhMOP (0.1mg, 1.4x10-2 μmol) were dissolved in 2 mL mixture of CH_2Cl_2:DMF (1:1). While stirring, 20 μL of an aqueous solution containing $CuSO_4$ (0.03 mg, 0.19 μmol) and THPTA (0.35 mg, 0.81 μmol) were added to the solution containing both $(N_3)_1$-RhMOP and $(alkyne)_{24}$-RhMOP. Finally, sodium ascorbate (20 μL, 0.3 M in H_2O) and five pieces of copper wire of an approximate weight of 2 mg were added to the reaction mixture. The reaction was kept under stirring for 7 days. Afterwards, the mixture was extracted twice with HCl 0.3 M (1 mL) and twice with H_2O (1 mL). The organic phase was kept and loaded with fresh catalysts to perform another reaction cycle. To this end, 1 mL of DMF and an aqueous solution containing $CuSO_4$ (0.03 mg, 0.19 μmol) and THPTA (0.35 mg, 0.81 μmol) were added to the organic phase. This mixture was kept stirring for another 7 days. Once the reaction was completed, the mixture was extracted twice with HCl 0.3 M (1 mL) and twice with H_2O (1 mL). Finally, the organic phase was evaporated to obtain a green solid.

In the second step, the previously obtained green solid (35.5 mg) was dissolved in 1 mL of THF. Then, an excess of TBAF 1 M in THF (82.0 µL, 82.0 µmol) was added to the solution, which was kept under stirring overnight. Afterwards, the resultant product was isolated by evaporating the THF and the obtained green solid was washed twice with HCl 0.3 M (1 mL) and twice with H_2O (1 mL). Then, this solid was dissolved in basic water (pH ≈ 12) and the solution was filtered using a centrifugal filter with a molecular weight cut-off of 50 kDa. The centrifugal process was repeated over five times (50 mL of water used as total). The final product was isolated by precipitation using 1 mL of HCl 0.3 M, and the green solid was washed twice with H_2O (2 mL) and three times with MeOH (2 mL). The obtained solid was dried under air (yield = 75%). ^{1}H-NMR (300 MHz, D_2O): δ = 3.45 (broad, 1952 H, -CH_2-); 8.39 (broad, 528 H, -CH-); 8.81 (broad, 264 H, CH-) ppm.

Acid digestions: $(N_3)_1$-RhMOP, $(alkyne)_1$-RhMOP, deprotected $(N_3)_1$-RhMOP, deprotected $(alkyne)_1$-RhMOP and MOP-dimer were digested as follows. 5 mg of the corresponding solid sample were suspended in 0.5 mL of MeOD-d_4 containing 20 µL of DCl (2 % in D_2O:MeOD-d_4, 1:10). The mixture was heated at 65ºC overnight.

$(COOH)_1$-RhMOP and $(alkyne)_{24}$-RhMOP were digested as follows. 5 mg of the corresponding sample were suspended in 0.5 mL of DMSO-d_6 containing 10 µL of DCl (20 % in D_2O). The resulting mixture was heated at 100ºC for 2 hours.

Samples activation: All samples were activated following this procedure. Solvent exchange with MeOH was performed during 1 week to 45 mg of sample. Finally, all solvent was removed through supercritical CO_2 drying.

3.3. Synthetic procedures of Chapter 5: Isoreticular synthesis of mesoporous metal-organic polyhedra with permanent porosity to gas and water

Synthesis of 4,4'-(9*H*-carbazole-3,6-diyl)dibenzoic acid (H_2L2):

*Synthesis of dimethyl 4,4'-(9H-carbazole-3,6-diyl)dibenzoate (**Me_2L2**)*

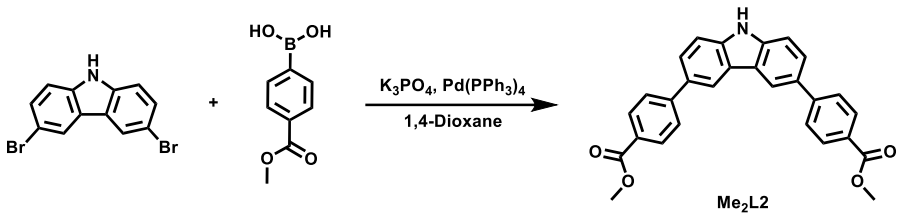

Scheme 1. Synthesis of Me_2L2.

3,6-dibromo-9*H*-carbazole (4.0 g, 12.3 mmol) and 4-methoxycarbonylphenylboronic acid (6.0 g, 33.3 mmol) were added to a 250 mL Schlenk flask equipped with a magnetic stirring bar. The mixture was purged using vacuum and filling with Ar for three consecutive cycles. Then, 1,4-dioxane dried over molecular sieve (40 mL) was added, and the resulting mixture was stirred under Ar

flow at room temperature for 30 minutes. After this time, K_3PO_4 (7.8 g, 33.9 mmol) was dissolved in H_2O (10 mL) and the solution was added into the Schlenk flask followed by the addition of $Pd(PPh_3)_4$ (355 mg, 0.3 mmol). The resulting reaction mixture was stirred under reflux conditions and argon atmosphere for 48 h. After the reaction time, H_2O (50 mL) was added to the reaction mixture to obtain a white precipitated that was isolated through filtration. The white precipitate was washed with H_2O (100 mL) and dichloromethane (100 mL). Finally, the solid was dried under vacuum at 85 °C to yield Me_2L2 (yield = 76 %). ^{1}H-NMR (300 MHz, DMSO-d_6): δ = 3.89 (s, 6H, -CH_3); 7.63 (d, 2H, -CH-); 7.85 (d, 2H, -CH-); 7.98 (d, 4H, -CH-); 8.08 (d, 4H, -CH-); 8.77 (s, 2H, -CH-); 11.63 (s, 1H, -NH) ppm.

*Synthesis of 4,4'-(9H-carbazole-3,6-diyl)dibenzoic acid (**H_2L2**)*

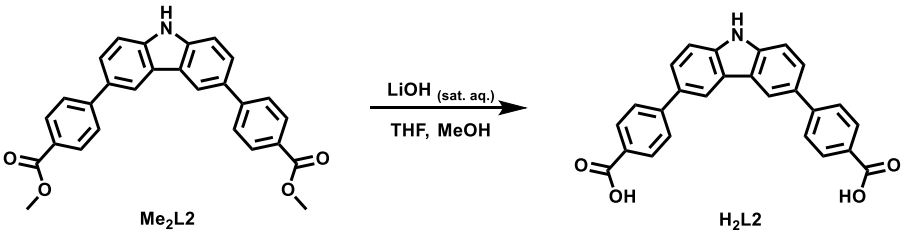

Scheme 2. Synthesis of H_2L2.

Me_2L2 (2.0 g, 4.76 mmol) was suspended in a mixture of THF (25 mL), methanol (25 mL) and saturated LiOH (25 mL), and the mixture was stirred under reflux at 85 °C overnight. Then, HCl 3 M (10 mL) was added to the reaction mixture to obtain a white precipitate that was isolated through filtration. The white precipitate was washed

with H_2O (50 mL) and methanol (50 mL) and dried under vacuum to yield H_2L2. (yield: 95 %). ^{1}H-NMR (300 MHz, DMSO-d_6): δ = 7.56 (d, 2H, -CH-); 7.78 (d, 2H, -CH-); 7.89 (d, 4H, -CH-); 8.00 (d, 4H, -CH-); 8.68 (d, 4H, -CH-); 11.49 (s, 1H, -NH); 12.84 (s, 2H, -COOH) ppm.

Synthesis of 4,4'-((9*H*-carbazole-3,6-diyl)bis(ethyne-2,1-diyl))dibenzoic acid (H_2L3):

*Synthesis of dimethyl 4,4'-((9H-carbazole-3,6-diyl)bis(ethyne-2,1-diyl))dibenzoate (**Me_2L3**)*

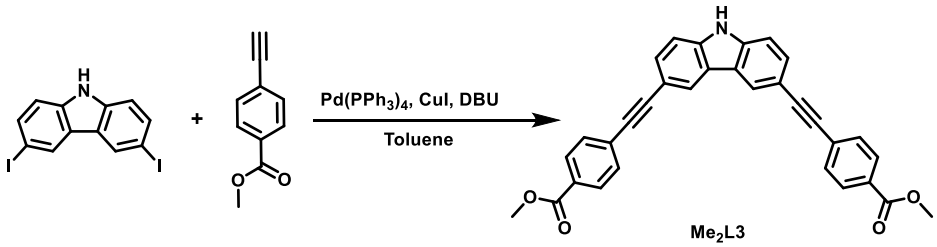

Scheme 3. Synthesis of Me_2L3.

3,6-diiodo-9*H*-carbazole (2.0 g, 4.77 mmol), methyl 4-ethynylbenzoate (2.30 g, 14.36 mmol), $Pd(PPh_3)_4$ (300 mg, 0.26 mmol) and CuI (80 mg, 0.42 mmol) were added to a 100 mL round bottom flask equipped with a magnetic stirring bar and flushed with Ar. Toluene (40 mL) was added to the flask containing the reagents. The solution was additionally degassed by bubbling Ar for 30 min. Then, DBU (2.0 mL, 13.40 mmol) was added, and the resulting mixture was stirred under Ar atmosphere at room temperature

overnight. After the reaction time, the solid obtained was filtered and washed three times with toluene, H_2O and pentane. Finally, Me_2L3 was dried under vacuum at 85 °C to yield an orange solid (yield = 91 %). ^{1}H-NMR (300 MHz, DMSO-d_6): δ = 3.89 (s, 6H, -CH_3); 7.59 (d, 2H, -CH-); 7.66 (d, 2H, -CH-); 7.72 (d, 4H, -CH-); 8.02 (d, 4H, -CH-); 8.77 (s, 2H, -CH-); 11.88 (s, 1H, -NH) ppm.

*Synthesis of 4,4'-((9H-carbazole-3,6-diyl)bis(ethyne-2,1-diyl))dibenzoic acid (**H_2L3**)*

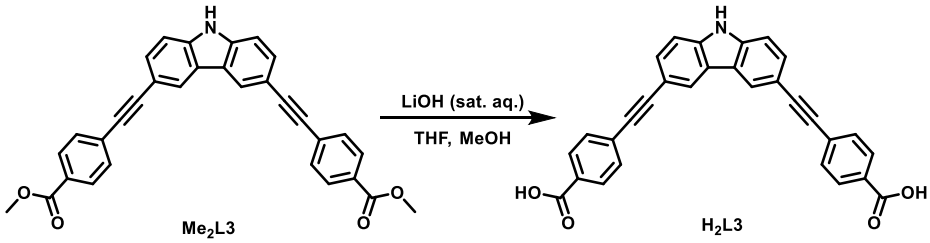

Scheme 4. Synthesis of H_2L3.

Me_2L3 (2 g, 4.27 mmol) was suspended in a mixture of THF (25 mL), methanol (25 mL) and saturated LiOH (25 mL), and the mixture was stirred under reflux at 85 °C overnight. Then, HCl 3 M (10 mL) was added to the reaction mixture to obtain a yellow precipitate that was isolated through filtration. The solid was washed with H_2O (50 mL) and methanol (50 mL) and dried under vacuum to yield H_2L3 (yield: 95 %). ^{1}H-NMR (300 MHz, DMSO-d_6): δ = 7.59 (d, 2H, -CH-); 7.65 (d, 2H, -CH-); 7.69 (d, 4H, -CH-); 8.00 (d, 4H, -CH-); 8.51 (s, 2H, -CH-); 11.88 (s, 1H, -NH)); 13.13 (s, 2H, -COOH) ppm.

Synthesis of 4,4'-((9-dodecyl-carbazole-3,6-diyl)bis(ethyne-2,1-diyl))dibenzoic acid (H_2L4):

*Synthesis of dimethyl 4,4'-((9-dodecyl-carbazole-3,6-diyl)bis(ethyne-2,1-diyl))dibenzoate (**Me_2L4**)*

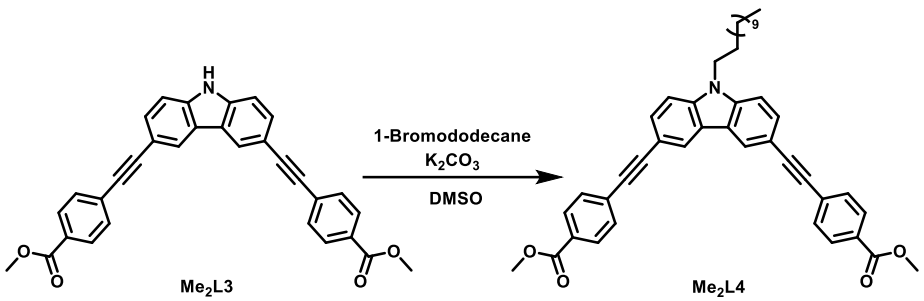

Scheme 5. Synthesis of Me_2L4.

Me_2L3 (2.0 g, 4.14 mmol) and K_2CO_3 (3.14 g, 22.72 mmol) were suspended in 20 mL of DMSO and left stirring for 30 min. Then, 1-bromododecane (3.30 mL, 13.74 mmol) was added to the slurry, and the resulting mixture was stirred overnight at 70 °C. After the reaction, the solution was poured into ice-water and stirred for 1 h. The precipitate was filtered and washed three times with H_2O and pentane. Me_2L4 was finally dried under vacuum to afford a yellow solid (yield: 60 %). ^{1}H-NMR (300 MHz, $CDCl_3$): δ = 0.90 (t, 3H, -CH_3); 1.26 (m, 18H, -CH_2-); 1.89 (t, 2H, -CH_2-); 3.96 (s, 6H, -CH_3); 4.31 (s,

2H, -CH_2-); 7.40 (d, 2H, -CH-); 7.65 (d, 4H, -CH-); 7.69 (d, 2H, -CH-); 8.06 (d, 4H, -CH-); 8.31 (s, 2H, -CH-) ppm.

*Synthesis of 4,4'-((9-dodecyl-carbazole-3,6-diyl)bis(ethyne-2,1-diyl))dibenzoic acid (**H_2L4**)*

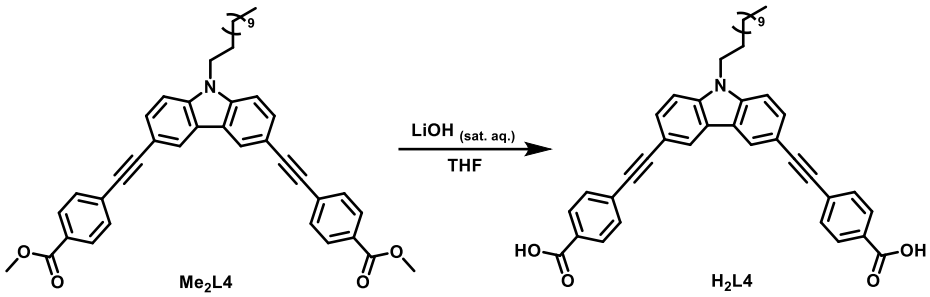

Scheme 6. Synthesis of H_2L4.

Me_2L4 (2.0 g, 3.07 mmol) was dissolved in THF (40 mL). Then, a saturated solution of LiOH (20 mL) was added and the mixture was stirred under reflux at 85 °C overnight. After the reaction, HCl 3 M (50 mL) was added to the crude to obtain a precipitate that was isolated through centrifugation. The solid was washed three times with H_2O and acetone and dried under vacuum to yield H_2L4 (yield: 99 %). ^{1}H-NMR (300 MHz, DMSO-d_6): δ = 0.83 (t, 3H, -CH_3); 1.22 (m, 18H, -CH_2-); 1.78 (t, 2H, -CH_2-); 4.45 (s, 2H, -CH_2-); 7.70 (d, 8H, -CH-); 8.00 (d, 4H, -CH-); 8.54 (s, 2H, -CH-); 13.13 (s, 2H, -COOH) ppm.

Synthesis of the parent octahedral microporous Rh-MOP: Rhodium acetate (20.0 mg, 0.04 mmol), Na_2CO_3 (24.0 mg, 0.23 mmol), H_2L1 (57.4 mg, 0.23 mmol) and 7 mL of DMA were added into

a 23 mL scintillation vial. The mixture was heated at 100°C for 48 h. A green solution was obtained and separated from the residual solids through centrifugation. The crude product was obtained by the addition of 10 mL of Et_2O to the solution yielding a green solid, which was washed with methanol (three times, 10 mL) and dried at room temperature. Single crystals were obtained by preparing a DMA solution (2.5 mg/mL) and exposing it to Et_2O vapor (Yield = 73 %).

Synthesis of the mixture of BCN-13, BCN-14, BCN-15 and BCN-16: Rhodium acetate (20.0 mg, 0.04 mmol), Na_2CO_3 (24.0 mg, 0.23 mmol), H_2L2 (92.2 mg, 0.23 mmol) and 10 mL of DMA were added into a 23 mL scintillation vial. The mixture was heated at 85°C for 48 h. A green solution was obtained and separated from the residual solids through centrifugation. The crude product was obtained by the addition of 30 mL of Et_2O to the solution yielding a green solid. The product was washed with methanol (three times, 10 mL) and dried to obtain a mixture of BCN-13, BCN-14, BCN-15 and BCN-16.

Isolation of BCN-13: A solution containing 2.5 mg of the crude mixture in 1 mL of DMA was prepared and exposed to methanol vapor. After four days, a green solid was obtained, consisting of a crystalline portion (A) and an amorphous portion (B). Both portions were re-suspended in methanol and allowed to settle. The crystalline fraction (A) settled faster than the amorphous portion and could be isolated. The crystals were washed three times with methanol (2 mL) and dried. Then, this solid A (2.5 mg, 0.41 μmol)

was again dissolved in DMA followed by the addition of 4-*tert*-butylpyridine (0.72 µL, 4.92 µmol) and exposed to acetonitrile vapor to yield BCN-13 as red rhombic-shaped crystals. Crystals were collected by centrifugation, washed three times with methanol (2 mL) and dried under open air for further characterization (Yield based on Rh = 2 %).

Isolation of BCN-14: Amorphous solid B was washed three times with methanol (2 mL) and dried. Then, 2.5 mg of the green solid were dissolved in 1 mL of DMA and the solution was exposed to acetonitrile vapor. After 2 days, the recrystallization process yielded a light purple solution (C) and a solid (D). The purple solution was separated from the solid. The purple solution (C) was placed in an open vial for 12 h, which induced the evaporation of the acetonitrile and the colour change of the solution from purple to green. Then, a green solid was precipitated from solution (C) by the addition of Et_2O. The solid was washed with methanol three times and dried at room temperature. After that, this solid (2.5 mg, 0.49 µmol) was dissolved in DMF followed by the addition of 4-*tert*-butylpyridine (0.72 µL, 4.92 µmol) and exposed to Et_2O vapor to yield BCN-14 as red rhombic-shaped crystals. Crystals were collected by centrifugation, washed three times with methanol (2 mL) and dried under open air for further characterization. (Yield based on Rh = 36 %)

Isolation of BCN-15: Amorphous solid B was washed three times with methanol (2 mL) and dried. Then, 2.5 mg of the green solid were

dissolved in 1 mL of DMA and the solution was exposed to acetonitrile vapor. After 2 days, the recrystallization process yielded a light purple solution C and a solid D. Solid D was composed of crystalline material (E) and amorphous spheres (F). Addition of DMA (0.5 mL) into solid D led to the solubilization of the amorphous spheres F and the separation of E as rectangular-shaped single crystals to afford BCN-15. Crystals were collected by centrifugation, washed three times with methanol (2 mL) and dried under open air for further characterization. (Yield based on Rh = 20 %)

Isolation of BCN-16: Amorphous solid B was washed three times with methanol (2 mL) and dried. Then, 2.5 mg of the green solid were dissolved in 1 mL of DMA and the solution was exposed to acetonitrile vapor. After 2 days, the recrystallization process yielded a light purple solution C and a solid D. Solid D was composed of crystalline material E and amorphous spheres F. Addition of DMA (0.5 mL) into solid D led to the solubilization of solid F. The green solution containing F was separated from the solid through centrifugation. The addition of Et_2O to the solution yielded a green solid, that was washed three times with methanol (2 mL) and dried. Finally, 2.5 mg of the solid obtained were dissolved in 1 mL of DMA and the solution was exposed to acetonitrile vapor to afford BCN-16 as rhombic-shaped single crystals. Crystals were collected by centrifugation, washed three times with methanol (2 mL) and dried under open air for further characterization. (Yield based on Rh = 32 %)

Synthesis of BCN-17: Rhodium acetate (10.0 mg, 0.02 mmol), Na_2CO_3 (12.0 mg, 0.11 mmol), H_2L4 (56.3 mg, 0.11 mmol) and 10 mL of DMA were added into a 23 mL scintillation vial. The mixture was heated at 85°C for 48 h. Rectangular green single crystals were obtained and washed with DMA (10 mL) three times (Yield = 68 %).

Prior to adsorption measurements the crystals were washed with a DMA solution of 1-heptyl-4-(4-pyridyl)pyridinium bromide (2 mL, 10 mg/mL) yielding a red amorphous solid, followed by DMA:HCl 0.3M (1:1) washings until the sample turned out green again, finally it was washed with MeOH (5 mL, three times).

Sample activation: All samples were activated using the following procedure: a solvent exchange with methanol was performed for one week on 45 mg of the sample. Finally, the solvent was removed through supercritical CO_2 drying.

3.4. References

[1] J. W. M. Osterrieth, J. Rampersad, D. Madden, N. Rampal, L. Skoric, B. Connolly, M. D. Allendorf, V. Stavila, J. L. Snider, R. Ameloot, J. Marreiros, C. Ania, D. Azevedo, E. Vilarrasa-Garcia, B. F. Santos, X. Bu, Z. Chang, H. Bunzen, N. R. Champness, S. L. Griffin, B. Chen, R. Lin, B. Coasne, S. Cohen, J. C. Moreton, Y. J. Colón, L. Chen, R. Clowes, F. Coudert, Y. Cui, B. Hou, D. M. D'Alessandro, P. W. Doheny, M. Dincă, C. Sun, C. Doonan, M. T. Huxley, J. D. Evans, P. Falcaro, R. Ricco, O. Farha, K. B. Idrees, T. Islamoglu, P. Feng, H. Yang, R. S. Forgan, D. Bara, S. Furukawa, E. Sanchez, J. Gascon, S. Telalović, S. K. Ghosh, S. Mukherjee, M. R. Hill, M. M. Sadiq, P. Horcajada, P. Salcedo-Abraira, K. Kaneko, R. Kukobat, J. Kenvin, S. Keskin, S. Kitagawa, K. Otake, R. P. Lively, S. J. A. DeWitt, P. Llewellyn, B. V. Lotsch, S. T. Emmerling, A. M. Pütz, C. Martí-Gastaldo, N. M. Padial, J. García-Martínez, N. Linares, D. Maspoch, J. A. Suárez del Pino, P. Moghadam, R. Oktavian, R. E. Morris, P. S. Wheatley, J. Navarro, C. Petit, D. Danaci, M. J. Rosseinsky, A. P. Katsoulidis, M. Schröder, X. Han, S. Yang, C. Serre, G. Mouchaham, D. S. Sholl, R. Thyagarajan, D. Siderius, R. Q. Snurr, R. B. Goncalves, S. Telfer, S. J. Lee, V. P. Ting, J. L. Rowlandson, T. Uemura, T. Iiyuka, M. A. van der Veen, D. Rega, V. Van Speybroeck, S. M. J. Rogge, A. Lamaire, K. S. Walton, L. W. Bingel, S. Wuttke, J. Andreo, O. Yaghi, B. Zhang, C. T. Yavuz, T. S. Nguyen, F. Zamora, C. Montoro, H. Zhou, A. Kirchon, D. Fairen-Jimenez, *Adv. Mater.* **2022**, *34*, 2201502.

[2] J. Juanhuix, F. Gil-Ortiz, G. Cuní, C. Colldelram, J. Nicolás, J. Lidón, E. Boter, C. Ruget, S. Ferrer, J. Benach, *J. Synchrotron Radiat.* **2014**, *21*, 679–689.

[3] W. Kabsch, *Acta Crystallogr. Sect. D Biol. Crystallogr.* **2010**, *66*, 133–144.

[4] G. M. Sheldrick, *Acta Crystallogr. Sect. A Found. Adv.* **2015**, *71*, 3–8.

[5] L. J. Farrugia, *J. Appl. Crystallogr.* **2012**, *45*, 849–854.

[6] G. M. Sheldrick, *Acta Crystallogr. Sect. C Struct. Chem.* **2015**, *71*, 3–8.

[7] O. V. Dolomanov, L. J. Bourhis, R. J. Gildea, J. A. K. Howard, H. Puschmann, *J. Appl. Crystallogr.* **2009**, *42*, 339–341.

[8] A. L. Spek, *J. Appl. Crystallogr.* **2003**, *36*, 7–13.

[9] A. P. Hammersley, *J. Appl. Crystallogr.* **2016**, *49*, 646–652.

[10] V. Martí-Centelles, T. K. Piskorz, F. Duarte, *J. Chem. Inf. Model.* **2024**, *64*, 5604–5616.

[11] J. Albalad, A. Carné-Sánchez, T. Grancha, L. Hernández-López, D. Maspoch, *Chem. Commun.* **2019**, *55*, 12785–12788.

[12] C. von Baeckmann, S. Ruiz-Relaño, I. Imaz, M. Handke, J. Juanhuix, F. Gándara, A. Carné-Sanchez, D. Maspoch, *Chem. Commun.* **2023**, *59*, 3423–3426.

04

SYNTHESIS OF GIANT OLIGOMERIC POROUS CAGE-BASED MOLECULES

4. Giant oligomeric porous cage-based molecules

4.1. Introduction

The overwhelming majority of known porous materials are either small (<5 nm) discrete cages (i.e. coordination and covalent cages),[1–5] or infinite networks (i.e. MOFs and COFs).[6–9] The chemical and dimensional (between 5 nm and 20 nm) space between these two classes has not been largely explored, due to the inherent synthetic and analytical challenges (Figure 4.1).[10–12] Specifically, using bottom-up approaches to assemble large porous discrete cages is not trivial.[13] Another challenge lies in stopping the polymerisation reaction of extended networks at the oligomeric regime, which is not thermodynamically favoured, thus leading to polydisperse and metastable materials.[14,15] Moreover, the downsizing of crystalline porous networks below the 20 nm

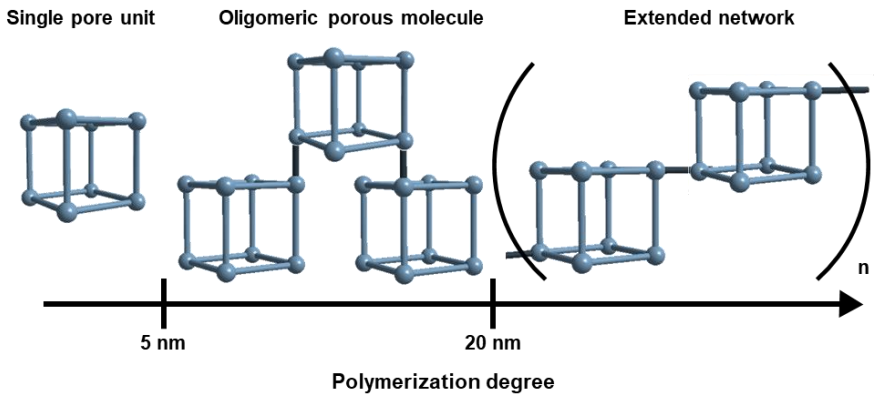

Figure 4.1. Illustrated scale of the regimes of reported porous materials.

threshold often entails the accumulation of defects that are detrimental to their characterisation and function.[16,17]

To overcome these challenges, one can take inspiration from the stepwise synthesis of giant organic[18–22] and metal-organic[23–25] molecules, in which each growing step proceeds through thermodynamic control. In the case of porous materials, this strategy entails the oligomerization of single pore units into giant multi-pore molecules. Pioneer studies have shown the viability of the pore oligomerization approach by either interlocking[26–29] or linking a defined number of cages[30–32] into multi-cage molecules. However, to the best of our knowledge, the permanent porosity of these giant molecules has not yet been demonstrated.

In this chapter we study the stepwise synthesis of permanently porous oligomeric molecules by the concatenation of a defined, finite number of MOCs or MOPs. The resultant giant oligomeric porous molecules potentially merge the properties that arise from linking pore-units (i.e. extrinsic porosity and inter-cavity cooperativity)[33,34] to the those typically observed in molecules, such as defined molecular weight, stoichiometric reactivity, and solubility in liquids, including water.[21,23,35]

In our synthetic route to oligomeric porous molecules, the building blocks are robust Rh(II)-based MOPs (Rh-MOPs).[36] Rh-MOPs can have up to 24 covalent reactive sites on their external surfaces,

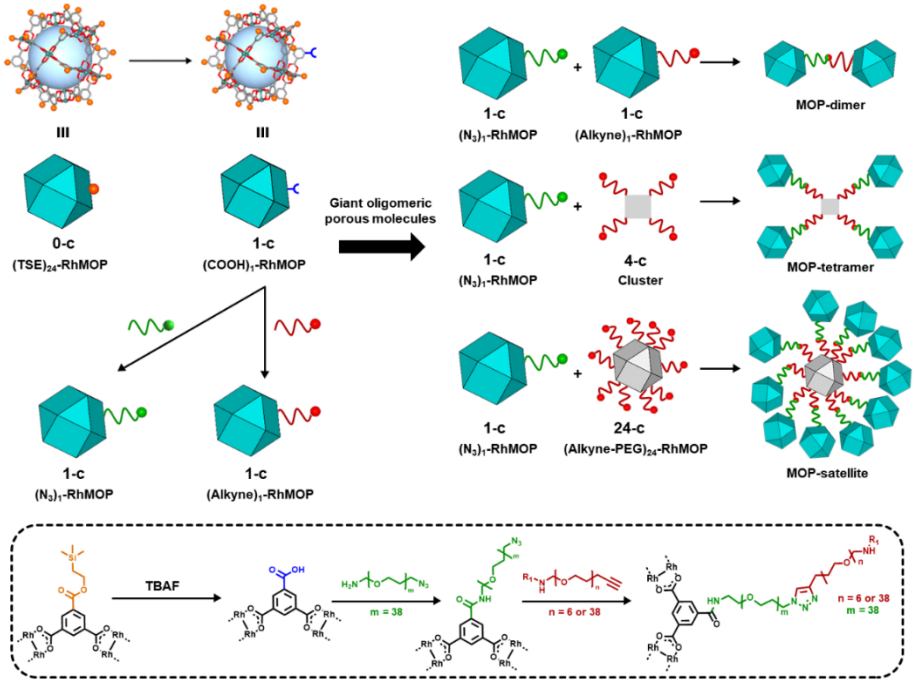

Figure 4.2. (Top) Schematic of the synthesis of 1-c MOPs terminated with azide or alkyne groups, and their subsequent linkage to other MOPs or clusters through click chemistry to form oligomeric porous dimeric, tetrameric or satellite-like molecules. (Bottom) Representative reaction schematic for the synthesis of giant, oligomeric, MOP-based molecules.

stemming from the 5-position of the BDC derivative used in their synthesis.[37] Consequently, the high connectivity of Rh-MOPs complicates the control of their polymerisation into well-defined oligomeric structures rather than extended networks.[38–41] To address this challenge, we aimed to create Rh-MOPs with only one reactive site on their surface. By employing protecting groups, we selectively masked the reactivity of 23 of the 24 reactive sites to yield 1-connected (1-c) Rh-MOPs.[42] Next, using orthogonal

chemistry, we assembled these 1-c MOPs with other 1-c MOPs or with 4-c clusters or 24-c Rh-MOPs to yield giant oligomeric molecules of three types: dimeric, tetrameric, or satellite-like (Figure 4.2).

4.2. Results and discussion

4.2.1. Synthesis of 1-connected Rh-MOPs

We began the synthesis of 1-c Rh-MOP from a Rh-MOP in which all of its 24 peripheral carboxylic acid groups were protected with 2-(trimethylsilyl)ethanol (TSE) groups. Selective cleavage of a single TSE group was achieved by treating the fully protected Rh-MOP with 1.5 equivalents (per MOP) of the deprotecting agent

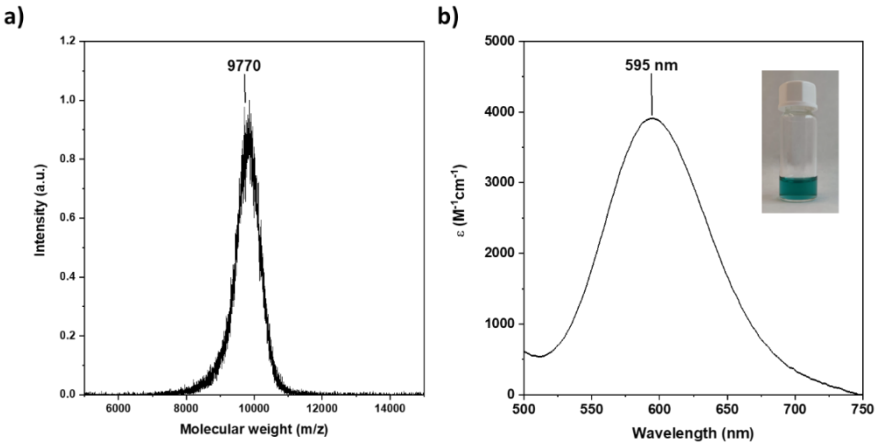

Figure 4.3. MALDI-TOF spectrum of $(COOH)_1$-RhMOP in DMF. The highlighted mass corresponds to the molecular formula of $[(COOTSE\text{-}BDC)_{23}(BTC)_1Rh_{24}+H^+]^+ \cdot 2H_2O$. Expected m/z = 9776 g mol^{-1}; found m/z = 9770 g mol^{-1}. **b)** UV-Vis spectrum of $(COOH)_1$-RhMOP in DMF with a concentration of 0.2 mM.

tetrabutylammonium fluoride (TBAF). This reaction afforded a new Rh-MOP species bearing only one accessible surface carboxylic acid group, with the molecular formula (COOTSE-BDC)$_{23}$(BTC)$_1$Rh$_{24}$, where BTC = 1,3,5-benzenetricarboxylate and COOTSE-BDC = 5-((2-(trimethylsilyl)ethoxy)carbonyl)-1,3-benzenedicarboxylate). The integrity and composition of the resulting mono-carboxylated Rh-MOP (hereafter, (COOH)$_1$-RhMOP) were confirmed by matrix-assisted laser desorption/ionisation Time-of-Flight (MALDI-TOF) mass spectrometry, which displayed a peak centered at 9770 m/z, consistent with the expected molecular formula of [(COOTSE-BDC)$_{23}$(BTC)$_1$Rh$_{24}$ + H$^+$]$^+$·2H$_2$O (calculated mass: 9776 g mol^{-1}) (Figure 4.3a). Furthermore, the integrity of the Rh(II)-Rh(II) paddlewheel was confirmed through UV-Vis spectroscopy of a DMF solution containing the (COOH)$_1$-RhMOP. The characteristic band that corresponds to the Band I of Rh(II)-Rh(II) paddlewheel is centred at 595 nm (Figure 4.3b).

Analysis of the ^{1}H-NMR spectrum of (COOH)$_1$-RhMOP demonstrated the absence of free ligand, with the presence of only broad bands ascribed to the MOP entity (Figure 4.4a). Additionally, ^{1}H-NMR analysis of acid-digested (COOH)$_1$-RhMOP confirmed the expected ratio between the aromatic and the

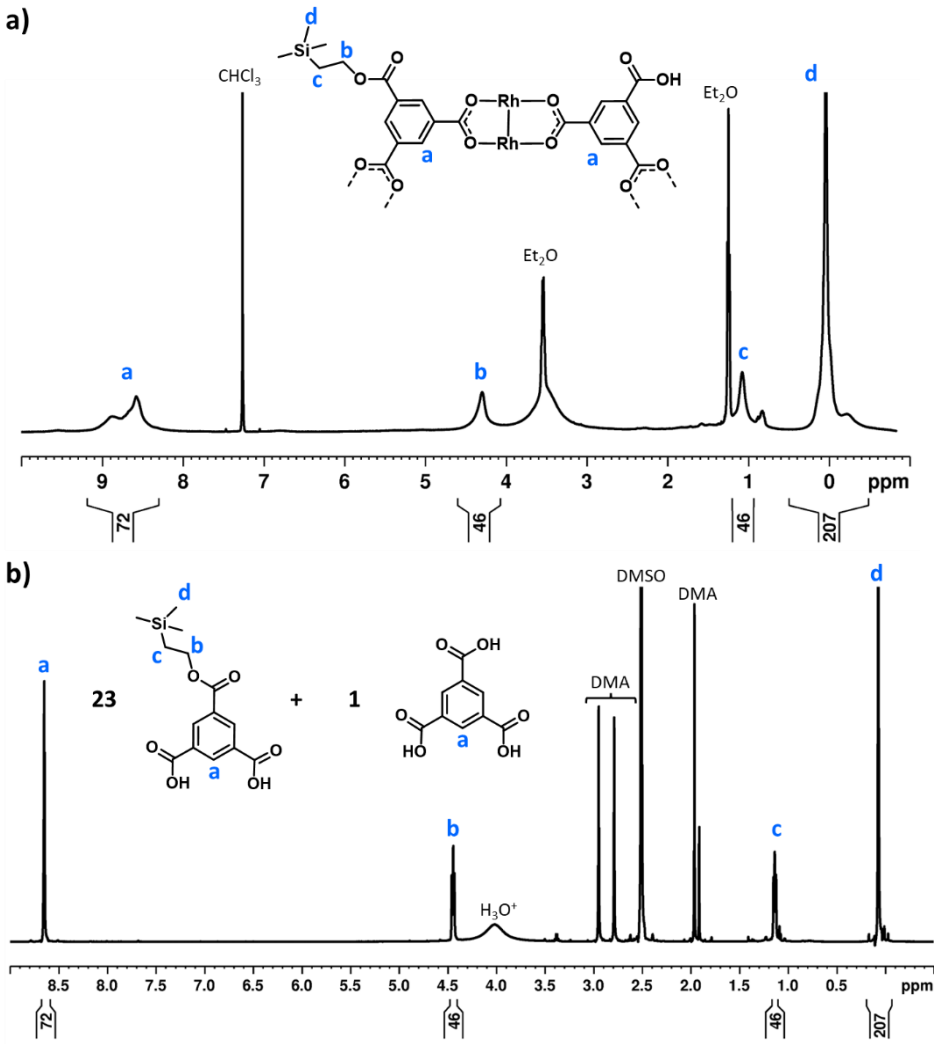

Figure 4.4*. *a) ^{1}H-NMR (500 MHz, 25ºC) spectrum of $(COOH)_1$-RhMOP in $CDCl_3$. ***b)*** ^{1}H-NMR (300 MHz, 25ºC) spectrum of $(COOH)_1$-RhMOP digested in DMSO-d_6 under acidic conditions (DCl 20 %, 100 ºC, 2 h). Note that in both spectra the relative integrations of the protons ascribed to the MOP core (*a*) and the aliphatic signals form the COOTSE group (*b,c* and *d*) correspond to the expected value for the proposed formula; that is, for each MOP core (24 COOTSE-BDC ligands: 72 aromatic protons *a*), there are 23 TSE protecting groups (46 protons *b* and *c* and 207 protons *d*).

aliphatic protons of the protected ligand, further verifying the removal of a single TSE group (Figure 4.4b).

Finally, diffusion-ordered spectroscopy (DOSY) NMR analysis of $(COOH)_1$-RhMOP in $CDCl_3$ revealed the same diffusion coefficient (1.9×10^{-10} m^2 s^{-1}) for both aliphatic and aromatic signals, confirming that the product retained 23 of the original 24 TSE groups (Figure 4.5).

To confer $(COOH)_1$-RhMOP with the orthogonal reactivity required to oligomerise it with additional MOPs, we functionalised its

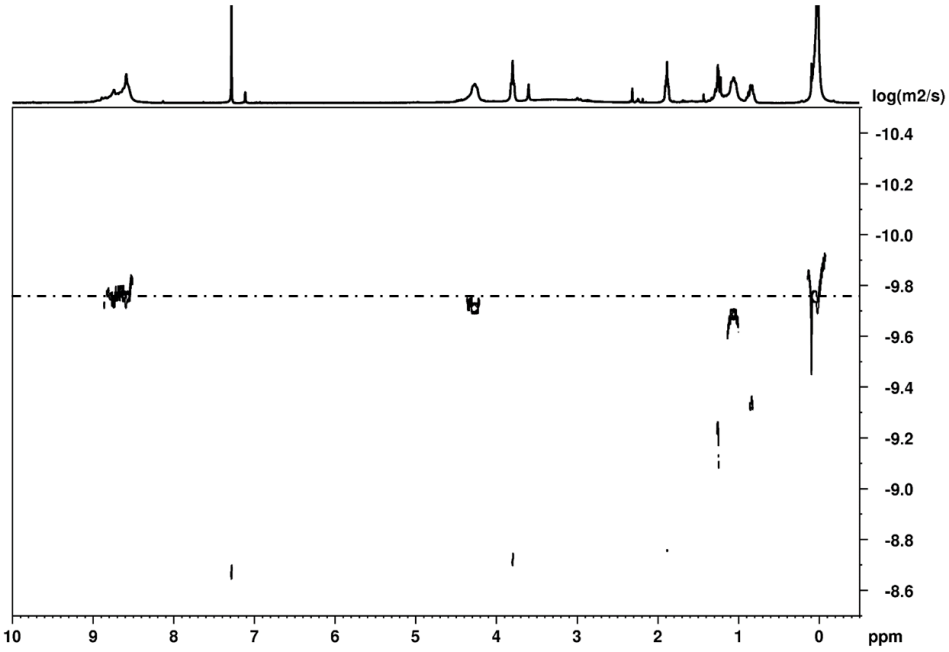

Figure 4.5. DOSY-NMR (300 MHz, 25ºC) spectrum of $(COOH)_1$-RhMOP in $CDCl_3$. The same diffusion coefficient ($D = 1{,}9 \cdot 10^{-10}$ $m^2 \cdot s^{-1}$) is identified for the aromatic signals and the aliphatic signals that correspond to the TMS. The diffusion coefficient of the $CHCl_3$ ($D = 2.3 \cdot 10^{-9}$ $m^2 \cdot s^{-1}$) was used as internal reference.

surface with a single polyethylene glycol (PEG) chain terminated with either alkyne or azide group. Thus, $(COOH)_1$-RhMOP was reacted with a PEG chain terminated at one end with a primary amine (for coupling to the surface carboxylic acid), and at the other end, with either an alkyne or azide moiety (for the oligomerisation). The coupling reactions between $(COOH)_1$-RhMOP and either NH_2-PEG_{38}-N_3 or NH_2-PEG_{38}-alkyne proceeded homogenously in DMF, using 1-hydroxybenzotriazole (HOBt), 2-(1H-benzotriazole-1-yl)-1,1,3,3-tetramethyluronium hexafluorophosphate (HBTU), and *N,N*-diisopropylethylamine (DIPEA) as coupling agents.

These reactions yielded two distinct MOPs derivatives, each bearing a single PEG chain attached at its surface: azide-terminated $(COOTSE\text{-}BDC)_{23}(N_3\text{-}PEG_{38}\text{-}BDC)Rh_{24}$ (hereafter, $(N_3)_1$-RhMOP) and the alkyne-terminated $(COOTSE\text{-}BDC)_{23}(alkyne\text{-}PEG_{38}\text{-}BDC)Rh_{24}$ (hereafter, $(alkyne)_1$-RhMOP). Successful coupling of a single functionalised PEG chain was confirmed by MALDI-TOF mass spectrometry, which showed the expected molecular masses: 11540 m/z for $(N_3)_1$-RhMOP) and 11521 m/z for $(alkyne)_1$-RhMOP (Figure 4.6a and b, respectively). These values are in agreement with the calculated molecular weights of 11544 ± 480 g mol^{-1} and 11521 ± 370 g mol^{-1}, respectively.

The structural integrity of the Rh(II)-Rh(II) paddlewheel was preserved post-functionalisation, as confirmed by UV-Vis

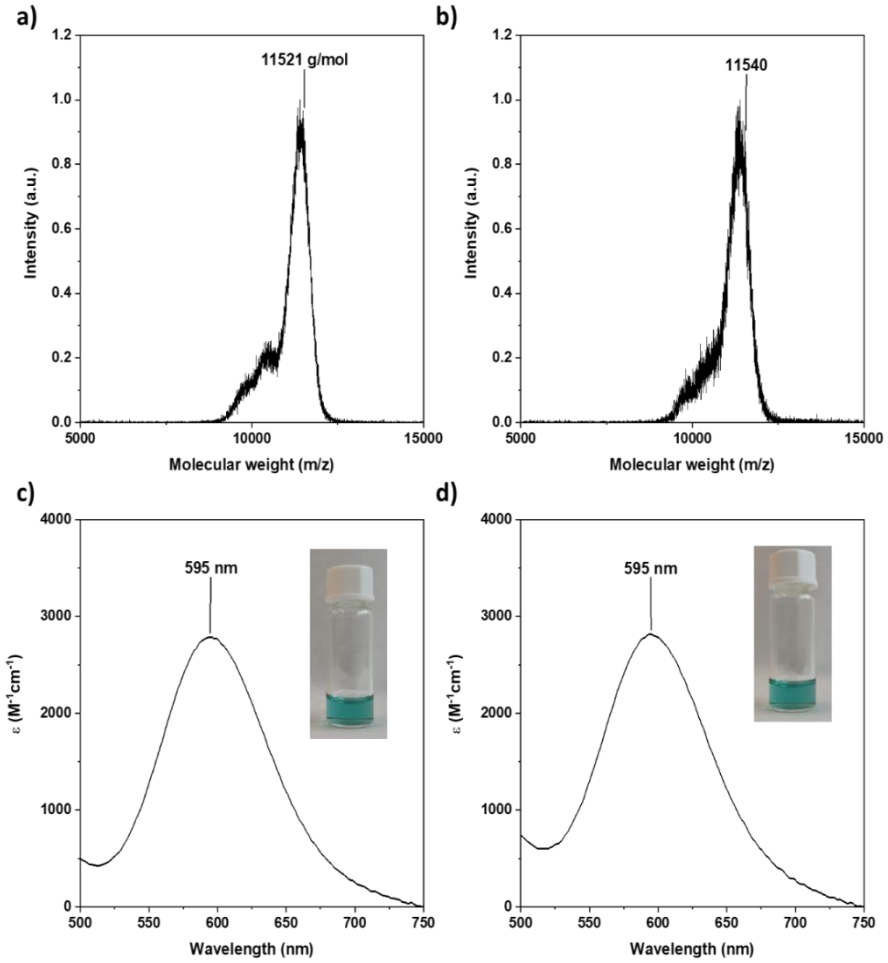

Figure 4.6. ***a,b)*** MALDI-TOF spectra of $(N_3)_1$-RhMOP in DMF (**a**), the highlighted mass corresponds to the molecular formula of $[(TMS\text{-}bdc)_{23}((N_3)\text{-}PEG_{39}\text{-}carbamoyl\text{-}bdc)_1Rh_{24}+H^+]^+$, expected molecular weight 11,544 g mol^{-1} and found molecular weight 11,540 g mol^{-1}, and of $(alkyne)_1$-RhMOP (**b**) in DMF, the highlighted mass corresponds to the molecular formula of $[(TMS\text{-}bdc)_{23}(alkyne\text{-}PEG_{39}\text{-}carbamoyl\text{-}bdc)_1Rh_{24}+H^+]^+$, expected molecular weight 11,521 g mol^{-1} and found molecular weight 11,521 g mol^{-1}. ***c,d)*** UV-Vis spectra of *$(N_3)_1$-RhMOP* ***(c)*** and $(alkyne)_1$-RhMOP (**d**) in DMF with a concentration of 0.2 mM.

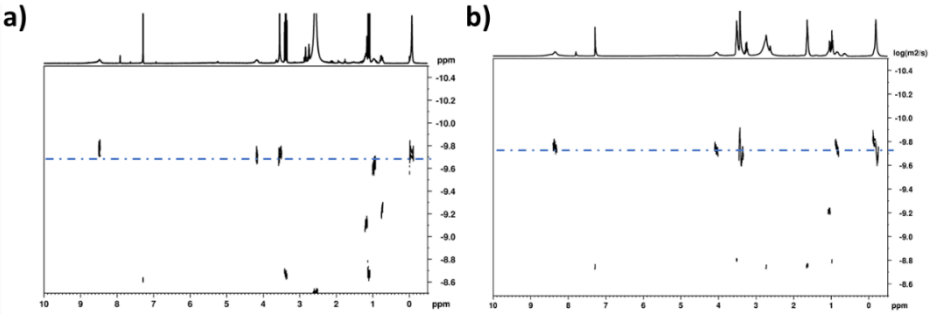

Figure 4.7. DOSY-NMR (300 MHz, 25ºC) spectra of $(N_3)_1$-RhMOP ***(a)*** and $(alkyne)_1$-RhMOP ***(b)*** in $CDCl_3$. The same diffusion coefficient ($D \approx 1.8 \cdot 10^{-10}$ $m^2 \cdot s^{-1}$ for $(N_3)_1$-RhMOP and $D \approx 1.7 \cdot 10^{-10}$ $m^2 \cdot s^{-1}$ for $(alkyne)_1$-RhMOP) is identified for the aromatic signals of the core of the Rh-MOP and the aliphatic signals from the COOTSE groups and the ones from the PEG, which evidences that all belong to the same molecule. The diffusion coefficient of the residual $CHCl_3$ ($D \approx 2.3 \cdot 10^{-9}$ $m^2 \cdot s^{-1}$) was used as internal reference.

spectroscopy, which exhibited the characteristic band at 595 nm in both cases (Figure 4.6c and d). The absence of shifts in this band also indicated complete removal of residual N-donor coupling agents. DOSY NMR analysis further validated the successful surface functionalisation, revealing a single diffusion coefficient for both MOP core and PEG chain in $(N_3)_1$-RhMOP (1.8×10^{-10} m^2 s^{-1}) and $(alkyne)_1$-RhMOP (1.7×10^{-10} m^2 s^{-1}) (Figure 4.7 a and b).

^{1}H NMR spectra of both $(N_3)_1$-RhMOP and $(alkyne)_1$-RhMOP confirmed the absence of free ligand, indicating structural stability (Figure 4.8). Acid-digested ^{1}H NMR spectra further supported the formation of a single amide bond per MOP unit, as evidenced by the appearance of two peaks attributed to the amide-

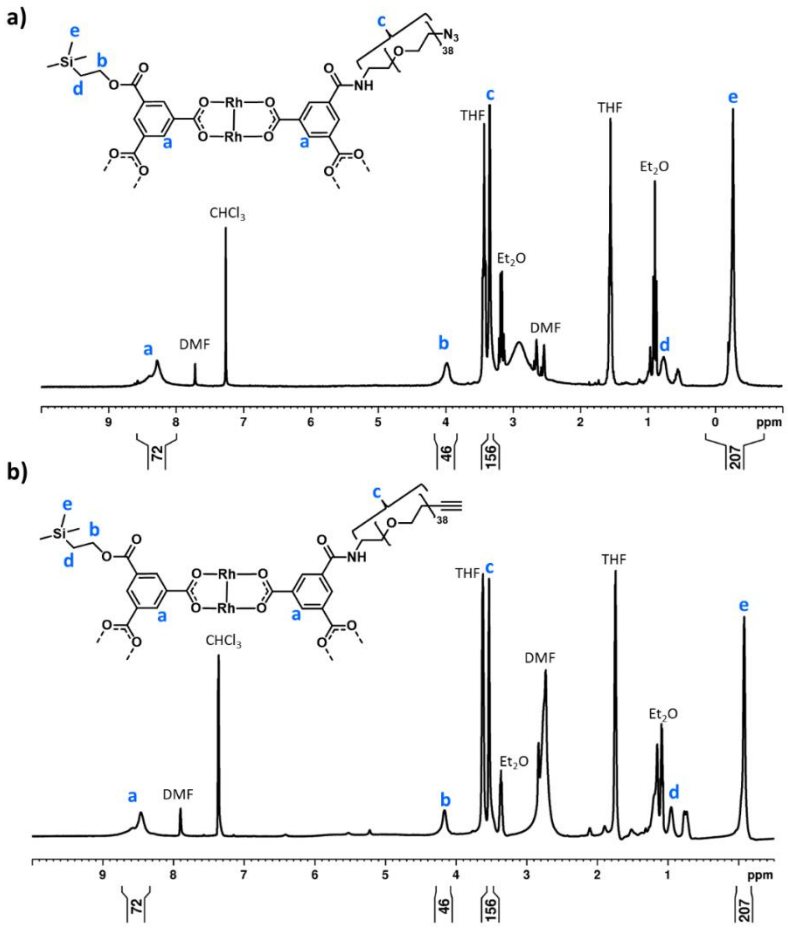

Figure 4.8. ^{1}H-NMR spectra (300 MHz, 25ºC) of $(N_3)_1$-RhMOP ***(a)*** and $(alkyne)_1$-RhMOP ***(b)*** in $CDCl_3$. Note that the relative integrations of the protons ascribed to the MOP core (*a*) and the and the aliphatic signals form the PEG chain (*c*) and TSE protecting group (*b* and *e*) correspond to the expected value for the proposed formula; that is, for each MOP core (24 COOTSE-BDC ligands with 72 aromatic protons *a*), there are 23 TSE protecting groups (46 protons *b* and 207 protons *e*) and a single PEG chain with *ca*. 156 aliphatic protons *c*.

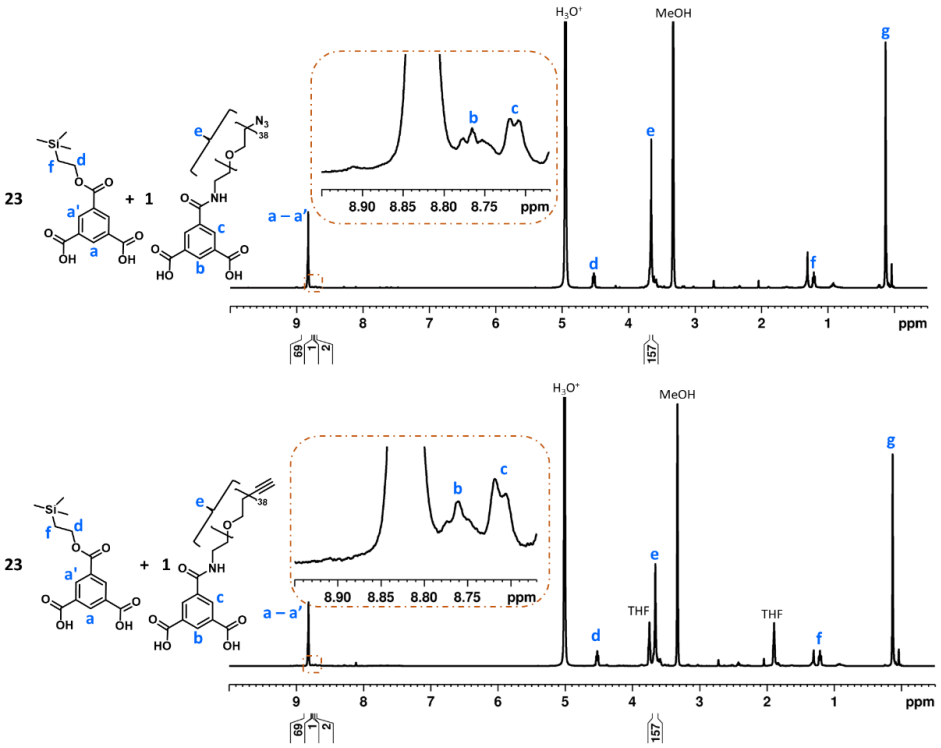

Figure 4.9. ^{1}H-NMR spectrum (500 MHz, 25ºC) of the digested $(N_3)_1$-RhMOP ***(a)*** and $(alkyne)_1$-RhMOP ***(b)*** in MeOD under acidic conditions (DCl 2%, 65ºC, overnight). The appearance of the new aromatic signals (*b* and *c*) confirms the formation of the amide bond. The analysis of the relative integrations in the spectrum of the digested sample confirm the expected ratio of COOTSE-BDC:PEG-functionalized ligand of 23:1. Note that the peaks at 4.27, 1.07 and 0.13 ppm (protons *d, f* and *g* respectively) could not be integrated due to the hydrolysis of the COOTSE ester under the acidic MeOD conditions employed for the digestion. Proton *a* was employed to determine the ligand ratio.

functionalised aromatic ligand (Figure 4.9). The ratio between PEG-functionalised BDC and COOTSE-BDC was confirmed to be 1:23 in both derivatives.

Interestingly, the remaining 23 TSE-protected carboxylic acid groups on the surface of $(N_3)_1$-RhMOP) and $(alkyne)_1$-RhMOP could

be quantitatively deprotected by treating them with an excess of TBAF. The removal of TSE groups was confirmed by a decrease in molecular weight observed in the MALDI-TOF spectra of the deprotected MOPs (Figure 4.10). Additionally, ^{1}H NMR spectra of the deprotected compounds showed complete disappearance of TSE-related signals, with only aromatic and PEG resonances remaining (Figure 4.11a and b), all sharing a consistent diffusion coefficient as demonstrated by DOSY-NMR (Figure 4.11c and d). Importantly, the amide linkage between the MOP core and the PEG chain was maintained after deprotection, as evidenced by the presence of two characteristic peaks at 8.71 and 8.77 ppm in the acid-digested ^{1}H NMR spectra (Figure 4.12).

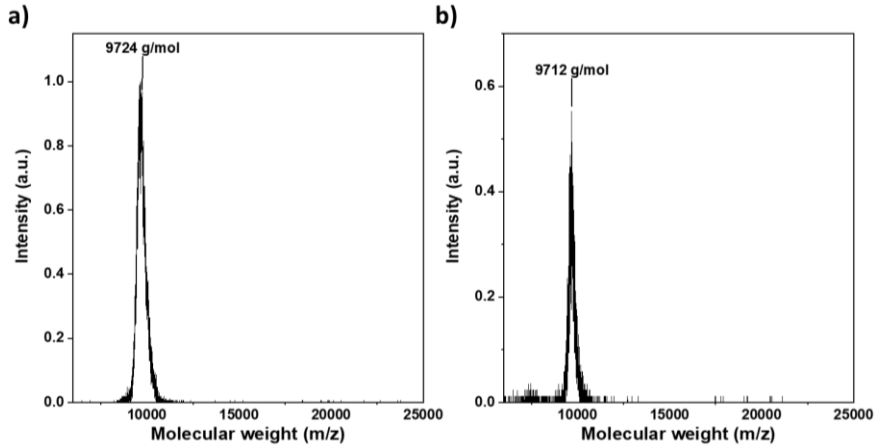

Figure 4.10. a) MALDI-TOF spectrum of the deprotected $(N_3)_1$-RhMOP in basic H_2O. The highlighted mass corresponds to the molecular formula of $[(COONa\text{-}BDC)_{23}((N_3)\text{-}PEG_{38}\text{-}BDC)_1Rh_{24}\text{-}Na^+]^-$. Expected m/z = 9726 ± 370 g mol^{-1}; found m/z = 9724 g mol^{-1}. ***b)*** MALDI-TOF spectrum of the deprotected $(Alkyne)_1$-RhMOP in basic H_2O. The highlighted mass corresponds to the molecular formula of $[(COONa\text{-}BDC)_{23}(Alkyne\text{-}PEG_{38}\text{-}BDC)_1Rh_{24}\text{-}Na^+]^-$. Expected m/z = 9706 ± 480 g mol^{-1}; found m/z = 9712 g mol^{-1}.

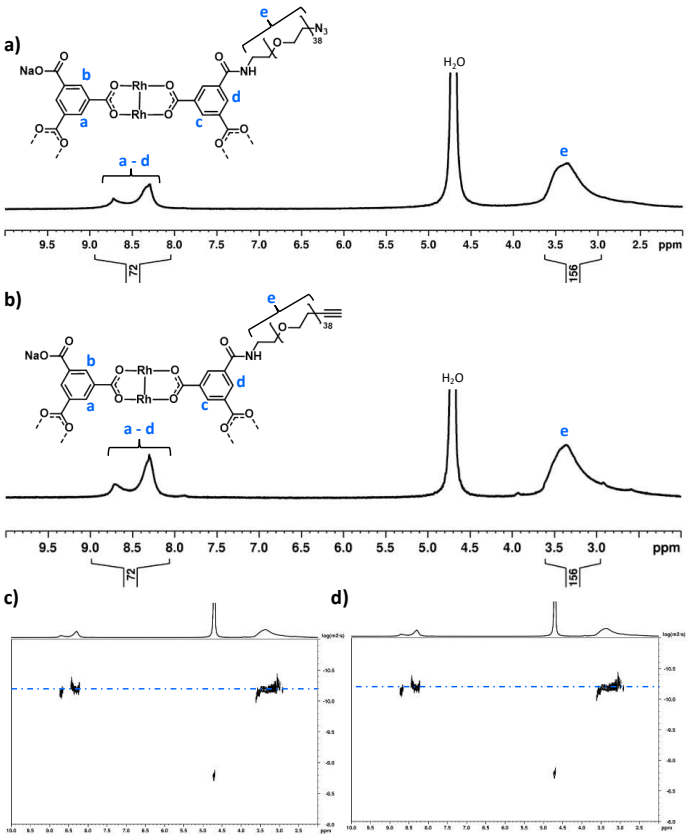

Figure 4.11. ***a,b)*** ^{1}H-NMR spectrum (300 MHz, 25ºC) of the deprotected $(N_3)_1$-RhMOP ***(a)*** and $(alkyne)_1$-RhMOP ***(b)*** in basic D_2O (pD ≈ 12). The relative integrations of the protons ascribed to the MOP core (*a-d*) and the aliphatic signals form the PEG chain (*e*) correspond to the expected value for the proposed formula; that is, for each MOP core (24 functionalized BDC ligands with 72 aromatic protons *a-d*), there is a single PEG chain with *ca*. 156 aliphatic protons *e*. ***c,d)*** DOSY-NMR (300 MHz, 25ºC) spectra of the deprotected $(N_3)_1$-RhMOP ***(c)*** and deprotected $(alkyne)_1$-RhMOP ***(d)*** in D_2O (pD ≈ 12). The same diffusion coefficient (D ≈ 6.6 · 10^{-10} $m^2 \cdot s^{-1}$ for deprotected $(N_3)_1$-RhMOP and D ≈ 6.9 · 10^{-10} $m^2 \cdot s^{-1}$ for deprotected $(alkyne)_1$-RhMOP) is identified for the aromatic signals that correspond to the MOP and for the PEG, demonstrating that all belongs to the same molecular entity. The diffusion coefficient of the remaining H_2O (D ≈ 2.3 · 10^{-9} $m^2 \cdot s^{-1}$) was used as internal reference.

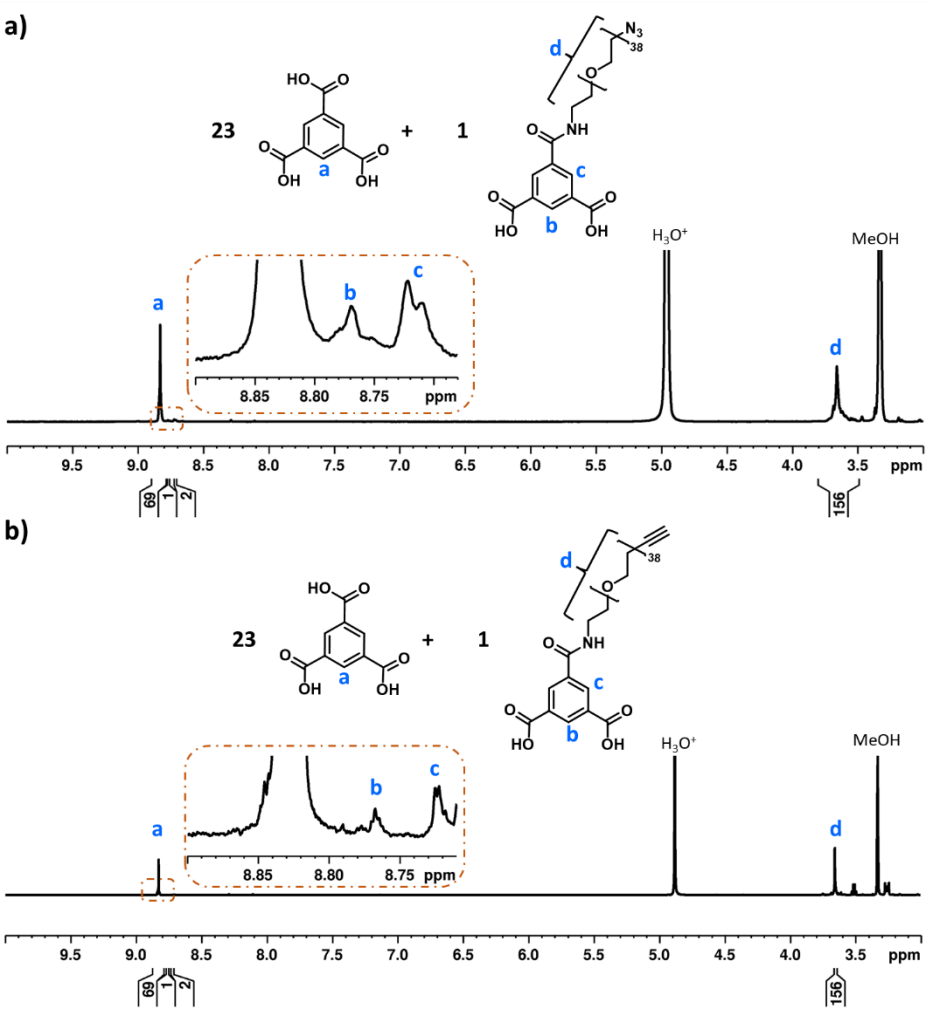

Figure 4.12. ^{1}H-NMR spectra (500 MHz, 25ºC) of the digested deprotected $(N_3)_1$-RhMOP ***(a)*** and deprotected $(alkyne)_1$-RhMOP ***(b)*** in MeOD under acidic conditions (DCl 2%, 65 ºC, overnight). The analysis of the relative integrations in the spectrum of the digested sample confirms the expected ratio of BTC:PEG-functionalized ligand of 23:1.

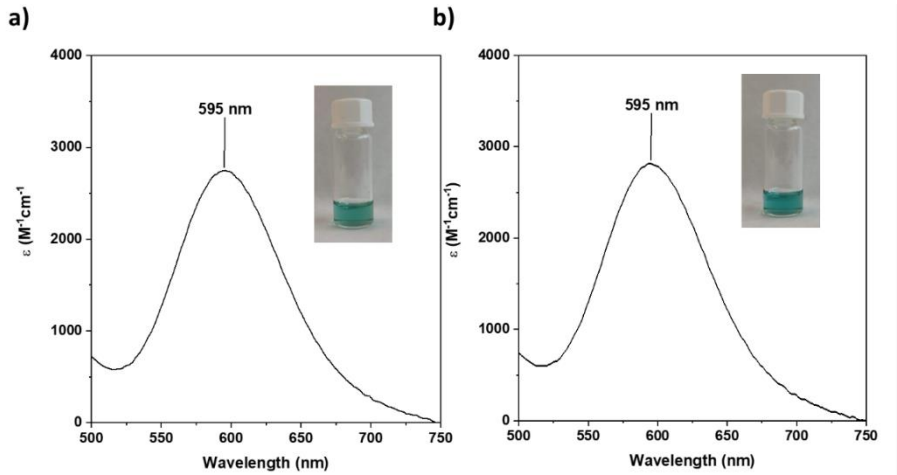

Figure 4.13. UV-Vis spectra of the deprotected $(N_3)_1$-RhMOP ***(a)*** and deprotected $(alkyne)_1$-RhMOP ***(b)*** in DMF with a concentration of 0.2 mM. λ_{max} is centered at 595 nm, confirming that the Rh(II) paddlewheel is maintained and that there is not remaining coordinated N-containing reactants (*i.e.* NH_2-PEG_{38}-alkyne).

Finally, UV-Vis spectroscopy confirmed the preservation of the Rh(II)-Rh(II) paddlewheel motif after deprotection, with the characteristic absorption band remaining centred at 595 nm in both compounds (Figure 4.13).

4.2.1.1. Control experiments

To corroborate the synthesis of pure $(COOH)_1$-RhMOP and the derived mono-PEGylated compounds, we performed a control experiment consisting of reacting $(COOH)_1$-RhMOP (obtained by treating a TSE-protected Rh-MOP with 1.5 mol eq. of TBAF) with an excess amount of NH_2-PEG_{38}-N_3 (5 mol. eq. per Rh-MOP). The product obtained from this reaction was analysed through MALDI-

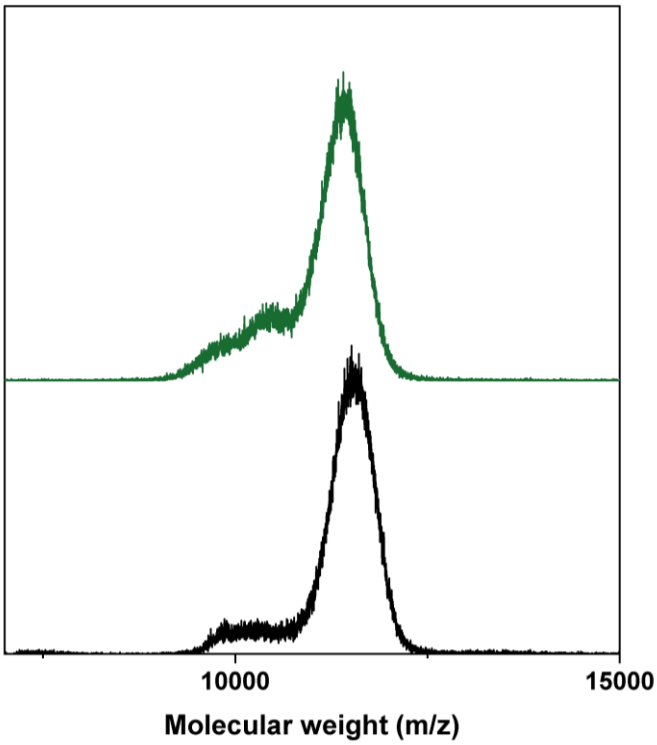

Figure 4.14. MALDI-TOF spectra comparison between $(N_3)_1$-RhMOP obtained through the reaction of $(COOH)_1$-RhMOP with 2 mol. eqs. of NH_2-PEG_{38}-N_3 (green, top) or 5 mol. eqs. of NH_2-PEG_{38}-N_3 (black, bottom).

TOF mass spectrometry, showing only the peak corresponding to $(N_3)_1$-RhMOP that contains one attached PEG chain on the MOP surface (Figure 4.14).

To ensure that the presence of more reactive carboxylic groups in the surface of the MOP would imply the attachment of a higher number of polymeric chains, TSE-protected Rh-MOP was treated with 3 and 5 mol. eq. of TBAF and subsequently reacted with 5 mol. eq. of NH_2-PEG_{38}-N_3. MALDI-TOF mass spectrometry analysis

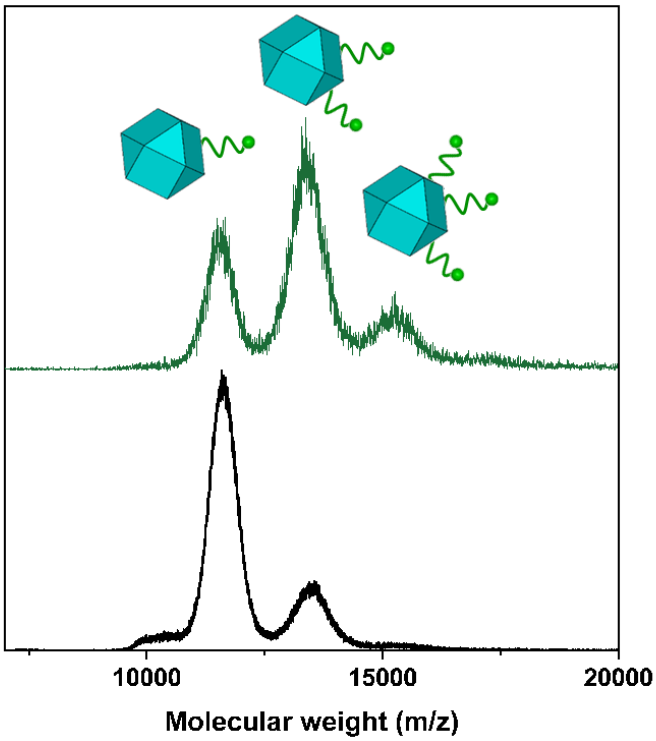

Figure 4.15. MALDI-TOF spectra of the products obtained after reacting 5 mol. eq. of NH_2-PEG_{38}-N_3 with TSE-protected Rh-MOPs treated with 3 mol. eq. of TBAF (black, bottom) and 5 mol. eq. of TBAF (green, top).

demonstrated the synthesis of a distribution of PEGylated Rh-MOP, with up to three polymeric chains attached (Figure 4.15).

These results collectively confirm the successful synthesis of pure $(COOH)_1$-RhMOP. If additional reactive carboxylic acid groups were present on the MOP surface, a distribution of PEGylated species would have been observed under excess NH_2-PEG_{38}-N_3, as evidenced in the control experiments.

4.2.2. Synthesis of dimeric MOP-based supramolecule

Once 1-c MOPs were synthesised and characterised, we targeted the synthesis of a dimeric MOP-based molecule (hereafter, MOP-dimer), by coupling $(N_3)_1$-RhMOP to $(alkyne)_1$-RhMOP through a copper(I)-catalysed, azide–alkyne cycloaddition (CuAAC) click reaction.[43] To this end, both MOPs were reacted under homogenous conditions in a mixture of CH_2Cl_2/DMF (1:1), using copper sulphate and sodium ascorbate as catalysts, to afford the corresponding crude products as a green solid. To facilitate the purification of the MOP-dimer, all surface TSE protecting groups were cleaved, which yielded a dimeric MOP in which each MOP unit had 23 available carboxylic acid groups. Next, the MOP-dimer was purified through successive washing with 0.3 M HCl and basic MeOH, in which the dimer is insoluble, but the catalyst and unreacted precursors are soluble. The obtained purified product exhibited pH-dependent aqueous solubility, which we ascribed to the presence of up to 46 available carboxylic groups. Once deprotonated, the carboxylate groups imparted negative charge to the resulting MOP-dimer, as confirmed by Z-potential measurements performed in basic water (pH = 12), which revealed a value of– 48.5 ± 6.9 mV for the MOP-dimer (Figure 4.16a).

To verify the structural integrity of the MOP-dimer following the CuAAC reaction and subsequent deprotection, UV-Vis spectroscopy was performed in DMF (Figure 4.16b). The

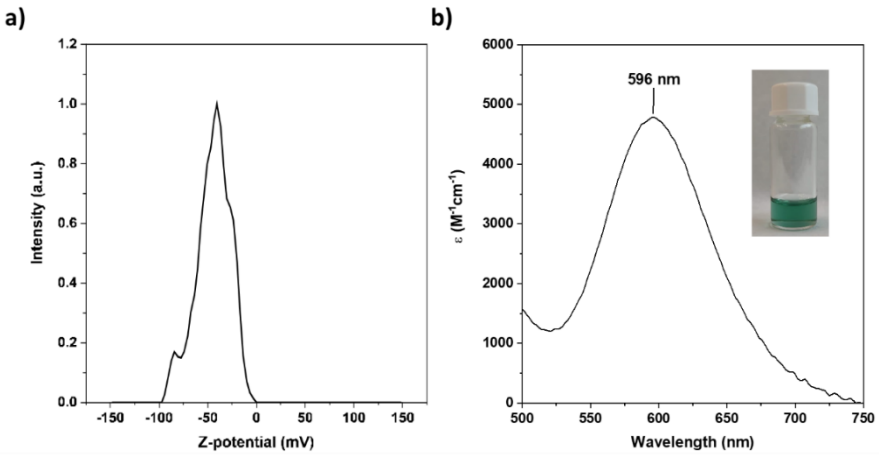

Figure 4.16. a) Z-potential distribution of MOP-dimer in basic water H_2O (pH = 12). ***b)*** UV-Vis spectrum of MOP-dimer in DMF with a concentration of 0.2 mM. λ_{max} is centered at 596 nm, confirming that the Rh(II) paddlewheel is maintained and that it is not coordinated to N-containing reagents (i. e. *i.e.* NH_2-PEG_{38}-Alkyne) or the triazole moiety present in the product.

absorption band centred at 596 nm indicated preservation of the Rh(II)-Rh(II) paddlewheel unit.

Further characterisation by ^{1}H NMR in basic D_2O confirmed the structural integrity of the dimer. The spectrum displayed broad signals characteristic of the intact MOP scaffold, with no detectable free ligand. Due to the chemical similarity between the MOP-dimer and the deprotected precursors, significant differences in chemical shifts were not observed (Figure 4.17a). Remarkably, an increase in size could be confirmed by DOSY-NMR, with a decrease in the diffusion coefficient from the deprotected 1-c MOP precursors (6.6×10^{-10} m^2 s^{-1} and 6.9×10^{-10} m^2 s^{-1}) to the MOP-dimer (6.2×10^{-10} m^2 s^{-1}) (Figure 4.17b).[44] Analogously,

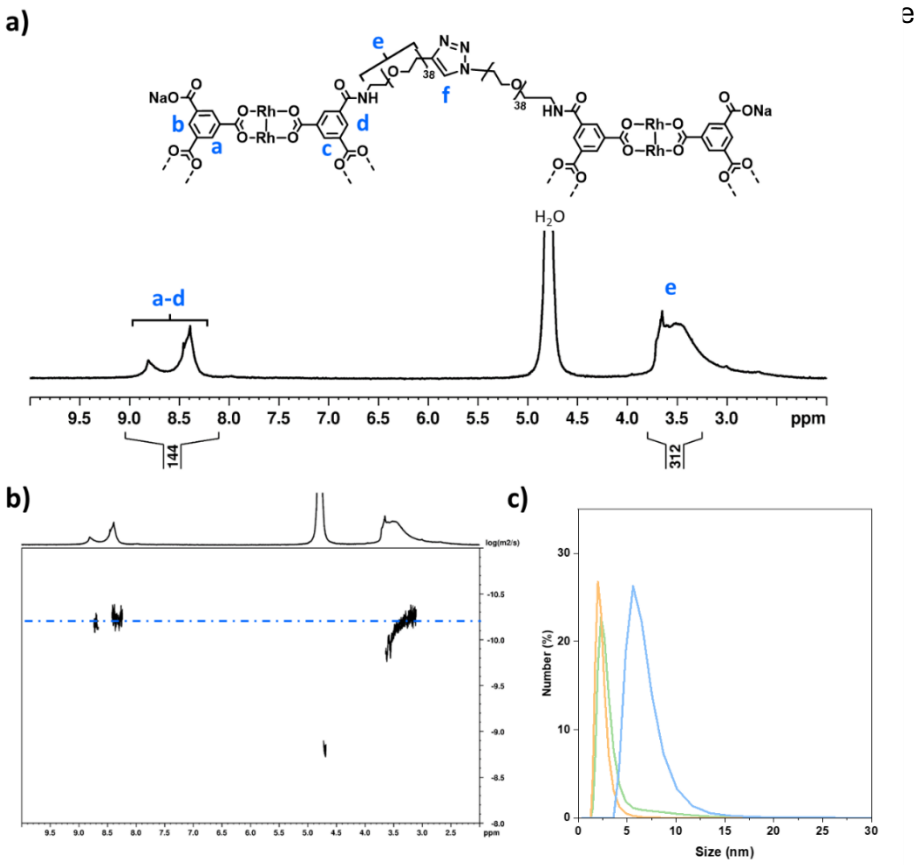

Figure 4.17. a) ^{1}H-NMR spectrum (300 MHz, 25ºC) of MOP-dimer in D_2O (pD ≈ 12). Note that under basic conditions the surface carboxylic groups are deprotonated affording solubility in water. The relative integrations of the protons ascribed to the MOP core (*a-d*) and the aliphatic signals form the PEG chain (e) correspond to the expected value for the proposed formula; that is, for each dimer, there are 2 MOPs with 144 aromatic protons (a-d) and a single PEG chain linking them with *ca*. 312 aliphatic protons (*e*). ***b)*** DOSY-NMR (300 MHz, 25ºC) spectrum of the MOP-dimer in basic D_2O (pD ≈ 12). The same diffusion coefficient ($D \approx 6.2 \cdot 10^{-10}$ $m^2 \cdot s^{-1}$) is identified for the aromatic signals that correspond to the MOP and for the PEG, demonstrating that all belongs to the same molecule. The diffusion coefficient of the residual H_2O ($D \approx 2.3 \cdot 10^{-9}$ $m^2 \cdot s^{-1}$) was used as internal reference. ***c)*** DLS spectra of MOP-dimer (blue), deprotected $(N_3)_1$-RhMOP (orange) and deprotected $(alkyne)_1$-RhMOP (green) in basic H_2O (pH ≈ 12) at a concentration of 0.3 mM.

molecule size in solution had increased from that of the deprotected $(N_3)_1$-RhMOP (2.6 ± 0.2 nm) or the deprotected $(alkyne)_1$-RhMOP (2.3 ± 0.3 nm), to that of the MOP-dimer (6.3 ± 1.1 nm) (Figure 4.17c).

The successful dimerization of two different MOPs was finally evidenced by MALDI-TOF. The spectrum exhibited a single broad peak centred at 18538 m/z, in good agreement with the expected mass (18539 ± 850 g mol^{-1}) for the MOP-dimer having a molecular formula of $[(COOH\text{-}BDC)_{46}(BDC\text{-}PEG_{38}\text{-}1H\text{-}1,2,3\text{-}triazol\text{-}4\text{-}yl\text{-}PEG_{38}\text{-}BDC)_1Rh_{48}\text{-}H^+]^-DMF$ (Figure 4.18).

To further confirm that the two MOPs in MOP-dimer were linked through a covalent bond (i.e. the triazole ring formed upon the

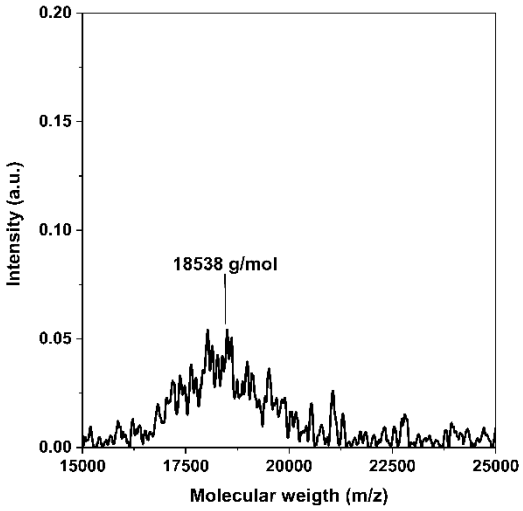

Figure 4.18. MALDI-TOF spectrum of MOP-dimer in DMF. The highlighted mass corresponds to the molecular formula of $[(COOH\text{-}BDC)_{46}(BDC\text{-}PEG_{38}\text{-}1H\text{-}1,2,3\text{-}triazol\text{-}4\text{-}yl\text{-}PEG_{38}\text{-}BDC)_1Rh_{48}\text{-}H^+]^-\cdot DMF$. Expected m/z = 18539 ± 850 g mol^{-1}; found m/z = 18538 g mol^{-1}.

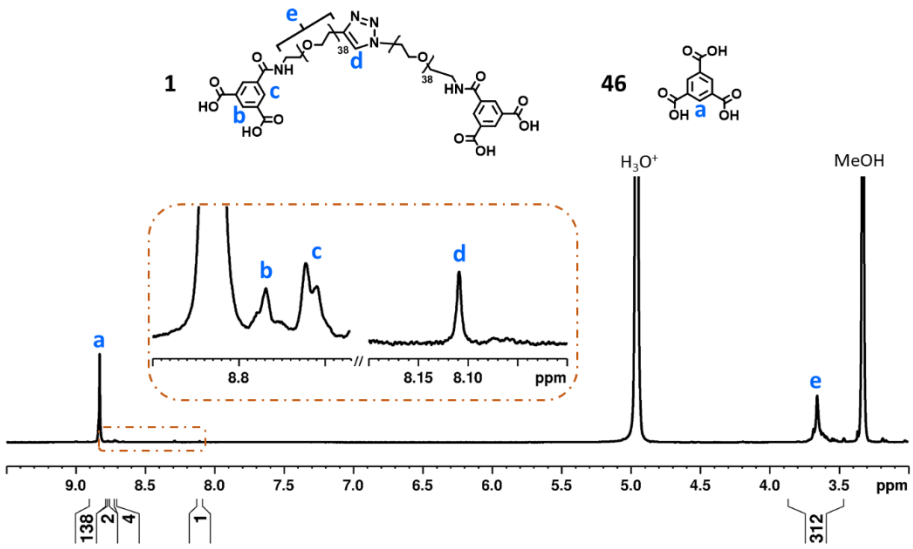

Figure 4.19. [1]H-NMR spectrum (500 MHz, 25ºC) of the digested MOP-dimer in MeOD under acidic conditions (DCl 2 %, 65º C, overnight). The appearance of a singlet at 8.11 ppm (proton *d*) confirms the formation of the triazole ring. The acidic digestion of the dimer should release 46 trimesic ligands (138 protons) and one molecule consisting of two functionalized BDC linkers bridged by a PEG chain (*ca*. 312 aliphatic protons). The analysis of the relative integrations in the spectrum of the digested sample confirms the expected ratio of BTC ligand:bridged functionalized BDC ligand of 46:1.

CuAAC reaction) and not simply entangled through supramolecular PEG-MOP interactions, we submitted it to acid digestion and then, analysed the resultant ligands through [1]H-NMR (Figure 4.19). The spectrum of the isolated PEG linker clearly showed a new peak at 8.11 ppm, which can be ascribed to the proton of the expected triazole ring. Further analysis of the relative integration of the triazole ring and the aromatic core belonging to the Rh-MOP confirmed that every 1-c Rh-MOP was linked through a triazole ring.

To further validate the assignment of the 8.11 ppm signal, a model CuAAC reaction was conducted between NH_2-PEG_{38}-N_3 and NH_2-PEG_{38}-alkyne. The resulting product exhibited the same characteristic 8.11 ppm signal in the ^1H NMR spectrum (Figure 4.20a). Additionally, a ^1H-^{13}C HSQC experiment revealed that this

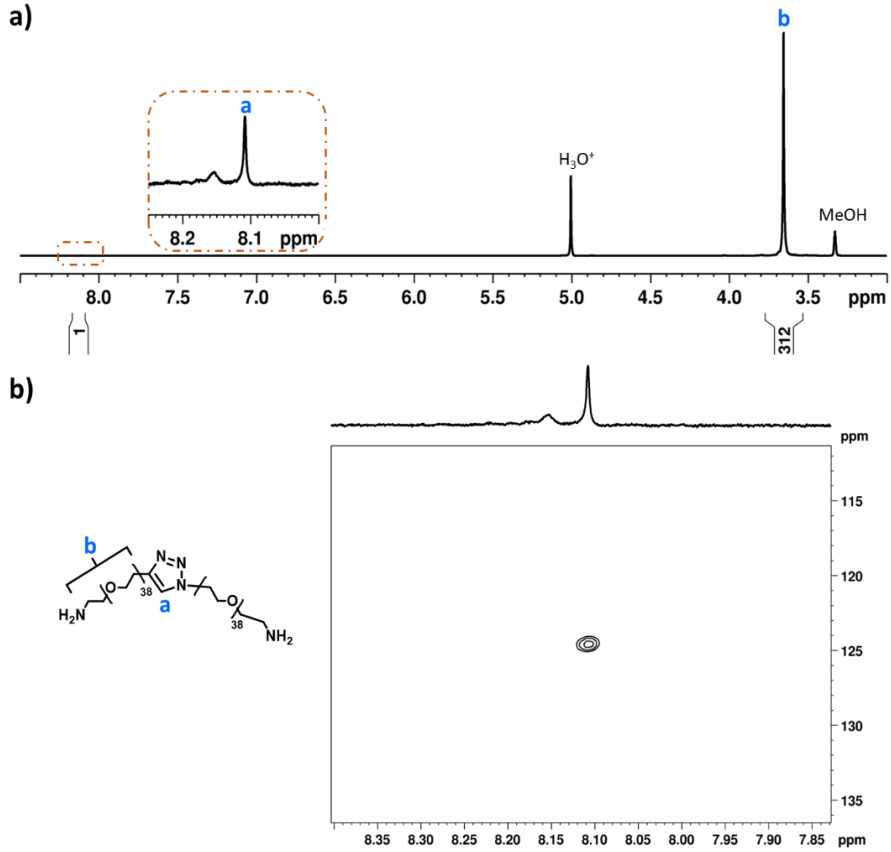

Figure 4.20. ***a)*** ^1H-NMR spectrum (500 MHz, 25ºC) of the digested product in MeOD under acidic conditions (DCl 2 %, 65º C, overnight) obtained after a blank click reaction between NH_2-PEG_{38}-(N_3) and NH_2-PEG_{38}-alkyne. A singlet appearing at 8.11 ppm can be ascribed to the triazole ring (a), as in the case of the spectrum of the digested MOP – dimer. ***b)*** ^1H-^{13}C- HSQC spectrum (500 MHz, 25ºC) of the product obtained after a blank click reaction.

proton correlates with a carbon signal at 124 ppm, which is consistent with the expected chemical shift for an aromatic carbon of a 1,2,3-triazole ring (Figure 4.20b). Collectively, these results confirm that the two 1-c MOP units were successfully and selectively dimerized through a single triazole linkage. This outcome demonstrates the efficacy of a strategy based on controlling the number of reactive sites on the MOP surface and exploiting orthogonal click chemistry to direct the assembly of well-defined multimeric architectures.

4.2.3. Increasing the connectivity in the synthesis of oligomeric MOP-based supramolecules

4.2.3.1. MOP-tetramer

Having confirmed the viability of the MOP oligomerisation, we next targeted oligomeric structures having a higher number of MOP units. We began by synthesising a tetrameric structure in which four 1-c MOPs are linked to a single 4-c node that comprises a dirhodium paddlewheel unit.

The synthesis began with the preparation of the 4-c core, for which we employed the reported $Rh_2(BDC)_4$ cluster.[45] This complex features four available carboxylic acid groups, which were used to couple four alkyne-terminated NH_2-PEG_6-alkyne chains *via* amide bonds formation, yielding $Rh_2(PEG_6\text{-alkyne})_4$ (Figure 4.21a). The successful obtention of the alkyne product was first

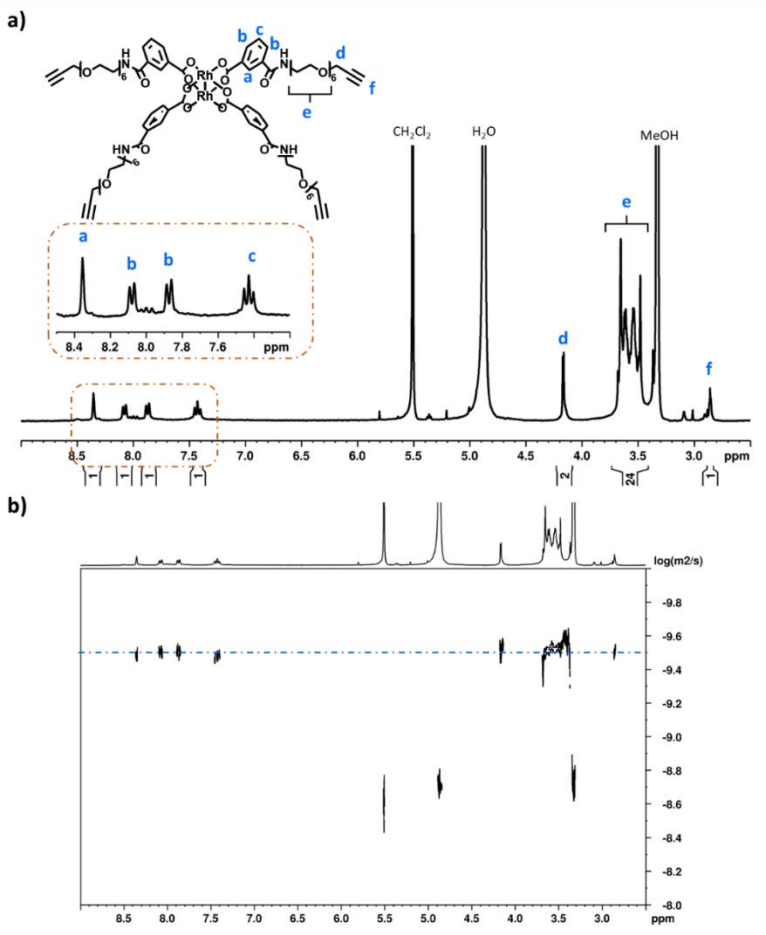

Figure 4.21. a) ^{1}H-NMR spectrum (300 MHz, 25ºC) of the 4-c $Rh_2(PEG_6\text{-alkyne})_4$ cluster in MeOD. The correct ratio between the aromatic and the aliphatic signals confirms the successful attachment of four NH_2-PEG_6-alkyne chains to the Rh_2BDC_4 cluster. ***b)*** DOSY-NMR (300 MHz, 25ºC) spectrum of the 4-c $Rh_2(PEG_6\text{-alkyne})_4$ cluster in MeOD. The same diffusion coefficient ($D \approx 3.1 \cdot 10^{-10}$ $m^2 \cdot s^{-1}$) is assigned for the aromatic and aliphatic protons, demonstrating that all belongs to the same molecule. The diffusion coefficient of the residual MeOH ($D \approx 2.4 \cdot 10^{-9}$ $m^2 \cdot s^{-1}$) was used as internal reference.

evidenced by ^{1}H-NMR in which the signals corresponding to the polymeric chain can be observed, indeed the integration of all the signals demonstrates that the 4 PEG chains have been attached (Figure 4.21a). Furthermore, DOSY-NMR shows that aromatic and the aliphatic signals have the same diffusion coefficient, D ≈ $3.1 \cdot 10^{-10}$ $m^2 \cdot s^{-1}$, thus suggesting that all belongs to the same entity (Figure 4.21b).

UV-Vis spectroscopy of the synthesised 4-c alkyne cluster in DMF displayed the expected absorption band centred at 585 nm,

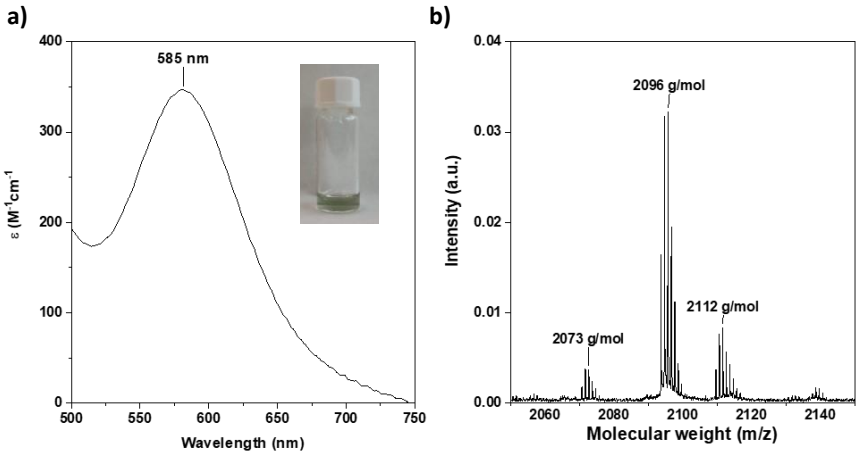

Figure 4.22. a) UV-Vis spectrum of the 4-c $Rh_2(PEG_6\text{-alkyne})_4$ cluster in DMF with a concentration of 1.6 mM. λ_{max} is centred at 585 nm, confirming that the Rh(II) paddlewheel is maintained and that is not coordinated to remaining N-containing reactants (*i.e.* $NH_2\text{-}PEG_6\text{-alkyne}$). ***b)*** MALDI-TOF spectrum of the 4-c $Rh_2(PEG_6\text{-alkyne})_4$ cluster in MeOH. The highlighted mass corresponds to the molecular formula of $[(alkyne\text{-}PEG_6\text{-}BDC)_4Rh_2 + H^+]^+ \cdot H_2O$. Expected: m/z = 2090; Found: m/z = 2096. The second peak at 2073 m/z corresponds to the loss of a water molecule (expected: m/z = 2072) whereas the peak centred at 2112 m/z corresponds to addition of a second water molecule (expected: m/z = 2108).

consistent with the preserved Rh(II) paddlewheel and absence of coordination with residual amine-containing precursors (Figure 4.22a). MALDI-TOF mass spectrometry confirmed the formation of the desired species, with a peak centred at 2073 m/z, corresponding to the molecular formula $[(\text{alkyne-PEG}_6\text{-BDC})_4\text{Rh}_2 + H^+]^+$ (calculated mass: 2072 g mol^{-1}). Additional peaks at 2090 and 2108 m/z were attributed to the addition of one and two water molecules, respectively (Figure 4.22b).

With the central 4-c node in hand, we proceed to synthesise the tetrameric MOP-based molecule by coupling it to 1-c MOP. Therefore, $(N_3)_1$-RhMOP (10 mol. eq.) was reacted with the synthesised alkyne-functionalised 4-c cluster in a mixture of CH_2Cl_2/DMF (1:1), using copper sulphate and sodium ascorbate as CuAAC catalysts. The reaction proceeded homogenously and, after 48 hours, it was quenched by extracting the crude reaction with 0.3 M HCl and water to remove the catalysts. The remaining organic solvent was removed in vacuo, and the resultant crude product was treated with TBAF to deprotect all the carboxylic acid groups present in the mixture. To purify the carboxylic acid-functionalised tetramer (hereafter, MOP-tetramer) from any unreacted 4-c cluster or $(N_3)_1$-RhMOP, the crude product was dissolved in basic water, and then filtered using a centrifugal filter with a molecular weight cut-off of 30 kDa. The MOP-tetramer was

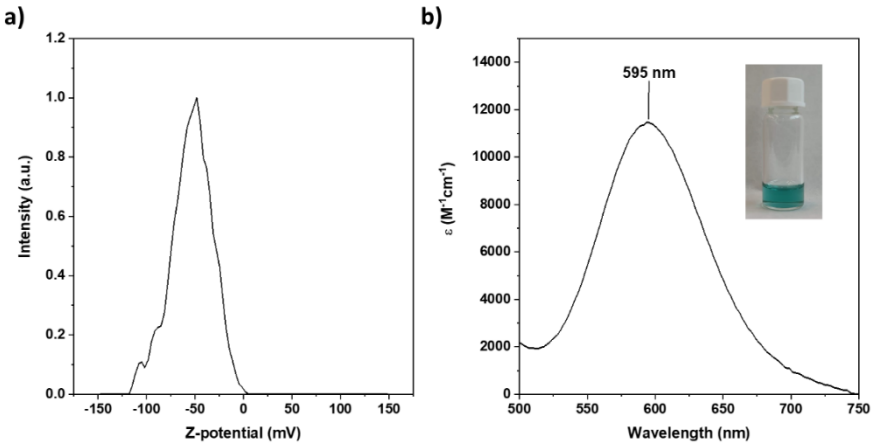

Figure 4.23. ***a*** Z-potential distribution of MOP-tetramer in basic water (pH = 12). ***b)*** UV-Vis spectrum of MOP-tetramer in DMF with a concentration of 0.1 mM. λ_{max} is centered at 595 nm, confirming that the Rh(II) paddlewheel is maintained and that it is not coordinated to the triazole group present in the product.

retained, whereas the smaller 4-c cluster and $(N_3)_1$-RhMOP passed through the filter. As observed for the MOP-dimer, the pH-dependent aqueous solubility was ascribed to the presence of the available carboxylic groups that once deprotonated imparted negative charge to the resulting structures, as confirmed by Z-potential measurements performed in basic water (pH = 12), which revealed a value of -50.3 ± 3.2 mV (Figure 4.23a).

To verify the structural integrity of the MOP-tetramer after the click reaction and deprotection steps, a UV-Vis spectrum in DMF was recorded. The absorption band at 595 nm confirmed that the Rh(II) paddlewheel architecture remained intact (Figure 4.23b).

MALDI-TOF mass spectrometry further validated the formation of the tetramer, with a broad peak centred at 39027 m/z, in agreement with the calculated mass of 39047 ± 1480 g mol^{-1} for a MOP-tetramer bearing the molecular formula [[(COOH-BDC)$_{23}$(BDC-PEG$_{38}$-1*H*-1,2,3-triazol-4-yl-PEG$_6$-BDC)$_1$Rh$_{24}$]$_4$Rh$_2$ + H$^+$]$^+$ (Figure 4.24).

Moreover, the ^{1}H-NMR spectrum of MOP-tetramer in basic D_2O confirmed the expected ratio of aliphatic PEG protons to aromatic protons in the 1-c MOP and the 4-c cluster, which had the same diffusion coefficient of 5.5 · 10^{-10}m^{2}s^{-1} (Figure 4.25a and b, respectively). Importantly, the higher oligomeric degree of MOP-tetramer compared to MOP-dimer was corroborated by its lower diffusion coefficient (5.5·10^{-10} m^2 s^{-1} *vs.* 6.2·10^{-10} m^2 s^{-1})

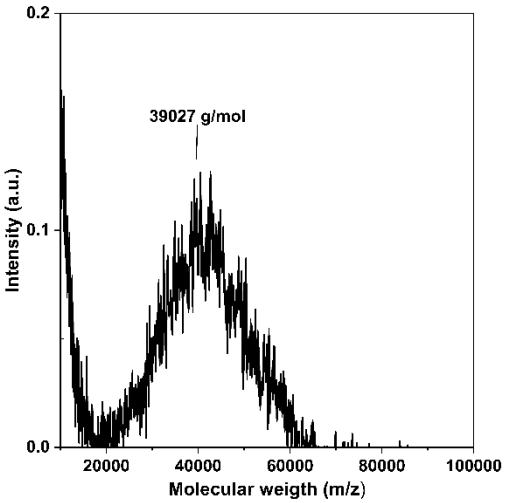

Figure 4.24. MALDI-TOF spectrum of the MOP-tetramer in DMF. The highlighted mass corresponds to the molecular formula of [[(COOH-BDC)$_{23}$(BDC-PEG$_{38}$-1*H*-1,2,3-triazol-4-yl-PEG$_6$-BDC)$_1$Rh$_{24}$)]$_4$Rh$_2$-H$^+$]$^-$. Expected: m/z = 39047 ± 1480 g mol^{-1}; found: m/z = 39027 g mol^{-1}.

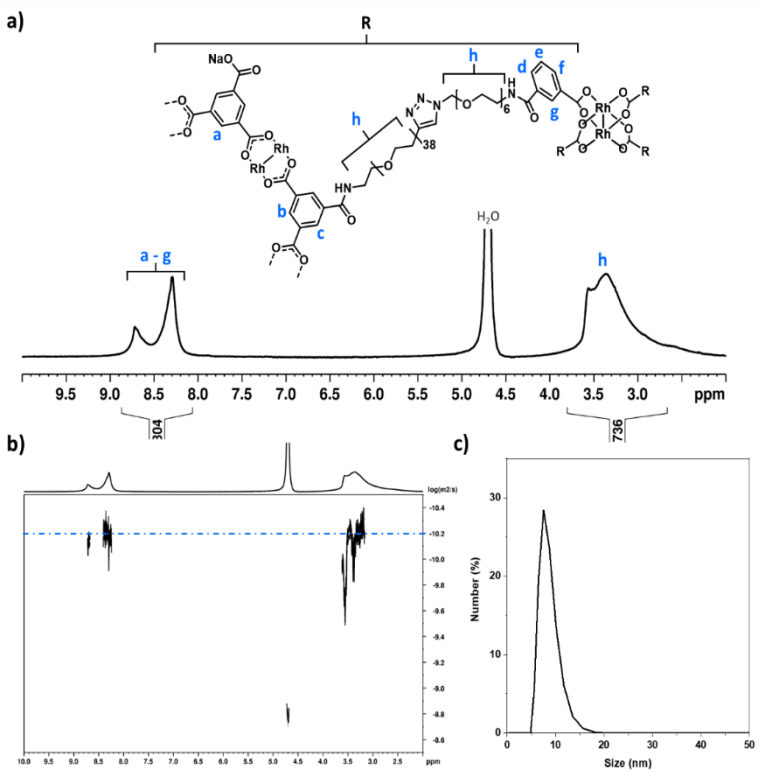

Figure 4.25. ***a)*** ^{1}H-NMR spectrum (300 MHz, 25ºC) of the MOP-tetramer in basic D_2O (pD ≈ 12). Note that, under basic conditions, the surface carboxylic groups are deprotonated affording solubility in water. The relative integrations of the protons ascribed to the MOP core and the 4-c cluster (*a*-*g*) and the aliphatic signals form the PEG chain (*h*) correspond to the expected value for the proposed formula; that is, for each MOP-tetramer, there are 4 MOPs and 1 4-c cluster that contribute with 304 aromatic protons (*a*-*g*) and four PEG chains with up to 736 aliphatic protons (*h*). ***b)*** DOSY-NMR (300 MHz, 25ºC) spectrum of MOP-tetramer in basic D_2O (pD ≈ 12). The same diffusion coefficient (D ≈ 5.5· 10^{-10} $m^2 \cdot s^{-1}$) is identified for the aromatic signals that correspond to the MOP and for the PEG, demonstrating that all belongs to the same molecule. The diffusion coefficient of the residual H_2O (D ≈ 2.3 · 10^{-9} $m^2 \cdot s^{-1}$) was used as internal reference. ***c)*** DLS spectrum of MOP-tetramer in basic H_2O (pH ≈ 12) at a concentration of 0.3 mM. The average diameter was found to be 7.2 ± 0.6 nm.

and by its greater particle-size (7.2 ± 0.6 nm *vs.* 6.3 ± 1.1 nm), as revealed by DOSY NMR and DLS measurements, respectively (Figure 4.25c).

4.2.3.2. MOP-satellite

Finally, to further extend the oligomeric degree of this family of MOP-based giant molecules, we sought to prepare a highly connected node. We reasoned that such a node could be synthesised from a cuboctahedral Rh-MOP, which can contain up to 24 reactive sites on its surface. Thus, a 24-c node was synthesised using a Rh-MOP with all its carboxylic acid groups available (hereafter, $COOH_{24}$-RhMOP). This entailed attaching 24 NH_2PEG_6-alkyne chains, *via* amide-coupling chemistry, onto the surface of the $COOH_{24}$-RhMOP to afford a 24-c node (hereafter, $(alkyne)_{24}$-RhMOP). The successful reaction was first evidenced by ^{1}H-NMR in which broad signals corresponding to the PEG chains appeared with the expected ratio for a MOP with 24 chains attached (Figure 4.26a). Furthermore, DOSY NMR demonstrates that all the signals correspond to the same entity, since they have the same diffusion coefficient, $D \approx 1.7 \cdot 10^{-10}$ m^2 s^{-1} (Figure 4.26b).

Additionally, acidic digestion of $(alkyne)_{24}$-RhMOP demonstrates the full conversion of all the carboxylic groups into amide bonds, and therefore the complete functionalization (Figure 4.26c).

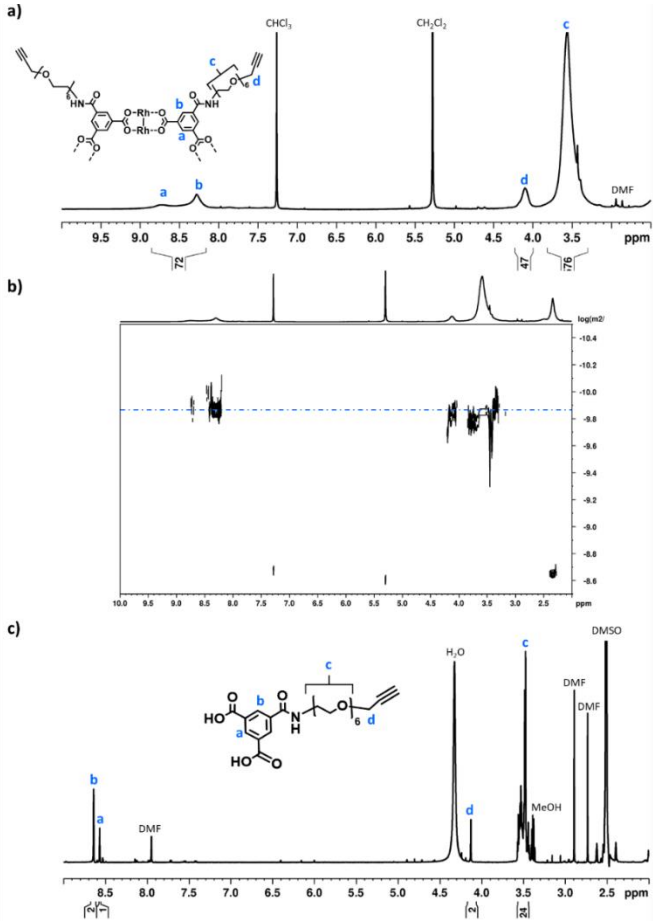

Figure 4.26. ***a)*** ^{1}H-NMR spectrum (300 MHz, 25ºC) of (alkyne)$_{24}$-RhMOP in $CDCl_3$. The relative integrations of the protons ascribed to the MOP core (*a* and *b*) and the aliphatic signals form the PEG chain (*c*) correspond to the expected value for the proposed formula; that is, for each (alkyne)$_{24}$-RhMOP, there are 72 aromatic protons (*a* and *b*) and *ca*. 576 aliphatic protons from the PEG chains (*c*). ***b)*** DOSY-NMR (300 MHz, 25ºC) spectrum of (alkyne)$_{24}$-RhMOP in $CDCl_3$. The same diffusion coefficient ($D \approx 1.7 \cdot 10^{-10}$ $m^2 \cdot s^{-1}$) is identified for the aromatic signals that correspond to the MOP core and for the PEG chains, demonstrating that they belong to the same molecule. The diffusion coefficient of the residual $CHCl_3$ ($D \approx 2.3 \cdot 10^{-9}$ $m^2 \cdot s^{-1}$) was used as internal reference. ***c)*** ^{1}H-NMR spectrum (300 MHz, 25ºC) of (alkyne)$_{24}$-RhMOP digested in DMSO-d_6 under acidic conditions (DCl 20%, 100 ºC, 2 hours). Signals *a* and *b* confirm the formation of the amide bond, and the correct ratio between all the signals evidences the quantitative reaction. Note that the alkyne proton cannot be assigned due to its overlapping with solvent signals.

MALDI-TOF mass spectroscopy further corroborates the formation of (alkyne)$_{24}$-RhMOP with a signal centred at 15409 m/z, which corresponds to the molecular formula of [(alkyne-PEG$_6$-BDC)$_{24}$Rh$_{24}$+H$^+$]$^+$ (expected mass 15408 g/mol) (Figure 4.27a). UV-Vis spectroscopy showed a band centred at 594 nm, confirming that the Rh(II) paddlewheel is maintained and that there is not remaining N-coordinated reactants (i.e. NH$_2$-PEG$_6$-alkyne, HOBt, HBTU, DIPEA) (Figure 4.27b).

Next, 24-c (alkyne)$_{24}$RhMOP was reacted with an excess of 1-c (N$_3$)$_1$-RhMOP (240 mol eq. per (alkyne)$_{24}$-RhMOP) in a CuAAC click reaction to yield a satellite-like, MOP-based, giant molecule. The

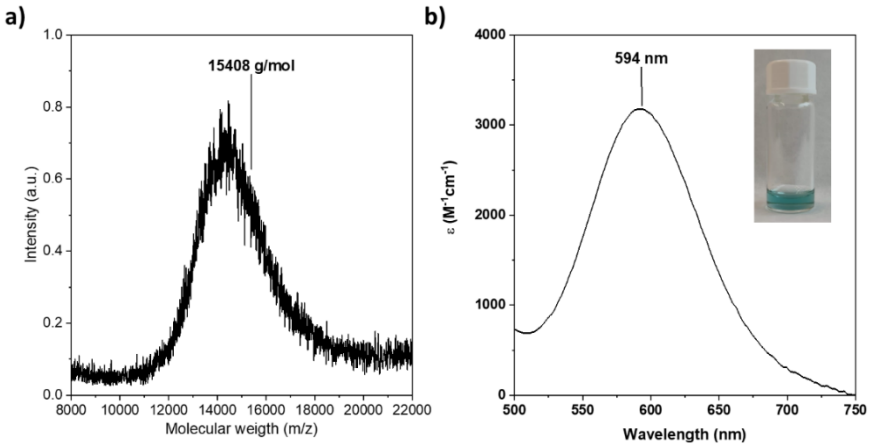

Figure 4.27. a) MALDI-TOF spectrum of (alkyne)$_{24}$-RhMOP in $CHCl_3$. The highlighted mass corresponds to the molecular formula of [(alkyne-PEG$_6$-BDC)$_{24}$Rh$_{24}$ + H$^+$]$^+$. Expected m/z = 15408 g mol^{-1}; found m/z = 15409 g mol^{-1}. ***b)*** UV-Vis spectrum of (alkyne)$_{24}$-RhMOP in DMF with a concentration of 2.2 mM. λ_{max} is centered at 594 nm, confirming that the Rh(II) paddlewheel is maintained and that there is not remaining N-coordinated reactants (*i.e.* NH$_2$-PEG$_6$-alkyne, HOBt, HBTU, DIPEA).

reaction proceeded homogenously in a mixture of CH_2Cl_2/DMF (1:1), using the same CuAAC catalysts as in the previous oligomerization reactions with the addition of tris(hydroxypropyltriazolylmethyl)amine (THPTA), for up to 14 days. Note that the chelating agent THPTA was used to avoid deactivation of the catalyst over the long reaction time.[46,47] The solvent was removed in vacuo to afford the crude product, which was then treated with TBAF to yield a deprotected, satellite-like molecule (hereafter, MOP-satellite) in which all the peripheral MOPs contained 23 surface carboxylic acid groups available for further reactions. MOP-satellite is soluble in basic water due to the presence of surface available COOH groups and could be

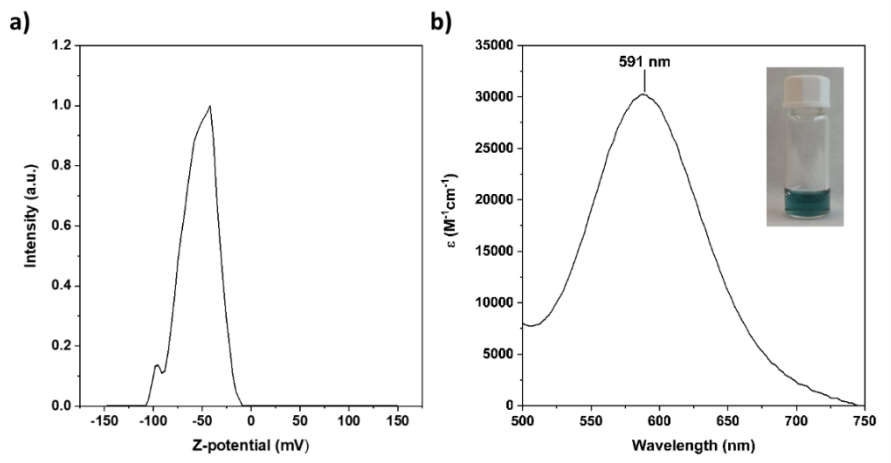

Figure 4.28. ***a)*** Z-potential distribution of MOP-satellite in basic water H_2O (pH = 12). ***b)*** UV-Vis spectrum of MOP-satellite in DMF with a concentration of $3.4 \cdot 10^{-2}$ mM. λ_{max} is centered at 595 nm, confirming that the Rh(II) paddlewheel is maintained and that it is not coordinated to N-containing reagents (i. e. THPTA) or the triazole moiety present in the product.

separated from unreacted $(N_3)_1$-RhMOPs using a centrifugal filter with a molecular weight cut-off of 50 kDa. Negative surface charge in basic water and Rh(II) paddlewheel integrity were confirmed through Z-potential and UV-Vis spectrometry, respectively (Figure 4.28a and b, respectively).

The isolated, purified MOP-satellite was then analysed through mass spectrometry, which revealed a peak centred at 107346 m/z, which we ascribed to a satellite structure having 10 peripheral MOPs and a molecular formula of $[[((COOH\text{-}BDC)_{23}(BDC\text{-}PEG_{38}\text{-}1H\text{-}1,2,3\text{-triazol-4-yl-}PEG_6\text{-}BDC)_1Rh_{24})_{10}(alkyne\text{-}PEG_6\text{-}BDC)_{14}Rh_{24}] + H^+]^+$ (expected molecular weight: 107678 ± 3700 g mol^{-1}) (Figure 4.29).

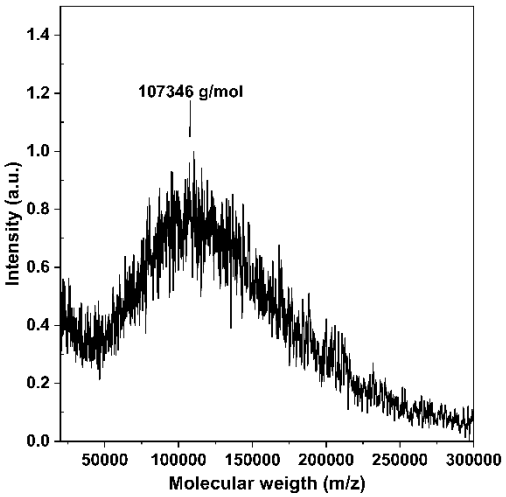

Figure 4.29. MALDI-TOF spectra of MOP-satellite in DMF. The highlighted mass corresponds to the molecular formula of $[[(COOH\text{-}BDC)_{23}(BDC\text{-}PEG_{38}\text{-}1H\text{-}1,2,3\text{-triazol-4-yl-}PEG_6\text{-}BDC)_1Rh_{24})_{10}(Alkyne\text{-}PEG_6\text{-}BDC)_{14}Rh_{24}]+H^+]^+$. Expected: m/z = 107678 ± 3,700 g mol^{-1}; found: m/z = 107346 g mol^{-1}.

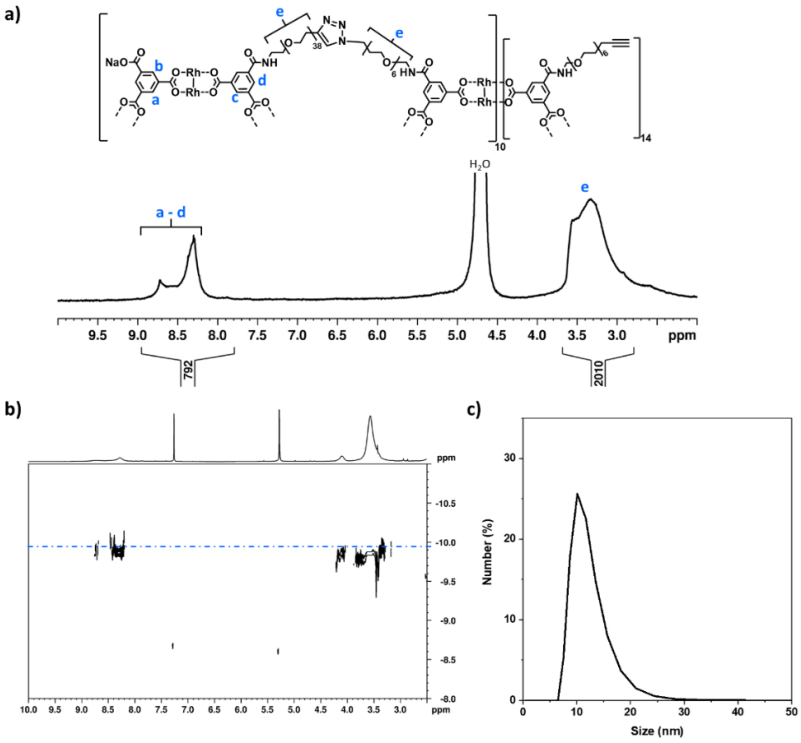

Figure 4.30. a) ^{1}H-NMR spectrum (300 MHz, 25ºC) of MOP-satellite in basic D_2O (pD ≈ 12). Note that, under basic conditions, the surface carboxylic groups are deprotonated affording solubility in water. The relative integrations of the aromatic protons ascribed to the central and peripheral MOP cores (*a* - *d*) and the aliphatic protons of the dangling and bridging PEG chains (*e*) correspond to the expected value for the proposed formula; that is, each MOP-satellite contains 11 MOPs: 1 central MOP and 11 peripheral MOPs. All these MOPs contribute with 792 aromatic protons. Regarding the PEG chains, there are two types of PEGs: 14 small alkyne terminated dangling PEG chains that are only coupled to the central MOP and that contribute with 392 aliphatic protons; and 10 bridging PEG chains that contribute with 1560 aliphatic protons. Overall, the expected ratio between aromatic to aliphatic protons is 0.41, which is very close to the experimental one (0.39). ***b)*** DOSY-NMR (300 MHz, 25ºC) spectrum of MOP-satellite in basic D_2O (pD ≈ 12). The same diffusion coefficient (D ≈ 4.7· 10^{-11} $m^2 \cdot s^{-1}$) is identified for the aromatic signals that correspond to the MOP and for the PEG, evidencing that all of them corresponds to the same molecule. The diffusion coefficient of the residual H_2O (D ≈ 2.3 · 10^{-9} $m^2 \cdot s^{-1}$) was used as internal reference. ***c)*** **.** DLS spectrum of MOP-satellite in basic water H_2O (pH ≈ 12) with a concentration of 0.3 mM.

The proposed molecular composition was further supported by the ^{1}H-NMR spectrum of the MOP-satellite in basic D_2O, in which the ratio of aromatic protons to aliphatic PEG protons was 0.39; in agreement with the expected value for a satellite with 10 peripheral MOPs (0.41) (Figure 4.30a). The aromatic and aliphatic signals displayed the same diffusion coefficient of $4.7 \cdot 10^{-11}$ m^2 s^{-1} (Figure 4.30b) which is the smallest value among those of the synthesised oligomeric MOP-based molecules, consistent with the MOP-satellite having the highest oligomeric degree and the largest molecule size (calculated: 8.6 nm; DLS value: 9.6 ± 0.8 nm) (Figure 4.30c).

4.2.4. Study of the adsorption capabilities of oligomeric molecules in solid state

Having prepared a family of giant oligomeric MOP-based molecules of increasing oligomeric degree, we next endeavoured to explore the functionality of the intrinsic voids stemming from their respective MOP cavities. We had envisioned that their oligomerisation would give rise to the first set of intrinsically porous oligomeric molecules. To demonstrate the permanent porosity of the three oligomeric MOP-based molecules, we subjected them to CO_2-adsorption/desorption experiments at 195 K (Figure 4.31). The measurements confimed that each giant molecule had retained the microporosity of its parent MOP, as

evidenced by the corresponding isotherms, all of which exhibit a type-1 shape. These isotherms were characterized by a sharp increase in the low-pressure range, followed by a plateau in the middle-to-high pressure range. This shape of the isotherm is consistent with the type-1 adsorption characteristic of microporous materials. The total CO_2-uptakes at 1 bar were: 54.4 mol mol^{-1} MOP unit (MOP-dimer), 30.8 mol mol^{-1} MOP unit (MOP-tetramer), and 35.1 mol mol^{-1} MOP unit (MOP-satellite). We ascribed the higher uptake of MOP-dimer to its lack of dangling free PEG chains, which can block porosity; indeed, such chains are found in MOP-satellite. It can also be attributed to its absence of non-porous structuring units (i.e. cluster); for example, these units are found in the MOP tetramer. Interestingly, CO_2-uptake was markedly higher for all the giant oligomeric molecules than for the deprotected 1-c $(N_3)_1$-RhMOP (6.1 mol mol^{-1} MOP unit), the deprotected 1-c $(alkyne)_1$-RhMOP (8.3 mol mol^{-1} MOP unit) and the 24-c $(alkyne)_{24}$-RhMOP (3.6 mol mol^{-1} MOP unit) precursors (Figure 4.31). We ascribed the greater porosity of the oligomeric molecules relative to their precursors to fact that the PEG chains are less mobile when they act as linkers in the former, than when they are dangling from the surface of the latter.

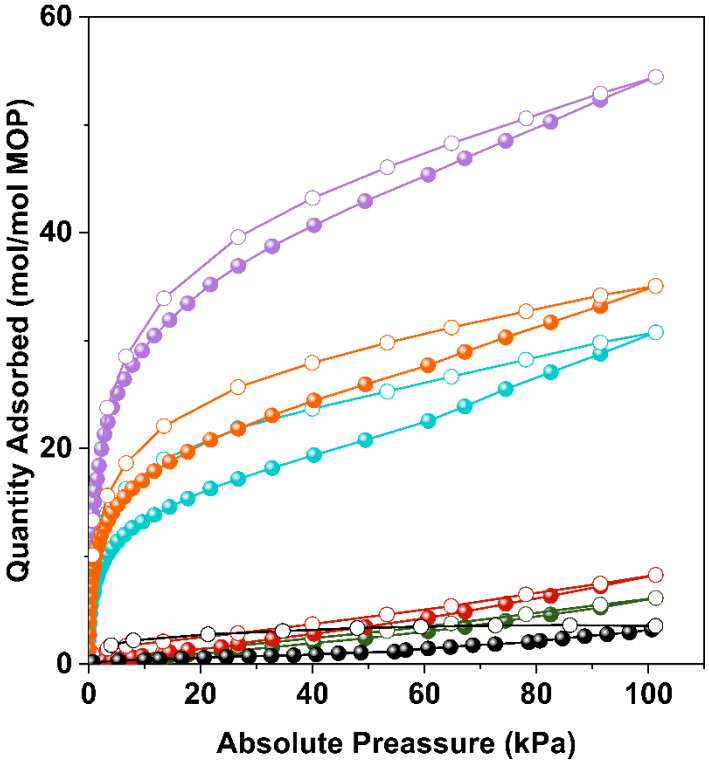

Figure 4.31. Isotherms of CO_2-adsorption at 195 K for deprotected $(N_3)_1$-RhMOP (green), deprotected $(alkyne)_1$-RhMOP (red), $(alkyne)_{24}$-RhMOP (black), MOP-dimer (purple), MOP-tetramer (blue), and MOP-satellite (orange).

4.3. Conclusions

In summary, we have synthesised, characterised, and functionally validated a new class of giant oligomeric porous cage-based molecules. Namely, we developed a new method for the stepwise assembly of individual MOP cavities into oligomeric molecules, based on two factors that enable oligomerisation, rather than

polymerisation. Firstly, the use of 1-c MOPs as building blocks enables termination of the linkage reaction at the oligomeric regime. Secondly, the use of an orthogonal reaction (in our case, CuAAC click chemistry) to link these blocks with other 1-c MOPs or with 4-c nodes or 24-c MOPs to yield molecules of increasing oligomeric degrees, precluding self-condensation between the precursors. Furthermore, gas-sorption experiments revealed that the giant oligomeric molecules retain the intrinsic porosity of the cavities of their parent MOP. We are confident that our results should inform the future design of new porous materials that will occupy the chemical and dimensional space between purely monomeric cavities and extended networks.

4.4. References

[1] S. Lee, H. Jeong, D. Nam, M. S. Lah, W. Choe, *Chem. Soc. Rev.* **2021**, *50*, 528–555.

[2] D. Zhang, T. K. Ronson, Y. Q. Zou, J. R. Nitschke, *Nat. Rev. Chem.* **2021**, *5*, 168–182.

[3] T. Hasell, A. I. Cooper, *Nat. Rev. Mater.* **2016**, *1*, 16053.

[4] A. J. Gosselin, C. A. Rowland, E. D. Bloch, *Chem. Rev.* **2020**, *120*, 8987–9014.

[5] G. Zhang, M. Mastalerz, *Chem. Soc. Rev.* **2014**, *43*, 1934–1947.

[6] O. K. Farha, I. Eryazici, N. C. Jeong, B. G. Hauser, C. E. Wilmer, A. A. Sarjeant, R. Q. Snurr, S. T. Nguyen, A. Ö. Yazaydin, J. T. Hupp, *J. Am. Chem. Soc.* **2012**, *134*, 15016–15021.

[7] N. Huang, P. Wang, D. Jiang, *Nat. Rev. Mater.* **2016**, *1*, 16068.

[8] K. Geng, T. He, R. Liu, S. Dalapati, K. T. Tan, Z. Li, S. Tao, Y. Gong, Q. Jiang, D. Jiang, *Chem. Rev.* **2020**, *120*, 8814–8933.

[9] G. Maurin, C. Serre, A. Cooper, G. Férey, *Chem. Soc. Rev.* **2017**, *46*, 3104–3107.

[10] A. V. Virovets, E. Peresypkina, M. Scheer, *Chem. Rev.* **2021**,

121, 14485–14554.

[11] J. V. Rival, P. Mymoona, K. M. Lakshmi, Nonappa, T. Pradeep, E. S. Shibu, *Small* **2021**, *17*, 1–33.

[12] H. Wang, Y. Li, N. Li, A. Filosa, X. Li, *Nat. Rev. Mater.* **2021**, *6*, 145–167.

[13] D. Fujita, Y. Ueda, S. Sato, N. Mizuno, T. Kumasaka, M. Fujita, *Nature* **2016**, *540*, 563–566.

[14] X. G. Wang, Q. Cheng, Y. Yu, X. Z. Zhang, *Angew. Chem. Int. Ed.* **2018**, *57*, 7836–7840.

[15] F. Caddeo, R. Vogt, D. Weil, W. Sigle, M. E. Toimil-Molares, A. W. Maijenburg, *ACS Appl. Mater. Interfaces* **2019**, *11*, 25378–25387.

[16] X. Cai, Z. Xie, D. Li, M. Kassymova, S.-Q. Zang, H.-L. Jiang, *Coord. Chem. Rev.* **2020**, *417*, 213366.

[17] J. Andreo, R. Ettlinger, O. Zaremba, Q. Peña, U. Lächelt, R. F. de Luis, R. Freund, S. Canossa, E. Ploetz, W. Zhu, C. S. Diercks, H. Gröger, S. Wuttke, *J. Am. Chem. Soc.* **2022**, *144*, 7531–7550.

[18] D. T. S. Rijkers, G. W. Van Esse, R. Merkx, A. J. Brouwer, H. J. F. Jacobs, R. J. Pieters, R. M. J. Liskamp, *Chem. Commun.* **2005**, *13*, 4581–4583.

[19] Z. Liu, S. Wang, G. Li, Z. Yang, Z. Gan, X. H. Dong, *Macromolecules* **2022**, *55*, 5954–5963.

[20] C. N. Urban, C. A. Bell, M. R. Whittaker, M. J. Monteiro, *Macromolecules* **2008**, *41*, 1057–1060.

[21] Y. Li, R. Biswas, W. P. Kopcha, T. Dubroca, L. Abella, Y. Sun, R. A. Crichton, C. Rathnam, L. Yang, Y. Yeh, K. Kundu, A. Rodríguez-Fortea, J. M. Poblet, K. Lee, S. Hill, J. Zhang, *Angew. Chem. Int. Ed.* **2023**, *62*, e202211704.

[22] A. Muñoz, D. Sigwalt, B. M. Illescas, J. Luczkowiak, L. Rodríguez-Pérez, I. Nierengarten, M. Holler, J. S. Remy, K. Buffet, S. P. Vincent, J. Rojo, R. Delgado, J. F. Nierengarten, N. Martín, *Nat. Chem.* **2016**, *8*, 50–57.

[23] A. Macdonell, N. A. B. Johnson, A. J. Surman, L. Cronin, *J. Am. Chem. Soc.* **2015**, *137*, 5662–5665.

[24] Z. Zhang, Y. Li, B. Song, Y. Zhang, X. Jiang, M. Wang, R. Tumbleson, C. Liu, P. Wang, X.-Q. Hao, T. Rojas, A. T. Ngo, J. L. Sessler, G. R. Newkome, S. W. Hla, X. Li, *Nat. Chem.* **2020**, *12*, 468–474.

[25] G. F. S. Whitehead, F. Moro, G. A. Timco, W. Wernsdorfer, S. J. Teat, R. E. P. Winpenny, *Angew. Chem* **2013**, *125*, 10116–10119.

[26] T. Hasell, X. Wu, J. T. A. Jones, J. Bacsa, A. Steiner, T. Mitra,

A. Trewin, D. J. Adams, A. I. Cooper, *Nat. Chem.* **2010**, *2*, 750–755.

[27] M. Frank, M. D. Johnstone, G. H. Clever, *Chem. – A Eur. J.* **2016**, *22*, 14104–14125.

[28] R. Zhu, I. Regeni, J. J. Holstein, B. Dittrich, M. Simon, S. Prévost, M. Gradzielski, G. H. Clever, *Angew. Chem. Int. Ed.* **2018**, *57*, 13652–13656.

[29] B. P. Benke, T. Kirschbaum, J. Graf, J. H. Gross, M. Mastalerz, *Nat. Chem.* **2023**, *15*, 413–423.

[30] C. Yu, P. Yang, X. Zhu, Y. Wang, *Sci. China Chem.* **2022**, *65*, 858–862.

[31] C. Yu, Y. Yang, Y. Wang, *New J. Chem.* **2021**, *45*, 22049–22052.

[32] R. L. Greenaway, V. Santolini, F. T. Szczypiński, M. J. Bennison, M. A. Little, A. Marsh, K. E. Jelfs, A. I. Cooper, *Chem. Eur. J.* **2020**, *26*, 3718–3722.

[33] A. Khobotov-Bakishev, L. Hernández-López, C. von Baeckmann, J. Albalad, A. Carné-Sánchez, D. Maspoch, *Adv. Sci.* **2022**, *9*, 2104753.

[34] E. Sánchez-González, M. Y. Tsang, J. Troyano, G. A. Craig, S. Furukawa, *Chem. Soc. Rev.* **2022**, *51*, 4876–4889.

[35] A. Fernandez, J. Ferrando-Soria, E. M. Pineda, F. Tuna, I. J. Vitorica-Yrezabal, C. Knappke, J. Ujma, C. A. Muryn, G. A. Timco, P. E. Barran, A. Ardavan, R. E. P. Winpenny, *Nat. Commun.* **2016**, *7*, 1–6.

[36] S. Furukawa, N. Horike, M. Kondo, Y. Hijikata, A. Carné-Sánchez, P. Larpent, N. Louvain, S. Diring, H. Sato, R. Matsuda, R. Kawano, S. Kitagawa, *Inorg. Chem.* **2016**, *55*, 10843–10846.

[37] J. Albalad, L. Hernández-López, A. Carné-Sánchez, D. Maspoch, *Chem. Commun.* **2022**, *58*, 2443–2454.

[38] T. Grancha, A. Carné-Sánchez, F. Zarekarizi, L. Hernández-López, J. Albalad, A. Khobotov, V. Guillerm, A. Morsali, J. Juanhuix, F. Gándara, I. Imaz, D. Maspoch, *Angew. Chem* **2021**, *133*, 5793–5797.

[39] J. Troyano, S. Horike, S. Furukawa, *J. Am. Chem. Soc.* **2022**, *144*, 19475–19484.

[40] A. Khobotov-Bakishev, C. Von Baeckmann, B. Ortín-Rubio, L. Hernández-López, A. Cortés-Martínez, J. Martínez-Esaín, F. Gándara, J. Juanhuix, A. E. Platero-Prats, J. Faraudo, A. Carné-Sánchez, D. Maspoch, *J. Am. Chem. Soc.* **2022**, *144*, 15745–15753.

[41] A. J. Gosselin, G. E. Decker, A. M. Antonio, G. R. Lorzing, G.

P. A. Yap, E. D. Bloch, *J. Am. Chem. Soc.* **2020**, *142*, 9594–9598.

[42] J. Albalad, A. Carné-Sánchez, T. Grancha, L. Hernández-López, D. Maspoch, *Chem. Commun.* **2019**, *55*, 12785–12788.

[43] L. Hernández-López, C. von Baeckmann, J. Martínez-Esaín, A. Cortés-Martínez, J. Faraudo, C. Caules, T. Parella, D. Maspoch, A. Carné-Sánchez, *Chem. – A Eur. J.* **2023**, *29*, e202301945.

[44] L. Avram, Y. Cohen, *Chem. Soc. Rev.* **2015**, *44*, 586–602.

[45] C. von Baeckmann, S. Ruiz-Relaño, I. Imaz, M. Handke, J. Juanhuix, F. Gándara, A. Carné-Sanchez, D. Maspoch, *Chem. Commun.* **2023**, *59*, 3423–3426.

[46] V. Hong, S. I. Presolski, C. Ma, M. G. Finn, *Angew. Chem. Int. Ed.* **2009**, *48*, 9879–9883.

[47] C. Uttamapinant, A. Tangpeerachaikul, S. Grecian, S. Clarke, U. Singh, P. Slade, K. R. Gee, A. Y. Ting, *Angew. Chem. Int. Ed.* **2012**, *51*, 5852–5856.

ISORETICULAR SYNTHESIS OF MESOPOROUS METAL-ORGANIC POLYHEDRA WITH PERMANENT POROSITY TO GAS AND WATER

5. Isoreticular synthesis of mesoporous metal-organic polyhedra with permanent porosity to gas and water

5.1. Introduction

Synthetic chemists have long been inspired by Nature's unparalleled ability to create large, well-defined and functional molecular architectures.[1,2] Seeking to replicate these remarkable structures, chemists have turned to supramolecular chemistry, the assembly of molecular building blocks into large molecules.[3,4] Among the different types of large molecular architectures,[5] MOCs in the mesoporous regime (cavity diameter > 2 nm) stand out due to their (macro)molecular host-guest chemistry. Mesoporous MOCs have typically been assembled either through the controlled assembly of numerous building blocks or the use of organic ligands with increasing sizes (Figure 5.1).

In the first approach, the bent angle of the organic ligand is carefully adjusted to achieve topologies with numerous building blocks, such as the Goldberg polyhedron, which is assembled from 144 components and has a diameter of 5.8 nm (Figure 5.1).[6] In the second approach, known as isoreticular expansion and commonly employed for MOFs,[7,8] the size of a parent cage is enlarged by using ligands of increasing size but having the same bent angle, such that the final structure retains the initial geometry (Figure 5.1).[8–11] Large MOCs assembled from either of these

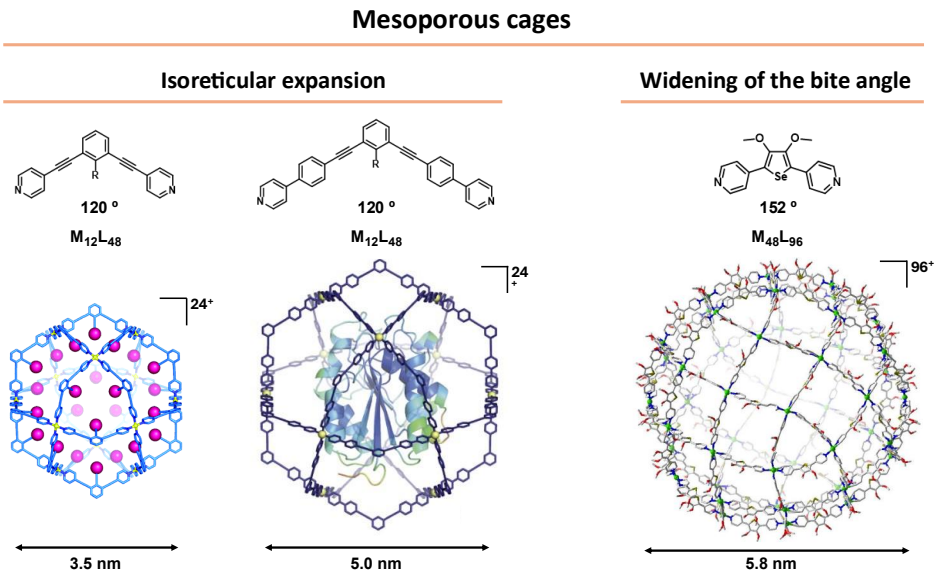

Figure 5.1. Structures of mesoporous cages achieved through the isoreticular expansion approach (left) and the widening of the bite angle strategy (right).

approaches are typically used in solution, in applications such as biomolecular storage, catalysis or separation.[12–17] However, fabricating robust, large MOCs that are permanently mesoporous in the solid state remains a challenge, given their tendency to collapse upon desolvation.[18] To overcome this challenge, the robustness of the cage backbone must be enhanced to withstand the capillary forces during desolvation and maintain the integrity of the empty cavity formed upon solvent removal. This principle is exemplified by permanently mesoporous organic cages, which, owing to strong covalent bonding, resist collapse.[19,20]

In this chapter, we demonstrate the synthesis of permanently porous MOCs with mesoporous cavities, highlighting that coordination bonds can stabilize large internal voids in discrete cages in the solid-state. To this end, we applied the isoreticular expansion approach to MOPs constructed from Rh(II) paddlewheel clusters (Figure 5.2). We hypothesized that the exceptional chemical properties and structural stability of these cluster units would enable the isoreticular expansion of the archetypal parent octahedral Rh(II)-based MOP, having the formula $Rh_{12}(L1)_{12}$ (where L1 is 9*H*-carbazole-3,6-dicarboxylate),

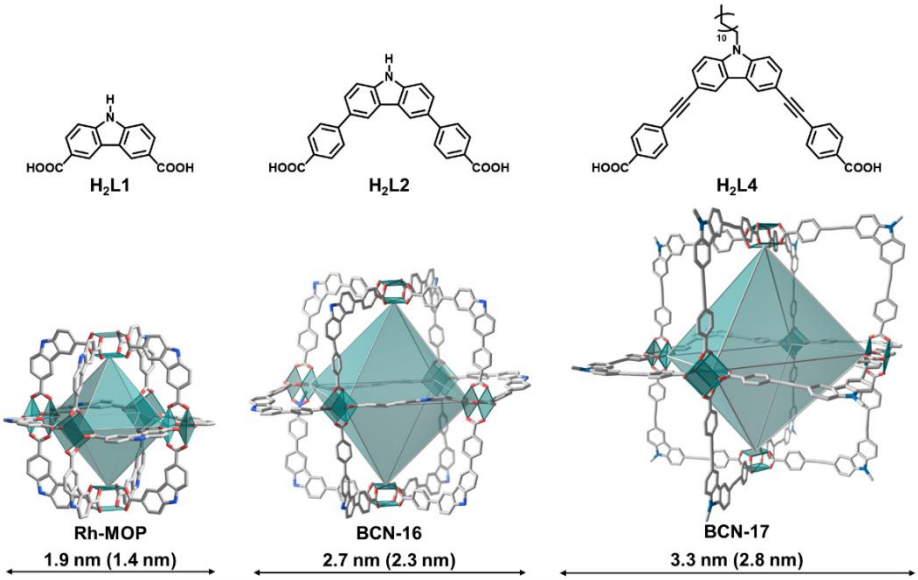

Figure 5.2. Representation of the ligands (top) used in the isoreticular expansion of octahedral Rh-MOPs (bottom), indicating their external size, measured as the distance between their two opposing Rh(II) paddlewheels vertices. The value in parentheses is the internal cavity size, as measured between identical paddlewheels. Note that, for clarity, only the first carbon atom of the C_{12} chains in BCN-17 has been shown.

while preserving its structural integrity upon desolvation.[21–23] This octahedral MOP, initially reported by Prof .S. Furukawa and coworkers and denoted as **oct** according to the Reticular Chemistry Structure Resource (RCSR) database,[24] features two opposite Rh(II) paddlewheel vertices separated by distance of 1.9 nm, and a microporous internal cavity of 1.4 nm^3 (Figure 5.2).[25,26] Building upon this octahedral MOP, we envisioned a double expansion of the carbazole ligand L1 to synthesize two new mesoporous isoreticular Rh(II)-based MOPs (hereafter named BCN-16 and BCN-17, where BCN stands for Barcelona Material), featuring two opposite Rh(II) paddlewheel vertices separated by respective internal distances of 2.3 nm (BCN-16) or 2.8 nm (BCN-17), and respective internal cavities of 6.5 nm^3 (BCN-16) or 12.5 nm^3 (BCN-17) (Figure 5.2). In the following section, the synthetic requirements towards these mesoporous cages will be discussed in addition to their porous properties.

5.2. Results and discussion

5.2.1. Synthesis of parent microporous Rh(II)-based octahedral MOP

We first targeted the synthesis of the parent microporous Rh(II)-based octahedral MOP that will serve as blueprint structure to be expanded. To this end, H_2L1 was reacted with Rh(II) acetate under solvothermal conditions by adapting the reported protocol from Prof. S. Furukawa and coworkers.[24] The complexation reaction yielded a green solution. The crude product was precipitated out with diethyl ether (Et_2O), which afforded a green solid that was further washed with MeOH to remove unreacted reagents and

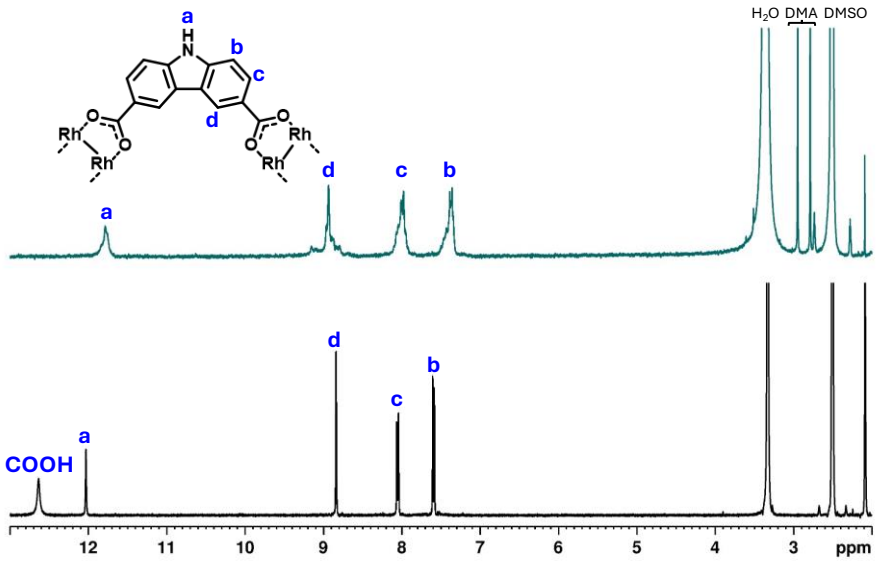

Figure 5.3. ^{1}H-NMR spectra (300 MHz, 25 ^{0}C) of parent octahedral Rh-MOP (top, green) and H_2L1 (bottom, black) in DMSO-d_6. The shift and broadening of the signals confirm the coordination of the ligand to the Rh(II) paddlewheel and the absence of free ligand.

then, dried. ^{1}H-NMR analysis of the redissolved crude product in DMSO-d_6 confirmed the success of the complexation reaction, as the aromatic signals appeared broader and shifted relative to the free ligand (Figure 5.3).

DOSY-NMR analysis of the crude product revealed a diffusion coefficient of $8.7 \cdot 10^{-11}$ m^2 s^{-1}, consistent with the synthesis of a nanoscopic discrete metal-organic assembly (Figure 5.4). Further confirmation of the successful synthesis of the octahedral MOP was obtained from MALDI-TOF mass spectroscopy of the crude product. In the spectrum two signals were observed at 4272.8 m/z and 4297.7 m/z, which corresponds to the molecular formulas of

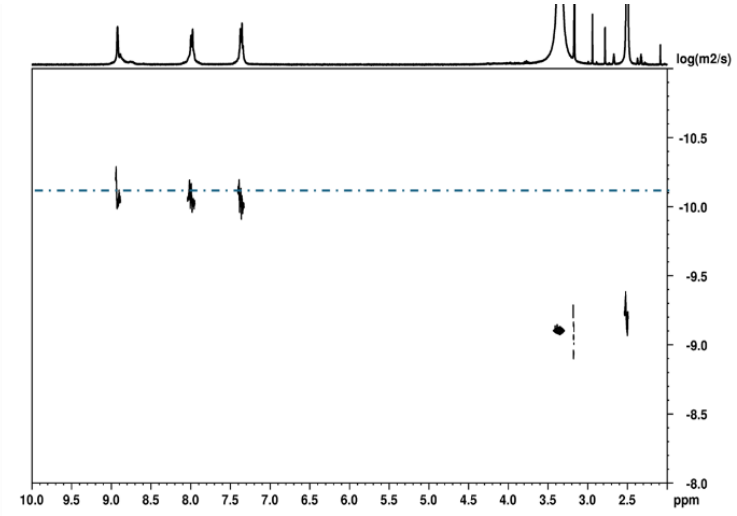

Figure 5.4. DOSY-NMR spectrum (300 MHz, 25 ^{0}C) of parent octahedral Rh-MOP in DMSO-d_6. The same diffusion coefficient (D ≈ $8.7 \cdot 10^{-11}$ m^2·s^{-1}) is identified for all the aromatic protons. The diffusion coefficient of the residual DMSO (D ≈ $8.0 \cdot 10^{-10}$ m^2·s^{-1}) was used as internal reference.

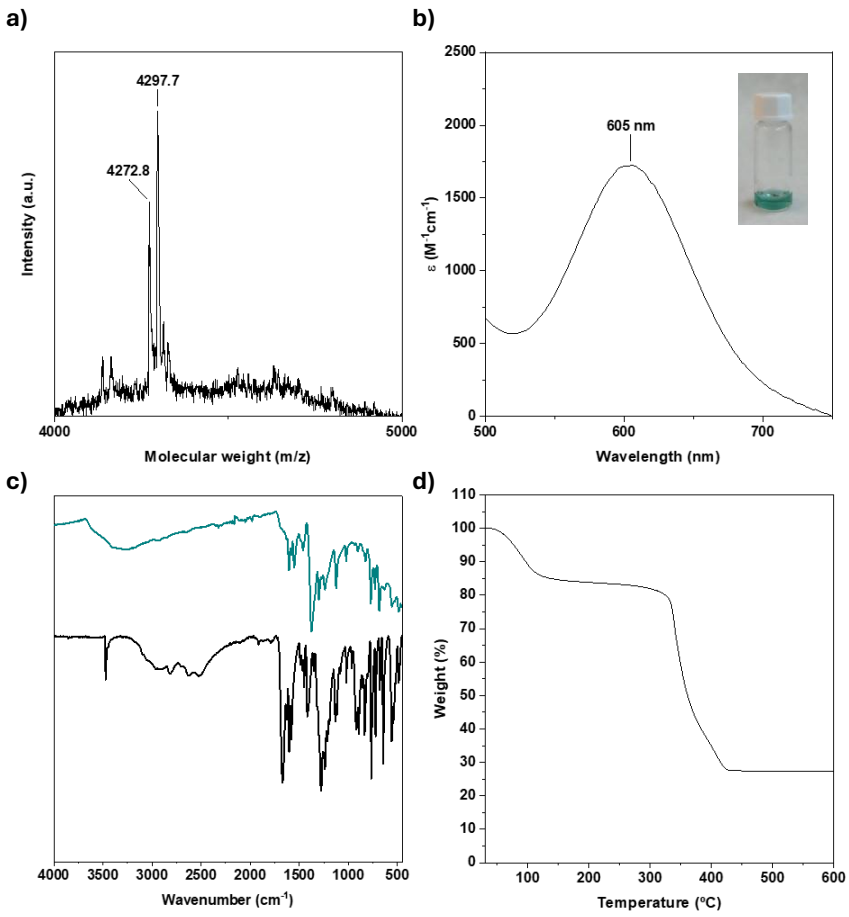

Figure 5.5. ***a)*** MALDI-TOF spectrum of parent octahedral Rh-MOP in DMA. The highlighted masses correspond to the molecular formula of $[Rh_{12}(L1)_{12}+H^+]^+$ (Expected m/z = 4273.6 g·mol^{-1}; found m/z = 4272.8 g·mol^{-1}) and $[Rh_{12}(L1)_{12} + H^+]^+$·MeOH (m/z = 4303.6 g·mol^{-1}; found m/z = 4297.7 g·mol^{-1}). ***b)*** UV-Vis spectrum of parent octahedral Rh-MOP in DMA at a concentration of 2.5 mg/mL. λ_{max} is centered at 605 nm, confirming the integrity of Rh (II) paddlewheel. ***c)*** FTIR spectrum of parent octahedral Rh-MOP (top, green) and H_2L1 (bottom, black). ***d)*** TGA of parent octahedral Rh-MOP. Note that the initial mass loss of *ca*. 15% is associated with the remaining solvent molecules coordinated to the metal-open sites of the Rh-paddlewheels. The decomposition temperature is *ca*. 330 °C.

$[Rh_{12}(L1)_{12}+H^+]^+$·MeOH (expected m/z = 4303.6 g·mol^{-1}), respectively (Figure 5.5a). Additionally, UV-Vis spectroscopy of the MOP dissolved in DMA confirmed the integrity of the Rh(II)-Rh(II) paddlewheel with the presence of a band centred at 605 nm (Figure 5.5b). FTIR further confirmed the purity of the sample and TGA demonstrated its stability up to *ca.* 330 ºC (Figure 5.5c and d, respectively).

To confirm the obtention of the desired MOP topology, single crystals were obtained through slow vapor diffusion of Et_2O into a DMA solution of the Rh(II)-MOP. This process led to the formation of green rhombic crystals that were suitable for SCXRD that confirmed the formation of the octahedral-shaped MOP. This

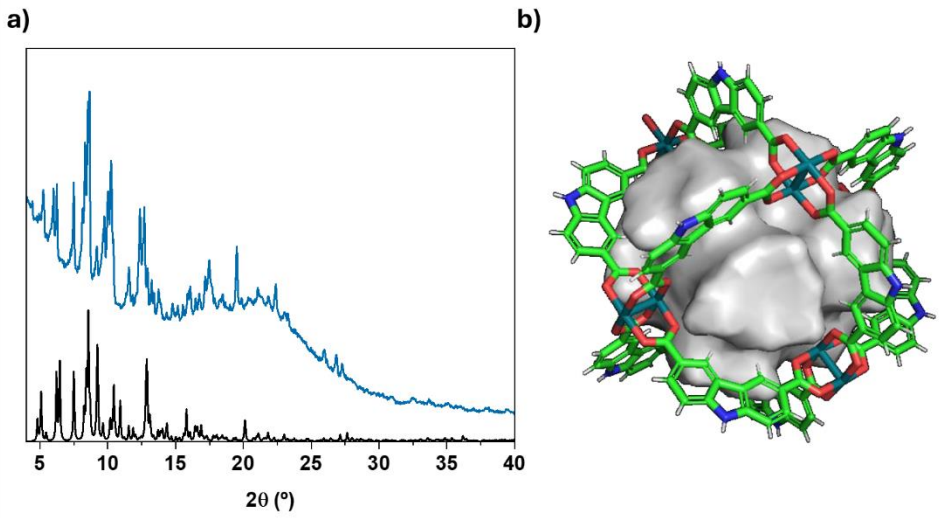

Figure 5.6. ***a)*** Simulated (black, bottom) and experimental (blue, top) PXRD patterns of parent octahedral Rh-MOP. ***b)*** Image of the calculated cavity for parent octahedral Rh-MOP.

structure crystallizes in the triclinic space group P_{-1} with corresponding cell parameters a = 19.6900(10), b = 20.780(2), c = 20.890(2) Å and α = 113.600(2), β = 113.950(2) and γ = 89.870(2)° (Table 2 in the crystallographic data section). Phase homogeneity of the bulk sample was confirmed through PXRD (Figure 5.6a).

As expected, this Rh(II)-MOP is composed by 12 Rh(II) paddlewheel nodes and 12 L1 ligands forming an octahedral structure that has an outer diameter of 1.9 nm, an inner one of 1.4 nm and the volume of its cavity is calculated to be 1.4 nm^3 (Figure 5.6b).

5.2.2. First isoreticular expansion of the Rh(II)-based octahedral MOP

To tackle the first isoreticular expansion of the parent $Rh_{12}(L1)_{12}$ MOP, we began with the synthesis of 4,4-(9*H*-carbazole-3,6-diyl)dibenzoic acid (H_2L2), an expanded version of H_2L1 that adds a benzene ring between the carbazole core and the adjacent carboxylic acid group. Once synthesized, H_2L2 was reacted with Rh(II) acetate under solvothermal conditions. The complexation reaction yielded a green solution. The crude product was precipitated out with Et_2O, which afforded a green solid that was further washed with MeOH to remove unreacted reagents and then, dried. ^{1}H-NMR analysis of the redissolved crude product in DMSO-d_6 confirmed the success of the complexation reaction, as

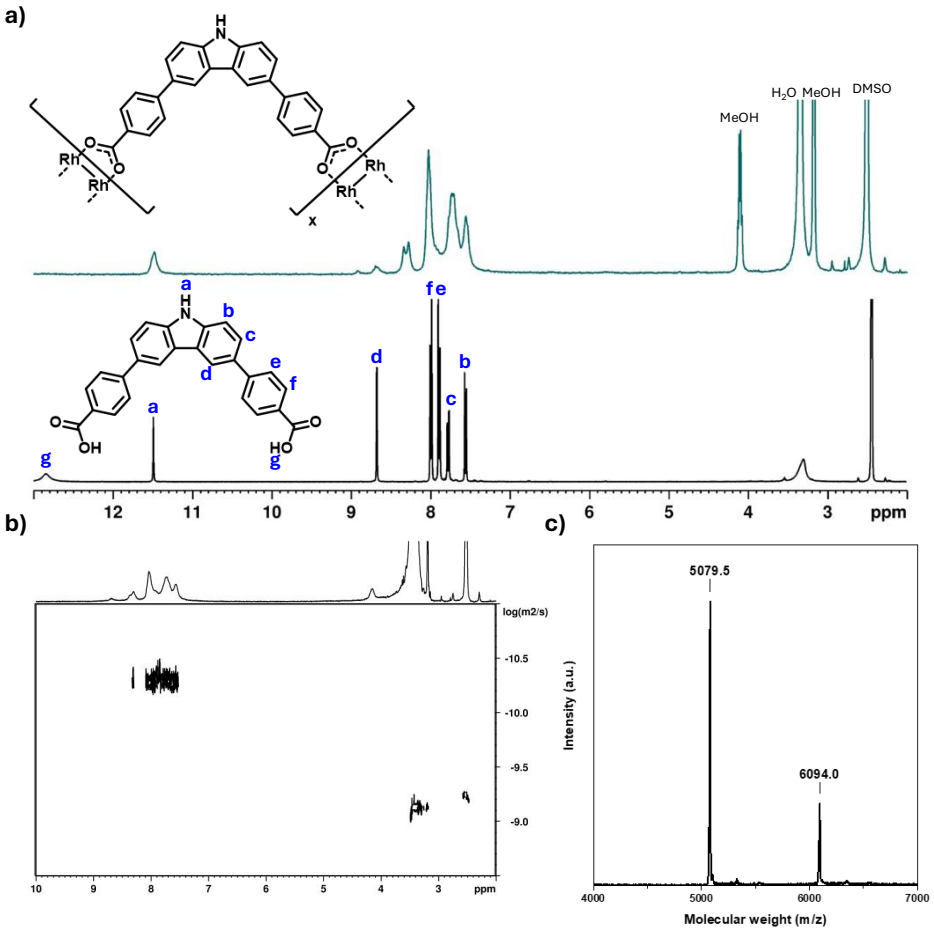

Figure 5.7. ***a)*** ^{1}H-NMR spectrum (300 MHz, 25 ^{0}C) of the re-dissolved crude product from the reaction between rhodium acetate and H_2L2 (where x = 10 or 12) in DMSO-d_6. The shift and broadening of the signals confirm the coordination of the ligand to the Rh(II) paddlewheel and the absence of free ligand. Note that integration of the signals is not possible due to their overlap. ***b)*** DOSY-NMR spectrum (300 MHz, 25 ^{0}C) of the re-dissolved crude product in DMSO-d_6. The same diffusion coefficient ($D \approx 5.1 \cdot 10^{-11}$ $m^2 \cdot s^{-1}$) is identified for all the aromatic protons. The diffusion coefficient of the residual DMSO ($D \approx 8.0 \cdot 10^{-10}$ $m^2 \cdot s^{-1}$) was used as internal reference. ***c)*** MALDI-TOF spectrum of the re-dissolved crude product in DMA. The highlighted masses correspond to the molecular formula of $[Rh_{12}(L2)_{12}+H^+]^+$ (expected m/z = 5084.0 $g \cdot mol^{-1}$; found m/z = 5079.5 $g \cdot mol^{-1}$) and $[Rh_{10}(L2)_{10}+H^+]^+$ (expected m/z = 6100.6 $g \cdot mol^{-1}$; found m/z = 6094.0 $g \cdot mol^{-1}$).

the aromatic signals appeared broad and shifted relative to the free ligand (Figure 5.7a). DOSY-NMR analysis of the crude product revealed a diffusion coefficient of $5.1 \cdot 10^{-11}$ m^2 s^{-1}, consistent with the synthesis of a metal-organic molecule (Figure 5.7b). MALDI-TOF mass spectroscopy of the crude product revealed that it contains at least two different metal-organic compounds, having the formulae $[Rh_{10}(L2)_{10}+H^+]^+$ (found mass 5079.5 m/z, expected mass 5084.0 g mol^{-1}) and $[Rh_{12}(L2)_{12}+H^+]^+$ (found mass 6100.6 m/z, expected mass 6100.6 g mol^{-1}) (Figure 5.7c).

Isolation of supramolecular compounds through conventional separation techniques such as chromatography is difficult, due to their similar affinity to the stationary phase. Accordingly, we aimed to purify the crude mixture by recrystallization (Figure 5.8).

To this end, we exposed a solution of the crude product in DMA to MeOH vapor, which yielded a microcrystalline material (A) and an amorphous solid (B). The crystalline material could be separated from the amorphous portion by sedimentation in MeOH, with the crystalline material A settling faster than did the amorphous fraction B. The crystalline product A was redissolved in DMA and recrystallized in the presence of 12 molecular equivalents of 4-*tert*-butylpyiridine and acetonitrile vapor. This crystallization yielded single crystals of sufficient quality for SCXRD analysis (yield based on Rh(II): 2%). Note that subjecting the crude mixture

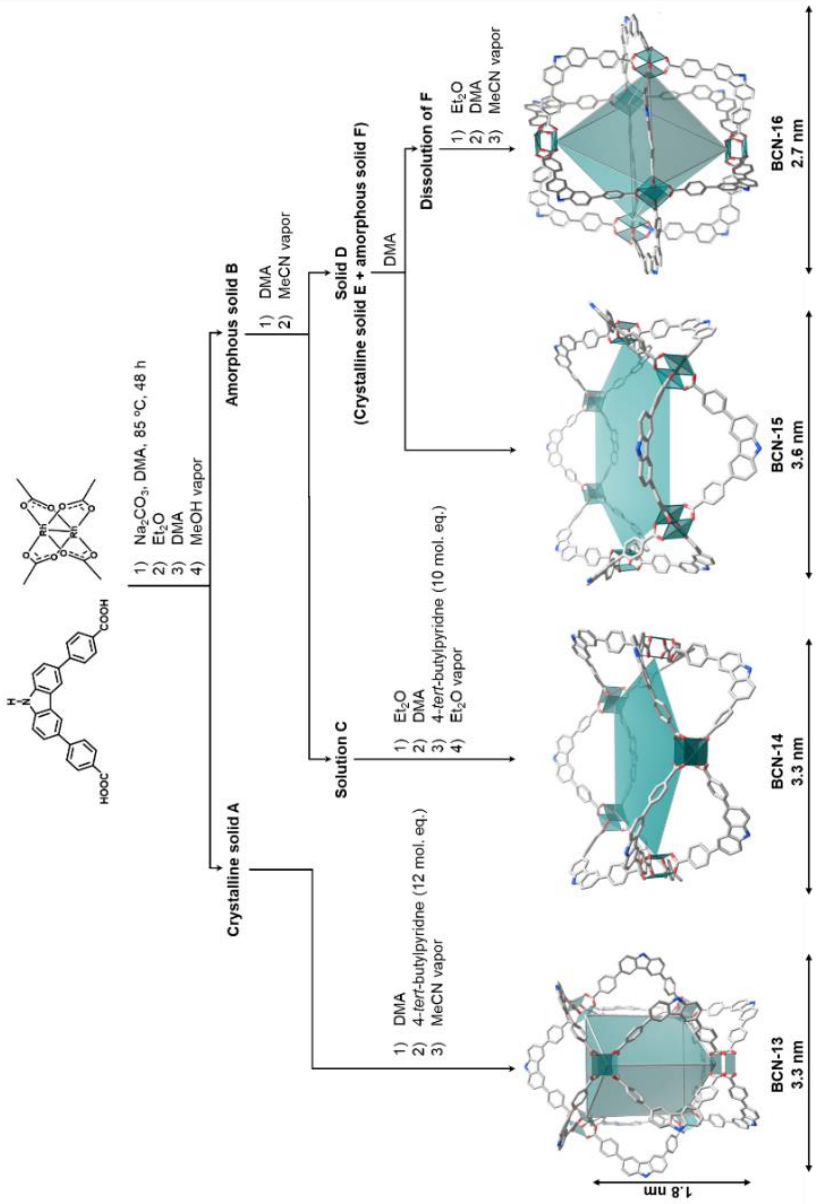

Figure 5.8. Schematic illustrating the synthesis of the four different MOPs and polygons (named BCN-13, BCN-14, BCN-15 and BCN-16) formed by reacting H_2L2 with Rh(II) acetate. Note that the size indicated for BCN-13 is calculated between Rh(II) paddlewheels at opposite vertices and from the N atoms of opposite ligands. For BCN-14, the size was calculated from the Rh(II) paddlewheel to the center of the opposite edge, whereas for BCN-15 and BCN-16, it was measured between the Rh(II) paddlewheels at opposite vertices.

to these crystallization conditions did not yield a crystalline material, indicating that the first purification step is required to obtain good quality single crystals. SCXRD analysis revealed formation of a peculiar trigonal prismatic MOP, which crystallizes in the orthorhombic space group *Ibam* with corresponding cell parameters a = 93.4627(6), b = 37.2998(4), c = 52.7312(3) Å (Table 3 in the crystallographic data section). This MOP (hereafter named BCN-13), which is denoted as **trp** according to the RCSR database, comprises six Rh(II) paddlewheel units and 12 L2 ligands (formula: $[Rh_{12}(L2)_{12}]$). The length and width of this trigonal prismatic structure is 1.8 nm and 3.3 nm, respectively. Although a few examples of this type of structure have been reported, to the best of our knowledge, this is the first-ever report of one with metal-paddlewheel clusters.[27,28]

The purity of BCN-13 was first confirmed through ^{1}H-NMR and DOSY-NMR, which confirmed the absence of free ligand (Figure 5.9a and b, respectively). Next, MALDI-TOF measurements showed a signal centred at 6100.3 m/z which corresponds to the molecular formula of $[Rh_{12}(L2)_{12}+H^{+}]^{+}$ (expected mass 6100.6 g mol^{-1}) (Figure 5.9c). Finally, the paddlewheel integrity in the material was assessed through UV-Vis spectroscopy of BCN-13 in DMA (Figure 5.9d). The band centred at 512 nm confirms the presence of the Rh(II)-Rh(II) paddlewheel. Remarkably, the large shift of the band (from *ca*. 600 nm) also suggests that

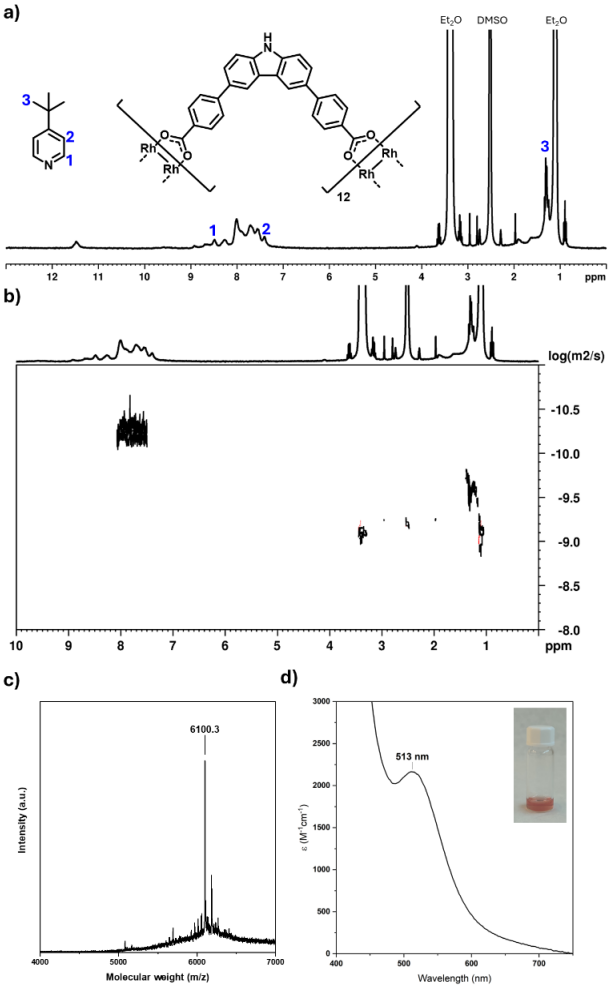

Figure 5.9. ***a)*** ^{1}H-NMR spectrum (300 MHz, 25 ^{0}C) of BCN-13 coordinated to 4-*tert*-butylpyridine in DMSO-d_6. Note that integration of the signals could not be done due to overlap. ***b)*** DOSY-NMR spectrum (300 MHz, 25 ^{0}C) of BCN-13 coordinated to 4-*tert*-butylpyridine in DMSO-d_6. The same diffusion coefficient ($D \approx 5.6 \cdot 10^{-11}$ $m^2 \cdot s^{-1}$) is identified for all the aromatic protons. The diffusion coefficient of the residual DMSO ($D \approx 8.0 \cdot 10^{-10}$ $m^2 \cdot s^{-1}$) was used as internal reference. ***c)*** MALDI-TOF spectrum of BCN-13 in DMA. The highlighted mass corresponds to the molecular formula of $[Rh_{12}(L2)_{12}+H^+]^+$. Expected m/z = 6100.6 g mol^{-1}; found m/z = 6100.3 g mol^{-1}. Note that the 4-*tert*-butylpyiridines coordinated to BCN-13 can not be observed in the spectrum since they are detached during the ionization due to the labile coordination bond. ***d)*** UV-Vis spectrum of BCN-13 coordinated to 4-*tert*-butylpyridine in DMA at a concentration of 2.5 mg/mL. λ_{max} is centered at 513 nm, confirming that the Rh(II) paddlewheel is present, and its coordination to 4-*tert*-butytlpyridine.

4-*tert*-butylpyridine is able to coordinate both the exohedral and endohedral axial sites of the MOP. This is consistent with the large windows of the structure in contrast with octahedral microporous MOPs.

After obtaining pure BCN-13 from the microcrystalline A, we purified the amorphous portion B. Firstly, it was redissolved in DMA and then, exposed to acetonitrile vapor. This yielded a purple solution (C) and a solid (D). Addition of Et_2O to C caused a solid to precipitate out, which was redissolved in DMF and then, crystallized in the presence of 4-*tert*-butylpyridine and Et_2O vapor to yield single crystals (yield based on Rh(II): 36%). SCXRD analysis revealed the formation of an unprecedented metal-organic polygon (hereafter named BCN-14), comprising a five-membered ring that crystallizes in the monoclinic space group $P2_{1/n}$ with corresponding cell parameters a = 34.4336(3), b = 28.8627(3), c = 58.0490(3) Å, and α = γ = 90°, β = 93.1923(7)° (Table 4 in the crystallographic data section). BCN-14 comprises five Rh(II) paddlewheel clusters and 10 L2 ligands in a double-walled configuration (formula: $[Rh_{10}(L2)_{10}]$). This novel structure has an inner diameter of 3.3 nm.

The purity of BCN-14 was confirmed by different spectroscopic and crystallographic techniques. PXRD showed the phase purity in the bulk sample (Figure 5.10a), while MALDI-TOF mass spectroscopy evidenced the successful separation of the

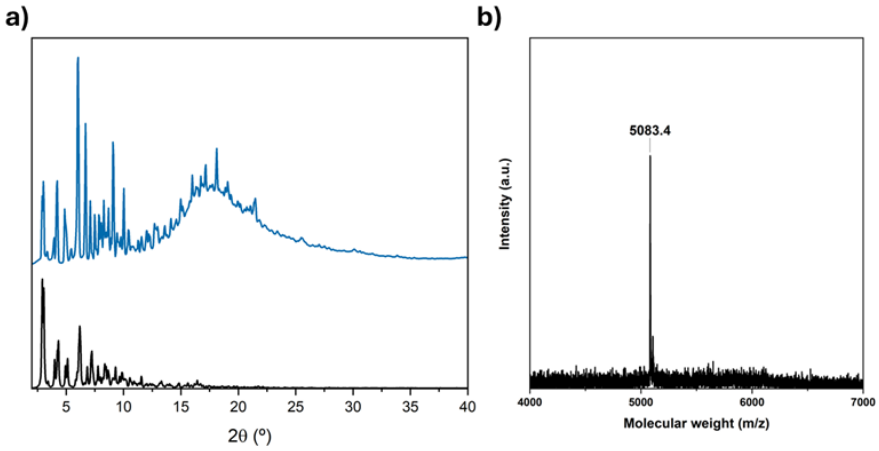

Figure 5.10. ***a)*** Simulated (bottom, black) and experimental (top, blue) PXRD patterns of BCN-14. ***b)*** MALDI-TOF spectrum of BCN-14 in DMA. The highlighted mass corresponds to the molecular formula of $[Rh_{10}(L2)_{10}+H^+]^+$ (expected m/z = 5084.0 g mol^{-1}; found m/z = 5083.4 g mol^{-1}).

pentagonal polygon with the presence of only one signal in the spectrum, which is centred at 5083.4 m/z and corresponds to the molecular formula of $[Rh_{10}(L2)_{10}+H^+]^+$ (expected m/z = 5084.0 g mol^{-1}) (Figure 5.10b).

^{1}H-NMR demonstrated the absence of free ligand and the presence of 4-*tert*-butylpyridine (Figure 5.11a). Interestingly, DOSY-NMR displayed a diffusion coefficient of $5.6 \cdot 10^{-11}$ $m^2 \cdot s^{-1}$, which corresponds to a hydrodynamic radius of 2.0 nm, confirming the large size of the molecule. (Figure 5.11b). Additionally, UV-Vis spectroscopy of BCN-14 dissolved in DMA confirmed the integrity of the Rh(II)-Rh(II) paddlewheel with the presence of a band centred at 522 nm, which also demonstrates the coordination of 4-*tert*-butylpyiridne to both external and internal Rh(II) axial sites

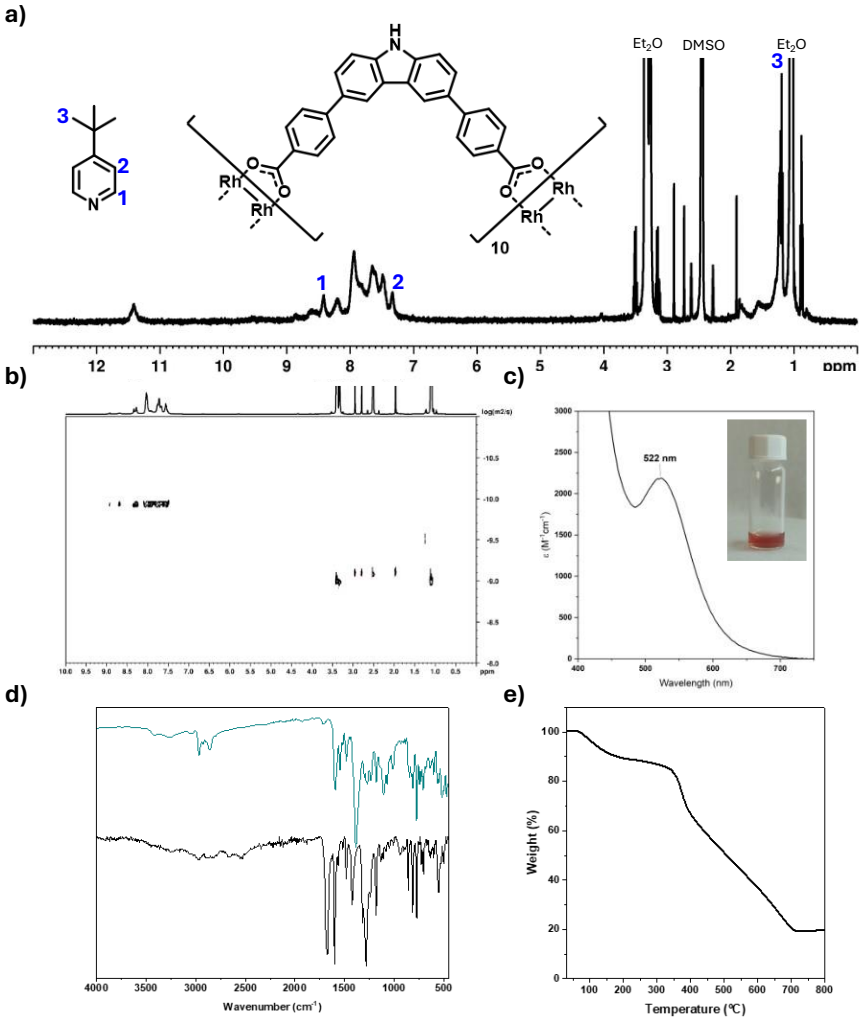

Figure 5.11. ***a***) ^{1}H-NMR spectrum (300 MHz, 25 ^{0}C) of BCN-14 coordinated to 4-*tert*-butylpyridine in DMSO-d_6. Note that integration of the signals could not be done due to its overlap. ***b)*** DOSY-NMR spectrum (300 MHz, 25 ^{0}C) of BCN-14 coordinated to 4-*tert*-butylpyridine in DMSO-d_6. The same diffusion coefficient ($D \approx 1.1 \cdot 10^{-10}$ $m^2 \cdot s^{-1}$) is identified for all the aromatic protons. The diffusion coefficient of the residual DMSO ($D \approx 8.0 \cdot 10^{-10}$ $m^2 \cdot s^{-1}$) was used as internal reference. ***c)*** UV-Vis spectrum of BCN-14 coordinated to 4-*tert*-butylpyridine in DMA with a concentration of 2.5 mg/mL. λ_{max} is centered at 522 nm, confirming that the Rh(II) paddlewheel is present and its coordination to 4-*tert*-butytlpyridine on their outer and inner axial sites. ***d)*** FTIR spectrum of BCN-14 (top, green) and H_2L1 (bottom, black). ***e)*** TGA of BCN-14. Note that the initial mass loss of *ca.* 10% is associated with the remaining solvent molecules. The decomposition temperature is *ca.* 340 °C.

(Figure 5.11c). Finally, FTIR further confirmed the purity of the sample and TGA demonstrated the stability of the cage up to *ca*. 340º C. (Figure 5.11d and e, respectively).

Having obtained crystalline BCN-14 from B, we next aimed to characterize D. Closer observation of D under optical microscope revealed that it comprises rectangular single crystals (E) and amorphous spheres (F) (Figure 5.12).

When DMA was added to the solid, F dissolved but E remained, enabling the obtention of the phase pure E (yield based on Rh(II): 20%). SCXRD analysis of the rectangular crystals E revealed

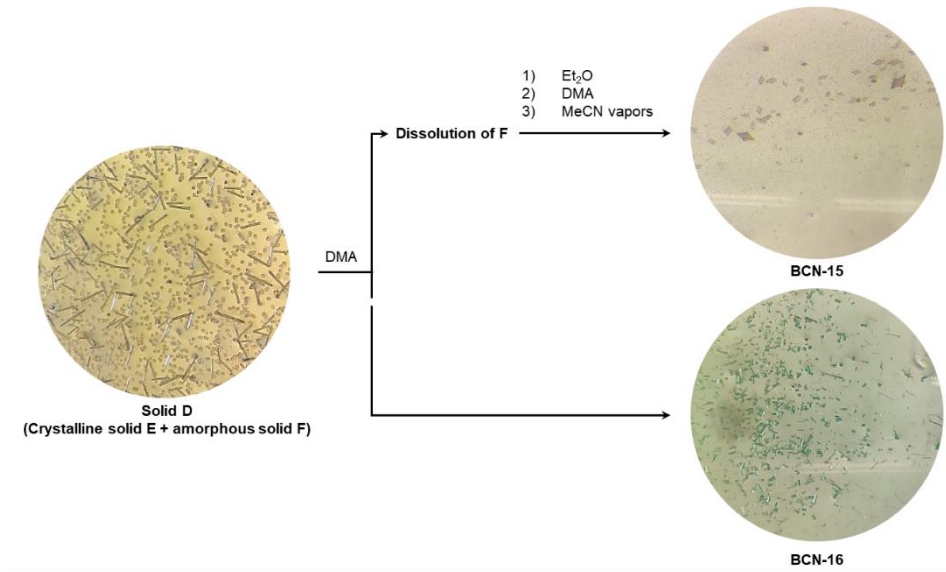

Figure 5.12. Image of solid D, where two different solids can be distinguished: rectangular single crystals (E) and amorphous solid (F) (left) and image of the single crystals obtained of BCN-15 and BCN-16 after their separation (right).

the formation of a second metal-organic polygon (hereafter named BCN-15), comprising a six-membered ring built up from six Rh(II) paddlewheel units and 12 double-walled L2 ligands (formula: $[Rh_{12}(L2)_{12}]$), which crystallizes in the monoclinic space group $P2_{1/c}$ with corresponding cell parameters a = 31.4498(3), b = 39.6841(5), c = 40.5297(4) Å, and α = γ = 90°, β = 90.4263(8)° (Table 5 in the crystallographic data section). This polygonal assembly has an inner diameter of 3.6 nm.

The phase purity of bulk BCN-15 was confirmed by PXRD, while FTIR demonstrated the absence of free ligand (Figure 5.13a and c, respectively). MALDI-TOF confirmed the obtention of the expected formula of $[Rh_{12}(L2)_{12}+H^+]^+$ (expected m/z = 6100.6 g mol^{-1}) with the presence of a signal at 6098.4 m/z in the spectrum (Figure 5.13b). TGA demonstrated the stability of the polygon up to ca. 325 ºC. (Figure 5.13d).

Finally, the DMA solution containing F was exposed to acetonitrile vapors, which afforded rhombic single crystals (hereafter named BCN-16; yield based on Rh(II): 32%). Note that BCN-16 could only be crystallized in the presence of acetonitrile after all the other compounds had already been isolated. SCXRD analysis corroborated formation of the initially expected octahedral isoreticular MOP, having molecular formula of $Rh_{12}(L2)_{12}$. Structure analysis revealed that BCN-16 is isostructural to the parent

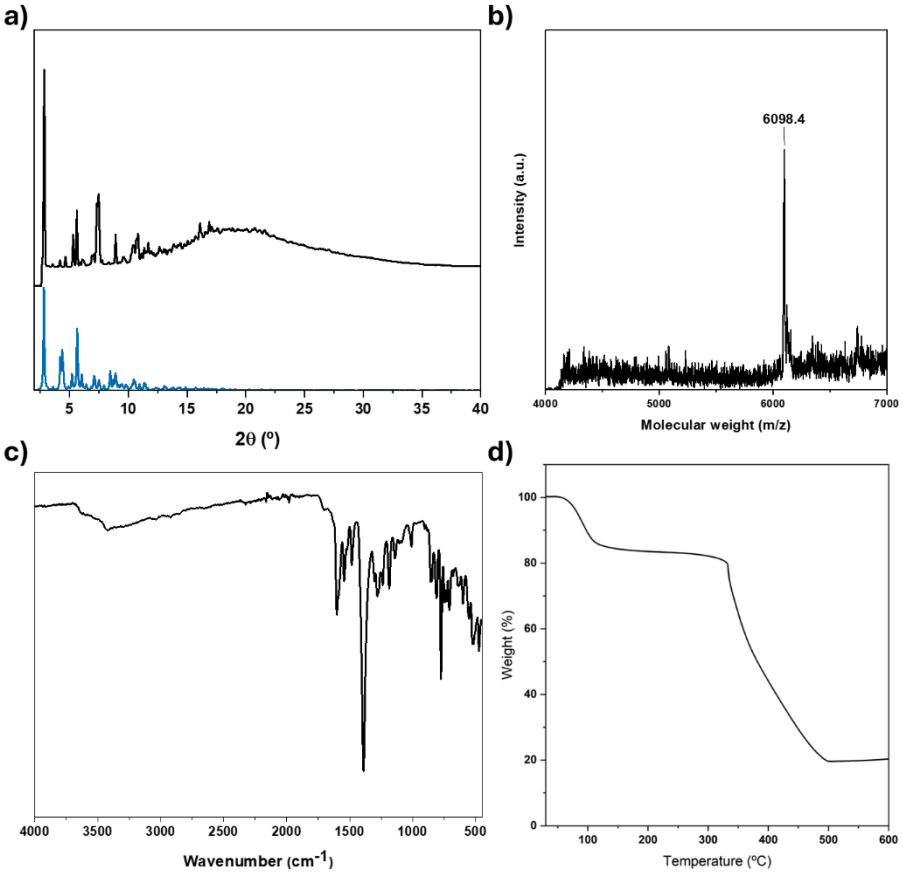

Figure 5.13. ***a)*** Simulated (bottom, black) and experimental (top, blue) PXRD patterns of BCN-15. ***b)*** MALDI-TOF spectrum of BCN-15 in DMA. The highlighted mass corresponds to the molecular formula of $[Rh_{12}(L2)_{12}+H^+]^+$ (expected m/z = 6100.6 g mol^{-1}; found m/z = 6098.4 g mol^{-1}). ***c)*** FT-IR spectrum of BCN-15. ***d)*** Thermogravimetric analysis of BCN-15. Note that the initial mass loss of *ca*. 15% is associated with the remaining water and solvent molecules coordinated to the metal-open sites of the Rh-paddlewheels. The decomposition temperature is *ca*. 325 ºC.

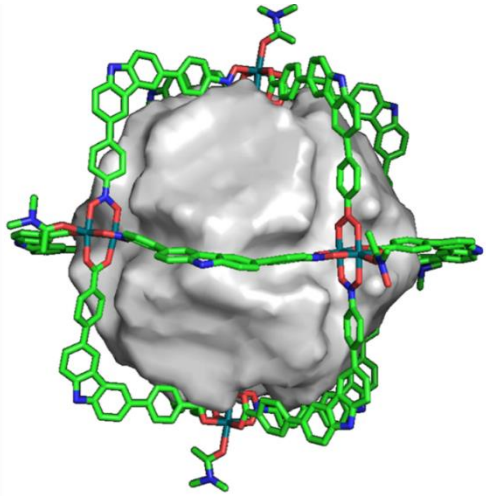

Figure 5.14. Image of the calculated cavity for BCN-16.

microporous octahedral $Rh_{12}(L1)_{12}$ MOP, crystallizing in the triclinic space group P_{-1} with corresponding cell parameters a = 27.2945(8), b = 28.0465(6), c = 29.7602(6) Å, and α = 111.087(2)°, β = 112.027(2)° and γ = 101.813(2)° (Table 6 in the crystallographic data section). BCN-16 exhibits internal and external diameters of 2.3 and 2.7 nm (calculated from opposite paddlewheel units in the octahedron), and an internal cavity of 6.5 nm^3 (Figure 5.14).

Phase purity of the bulk material was confirmed through PXRD (Figure 5.15a). MALDI-TOF confirmed the obtention of the expected formula of $[Rh_{12}(L2)_{12}+H^+]^+$ (expected m/z = 6100.6 g mol^{-1}) with the presence of a signal at 6098.4 m/z in the spectrum (Figure 5.15b). The absence of free ligand was corroborated through ^{1}H-NMR (Figure 5.15c). Additionally, DOSY-NMR shows one only diffusion coefficient, 6.5 $\cdot 10^{-11}$ $m^2 \cdot s^{-1}$ (hydrodynamic

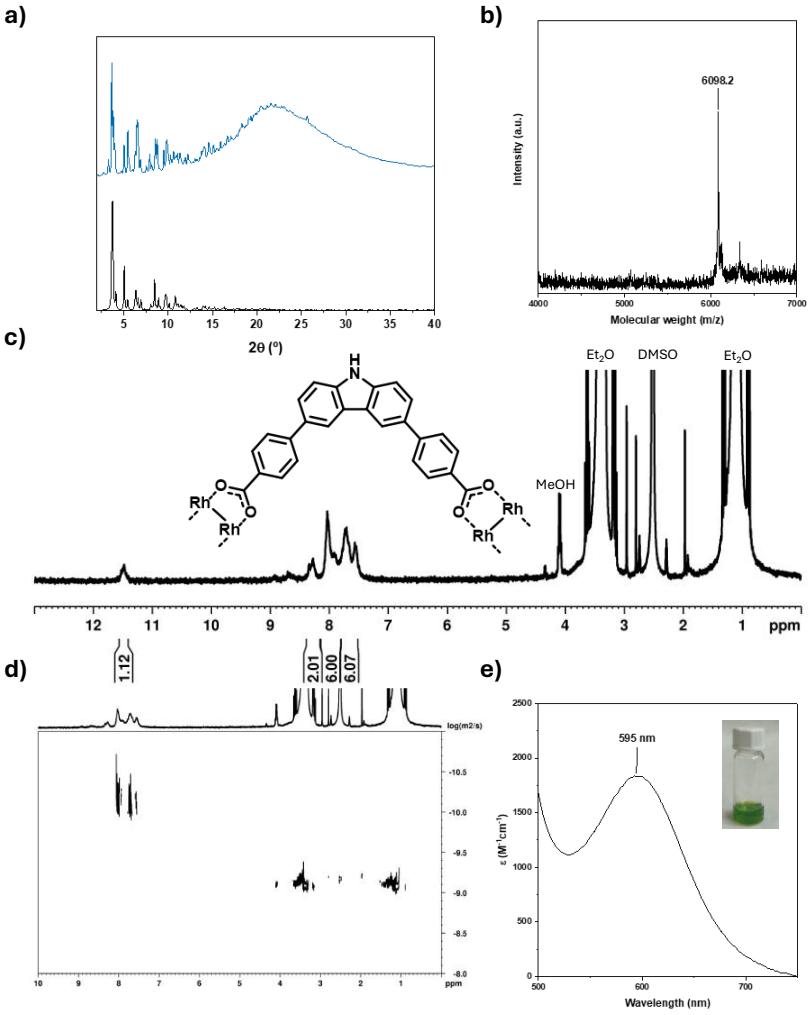

Figure 5.15. ***a)*** Simulated (bottom, black) and experimental (top, blue) PXRD patterns of BCN-16. ***b)*** MALDI-TOF spectrum of BCN-16 in DMA. The highlighted mass correspond to the molecular formula of $[Rh_{12}(L2)_{12}+H^+]^+$ (expected m/z = 6100.6 g mol^{-1}; found m/z = 6098.2 g mol^{-1}). ***c)*** ^{1}H-NMR spectrum (300 MHz, 25 ^{0}C) of BCN-16 in DMSO-d_6. ***d)*** DOSY-NMR spectrum (300 MHz, 25 ^{0}C) of BCN-16 in DMSO-d_6. The same diffusion coefficient ($D \approx 6.5 \cdot 10^{-11}$ m^2·s^{-1}) is identified for all the aromatic protons. The diffusion coefficient of the residual DMSO ($D \approx 8.0 \cdot 10^{-10}$ m^2·s^{-1}) was used as internal reference. ***e)*** UV-Vis spectrum of BCN-16 in DMA with a concentration of 2.5 mg/mL. λ_{max} is centered at 595 nm, confirming that the Rh(II) paddlewheel is present.

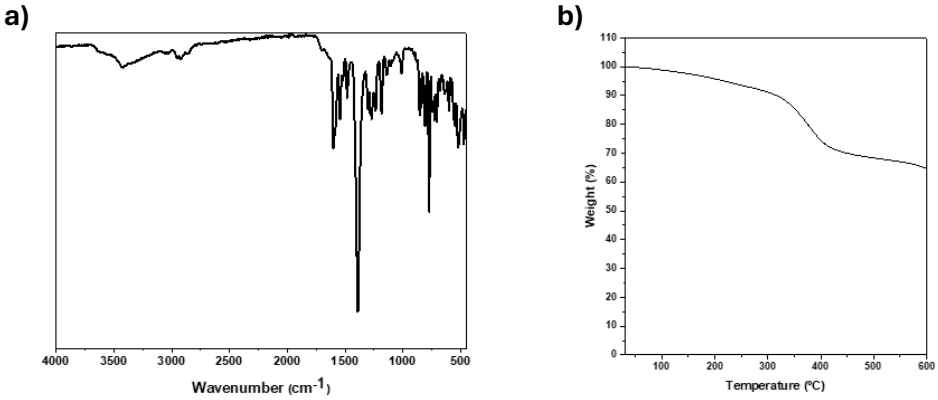

Figure 5.16. ***a)*** FTIR spectrum of BCN-16. ***b)*** TGA of BCN-16. Note that the initial mass loss of *ca*. 10% is associated with the remaining water and solvent molecules coordinated to the metal-open sites of the Rh(II)-paddlewheels. The decomposition temperature is *ca*. 310 °C.

radius of 1.7 nm), for all the aromatic signals, confirming the presence of of a big assembly (Figure 5.15d).

Moreover, UV-Vis spectroscopy of BCN-16 solubilised in DMA confirmed the maintenance of the Rh(II)-Rh(II) paddlewheel with the presence of a band centred at 595 nm (Figure 5.15e).Further confirmation of the absence of free ligand was obtained from FTIR (Figure 5.16a). Finally, TGA exhibited that this MOP is stable up to *ca*. 310 ºC (Figure 5.16b).

5.2.3. Geometry mismatch in discrete metal-organic assemblies

Given the wide structural diversity upon the assembly of Rh(II)-paddlewheel and H_2L2 ligands, we sought to rationalize the underlying factors governing this variability. We started by analysing the structures of BCN-13, BCN-15, and BCN- 16, which are isomers that comprises six rhodium paddlewheel units and 12 L2 ligands. However, they differ vastly by geometry, chiefly by the connectivity of their respective Rh(II) paddlewheel clusters. Paddlewheel metal centers are commonly understood to be 4-c clusters; therefore, we had expected this connectivity and indeed observed it in the octahedral cage BCN-16. In this structure, the L2 ligand is planar, yielding what it has been denoted as the "single-walled configuration" of the ligand (Figure 5.17a).[29,30]

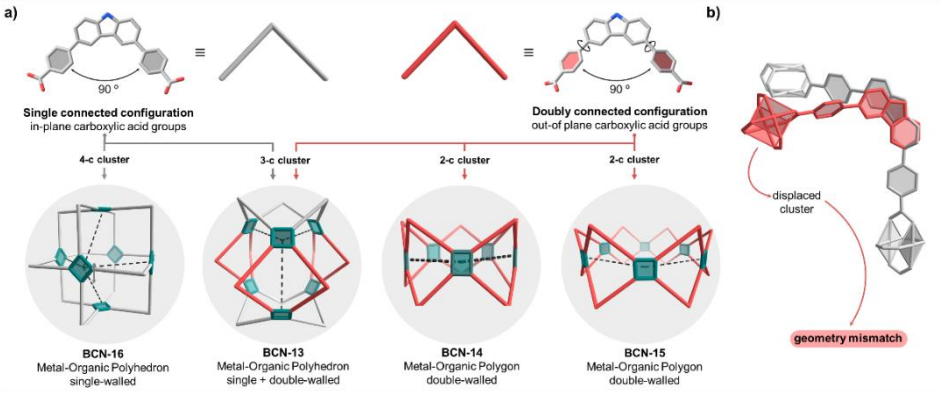

Figure 5.17. ***a)*** Representation of L2 showing its two possible conformations: planar (left, grey) and twisted (right, red), along with their positions in the different polygons and MOPs, which force different cluster connectivities. ***b)*** Schematic illustrating how the configuration of L2 (single- or double-walled) changes the positions of the clusters.

Consequently, BCN-16 can be considered as the default structure for the L2 ligand in combination with a paddlewheel metal cluster.

Conversely, BCN-15 adopts a geometrically mismatched structure, influenced by the twist of the phenyl groups surrounding the carbazole core, which renders the ligand non-planar (Figure 5.17b). In this arrangement, each paddlewheel behaves as a 2-c cluster due to the double-walled configuration of the ligands (Figure 5.17). Although not isomeric to BCN-15, BCN-14 exhibits an analogous non-planar double-walled ligand configuration, forming a pentagonal metal-organic polygon with 2-c Rh(II) paddlewheel clusters. The Rh(II) paddlewheel cluster remains undistorted in both polygons, with the only difference being the twist angle of the L2 ligand, measured as 56.3 ± 5.8° for BCN-14 and 58.2 ± 6.5° for BCN-15 (Figure 5.18a and b, respectively). Therefore, we attributed

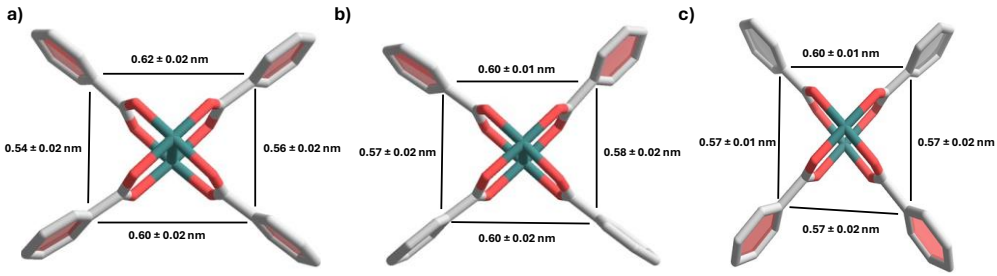

Figure 5.18. Rh(II)-paddlewheel cluster of BCN-14 (***a***), BCN-15 (***b***) and BCN-13 (***c***) with the measurement of distances from one C of a phenyl ring to the C of the adjacent phenyl ring, showing that the cluster is not distorted. Note that the phenyl rings in red present double-walled configuration, whereas the ones in grey present single-walled configuration.

the formation of both polygons to slight change in the twist angle of the L2 ligand. These small differences in ligand conformation are likely close in energy, allowing both polygons to form under the tested reaction conditions.

The structure of BCN-13 arises from the combination of planar and non-planar arrangements of L2, leading to the uncommon 3-c Rh(II) paddlewheel cluster (Figure 5.17). Specifically, the 3-c Rh(II) paddlewheel clusters result from the double-walled configuration of the ligands, which account for the edges of each lateral rectangular face, whereas only single-walled ligands compose both triangular bases of the structure.[31–33] As with the structures analyzed above, the Rh(II) paddlewheel cluster in this case remains undistorted, with the final structure being attributed to the twist of the ligand, which is 55.1 ± 9.2° for the ligands with double-walled configuration and 14.4 ± 6.2° for those with single-walled configuration (Figure 5.18c). Overall, these results highlight that the twist angle between the carbazole and the adjacent benzene ring is as important as their bite angle in determining the structural outcome of the assembly reaction, in line with previous reports showing that subtle variations in ligand conformation -particularly twist angles- can direct the formation of distinct cage topologies.[3,34,35]

5.2.4. Second isoreticular expansion of the Rh(II)-based octahedral MOP

Geometrical analysis of the structures formed with H_2L2 revealed that the final structure depends not only on the ligand's bite angle but also on the twist of the linker. Notably, the octahedral cage formed only when the ligand had adopted a planar conformation. Guided by this observation, we designed the ligand for the second isoreticular expansion to induce planarity between the carbazole core, the benzene ring, and the carboxylic acid groups. To this end, an alkyne bond was introduced between the phenyl and carbazole moieties to enable synthesis of 4,4-((9*H*-carbazole-3,6-diyl)bis(ethyne-2,1-diyl))dibenzoic acid (H_2L3). However, all solvothermal reactions performed with H_2L3 and Rh(II) acetate resulted in insoluble amorphous precipitates that could not be characterized. We then explored strategies to increase the solubility of the ligand and avoid early kinetic traps in the form of amorphous solids during the complexation reaction. To this end, an alkane chain was added to the carbazole core of the ligand to enable synthesis of 4,4-((9-dodecyl-carbazole-3,6-diyl)bis(ethyne-2,1-diyl))dibenzoic acid (H_2L4), which was then reacted with Rh(II) acetate under solvothermal conditions to yield green rectangular single crystals in good yield (68%). These crystallize in the triclinic space group P_{-1} with corresponding cell parameters a = 30.8769(2), b = 33.8701(3), c = 36.1112(2) Å, and α

= 107.5252(6)°, β = 100.1424(6)° and γ = 114.2237(6)° (Table 7 in the crystallographic data section). SCXRD analysis corroborated formation of the expected octahedral cage (hereafter named BCN-17), isostructural to the parent microporous octahedral Rh-MOP and BCN-16. Remarkably, BCN-17 possesses internal and external diameters of 2.8 and 3.3 nm (calculated from opposite paddlewheel units in the octahedron), and an internal cavity of 12.5 nm^3 (Figure 5.19), which represents the biggest cavity reported for a paddlewheel-based MOP (Table 1).

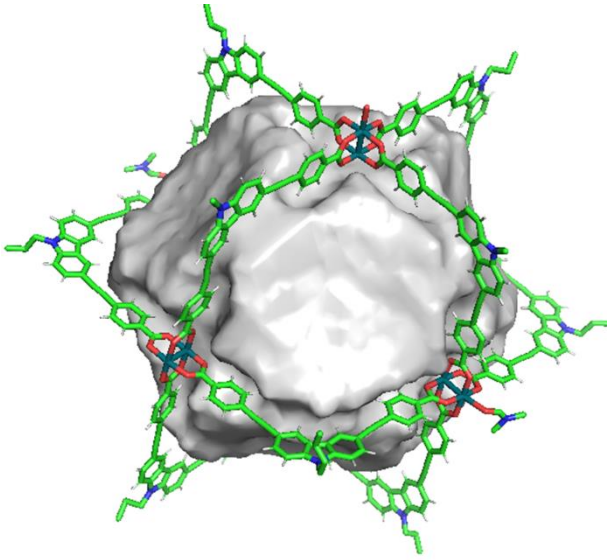

Figure 5.19. Image of the calculated cavity for BCN-17.

Table 1. Calculated cavity for some paddlewheel-based MOPs

Ligand	Metal	Cavity (nm^3)	Reference
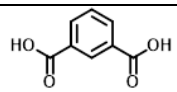	Cu	1.8	[36]
	Rh	1.9	[23]
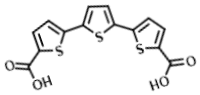	Cu	3.7	[37]
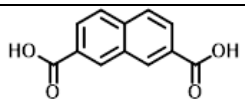	Cu	4.3	[9]
	Mo	4.5	[10]
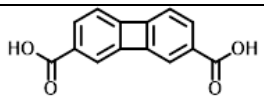	Cu	6.8	[9]
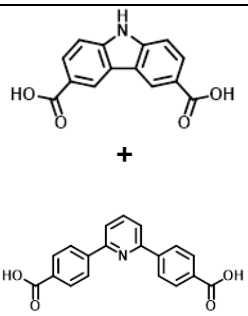	Cu	6.9	[38]
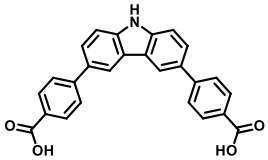	Mo	6.9	[10]
	Rh	6.4	This work
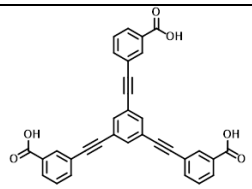	Cu	10.5	[39]
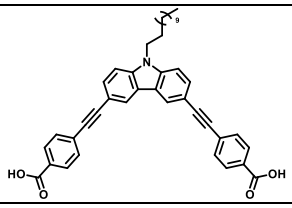	Rh	12.5	This work

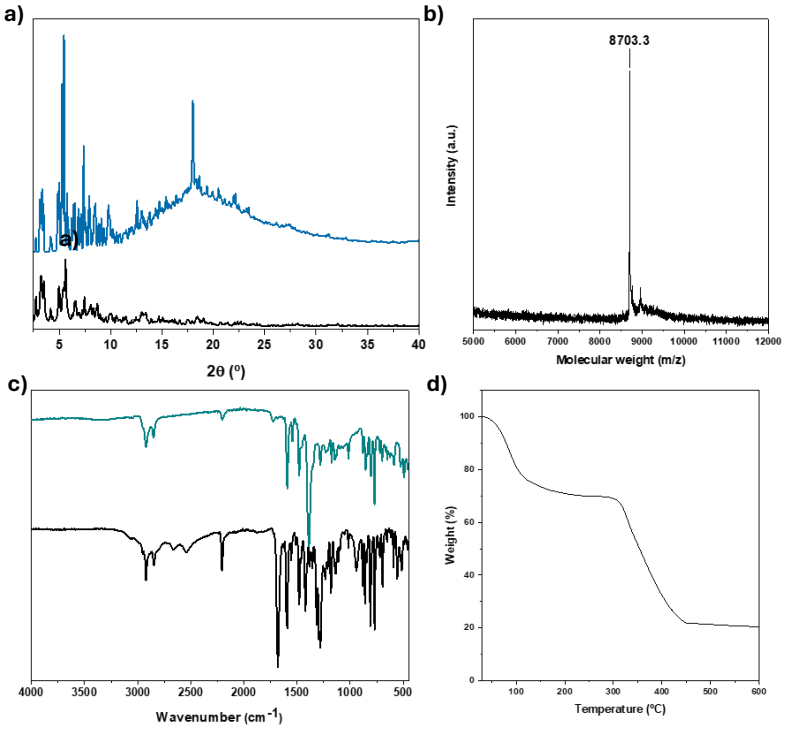

Figure 5.20. ***a)*** Simulated (bottom, black) and experimental (top, blue) PXRD patterns of BCN-17. The signal at 17.6º is ascribed to frozen solvent as the measurement was performed under flow of liquid N_2. ***b)*** MALDI-TOF spectrum of BCN-17. The highlighted mass corresponds to the molecular formula of $[Rh_{12}(L4)_{12}+H^+]^+$ (expected m/z = 8697.3 g mol^{-1}; found m/z = 8703.3 g mol^{-1}). ***c)*** FTIR spectrum of BCN-17(top, green) and H_2L4 (bottom, black). ***d)*** TGA of BCN-17. Note that the initial mass loss of *ca*. 25% is associated with the remaining solvent molecules coordinated to the metal-open sites of the Rh(II)-paddlewheels. The decomposition temperature is *ca*. 315 °C.

Phase purity of the bulk material was confirmed through PXRD (Figure 5.20a). Further confirmation of the purity of the product was assessed with MALDI-TOF. The spectrum showed a signal centred at 8703.3 m/z, which corresponds to the molecular formula of $[Rh_{12}(L4)_{12}+H^+]^+$ (expected m/z = 8697.3 g mol^{-1}) (Figure 5.20b). Additionally, FTIR shows the absence of free ligand (Figure 5.20c) and TGA exhibits that BCN-17 is stable up to *ca*. 315 ºC (Figure 5.20d).

5.2.5. Solid-state properties of isoreticular octahedral Rh(II)-based MOPs

To evaluate the solid-state adsorption properties of the synthesized octahedral MOPs, we conducted gas- and vapor-adsorption studies on BCN-16, BCN-17 and their parent microporous octahedral Rh-MOP, and compared their respective values. To this end, all three MOPs were initially fully evacuated by first exchanging them with MeOH and then, drying them with supercritical CO_2. This evacuation process resulted in the amorphization of BCN-16 and BCN-17, and a partial loss of crystallinity in the parent microporous octahedral Rh-MOP (Figure 5.21a, b and c, respectively). However, the molecular structure of all tested MOPs was preserved in all cases, as confirmed by MALDI-TOF analysis of the activated samples (Figure 5.21d, e and f, respectively).

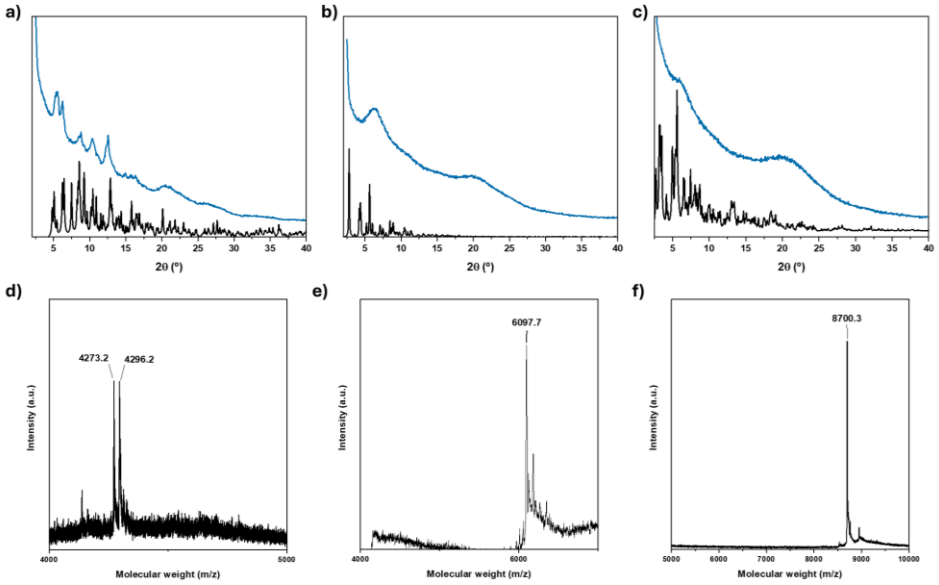

Figure 5.21. Simulated (bottom, black) and experimental (top, blue) PXRD patterns of parent Rh(II)-MOP (***a***), BCN-16 (***b***) and BCN-17 (***c***) after activation. MALDI-TOF spectrum of parent Rh(II)-MOP (***d***), BCN-16 (***e***) and BCN-17 (***f***) after activation.

Next, we ran N_2-sorption experiments at 77 K on all three MOPs, which demonstrated their permanent porosity, as evidenced by their corresponding BET surface areas: 812 $m^2\ g^{-1}$ for the parent Rh-MOP; 780 $m^2\ g^{-1}$ for BCN-16; and 121 $m^2\ g^{-1}$ for BCN-17 (**Error! Reference source not found.**a). The parent microporous octahedral Rh-MOP exhibited the expected type I isotherm, whereas BCN-16 and BCN-17 exhibited type IV isotherms, as typically observed in mesoporous materials (**Error! Reference source not found.**a).[40] We attributed the slight decrease in the BET surface area after the first isoreticular expansion to the higher

molecular weight of BCN-16 than of the parent microporous Rh-MOP. However, when the isotherm is normalized per mol of MOP, BCN-16 outperforms the parent microporous Rh(II)-MOP (87.2 mol N_2 mol^{-1} BCN-16 *versus* 49.5 mol N_2 mol^{-1} Rh-MOP at 1 bar). In contrast, we attributed the lower BET surface area and maximum uptake (36.4 mol N_2 mol^{-1} BCN-17 at 1 bar) of BCN-17 to its large cavity-volume-to-surface ratio and to the presence of its surface alkane chains, which can block gas diffusion pathways to the inner pore. The detrimental effect of bulky surface groups on the solid-state adsorption properties of MOPs has been previously reported.[41,42]

The permanent porosity of all synthesized Rh-MOPs was further confirmed through CO_2-adsorption measurements ran at 200 K, which revealed a similar trend to the N_2-adsorption experiments.

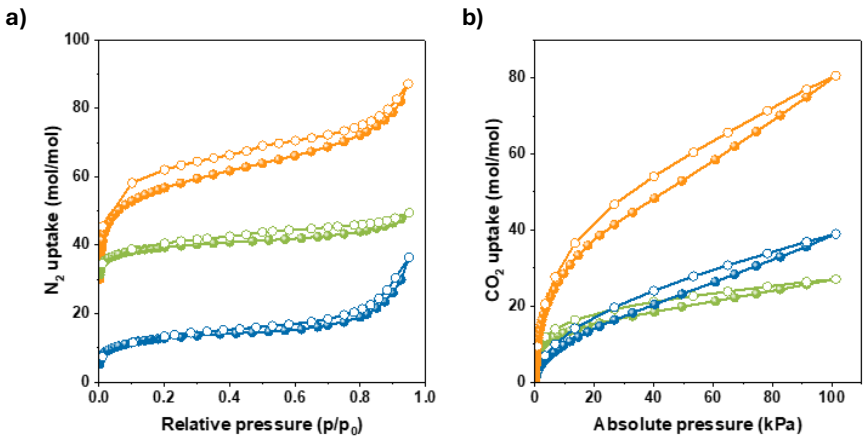

Figure 5.22. ***a)*** N_2 adsorption isotherm at 77 K of parent Rh(II)-MOP (green), BCN-16 (orange) and BCN-17 (blue). ***b)*** CO_2 adsorption isotherm at 200 K of parent Rh(II)-MOP (green), BCN-16 (orange) and BCN-17 (blue).

BCN-16 exhibited the greatest adsorption, with an uptake of 80 mol CO_2 mol^{-1} BCN-16 at 1 bar which we attributed to its large, accessible cavity, while microporous parent Rh(II)-MOP and BCN-17 have a total uptake of 27.1 mol CO_2 mol^{-1} MOP at 1 bar and 39.0 mol CO_2 mol^{-1} BCN-17 at 1 bar, respectively (**Error! Reference source not found.**b).

Next, we investigated the water-adsorption properties of the three Rh-MOPs. To this end, we ran water-adsorption isotherms at 298 K, in which the final water uptake at 90% relative humidity increased with cavity size, reaching 0.08 g g^{-1} (98.2 cm^3 g^{-1}, 18.7 mol H_2O mol^{-1} MOP) for the parent Rh-MOP; 0.24 g g^{-1} (304.4 cm^3 g^{-1}, 82.9 mol H_2O mol^{-1} BCN-16) for BCN-16; and 0.47 g g^{-1} (584.8 cm^3 g^{-1}, 225.7 mol H_2O mol^{-1} BCN-17) for BCN-17 (Figure 5.2). The water uptake value for BCN-17 represents the highest value reported for a cage[43] and is comparable to values for other absorbent materials such as MOFs or COFs.[44,45] A deeper analysis of the water-adsorption isotherms revealed that the parent microporous octahedral Rh(II)-MOP exhibits a reversible isotherm without a step and a moderate final uptake, consistent with the pore filling mechanism observed in microporous hydrophilic materials, such

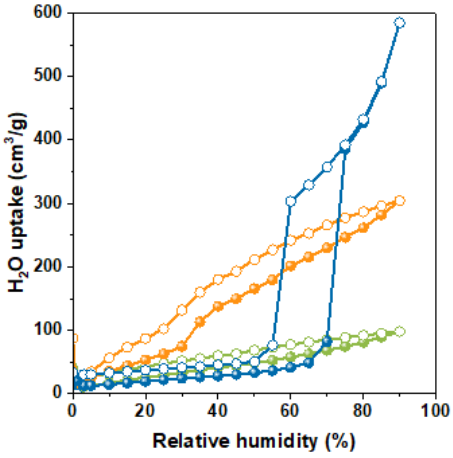

Figure 5.223. ***a)*** Water vapor uptake isotherms of parent Rh(II)-MOP (green), BCN-16 (orange) and BCN-17 (blue).

as zeolites and MOFs.[46] Conversely, the isotherms (type V) for both mesoporous BCN-16 and BCN- 17 feature a step that indicates the occurrence of capillary condensation, characteristic of adsorbents with pore sizes exceeding 2 nm.[47,48] For BCN-16, the step of the "S"- shaped isotherm occurs at α = 0.45 (where α is the relative humidity at 50% uptake). More remarkably, in the case of BCN-17, the water adsorption is entirely dominated by capillary condensation exhibiting an "S"-shaped isotherm that resembles that of mesoporous materials such as MCM-41 and MIL-101.[49,50] We ascribed the high relative humidity at which the step occurs in the isotherm of BCN-17 (α = 0.57) to the hydrophobicity of BCN-17, imparted by its surface alkyl chains. The hydrophobic character of BCN-17 was further confirmed by contact-angle measurements, which revealed a value of 88.83 ± 0.71° (Figure 5.2a), in contrast to BCN-16, which showed complete wetting with a contact angle of 0° (Figure 5.2b). These findings are consistent with

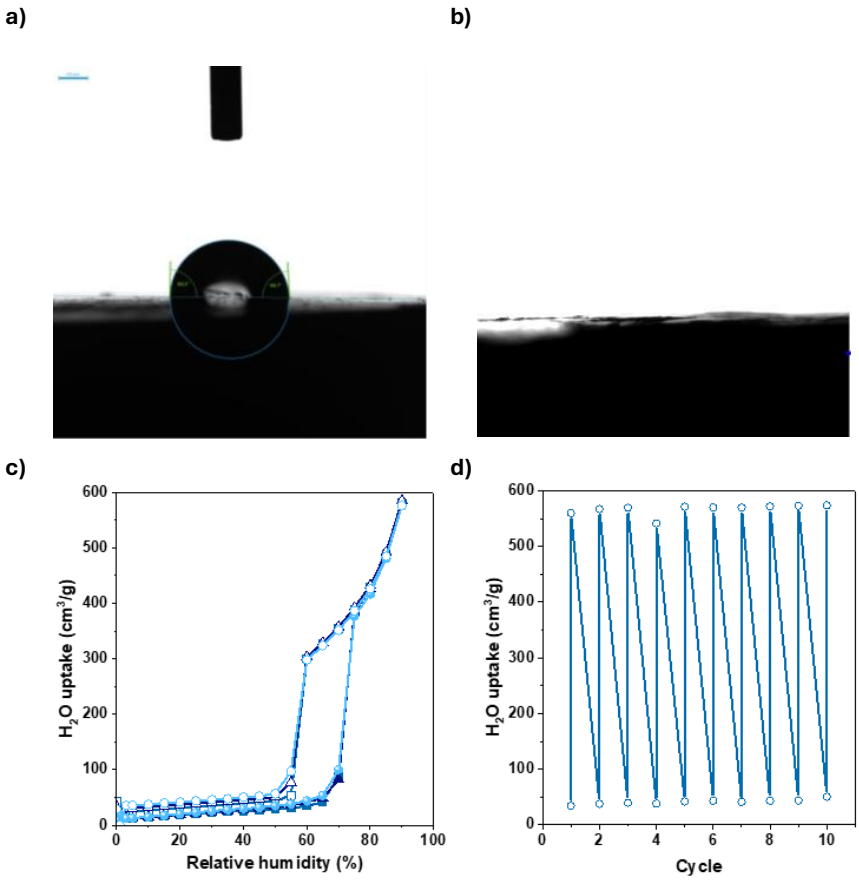

Figure 5.234. ***a)*** Contact angle measurement of BCN-17. Photograph of immediately after the water droplet contacted BCN-17. ***b)*** Contact angle measurement of BCN-16. Photograph of the immediately after the water droplet contacted BCN-16.***c)*** Three consecutive water vapor uptake isotherms of BCN-17. The sample was activated under vacuum prior each uptake isotherm**.** ***d)*** Water uptake of BCN-17 at high (90%) and low (20%) RH over ten consecutive cycles.

observations in mesoporous MOFs, where total uptake is mainly governed by the mesopore size, while the position of the adsorption step is primarily dictated by the hydrophilic or hydrophobic nature of the framework.[51,52]

Finally, we sought to evaluate the potential of BCN-17 as a water adsorbent. In addition to high water-uptake and stepwise adsorption at ambient pressure, a good water adsorbent must also exhibit cyclability and facile regeneration.[45] Thus, we subjected BCN-17 to three consecutive adsorption-desorption water isotherms, which did not reveal any significant differences between cycles (Figure 5.2c). Moreover, to assess its regeneration and recyclability, BCN-17 was exposed to alternating high (90%) and low (20%) relative humidity (Figure 5.2d), which confirmed that it can maintain its performance over 10 cycles. Overall, the performance of BCN-17, characterized by high water-uptake, an S-shaped isotherm, and ease of regeneration and recyclability, meets the key requirements for materials used in humidity control.[53]

5.3. Conclusions

In summary, in this chapter, we have shown the synthesis of a series of isoreticularly expanded, Rh(II)-based, octahedral MOPs exhibiting internal cavities within the mesoporous regime. We have demonstrated that linker planarity is crucial for developing novel

finite structures, as evidenced in the synthesis of the first expanded MOP, BCN-16, in which three additional finite structures, a trigonal prismatic MOP, an hexagonal polygon, and a pentagonal polygon, are simultaneously assembled. We attributed formation of these additional structures to the torsional flexibility of the linker L2. Furthermore, since two of these additional finite structures are isomeric species of BCN-16, our results highlight the importance of characterizing products by PXRD together with MALDI-TOF to confirm the purity of any newly synthesized cage or MOP before its practical use. Finally, gas- and vapor-sorption studies revealed that the enlarged octahedral Rh-MOPs withstand the desolvation process, making them viable mesoporous materials for solid-state adsorption applications. In fact, the larger Rh-MOP, BCN-17, exhibited high water uptake (0.47 g g^{-1}), accompanied by an "S"-shaped water sorption isotherm with a hysteresis loop. We are confident that our new processable materials will open avenues in water sorption-based applications.

5.4. References

[1] Y. Hsia, J. B. Bale, S. Gonen, D. Shi, W. Sheffler, K. K. Fong, U. Nattermann, C. Xu, P. S. Huang, R. Ravichandran, S. Yi, T. N. Davis, T. Gonen, N. P. King, D. Baker, *Nature* **2016**, *535*, 136–139.

[2] R. Divine, H. V. Dang, G. Ueda, J. A. Fallas, I. Vulovic, W. Sheffler, S. Saini, Y. T. Zhao, I. X. Raj, P. A. Morawski, M. F. Jennewein, L. J. Homad, Y.-H. Wan, M. R. Tooley, F. Seeger, A. Etemadi, M. L. Fahning, J. Lazarovits, A. Roederer, A. C. Walls, L. Stewart, M. Mazloomi, N. P. King, D. J. Campbell, A. T. McGuire, L. Stamatatos, H. Ruohola-Baker, J. Mathieu, D. Veesler, D. Baker, *Science* **2021**, *372*, 136–139.

[3] J. A. Davies, T. K. Ronson, J. R. Nitschke, *Chem* **2022**, *8*, 1099–1106.

[4] H. Wu, Y. Wang, L. Đorđević, P. Kundu, S. Bhunia, A. X.-Y. Chen, L. Feng, D. Shen, W. Liu, L. Zhang, B. Song, G. Wu, B.-T. Liu, M. Y. Yang, Y. Yang, C. L. Stern, S. I. Stupp, W. A. Goddard, W. Hu, J. F. Stoddart, *Nature* **2025**, *637*, 347–353.

[5] A. V. Virovets, E. Peresypkina, M. Scheer, *Chem. Rev.* **2021**, *121*, 14485–14554.

[6] D. Fujita, Y. Ueda, S. Sato, N. Mizuno, T. Kumasaka, M. Fujita, *Nature* **2016**, *540*, 563–566.

[7] H. Deng, S. Grunder, K. E. Cordova, C. Valente, H. Furukawa, M. Hmadeh, F. Gándara, A. C. Whalley, Z. Liu, S. Asahina, H. Kazumori, M. O'Keeffe, O. Terasaki, J. F. Stoddart, O. M. Yaghi, *Science* **2012**, *336*, 1018–1023.

[8] M. Eddaoudi, J. Kim, N. Rosi, D. Vodak, J. Wachter, M. O'Keeffe, O. M. Yaghi, *Science* **2002**, *295*, 469–472.

[9] H. Furukawa, J. Kim, N. W. Ockwig, M. O'Keeffe, O. M. Yaghi, *J. Am. Chem. Soc.* **2008**, *130*, 11650–11661.

[10] J.-R. Li, A. A. Yakovenko, W. Lu, D. J. Timmons, W. Zhuang, D. Yuan, H.-C. Zhou, *J. Am. Chem. Soc.* **2010**, *132*, 17599–17610.

[11] M. Tominaga, K. Suzuki, T. Murase, M. Fujita, *J. Am. Chem. Soc.* **2005**, *127*, 11950–11951.

[12] T. Xie, K. Guo, Z. Guo, W. Gao, L. Wojtas, G. Ning, M. Huang, X. Lu, J. Li, S. Liao, Y. Chen, C. N. Moorefield, M. J. Saunders, S. Z. D. Cheng, C. Wesdemiotis, G. R. Newkome, *Angew. Chem.* **2015**, *127*, 9356–9361.

[13] B. Olenyuk, J. A. Whiteford, A. Fechtenkötter, P. J. Stang, *Nature* **1999**, *398*, 796–799.

[14] K. Harris, D. Fujita, M. Fujita, *Chem. Commun.* **2013**, *49*, 6703.

[15] J. Koo, I. Kim, Y. Kim, D. Cho, I.-C. Hwang, R. D. Mukhopadhyay, H. Song, Y. H. Ko, A. Dhamija, H. Lee, W. Hwang, S. Kim, M.-H. Baik, K. Kim, *Chem* **2020**, *6*, 3374–3384.

[16] D. Fujita, Y. Ueda, S. Sato, H. Yokoyama, N. Mizuno, T. Kumasaka, M. Fujita, *Chem* **2016**, *1*, 91–101.

[17] M.-T. Chen, Q.-F. Xu, M. Aibibula, X.-J. Kong, L.-S. Long, L.-S. Zheng, *J. Am. Chem. Soc.* **2024**, *146*, 22134–22139.

[18] S. Klotzbach, T. Scherpf, F. Beuerle, *Chem. Commun.* **2014**, *50*, 12454–12457.

[19] S. Hong, M. R. Rohman, J. Jia, Y. Kim, D. Moon, Y. Kim, Y. H. Ko, E. Lee, K. Kim, *Angew. Chem. Int. Ed.* **2015**, *54*, 13241–13244.

[20] G. Zhang, O. Presly, F. White, I. M. Oppel, M. Mastalerz, *Angew. Chem. Int. Ed.* **2014**, *53*, 1516–1520.

[21] B. Doñagueda Suso, A. Legrand, C. Weetman, A. R. Kennedy, A. J. Fletcher, S. Furukawa, G. A. Craig, *Chem. Eur. J.* **2023**, *29*, e202300732.

[22] A. Carné-Sánchez, J. Martínez-Esaín, T. Rookard, C. J. Flood, J. Faraudo, K. C. Stylianou, D. Maspoch, *ACS Appl. Mater. Interfaces* **2023**, *15*, 6747–6754.

[23] S. Furukawa, N. Horike, M. Kondo, Y. Hijikata, A. Carné-Sánchez, P. Larpent, N. Louvain, S. Diring, H. Sato, R. Matsuda, R. Kawano, S. Kitagawa, *Inorg. Chem.* **2016**, *55*, 10843–10846.

[24] T. Tateishi, J. Troyano, S. Tokuda, G. A. Craig, S. Krause, A. López-Olvera, I. A. Ibarra, S. Furukawa, *Inorg. Chem.* **2024**, *63*, 6571–6575.

[25] M. O'Keeffe, M. A. Peskov, S. J. Ramsden, O. M. Yaghi, *Acc. Chem. Res.* **2008**, *41*, 1782–1789.

[26] V. Martí-Centelles, T. K. Piskorz, F. Duarte, *J. Chem. Inf. Model.* **2024**, *64*, 5604–5616.

[27] S. Wang, X. Gao, X. Hang, X. Zhu, H. Han, W. Liao, W. Chen, *J. Am. Chem. Soc.* **2016**, *138*, 16236–16239.

[28] J. P. Carpenter, C. T. McTernan, T. K. Ronson, J. R. Nitschke, *J. Am. Chem. Soc.* **2019**, *141*, 11409–11413.

[29] T.-Y. Liu, X.-L. Qu, Y. Zhang, B. Yan, *Inorg. Chem.* **2021**, *60*, 8613–8620.

[30] X. Sun, X. Li, S. Yao, R. Krishna, J. Gu, G. Li, Y. Liu, *J. Mater. Chem. A* **2020**, *8*, 17106–17112.

[31] F. Haase, G. A. Craig, M. Bonneau, K. Sugimoto, S. Furukawa, *J. Am. Chem. Soc.* **2020**, *142*, 13839–13845.

[32] T. Abe, K. Takeuchi, M. Higashi, H. Sato, S. Hiraoka, *Nat. Commun.* **2024**, *15*, 7630.

[33] V. Guillerm, D. Maspoch, *J. Am. Chem. Soc.* **2019**, *141*, 16517–16538.

[34] S. Bhattacharyya, S. Argent, B. Pilgrim, **2025**, DOI 10.26434/chemrxiv-2025-x4qf8.

[35] M. R. Black, S. Bhattacharyya, S. P. Argent, B. S. Pilgrim, *J. Am. Chem. Soc.* **2024**, 28233-28241.

[36] M. Eddaoudi, J. Kim, J. B. Wachter, H. K. Chae, M. O'Keeffe, O. M. Yaghi, *J. Am. Chem. Soc.* **2001**, *123*, 4368–4369.

[37] Z. Ni, A. Yassar, T. Antoun, O. M. Yaghi, *J. Am. Chem. Soc.* **2005**, *127*, 12752–12753.

[38] J. Li, H. Zhou, *Angew. Chem. Int. Ed.* **2009**, *48*, 8465–8468.

[39] K. Byrne, M. Zubair, N. Zhu, X.-P. Zhou, D. S. Fox, H. Zhang, B. Twamley, M. J. Lennox, T. Düren, W. Schmitt, *Nat. Commun.* **2017**, *8*, 15268.

[40] L. Peng, J. Zhang, Z. Xue, B. Han, X. Sang, C. Liu, G. Yang, *Nat. Commun.* **2014**, *5*, 4465.

[41] P. S. Reiss, M. A. Little, V. Santolini, S. Y. Chong, T. Hasell, K. E. Jelfs, M. E. Briggs, A. I. Cooper, *Chem. – A Eur. J.* **2016**, *22*, 16547–16553.

[42] T.-H. Chen, L. Wang, J. V. Trueblood, V. H. Grassian, S. M. Cohen, *J. Am. Chem. Soc.* **2016**, *138*, 9646–9654.

[43] J. Troyano, S. Horike, S. Furukawa, *J. Am. Chem. Soc.* **2022**, *144*, 19475–19484.

[44] M. J. Kalmutzki, C. S. Diercks, O. M. Yaghi, *Adv. Mater.* **2018**, *30*, 1704304.

[45] S. M. Towsif Abtab, D. Alezi, P. M. Bhatt, A. Shkurenko, Y. Belmabkhout, H. Aggarwal, Ł. J. Weseliński, N. Alsadun, U. Samin, M. N. Hedhili, M. Eddaoudi, *Chem* **2018**, *4*, 94–105.

[46] F. Jeremias, V. Lozan, S. K. Henninger, C. Janiak, *Dalt. Trans.* **2013**, *42*, 15967.

[47] J. Canivet, A. Fateeva, Y. Guo, B. Coasne, D. Farrusseng, *Chem. Soc. Rev.* **2014**, *43*, 5594–5617.

[48] B. Coasne, A. Galarneau, R. J. M. Pellenq, F. Di Renzo, *Chem. Soc. Rev.* **2013**, *42*, 4141.

[49] G. Akiyama, R. Matsuda, H. Sato, A. Hori, M. Takata, S. Kitagawa, *Microporous Mesoporous Mater.* **2012**, *157*, 89–93.

[50] S. Kittaka, S. Ishimaru, M. Kuranishi, T. Matsuda, T. Yamaguchi, *Phys. Chem. Chem. Phys.* **2006**, *8*, 3223.

[51] B. Zhang, Z. Zhu, X. Wang, X. Liu, F. Kapteijn, *Adv. Funct. Mater.* **2024**, *34*, 2304788.

[52] B. Li, F. Lu, X. Gu, K. Shao, E. Wu, G. Qian, *Adv. Sci.* **2022**, *9*, 2105556.

[53] R. G. AbdulHalim, P. M. Bhatt, Y. Belmabkhout, A. Shkurenko, K. Adil, L. J. Barbour, M. Eddaoudi, *J. Am. Chem. Soc.* **2017**, *139*, 10715–10722.

5.5. Crystallographic data

Table 2. Crystal data and structure refinement for parent octahedral Rh-MOP.

CCDC number	2427442
Empirical formula	$C_{186}H_{126}N_{18}O_{60}Rh_{12}$
Formula weight	4807.96
Temperature/K	100(2)
Crystal system	triclinic
Space group	*P*-1
a/Å	19.6900(10)
b/Å	20.780(2)
c/Å	20.890(2)
α/°	113.600(2)
β/°	113.950(2)
γ/°	89.870(2)
Volume/Å^3	7025.8(10)
Z	1
ρ_{calc}g/cm^3	1.136
μ/mm^{-1}	1.120
F(000)	2388.0
Crystal size/mm^3	0.1 × 0.07 × 0.07
Radiation	synchrotron (λ = 0.82653)
2Θ range for data collection/°	2.534 to 68.068
Index ranges	-24 ≤ h ≤ 24, -27 ≤ k ≤ 27, -26 ≤ l ≤ 26
Reflections collected	92846
Independent reflections	27615 [R_{int} = 0.0582, R_{sigma} = 0.0600]
Data/restraints/parameters	27615/20/1243
Goodness-of-fit on F^2	1.005
Final R indexes [I>=2σ (I)]	R_1 = 0.0935, wR_2 = 0.2890
Final R indexes [all data]	R_1 = 0.1285, wR_2 = 0.3226
Largest diff. peak/hole / e Å^{-3}	1.94/-0.58

Table 3. Crystal data and structure refinement for BCN-13.

CCDC number	2427447
Empirical formula	$C_{357}H_{232}N_6O_{68}Rh_{12}$
Formula weight	6928.39
Temperature/K	100
Crystal system	orthorhombic
Space group	*Ibam*
a/Å	93.4627(6)
b/Å	37.2998(4)
c/Å	52.7312(3)
α/°	90
β/°	90
γ/°	90
Volume/Å^3	183828(3)
Z	8
ρ_{calc}g/cm^3	0.501
μ/mm^{-1}	0.355
F(000)	28000.0
Crystal size/mm^3	0.8 × 0.1 × 0.07
Radiation	synchrotron (λ = 0.82653)
2Θ range for data collection/°	1.368 to 41.006
Index ranges	0 ≤ h ≤ 79, 0 ≤ k ≤ 31, 0 ≤ l ≤ 44
Reflections collected	382443
Independent reflections	29804 [R_{int} = 0.1006, R_{sigma} = 0.0417]
Data/restraints/parameters	29804/269/1752
Goodness-of-fit on F^2	1.222
Final R indexes [I>=2σ (I)]	R_1 = 0.1138, wR_2 = 0.3120
Final R indexes [all data]	R_1 = 0.1386, wR_2 = 0.3424
Largest diff. peak/hole / e Å^{-3}	0.93/-0.66

Table 4. Crystal data and structure refinement for BCN-14.

CCDC number	2427446
Empirical formula	$C_{260}H_{139}N_{0.25}O_{55}Rh_{10}$
Formula weight	5175.31
Temperature/K	100
Crystal system	monoclinic
Space group	$P2_1/n$
a/Å	34.4336(3)
b/Å	28.8627(3)
c/Å	58.0490(3)
α/°	90
β/°	93.1923(7)
γ/°	90
Volume/Å^3	57602.3(8)
Z	4
ρ_{calc}g/cm^3	0.597
μ/mm^{-1}	0.466
F(000)	10363.0
Crystal size/mm^3	0.1 × 0.1 × 0.09
Radiation	synchrotron (λ = 0.82653)
2Θ range for data collection/°	1.634 to 45
Index ranges	-31 ≤ h ≤ 31, 0 ≤ k ≤ 26, 0 ≤ l ≤ 53
Reflections collected	304898
Independent reflections	47386 [R_{int} = 0.0709, R_{sigma} = 0.0448]
Data/restraints/parameters	47386/346/2470
Goodness-of-fit on F^2	1.219
Final R indexes [I>=2σ (I)]	R_1 = 0.1082, wR_2 = 0.3189
Final R indexes [all data]	R_1 = 0.1390, wR_2 = 0.3566
Largest diff. peak/hole / e Å^{-3}	1.07/-0.79

Table 5. Crystal data and structure refinement for BCN-15.

CCDC number	2427445
Empirical formula	$C_{312}H_{168}N_{0.5}O_{70}Rh_{12}$
Formula weight	6278.38
Temperature/K	100
Crystal system	monoclinic
Space group	$P2_1/c$
a/Å	31.4498(3)
b/Å	39.6841(5)
c/Å	40.5297(4)
α/°	90
β/°	90.4263(8)
γ/°	90
Volume/Å^3	50582.0(9)
Z	2
ρ_{calc}g/cm^3	0.412
μ/mm^{-1}	0.319
F(000)	6287.0
Crystal size/mm^3	0.1 × 0.08 × 0.07
Radiation	synchrotron (λ = 0.82653)
2Θ range for data collection/°	1.506 to 42.13
Index ranges	-27 ≤ h ≤ 27, 0 ≤ k ≤ 34, 0 ≤ l ≤ 35
Reflections collected	228271
Independent reflections	34775 [R_{int} = 0.0808, R_{sigma} = 0.0487]
Data/restraints/parameters	34775/51/1570
Goodness-of-fit on F^2	1.073
Final R indexes [I>=2σ (I)]	R_1 = 0.1033, wR_2 = 0.2852
Final R indexes [all data]	R_1 = 0.1282, wR_2 = 0.3133
Largest diff. peak/hole / e Å^{-3}	0.72/-0.63

Table 6. Crystal data and structure refinement for BCN-16.

CCDC number	2427443
Empirical formula	$C_{48}H_{32}N_{12}O_{12}Rh_{12}$
Formula weight	2203.77
Temperature/K	100
Crystal system	triclinic
Space group	*P*-1
a/Å	27.2945(8)
b/Å	28.0465(6)
c/Å	29.7602(6)
α/°	111.087(2)
β/°	112.027(2)
γ/°	101.813(2)
Volume/Å^3	18121.8(8)
Z	14
ρ_{calc}g/cm^3	2.827
μ/mm^{-1}	3.791
F(000)	14560.0
Crystal size/mm^3	0.08 × 0.08 × 0.06
Radiation	synchrotron (λ = 0.82653)
2Θ range for data collection/°	1.692 to 31.77
Index ranges	-20 ≤ h ≤ 19, -21 ≤ k ≤ 19, 0 ≤ l ≤ 22
Reflections collected	56602
Independent reflections	16475 [R_{int} = 0.2694, R_{sigma} = 0.3206]
Data/restraints/parameters	16475/958/885
Goodness-of-fit on F^2	0.995
Final R indexes [I>=2σ (I)]	R_1 = 0.1093, wR_2 = 0.2946
Final R indexes [all data]	R_1 = 0.1530, wR_2 = 0.3216
Largest diff. peak/hole / e Å^{-3}	1.35/-0.60

Table 7. Crystal data and structure refinement for BCN-17.

CCDC number	2427444
Empirical formula	$C_{1144}H_{858}NO_{572}Rh_{156}$
Formula weight	39824.23
Temperature/K	100
Crystal system	Triclinic
Space group	*P*-1
a/Å	30.8769(2)
b/Å	33.8701(3)
c/Å	36.1112(2)
α/°	107.5252(6)
β/°	100.1424(6)
γ/°	114.2237(6)
Volume/Å^3	30830.2(4)
Z	1
ρ_{calc}g/cm^3	2.145
μ/mm^{-1}	3.194
F(000)	19325.0
Crystal size/mm^3	0.1 × 0.09 × 0.08
Radiation	synchrotron (λ = 0.82653)
2Θ range for data collection/°	1.686 to 43.344
Index ranges	-26 ≤ h ≤ 26, -30 ≤ k ≤ 28, 0 ≤ l ≤ 32
Reflections collected	151592
Independent reflections	43744 [R_{int} = 0.0551, R_{sigma} = 0.0861]
Data/restraints/parameters	43744/390/1873
Goodness-of-fit on F^2	1.007
Final R indexes [I>=2σ (I)]	R_1 = 0.1018, wR_2 = 0.2799
Final R indexes [all data]	R_1 = 0.1294, wR_2 = 0.3049
Largest diff. peak/hole / e Å^{-3}	0.77/-0.71

06

CONCLUSIONS

6. General conclusions

The development of this Thesis focused on the synthesis of giant self-assembled molecules and the study of their properties, with special attention to their porous behaviour in the solid state. Two main types of giant metal-organic structures have been proposed in the literature: mesoporous cages and oligomeric supramolecules. In this work, both types were successfully targeted.

Within this framework, we first demonstrated the potential of Rh(II)-based MOPs to act as monomeric units for the synthesis of oligomeric supramolecules. This strategy was made possible through the stepwise assembly of individual MOP cavities, based on two key factors that favor oligomerization over polymerization. First, we synthesized 1-c MOPs using a protection–deprotection approach. This enabled the introduction of a single reactive group on the MOP surface, out of the 24 pendant groups typically present in a cuboctahedral MOP. This method provided remarkable stoichiometric control over surface reactivity. We obtained a 1-c MOP bearing one carboxylic acid group, which was further reacted with NH_2-PEG-X (where X is an azide or alkyne) *via* amide coupling. The resulting MOP-PEG-X derivatives were used as monomeric units. Second, the use of orthogonal reactivity, specifically, CuAAC click chemistry, prevented self-condensation of the precursors. This allowed us to react the 1-c MOP-PEG-X monomers with another 1-c MOP, a 4-connected cluster, and a 24-c MOP to form a dimer, a tetramer, and a satellite-like structure, respectively. Importantly, the permanent porosity of this new family of oligomeric cage-based molecules was confirmed

through CO_2 adsorption, demonstrating retention of the internal cavity. These results expand the field of cage-based oligomeric supramolecules by enabling precise control over MOP connectivity through stepwise assembly.

On the other hand, we successfully self-assembled a family of isoreticularly expanded MOPs, resulting in two novel mesoporous cages. In a first step, we selected a microporous octahedral MOP and synthesized an extended version of its organic linker by adding a phenyl ring. The self-assembly with this larger linker led to the formation of an expanded octahedral MOP, named BCN-16, as well as three additional structures: a trigonal prism (BCN-13), an hexagonal macrocycle (BCN-14), and a pentagonal macrocycle (BCN-15). Structural analysis revealed that these diverse architectures resulted from torsion within the linker, highlighting the critical role of ligand planarity. With this knowledge, we modified the ligand by introducing an alkyne bond to enhance planarity. The self-assembly with this planar linker yielded a single product, the expected octahedral MOP, named BCN-17. This cage exhibited an internal cavity volume of 12.5 nm^3, representing the largest cavity reported to date for a paddlewheel-based MOP. Furthermore, the permanent porosity of the isoreticularly expanded MOP family was demonstrated through N_2, CO_2, and H_2O adsorption measurements. In particular, H_2O isotherms revealed the mesoporous nature of both BCN-16 and BCN-17, each displaying a type V isotherm with a characteristic S-shape. Notably, BCN-17 exhibited a total H_2O uptake of 0.47 $g(H_2O) \cdot g(MOP)^{-1}$, the highest value reported for a discrete cage. The recyclability and reusability of BCN-17 were also confirmed. This work provides a

blueprint for the design and synthesis of permanently porous cages in the mesoporous regime. It also demonstrates the fundamental role of ligand planarity in the structural engineering of metal-organic assemblies.

Overall, the results presented in this Thesis challenge the notion that giant or mesoporous cages are too labile to retain their structure and function in the solid state. These findings broaden the scope and potential of discrete metal-organic assemblies.

07

GLOSSARY

7. Glossary

1- hydroxybenzotriazole	HOBt
1-connected	1-c
1,3-benzenedicarboxylate	BDC
1,3,5-benzenetricarboxylate	BTC
1,8-diazabicyclo[5.4.0]undec-7-ene	DBU
2-(1*H*-benzotriazole-1-yl)-1,1,3,3-tetramethyluronium hexafluorophosphate	HBTU
2-(trimethylsilyl)ethyl	TSE
4,4-(9*H*-carbazole-3,6-diyl)dibenzoic acid	H_2L2
4,4-((9-dodecyl-carbazole-3,6-diyl)bis(ethyne-2,1-diyl))dibenzoic acid	H_2L4
4,4-((9*H*-carbazole-3,6-diyl)bis(ethyne-2,1-diyl))dibenzoic acid	H_2L3
5-((2-(trimethylsilyl)ethoxy)carbonyl)-1,3-benzenedicarboxylate	COOTSE-BDC
Barcelona Material	BCN
Brunauer–Emmett–Teller	BET
Carboxylate-metal	COO-M
Covalent organic framework	COF
Copper(I)-catalysed, azide–alkyne cycloaddition	CuAAC
Cyclic voltammetry	CV

Diethyl ether	Et_2O
Dichloromethane	CH_2Cl_2
Dimethyl 4,4-(9*H*-carbazole-3,6-diyl)dibenzoate	Me_2L2
Dimethyl 4,4-((9-dodecyl-carbazole-3,6-diyl)bis(ethyne-2,1-diyl))dibenzoate	Me_2L4
Dimethyl 4,4-((9*H*-carbazole-3,6-diyl)bis(ethyne-2,1-diyl))dibenzoate	Me_2L3
Dimethyl sulfoxide	DMSO
Diffusion-ordered spectroscopy	DOSY
Dynamic light scattering	DLS
Fourier-transform infrared spectroscopy	FTIR
Hard and soft acid–base	HSAB
Heteronuclear multiple bond correlation	HMBC
Heteronuclear single quantum correlation spectroscopy	HSQC
Homonuclear correlation spectroscopy	COSY
Inductive coupled plasma mass spectrometry	ICP-MS
Matrix-assisted laser desorption/ionisation Time-of-Flight	MALDI-TOF
Material Institute Lavoisier	MIL
Methanol	MeOH
Metal-ligand	M-L
Metal-organic cages	MOCs

Metal-organic frameworks	MOFs
Metal-organic polyhedra	MOP
Mobile composition of matter	MCM
Molar equivalent	Mol. Eq.
N,N-diisopropylethylamine	DIPEA
N,N-dimethylacetamide	DMA
N,N-dimethylformamide	DMF
Nuclear magnetic resonance	NMR
Octahedron	oct
Polyethylene glycol	PEG
Powder X-ray diffraction	PXRD
Reticular Chemistry Structure Resource	RCSR
Rh(II)-based MOPs	Rh-MOPs
Single-crystal X-ray diffraction	SC-XRD
Three dimensional	3D
Trigonal prism	trp
Tris(hydroxypropyltriazolylmethyl)amine	THPTA
Two dimensional	2D
Tetrabutylammonium fluoride	TBAF
Ultraviolet-visible	UV-Vis

08

ANNEX:

LIST OF PUBLICATIONS

8. List of publications

The scientific publications of the author of this PhD Thesis are listed below:

1. Hernández-López, L., Cortés-Martínez, A., Parella, T., Carné-Sánchez, A., Maspoch, D. pH-Triggered Removal of Nitrogenous Organic Micropollutants from Water by Using Metal-Organic Polyhedra. *Chem. Eur. J.* **2022**, *28*, e202200357.
2. Khobotov-Bakishev, A., von Baeckmann, C., Ortín-Rubio, B., Hernández-López, L., Cortés-Martínez, A., Martínez-Esaín, J., Gándara, F., Juanhuix, J., Platero-Prats, A.E., Faraudo, J., Carné-Sánchez, A., Maspoch, D. Multicomponent, Functionalized HKUST-1 Analogues Assembled via Reticulation of Prefabricated Metal–Organic Polyhedral Cavities. *J. Am. Chem. Soc.* **2022**, *144 (34),* 15745-15753.
3. Hernández-López, L., von Baeckmann, C., Martínez-Esaín, J., Cortés-Martínez, A., Faraudo, J., Caules, C., Parella, T., Maspoch, D., Carné-Sánchez, A., *Chem. Eur. J.* **2023**, *29*, e202301945.
4. Cortés-Martínez, A., von Baeckmann, C., Hernández-López, L., Carné-Sánchez, A., Maspoch, D. Giant oligomeric porous cage-based molecules. *Chem. Sci.*, **2024**, *15*, 7992-7998.
5. Ruiz-Relaño, S., Nam, D., Albalad, J., Cortés-Martínez, A., Juanhuix, J., Imaz, I., Maspoch, D. Synthesis of Metal–Organic

Cages via Orthogonal Bond Cleavage in 3D Metal–Organic Frameworks. *J. Am. Chem. Soc.* **2024**, *146 (39*), 26603-26608.

6. Nam, D., Albalad, J., Sánchez-Naya, R., Ruiz-Relaño, S., Cortés-Martínez, A., Yang, Y., Juanhuix, J., Imaz, I., Maspoch, D. Isolation of the Secondary Building Unit of a 3D Metal–Organic Framework through Clip-Off Chemistry, and Its Reuse To Synthesize New Frameworks by Dynamic Covalent Chemistry. *J. Am. Chem. Soc.* **2024**, *146 (40),* 27255-27261.
7. Hernández-López, L., Khobotov-Bakishev, A., Cortés-Martínez, A., Garrido-Ribó, E., Samanta, P., Royuela, S., Zamora, F., Maspoch, D., Carné-Sánchez, A. DNA-Based Networks Formed by Coordination Cross-Linking of DNA with Metal–Organic Polyhedra: From Gels to Aerogels to Hydrogels. *J. Am. Chem. Soc.* **2025***, 147 (19)*, 16560-16567.
8. Cortés-Martínez, A., Fernández-Seriñán, P., von Baeckmann, C., Caules, C., Hernández-López, L., Gutiérrez Gómez, M.S., Yang, Y., Sánchez-Naya, R., Suárez del Pino, J. A., Juanhuix, J., Imaz, I., Carné-Sánchez, A., Maspoch, D. Isoreticular Synthesis of Mesoporous Metal-Organic Polyhedra with Permanent Porosity to Gas and Water *Angew. Chem. Int. Ed.* **2025**, e202505682.

9. Sánchez-Naya, R., Cavalieri, J. P., Albalad, J., Cortés-Martínez, A., Wang, K., Fuertes-Espinosa, C., Parella, T., Fiori, S., Ribas, E., Mugarza, A., Ribas, X., Faraudo, J., Yaghi, O. M., Imaz, I., Maspoch, D. Excision of organic macrocycles from covalent organic frameworks. *Science*, **2025**, *388*,1318-1323.

Check for updates

Chemistry–A European Journal

Research Article
doi.org/10.1002/chem.202200357

Chemistry Europe
European Chemical Societies Publishing

www.chemeurj.org

pH-Triggered Removal of Nitrogenous Organic Micropollutants from Water by Using Metal-Organic Polyhedra

Laura Hernández-López,[a, b] Alba Cortés-Martínez,[a, b] Teodor Parella,[c] Arnau Carné-Sánchez,*[a, b] and Daniel Maspoch*[a, b, d]

Abstract: Water pollution threatens human and environmental health worldwide. Thus, there is a pressing need for new approaches to water purification. Herein, we report a novel supramolecular strategy based on the use of a metal-organic polyhedron (MOP) as a capture agent to remove nitrogenous organic micropollutants from water, even at very low concentrations (ppm), based exclusively on coordination chemistry at the external surface of the MOP. Specifically, we exploit the exohedral coordination positions of Rh^{II}-MOP to coordinatively sequester pollutants bearing N-donor atoms in aqueous solution, and then harness their exposed surface carboxyl groups to control their aqueous solubility through acid/base reactions. We validated this approach for removal of benzotriazole, benzothiazole, isoquinoline, and 1-napthylamine from water.

Introduction

Hazardous organic micropollutants are found in natural water resources worldwide, posing a threat to human health and to ecosystems.[1,2] Thus, there is a pressing need to develop strategies and materials for water purification. Among the most efficient strategies for removal of organic micropollutants from water is adsorptive removal, which in some cases is followed by degradation of the pollutant. Effective adsorbents must combine high surface areas with strong chemical affinity for the target pollutants. Promising candidates include porous materials such as zeolites, activated carbon, covalent organic frameworks, and metal-organic frameworks, all of which offer large surface areas and whose pores can be chemically modified.[3–6] Other candidates are nanomaterials (e.g., nanoparticles, nanotubes, graphene, etc.), which boast high surface area-to-volume ratios, given their small size. Additionally, some nanomaterials exhibit highly reactive surfaces that can be functionalised for catalysing the degradation of the adsorbed pollutants.[7,8]

Researchers have recently begun to develop supramolecular strategies based on host-guest chemistry to capture and separate substances of interest.[9–12] In these strategies, discrete molecular compounds can be used in solution to selectively recognise, adsorb, and entrap the substance of interest inside their cavities.[13–16] The resultant host-guest complex is then isolated in solution by liquid/liquid extraction or phase transfer. Finally, the guest molecule is liberated from the host upon breakage of the host-guest interaction. For example, metal-organic coordination cages have been used to selectively separate specific polycyclic aromatic hydrocarbons from a mixture of similar molecules by phase-transfer phenomena.[17] Alternatively, multitopic ion-pair receptors based on calix[4]pyrrole derivatives have been employed to remove inorganics (K^+, Li^+, and Cs^+) from aqueous solution by liquid/liquid extraction.[18,19]

Our group recently reported an interesting alternative to the aforementioned host-guest approach to capture species of interest: rather than do coordination chemistry in the pores or cavities of molecular systems such as cages, we instead focus on coordination chemistry at the external surface of metal-organic cages or polyhedra (MOP). As proof-of-concept, we used the prototypical Rh^{II}-based MOP that comprises 12 divalent Rh–Rh paddlewheel clusters and 24 angular benzene-1,3-dicarboxylate (bdc) linkers, exhibits a cuboctahedral shape, and has an external diameter of 2.5 nm. Given the nanoscopic

[a] L. Hernández-López, A. Cortés-Martínez, Dr. A. Carné-Sánchez, Prof. D. Maspoch
Catalan Institute of Nanoscience and Nanotechnology (ICN2)
CSIC and The Barcelona Institute of Science and Technology
Campus UAB, Bellaterra, 08193 Barcelona (Spain)
E-mail: arnau.carne@icn2.cat
daniel.maspoch@icn2.cat

[b] L. Hernández-López, A. Cortés-Martínez, Dr. A. Carné-Sánchez, Prof. D. Maspoch
Departament de Química, Facultat de Ciències
Universitat Autònoma de Barcelona
08193 Bellaterra (Spain)

[c] Dr. T. Parella
Servei de Ressonància Magnètica Nuclear
Universitat Autònoma de Barcelona
Campus UAB, Bellaterra, 08193 Barcelona (Spain)

[d] Prof. D. Maspoch
ICREA
Pg. Lluís Companys 23, 08010 Barcelona (Spain)

Supporting information for this article is available on the WWW under https://doi.org/10.1002/chem.202200357

size and functional outer surface of this MOP, using it to capture species resembles the use of nanoparticle to do the same, albeit with the benefit of stoichiometric precision. This precision stems from the 84 available positions on the outer surface of the MOP, of two types. The first type, of which there are 12, are located in the 12 Rh–Rh paddlewheels. Each of these clusters expose a single exohedral axial coordination site that can be harnessed to bind coordinating molecules.

The second type, of which there are 72, derive from the 24 bdc linkers, each of which can be functionalised at three positions (4, 5 and 6) of its phenyl ring by conventional organic chemistry.[20] Our group previously demonstrated that this surface chemistry could be used to separate physicochemically similar molecules that differ in their affinity to the exohedral Rh^{II} axial site (separation by phase-transfer)[21] and in the steric hindrance around their coordinating atom (separation by liquid/liquid extraction).[22]

In the work that we report here, we adapted our previous surface chemistry approach to develop a new supramolecular strategy that uses the cuboctahedral Rh^{II}-MOP as a capture agent to remove organic micropollutants from water by pH-controlled precipitation (Figure 1). This strategy is based on combining the coordination ability of the Rh^{II} sites to capture organic pollutants that bear functional groups, with a simple acid-based reaction performed on the bdc linkers to control the solubility of the MOP in water. Thus, each one of the characteristic 12 exohedral axial coordination sites of these cuboctahedral Rh^{II}-MOPs is used to capture and bind coordinating pollutants from water by coordination chemistry. Moreover, among the different members of these cuboctahedral MOPs, we selected $[Rh_2(COOH\text{-}bdc)_2]_{12}$ (hereafter named COOHRhMOP; where COOH-bdc = 5-carboxy-1,3-benzenedicarboxylate). This MOP is functionalised with a carboxylic acid group at the 5-position of the phenyl ring of each bdc linker, such that its external surface is functionalised with a total of 24 carboxylic acid groups.[23] These groups are essential for our supramolecular strategy, as they confer the MOP with pH-dependent aqueous solubility. Indeed, when COOHRhMOP is exposed to a base (e.g., NaOH), it becomes an anionic, water-soluble MOP of formula $Na_{24}[Rh_2(COO\text{-}bdc)_2]_{12}$ (hereafter named COONaRhMOP; where COO-bdc = 1,3,5-benzenetricarboxylate). COONaRhMOP can then be reprotonated upon exposure to an acid (e.g., HCl), which precipitates it out from water such that it can be recovered by filtration or centrifugation. We envisioned that this pH-based solubility could serve as a trigger in a pollutant-removal system, reasoning that, once a coordinating molecule had become anchored to the surface of a MOP, the latter would govern the solubility of the former.

Thus, our supramolecular process for pollutant-removal is based on four steps. Firstly, coordinative interactions between the organic pollutant and the water-soluble COONaRhMOP are established in solution (Figure 1). Secondly, the COONaRhMOP-pollutant complex is precipitated out, by lowering the pH using HCl, and subsequently isolated from water by filtration or centrifugation. Thirdly, the precipitate is washed with aq. $CaCl_2$, leading to liberation of the pollutant. Through this washing step, Ca^{II} ions coordinate strongly to the organic micropollutant, breaking the COOHRhMOP-pollutant coordination interaction and dissolving the pollutant back into an aqueous solution. In the fourth and final step, the COOHRhMOP is treated with NaOH, causing it to redissolve in the remaining solution, which might contain residual pollutants, thereby enabling its reuse for subsequent cycles of water purification.

Results and Discussion

Removal of benzotriazole as a test-case. Step 1: Coordination between benzotriazole and COONaRhMOP in water

As proof-of-concept, we chose to test our MOP-based strategy by attempting to remove benzotriazole (BT) from water. Benzotriazole is broadly used both in industrial and household products: for instance, as a corrosion inhibitor; as an ultraviolet light-stabilizer in plastics; as an ultraviolet filter; as antifogging or defogging agent; and in de-icing/anti-icing fluids. The high amount of BT disposed by such activities, the high water-solubility of BT (ca. 20 $g \cdot L^{-1}$), and the slow biodegradation of BT lead to its high persistence in aquatic environments, where, at concentrations above about 5 ppm,[24,25] it causes environ-

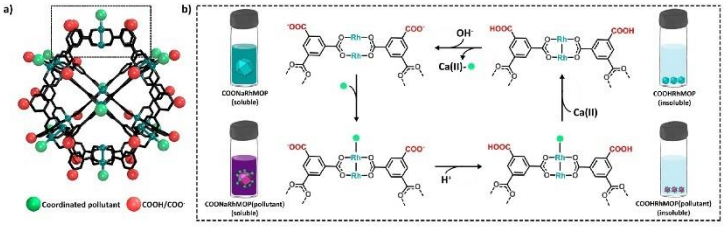

Figure 1. a) Structure of the cuboctahedral Rh^{II}-MOP, highlighting the 5-positions in the organic backbone (red balls) and the axial sites of its dirhodium paddlewheels (green balls). b) Schematic of the pH-triggered supramolecular removal strategy.

mental harmful long-term effects.[26-28] In fact, BT has been proposed as a micropollutant indicator of water contamination through anthropogenic activities, due to its ubiquity in surface water and its environmental toxicity.[29] Given that BT contains a triazole functional group fused to a benzene ring, we envisaged that we could anchor the molecule to the surface of COONaRhMOP, by coordinating the free N-donor atoms in the triazole of the former to the exposed axial sites of the Rh–Rh paddlewheels in the latter. To confirm this, we added BT to an aqueous solution of COONaRhMOP, and then monitored their interaction by naked eye. We found that the addition of BT (24 mol equiv, 380 ppm) to an aqueous solution of COONaRh-MOP (0.133 μmol, 1 mL) induced an immediate change in colour of the solution, from blue to purple, suggesting a coordinative interaction between the BT and the Rh–Rh paddlewheel. Next, we monitored this interaction by UV-Vis spectroscopy, focusing on the bands centred at 500 to 600 nm, which correspond to the $\pi^*\rightarrow\sigma^*$ transitions (λ_{max}) of the Rh – Rh bonds. A shift in the Rh–Rh bond absorption band (λ_{max}), from 585 to 551 nm, corroborated coordination of the BT to the Rh–Rh paddlewheel (Figure S3 in the Supporting Information).[30,31] To further study the coordination of BT to the Rh–Rh paddlewheel units, we followed the titration of COONaRhMOP with BT by UV-Vis spectroscopy. We found that, below 10 mol equiv (159 ppm) of BT, the isosbestic point is preserved, indicating that each exohedral dirhodium axial site behaves independently.[22] Finally, we gained additional evidence that coordination of BT to COONaRhMOP proceeds through the exposed surface dirhodium axial sites, upon observing a marginal shift in λ_{max} above 12 mol equiv of BT (190 ppm).

Step 2: pH-triggered precipitation of COONaRhMOP(BT)

Having demonstrated the coordination of BT to COONaRhMOP, we reasoned that the captured BT could then be removed from water through in situ precipitation of the formed complex (hereafter named COONaRhMOP(BT)). Our hypothesis was based on the premise that, once the coordination between COONaRhMOP and BT had occurred, the solubility of the latter would be dictated by the solubility of the COONaRhMOP. Therefore, we expected that protonation of the surface carboxylate groups of COONaRhMOP(BT) would induce its precipitation, as we had already observed for COONaRhMOP alone (Figures S1 and S2). We expected that the precipitate (hereafter named COOHRhMOP(BT)) could then be easily removed by using simple techniques such as centrifugation or filtration. To this end, we optimised the pH at which a quantitative precipitation of the MOP occurs, while minimising protonation-induced cleavage of the BT–Rh^{II}–MOP coordination bond. These experiments were performed by preparing two different mixtures containing COONaRhMOP (0.133 μmol, 1 mL) and 6 mol equiv (95 ppm) or 24 mol equiv (380 ppm) of BT, being these two concentrations representative examples of defective and excess concentrations with respect to the 12 exohedral axial sites present in the MOP structure. Both resulting solutions (final pH = 8.6 and 7.8, respectively) were incubated for only 10 s and subsequently precipitated by lowering the pH with different amounts of HCl acid. The precipitation solids were isolated by centrifugation. Once the solids had been isolated, the optimum amount of acid for the precipitation process was determined by analysing the remaining BT in the aqueous solution after the precipitation step by means of UV-Vis measurements and establishing its removal efficiency (Figure S4). For both mixtures, the best performance was observed under milder acidic conditions when 10 μL of HCl 1 M (final pH = 2.3) were used to precipitate out the COOHRhMOP(BT). Based on this amount of acid, the following removal efficiency values were determined: 77% for the solution initially containing 6 mol equiv of BT; and 53% for the one containing 24 mol equiv of BT (see Section S3.5 in the Supporting Information). In both cases, the amount of MOP remaining in solution was lower than 0.1% (Table S1). Importantly, blank experiments (i.e., lacking COONaRhMOP) were performed in solution. These experiments revealed that the concentration of BT remained constant throughout the pH range studied (pH: 5.8 to 1.9), demonstrating the high aqueous solubility of BT and indicating that the solubility of the COOHRhMOP(BT) complex is indeed governed by that of COOHRhMOP itself (Figure S5).

Influence of the pH, the incubation time, and the concentration of BT on the removal efficiency

Once we had optimised the pH at which COOHRhMOP(BT) precipitates, we sought to elucidate the influence of the pH of the polluted water on the coordination of BT to COONaRhMOP and therefore, on the pollutant removal efficiency. This parameter might influence the removal efficiency of our proposed pH-triggered pollutant removal methodology due to the amphoteric properties of BT (pK_{a1}: 0.42, pK_{a2}: 8.27). To this end, we ran new experiments. Thus, three aqueous solutions containing COONaRhMOP (0.133 μmol, 1.03 mL) and BT (24 mol equiv; 380 ppm) were prepared. Each of these solutions, were brought to a different pH: either acidic (pH: 4.3), neutral (pH: 7.6) or basic (pH: 9.9). The UV-Vis spectrum of each aqueous phase revealed that the largest λ_{max} shifts were observed for the acidic conditions (Figure S10). This result is consistent with the fact that, at basic pH, BT can be deprotonated, which weakens its coordination to COONaRhMOP due to electrostatic repulsion. Contrariwise, acidic conditions lead to the formation of neutral BT, thereby favouring the formation of COONaRhMOP(BT) (Figure S9). However, these differences in the coordination of BT to COONaRHMOP did not translate into significative differences in the removal efficiencies after the precipitation step. Thus, after addition of the proper amount of diluted HCl (1 M) to each solution (1 μL to the acidic solution; 10 μL to the neutral one; and 10 μL to the basic one) to reach the optimised precipitating pH 2.3, the removal efficiency for BT was found to be around 54% in all cases (see Section S3.6). Altogether, these results highlight that our supramolecular strategy works in polluted water samples that vary in their initial pH level.

The experiments that we have described so far indicate that the interaction between COONaRhMOP and BT is fast, due to the absence of diffusion barriers, making a rapid method for pollutant removal feasible. To further confirm the lack of significant diffusion barriers in our proposed method, we performed new experiments to assess the impact of the incubation time prior the precipitation step on the BT removal efficiency. Accordingly, four independent aqueous solutions containing COOHNaRhMOP (0.133 μmol, 1 mL) and 6 mol equiv of BT (95 ppm) were prepared. Each solution was incubated for a different time (either 10 s, 10 min, 30 min, or 60 min), and then subjected to the aforementioned precipitation procedure. The UV-Vis spectra did not indicate any significant differences in the removal efficiencies, all of which were >70%, suggesting that the incubation time does not influence the removal efficiency (Figure 2a, green dots, see Section S3.7.1). These results further confirmed the rapid capture and binding of BT to COONaRhMOP.

Once we had demonstrated that our pH-triggered, COONaRhMOP-based strategy could indeed remove BT from water, we next evaluated its performance at different concentrations of BT (Figure 2b, see Section S3.8). The initial and final concentrations were determined by either UV-Vis spectroscopy (conc. BT: >16 ppm) or ^{1}H NMR spectroscopy (conc. BT: <16 ppm; Figures S21 and S23). The consistency of the results obtained using both techniques was corroborated by analysing samples at an intermediate concentration (6 mol equiv, 95 ppm), using both techniques (Figures S21c and S22, Tables S6 and S7). The removal efficiency of BT for the solutions that had initially contained between 1 mol equiv (16 ppm) and 10 mol equiv (158 ppm) was found to be >70% in all cases, with a linear increase in BT removed per MOP with increasing initial conc. of BT (Figure 2b). Remarkably, the removal efficiency was up to 90% in solutions that had contained BT at initial concentrations of 16 ppm. In this case, the remaining BT was below 1.6 ppm, which is below the level considered to be environmentally toxic (ca. 5 ppm).[24,25] Contrariwise, when 24 mol equiv (380 ppm) were initially present in the solution, the final amount of pollutant dropped to 10 mol equiv (158 ppm; removal efficiently: 55%). These experiments confirmed that the ratio between pollutant and exohedral axial coordination metal sites in the COONaRhMOP determines the performance of our pH-triggered coordination-removal strategy.

Step 3: Regeneration and reusability of COOHRhMOP

Rapid and easy regeneration of the COOHRhMOP is essential for the feasibility of the proposed removal supramolecular strategy. Initially, we reasoned that exposing the COOHRhMOP(BT) solid to harsh acidic conditions would promote the formation of the protonated form of BT and consequently, its detachment from COOHRhMOP. However, we found that the detachment of BT required incubation under extremely acidic (3 M HCl) conditions, which we rule out, as they endangered the structural stability of the Rh^{II}-MOP (Figure S25). Alternatively, we sought a milder methodology that would entail washing of the precipitate with an aqueous solution containing a competing metallic centre for the coordination of BT. The formation of a new metal-BT complex would thus favour the regeneration of the occupied axial coordination sites of COOHRhMOP, whereby

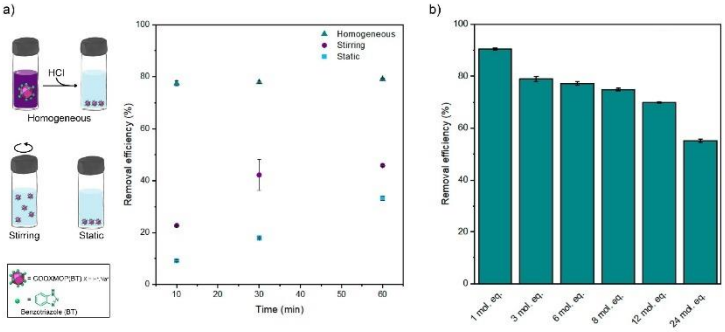

Figure 2. a) Left: Three methods for using COOHRhMOP to remove benzothiazole (BT; 6 mol equiv; 95 ppm) from water: as a porous solid under heterogeneous conditions, either with stirring or in a static reaction; or dissolved under homogeneous conditions, in our proposed, pH-triggered, supramolecular strategy. Right: Plot of the influence of reaction/incubation time on removal efficiency for each method: stirring, static, or homogeneous reactions. b) Removal efficiency of COONaRhMOP for BT at different concentrations of BT, ranging from 1 mol equiv (16 ppm) and 24 mol equiv (380 ppm), by using the supramolecular strategy. In both graphs, the data are reported as average values from triplicate experiments. Errors bars indicate standard deviation.

new uptake cycles could be performed. To this end, Ca^{II} was selected as a competing metallic centre, because of its reduced toxicity as well as its low cost. To explore its efficacy, we performed a preliminary washing experiment. To this end, the solid COOHRhMOP(BT) was washed twice by incubating it in a saturated solution of aq. $CaCl_2$ for 30 s. Note that this COOHRhMOP(BT) was initially precipitated from 5 mL solution of BT (6 mol equiv; 95 ppm), to which the removal strategy had earlier been applied using COONaRhMOP (0.67 μmol). After both washing steps, the remaining COOHRhMOP was quantitatively transformed into COONaRhMOP through basification with NaOH (16.1 μmol). This basification step caused the Rh^{II}-MOP to redissolve in the (now basic) aqueous solution. The success of the regeneration procedure was confirmed by UV-Vis analysis, as the initial λ_{max} of 583 nm characteristic of COONaRhMOP was obtained, thus further corroborating the detachment of BT from the outer surface of the Rh^{II}-MOP (Figures S26 and S27). Finally, the recovery and reusability of COONaRhMOP was confirmed by comparing the BT removal efficiency for three additional cycles of uptake (using the same conditions as in Cycle 1), precipitation, and regeneration. Remarkably, the recovered COONaRhMOP maintained its removal efficiency for BT for at least three consecutive cycles (Figures S28 and S29, Table S9). Moreover, the integrity of COONaRhMOP was maintained through the whole cycle, as evidenced by UV-Vis, ^{1}H NMR, and mass spectrometry (MS; see Section S3.10).

Use of filtration in the pH-triggered, supramolecular strategy

Next, we simplified our supramolecular strategy by replacing the centrifugation steps with a unified filtration process in which recovery of COOHRhMOP(BT), detachment of BT, and regeneration of COONaRhMOP occur sequentially. To this end, a test was run on 5 mL of a solution of BT (6 mol equiv; 95 ppm), to which the removal strategy was applied using COONaRhMOP (0.67 μmol). After precipitation with HCl, the aqueous solution was passed through a nylon syringe-filter (0.45 μm). The filter captured the COOHRhMOP(BT), observed as a purple solid, and the aqueous supernatant was recovered and analysed by means of UV-Vis spectroscopy (Figure 3a). This analysis revealed a comparable removal efficiency to that previously obtained (73%; Figures 3b, S33, Table S10). The filter was then treated with saturated aq. $CaCl_2$, which induced an immediate change in colour of the solid, from purple to blue, representative of cleavage of the Rh-BT coordination bond and subsequent release of the BT into the $CaCl_2$ solution. Finally, aq. NaOH was passed through the filter to redissolve the resultant COOHRhMOP, through formation of COONaRhMOP (Figures 3a and S34). Importantly, a blank experiment (i.e., without COOHRhMOP) revealed that the nylon syringe-filter alone does not contribute to any removal of BT (Figure S32). Interestingly, the strategy also proved successful when, instead of Milli-Q water, regular tap water was employed throughout the entire process (Section S3.12).

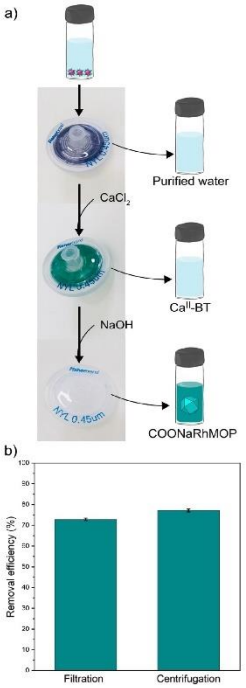

Figure 3. a) Schematic of the partial removal of BT by the pH-triggered, supramolecular strategy using filtration (rather than centrifugation) to isolate the capture agent. b) Comparison of removal efficiency for filtration vs. centrifugation. The data are reported as the average uptake value from duplicate experiments. Error bars indicate the standard deviation.

Comparison of the removal of benzotriazole using COOHRhMOP as a porous solid

To evaluate the possible influence of classical diffusion barriers on the efficiency of COOHRhMOP at removing BT from water, we next ran tests under heterogeneous conditions. To this end, COOHRhMOP powder (5 mg, 0.67 mmol) was soaked in a solution containing BT (6 mol equiv; 95 ppm; 5 mL) at a pH of 6.0. This pH was selected to ensure that the MOP remains in its neutral form, and that the BT is predominantly in its more-coordinative state. The heterogeneous removal tests were performed both with stirring and without (hereafter called

static), and the removal efficiency was quantified after different incubation times. Interestingly, the removal efficiency was slightly higher in the stirred reactions (46%) than in the static one (33%; Figure 2b, purple and sky-blue dots, and Section S3.7.2). For both conditions, the best performance was observed after 1 h of incubation. Altogether, these results evidence the detrimental effect of diffusion barriers in the coordination of BT to COOHRhMOP under when used as a solid powder (i.e., heterogeneous conditions), for which the kinetics are less favourable – and consequently, the removal efficiency, lower – compared to using COONaRhMOP in solution (i.e., homogeneous conditions).

Expanding the scope of the pH-triggered coordinative-removal supramolecular strategy

We reasoned that our strategy might become more challenging to apply to removal of pollutants that contain coordinating groups that are more pH-sensitive than BT, as protonation of these groups preclude the interaction between the pollutant and the COONaRhMOP. To explore this hypothesis, we tested the performance of our strategy at removing other nitrogenous organic micropollutants from water, whose coordinating groups are easier to protonate than are the coordinating N-atoms in the triazole ring of BT (pK_{a1}: 0.42). Thus, we chose three polar pollutants commonly found in water: i) benzothiazole (BTZ; pK_a: 2.28), which is used as vulcanisation accelerator in rubber manufacture and as an herbicide;[32,33] ii) 1-naphtylamine (NA; pK_a: 4.25), used both as a fungicide and as a precursor of azo-dyes, which is classified as a carcinogen;[34,35] and iii) isoquinoline (IQ; pK_a: 5.26),[36,37] which is a potentially genotoxic compound found in coking wastewaters (Figure 4, right). Firstly, the coordination of BTZ, NA, or IQ to COONaRhMOP was confirmed by UV-Vis spectroscopy (Figures S37, S50 and S66). Then, the precipitation conditions for each pollutant were optimised, using a similar approach to that previously followed for BT, whereby a balance between the removal efficiency and the complete precipitation of COOHRHMOP(pollutant) was found. For all these experiments, UV-Vis and ^{1}H NMR were employed to quantitatively evaluate the removal efficiency. As depicted in Figure 4, very high removal efficiencies were found for BTZ (ca. 80% to 90%) throughout the tested concentration range, with values even higher than those for BT. We attributed this performance to the greater hydrophobicity of BTZ relative to BT, which facilitates its removal from water (Section S4.2.4). The removal of pollutants containing weak bases/nucleophiles could be limited by the weakness of the coordination bonds. However, despite the weak coordination observed between NA and the dirhodium paddlewheel (Figure S50), the removal efficiency for NA was 80% at low concentrations (1 mol equiv; 19 ppm; Section S4.3.4). Moreover, although the required pH for the precipitation of either COOHRhMOP(NA) or COOHRhMOP(IQ) was lower (ca. 3.5) than the reported pK_a for either NA or IQ, the removal efficiency for both pollutants was 70% (Sections S4.3.4 and S4.4.4). These results confirm that the respective coordinative bonds remain intact at these (more acidic) pH values. Lastly, in all cases, the complexes obtained from precipitation were recoverable again by using Ca^{II} as a competing metallic centre for the coordination of the organic coordinating pollutants). Note that both NA and IQ could also be recovered by using an acidic (0.3 M HCl) wash, as their easier protonation allowed the complete recovery without endangering the MOP structure. Additionally, the recovered materials were reusable, as they demonstrated comparable removal efficiency values in subsequent cycles structure (Sections S4.2.5, S4.3.5 and S4.4.5). The integrity of COONaRhMOP was further evidenced by UV-Vis, ^{1}H NMR, and MS (Sections S4.2.6, S4.3.6 and S4.4.6).

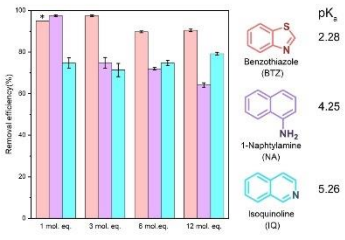

Figure 4. Efficiency of COONaRhMOP at removing BTZ, NA, and IQ from aqueous solutions. *A removal efficiency of >95% was assumed for BTZ at 1 mol equiv (18 ppm) because the residual concentration of BTZ in the remaining aqueous solution was below the limit of quantification (0.9 ppm). All values are reported as an average of triplicate experiments. Errors bars indicate standard deviation.

Simultaneous removal of multiple nitrogenous organic micropollutants from an aqueous solution

Encouraged by our results, we envisaged that we could use our pH-triggered supramolecular strategy to simultaneously remove multiple organic pollutants from water. To this end, we performed a test in an aqueous solution containing a mixture of BT, BTZ, NA, and IQ. Thus, a 3 mL of an aqueous solution containing COONaRhMOP (0.4 μmol) and equimolar mixture of BT (6 mol equiv; 95 ppm), BTZ (6 mol equiv; 108 ppm), NA (6 mol equiv; 114 ppm), and IQ (6 mol equiv; 102 ppm) was prepared. Then, this mixture was subjected to multiple cycles of pollutant removal/capture-agent regeneration. As indicated by ^{1}H NMR spectra taken before and after the first cycle, the removal efficiency values were, from highest to lowers: 87% (BTZ), 85% (NA), 74% (IQ) and 66% (BT; Figure 5). Although a similar value was observed for removal of BTZ from this multi-pollutant solution compared to from the mono-pollutant solution, the corresponding values for the other pollutants did differ. Interestingly, the values for removal of NA and IQ were higher than from the respective mono-pollutant solutions, whereas that for BT was slightly lower. Overall, these values confirm that each COONaRhMOP can capture more than 12

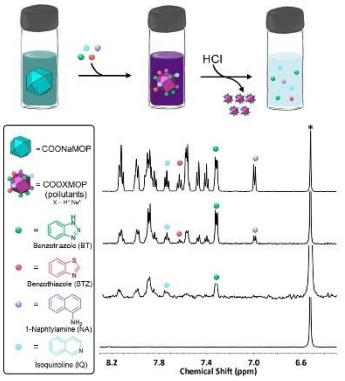

Figure 5. Top: Schematic of the simultaneous removal of various organic micropollutant pollutants from an aqueous multipollutant solution by the pH-triggered, supramolecular strategy. Bottom: Stacked ^{1}H NMR spectra of a D_2O solution before (top) and after three subsequent (from high to low) removal/regeneration cycles. Left: Legend for both parts.

pollutant molecules (ca. 20). We attributed the results to the contribution of cooperative hydrophobic and Van der Waals interactions, which can enhance the performance of the capturing agent once all the specific binding sites have been occupied. Next, the capture agent was regenerated, and the remaining aqueous solution with the four residual pollutants was subjected to additional removal/regeneration cycles. By the second cycle, all of the BTZ and NA had been fully removed, and by the third cycle all of the BT and IQ had been removed (Section S5.3). Again, the stability of the COONaRhMOP was maintained throughout each cycle, as confirmed by UV-Vis, ^{1}H NMR, and MS (Section S5.4).

Conclusion

Through this proof-of-concept study, we have demonstrated that robust, water-soluble MOPs can be harnessed to remove organic pollutants from water in a pH-triggered fashion. We engineered a novel organic-pollutant removal supramolecular strategy based on the pH-dependent solubility of COOHRhMOP. At high pH, the anionic, water-soluble COONaRhMOP is formed, whose outer surface interacts, through coordination chemistry, with organic pollutants bearing basic N-donor atoms. A rapid decrease in pH forces the precipitation of the resultant MOP-pollutant complex from purified water. We demonstrated the efficacy of our approach at removing four common micropollutants – benzotriazole, benzothiazole, isoquinoline, and 1-naphthylamine – from water at various concentrations, using both single and multiple-pollutant solutions. In all cases, the COOHRhMOP can be easily regenerated by using readily available and mild reagents ($CaCl_2$ and NaOH), and its performance is maintained through multiple cycles of removal/regeneration. Our work lays the foundation for the development of pH-induced precipitation of organic pollutants, akin to currently used methods for the removal of inorganic salts. Moreover, we envisage that the wide structural versatility of MOPs will enable our approach to be extended to many other organic pollutants, especially by exploiting other MOP-pollutant interactions than (or in addition to) coordination chemistry, including host-guest, π–π and electrostatic interactions, and combinations thereof. Thus, the results presented here widen the scope of applications for the emerging water-soluble metal-organic cages toward pollutant removal and environmental applications.[18]

Acknowledgements

This work was supported by the Spanish MINECO (project RTI2018-095622-B–I00) and the Catalan AGAUR (project 2017 SGR 238). It was also funded by the CERCA Programme/Generalitat de Catalunya and through a fellowship (LCF/BQ/PR20/11770011) from the "la Caixa" Foundation (ID 100010434). ICN2 is supported by the Severo Ochoa programme from the Spanish MINECO (grant no. SEV-2017-0706). L.H.L. acknowledges the support from the Spanish State Research Agency (PRE2019-088056).

Conflict of Interest

The authors declare no conflict of interest.

Data Availability Statement

The data that support the findings of this study are available on request from the corresponding author. The data are not publicly available due to privacy or ethical restrictions.

Keywords: coordinative removal · metal-organic polyhedra · pH-responsive · organic micropollutants · pollutant removal

[1] R. P. Schwarzenbach, B. I. Escher, K. Fenner, T. B. Hofstetter, C. A. Johnson, U. von Gunten, B. Wehrli, *Science* **2006**, *313*, 1072–1077.
[2] S. D. Richardson, T. A. Ternes, *Anal. Chem.* **2014**, *86*, 2813–2848.
[3] M. Mon, R. Bruno, J. Ferrando-Soria, D. Armentano, E. Pardo, *J. Mater. Chem. A* **2018**, *6*, 4912–4947.
[4] M. Mon, R. Bruno, E. Tiburcio, M. Viciano-Chumillas, L. H. G. Kalinke, J. Ferrando-Soria, D. Armentano, E. Pardo, *J. Am. Chem. Soc.* **2019**, *141*, 13601–13609.
[5] J. L. Fenton, D. W. Burke, D. Qian, M. Olvera de la Cruz, W. R. Dichtel, *J. Am. Chem. Soc.* **2021**, *143*, 1466–1473.
[6] S. Rojas, P. Horcajada, *Chem. Rev.* **2020**, *120*, 8378–8415.
[7] J. You, L. Wang, Y. Zhao, W. Bao, *J. Cleaner Prod.* **2021**, *281*, 124668.
[8] L. Marcon, J. Oliveras, V. F. Puntes, *Sci. Total Environ.* **2021**, *791*, 148324.

[9] B. Shi, H. Guan, L. Shangguan, H. Wang, D. Xia, X. Kong, F. Huang, *J. Mater. Chem. A* **2017**, *5*, 24217–24222.
[10] L.-P. Yang, H. Ke, H. Yao, W. Jiang, *Angew. Chem. Int. Ed.* **2021**, *60*, 21404–21411.
[11] X. Wang, L. Xie, K. Lin, W. Ma, T. Zhao, X. Ji, M. Alyami, N. M. Khashab, H. Wang, J. L. Sessler, *Angew. Chem. Int. Ed.* **2021**, *60*, 7188–7196.
[12] D. Zhang, T. K. Ronson, Y. Q. Zou, J. R. Nitschke, *Nat. Chem. Rev.* **2021**, *5*, 168–182.
[13] D. Zhang, T. K. Ronson, J. Mosquera, A. Martinez, J. R. Nitschke, *Angew. Chem. Int. Ed.* **2018**, *57*, 3717–3721; *Angew. Chem.* **2018**, *130*, 3779–3783.
[14] Y. J. Hou, K. Wu, Z. W. Wei, K. Li, Y. L. Lu, C. Y. Zhu, J. S. Wang, M. Pan, J. J. Jiang, G. Q. Li, C. Y. Su, *J. Am. Chem. Soc.* **2018**, *140*, 18183–18191.
[15] H. N. Zhang, Y. Lu, W. X. Gao, Y. J. Lin, G. X. Jin, *Chem. Eur. J.* **2018**, *24*, 18913–18921.
[16] A. B. Grommet, J. B. Hoffman, E. G. Percástegui, J. Mosquera, D. J. Howe, J. L. Bolliger, J. R. Nitschke, *J. Am. Chem. Soc.* **2018**, *140*, 14770–14776.
[17] D. Zhang, T. K. Ronson, R. Lavendomme, J. R. Nitschke, *J. Am. Chem. Soc.* **2019**, *141*, 18949–18953.
[18] Q. He, N. J. Williams, J. H. Oh, V. M. Lynch, S. K. Kim, B. A. Moyer, J. L. Sessler, *Angew. Chem. Int. Ed.* **2018**, *57*, 11924–11928.
[19] S. K. Kim, B. P. Hay, J. S. Kim, B. A. Moyer, J. L. Sessler, *Chem. Commun.* **2013**, *49*, 2112–2114.
[20] A. Carné-Sánchez, J. Albalad, T. Grancha, I. Imaz, J. Juanhuix, P. Larpent, S. Furukawa, D. Maspoch, *J. Am. Chem. Soc.* **2019**, *141*, 4094–4102.
[21] T. Grancha, A. Carné-Sánchez, L. Hernández-López, J. Albalad, I. Imaz, J. Juanhuix, D. Maspoch, *J. Am. Chem. Soc.* **2019**, *141*, 18349–18355.
[22] L. Hernández-López, J. Martínez-Esaín, A. Carné-Sánchez, T. Grancha, J. Faraudo, D. Maspoch, *Angew. Chem. Int. Ed.* **2021**, *60*, 11406–11413.
[23] J. Albalad, A. Carné-Sánchez, T. Grancha, L. Hernández-López, D. Maspoch, *Chem. Commun.* **2019**, *55*, 12785–12788.
[24] A. Seeland, M. Oetken, A. Kiss, E. Fries, J. Oehlmann, *Environ. Sci. Pollut. Res. Int.* **2012**, *19*, 1781–1790.
[25] Y.-J. Shin, B. Kim, H. Kim, K. Kim, K. Park, J. Kim, H. Kim, P. Kim, *Sci. Total Environ.* **2022**, *815*, 152846.
[26] M. D. Alotaibi, A. J. McKinley, B. M. Patterson, A. Y. Reeder, *Water Air Soil Pollut.* **2015**, *226*, 226.
[27] T. V. Wagner, J. R. Parsons, H. H. M. Rijnaarts, P. de Voogt, A. A. M. Langenhoff, *J. Hazard. Mater.* **2020**, *384*, 121314.
[28] T. Reemtsma, U. Miehe, U. Duennbier, M. Jekel, *Water Res.* **2010**, *44*, 596–604.
[29] M. Jekel, W. Dott, A. Bergmann, U. Dünnbier, R. Gnirß, B. Haist-Gulde, G. Hamscher, M. Letzel, T. Licha, S. Lyko, U. Miehe, F. Sacher, M. Scheurer, C. K. Schmidt, T. Reemtsma, A. S. Ruhl, *Chemosphere* **2015**, *125*, 155–167.
[30] E. B. Boyar, S. D. Robinson, *Coord. Chem. Rev.* **1983**, *50*, 109–208.
[31] E. Warzecha, T. C. Berto, C. C. Wilkinson, J. F. Berry, *J. Chem. Educ.* **2019**, *96*, 571–576.
[32] L. Wang, J. Zhang, H. Sun, Q. Zhou, *Environ. Sci. Technol.* **2016**, *50*, 2709–2717.
[33] C. Liao, U.-J. Kim, K. Kannan, *Environ. Sci. Technol.* **2018**, *52*, 5007–5026.
[34] J. Hu, D. Shao, C. Chen, G. Sheng, X. Ren, X. Wang, *J. Hazard. Mater.* **2011**, *185*, 463–471.
[35] W. Zhang, C. Hong, B. Pan, Z. Xu, Q. Zhang, L. Lv, *J. Hazard. Mater.* **2008**, *158*, 293–299.
[36] D. R. Joshi, Y. Zhang, H. Zhang, Y. Gao, M. Yang, *J. Environ. Sci.* **2018**, *63*, 105–115.
[37] K. V. Padoley, S. N. Mudliar, R. A. Pandey, *Bioresour. Technol.* **2008**, *99*, 4029–4043.
[38] E. G. Percástegui, T. K. Ronson, J. R. Nitschke, *Chem. Rev.* **2020**, *120*, 13480–13544.

Manuscript received: February 4, 2022
Accepted manuscript online: March 29, 2022
Version of record online: April 22, 2022

JACS
JOURNAL OF THE AMERICAN CHEMICAL SOCIETY
pubs.acs.org/JACS
Article

Multicomponent, Functionalized HKUST-1 Analogues Assembled via Reticulation of Prefabricated Metal–Organic Polyhedral Cavities

Akim Khobotov-Bakishev, Cornelia von Baeckmann, Borja Ortín-Rubio, Laura Hernández-López, Alba Cortés-Martínez, Jordi Martínez-Esaín, Felipe Gándara, Judith Juanhuix, Ana E. Platero-Prats, Jordi Faraudo, Arnau Carné-Sánchez,* and Daniel Maspoch*

Cite This: J. Am. Chem. Soc. 2022, 144, 15745−15753
Read Online

ABSTRACT: Metal−organic frameworks (MOFs) assembled from multiple building blocks exhibit greater chemical complexity and superior functionality in practical applications. Herein, we report a new approach based on using prefabricated cavities to design isoreticular multicomponent MOFs from a known parent MOF. We demonstrate this concept with the formation of multicomponent HKUST-1 analogues, using a prefabricated cavity that comprises a cuboctahedral Rh(II) metal−organic polyhedron functionalized with 24 carboxylic acid groups. The cavities are reticulated in three dimensions via Cu(II)-paddlewheel clusters and (functionalized) 1,3,5-benzenetricarboxylate linkers to form three- and four-component HKUST-1 analogues.

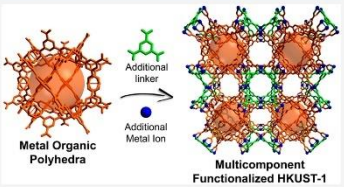

INTRODUCTION

The combination of multiple organic linkers and metal ions into multicomponent or multivariate metal−organic frameworks (MOFs) is a fruitful strategy to achieve greater chemical complexity in MOFs, expand the catalogue of MOFs accessible by synthesis, and optimize the use of MOFs for applications such as gas storage,[1] water harvesting,[2] and catalysis.[3] In these MOFs, complexity derives from the random or periodic arrangement of multiple organic and metallic functionalities into the same structure.[4] To date, strategies to design multicomponent or multivariate MOFs include bottom-up synthesis by using any of the following: distinct linkers that have identical backbones but differ in their respective side groups or isostructural clusters comprising different metal ions, to produce multivariate MOFs;[5,6] or structurally different linkers or metal clusters, to generate ordered multicomponent MOFs.[7−10] Alternatively, the complexity of parent MOF structures can be augmented through post-synthetic modification via covalent and coordination chemistry,[11,12] ligand installation,[13] and linker- or metal-exchange.[14]

Herein we propose a new approach to isoreticular, multicomponent MOFs by starting with a known MOF. Reticular chemistry enables the rational synthesis of MOFs through the connection of basic molecular building blocks (MBBs).[15,16] For example, the archetypical HKUST-1 is typically described as a 3,4-connected (3,4-c) network with an underlying **tbo** topology that is assembled from two MBBs: the 4-c Cu(II)-paddlewheel cluster and the 3-c 1,3,5-benzenetricarboxylate (btc) linker.[17] However, on a conceptual level, MOFs can also be seen as the product of connecting higher order structures[18,19] such as different cavities or metal−organic polyhedral (MOP)[20] units, whether directly or through additional, small MBBs.[21,22] Herein, we propose using MOPs as prefabricated cavities from which a parent MOF structure can be replicated, whereby its composition is changed.

Our strategy begins with a de-reticulation exercise in which a repetitive cavity of the parent MOF is identified. Following the example of HKUST-1, this enabled us to identify a repetitive cavity that defines a 24-c cuboctahedral MOP. Thus, we reasoned that the formation of the HKUST-1 structure would require the connection of these MOPs through the original 4-c Cu(II)-paddlewheel cluster and the 3-c btc. This leads to a change in the structural description of HKUST-1, from a binary 3,4-c structure that comprises one inorganic (Cu(II)-paddlewheel cluster) and one organic (btc) MBB to a tertiary 3,4,24-c structure that comprises these two MBBs and the 24-c MOP. We anticipated that this would enable use of three components in the synthesis of HKUST-1 that, if distinct, would occupy specific positions in the replicated structure, thereby generating ordered multicomponent MOFs isoreticular to HKUST-1. The basis of our approach is also supported

Received: June 12, 2022
Published: August 16, 2022

https://doi.org/10.1021/jacs.2c06131
J. Am. Chem. Soc. 2022, 144, 15745−15753

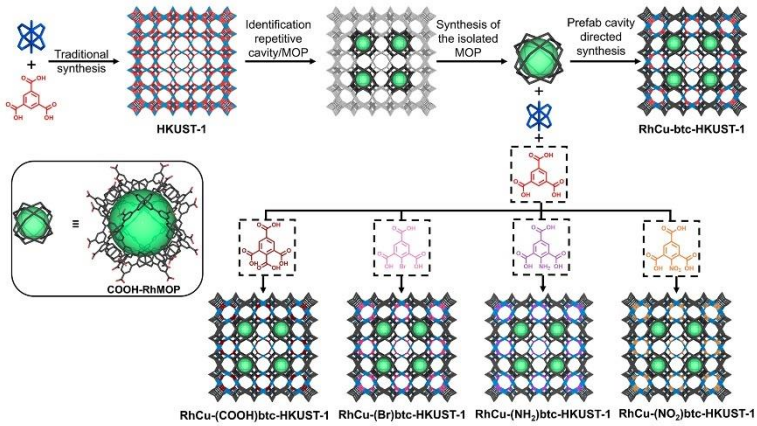

Figure 1. Schematic of the synthesis of three- and four-component HKUST-1 analogues using our design approach to multicomponent MOFs, based on the identification and exploitation of prefabricated cavities in the corresponding parent MOF.

by the supermolecular building block approach described by Eddaoudi et al., in which an *in situ*-synthesized[23,24] or pre-assembled[25] MOP is used as a highly connected node encoded with specific geometric and connectivity information to reduce the degrees of freedom of the network's constituents and direct their assembly toward a target highly connected structure. However, herein, we use MOPs in a different way. In the prefabricated directed synthesis, the MOP does not behave as an *in situ*-formed node in a network, but rather as a preformed tiling of the targeted network, one which dictates the arrangement of the metallic and organic MBBs around it to ultimately generate a structure that is not necessarily described as highly connected (in this case, HKUST-1). Thus, the work that we present here expands the utility of MOPs in MOF chemistry, thereby providing a new route to complex multicomponent networks.

■ RESULTS AND DISCUSSION

Prefabricated Cavity-Directed Synthesis of Multimetallic HKUST-1. We first applied our prefabricated cavity approach to HKUST-1 (Figure 1), choosing our previously reported Rh(II) cuboctahedral MOP functionalized with 24 carboxylic acid groups (hereafter named COOH-RhMOP) as the prefabricated cavity.[25,26] We selected COOH-RhMOP because of its high chemical stability[27] and its structural difference relative to its Cu(II) analogue, which would lead to pure HKUST-1. Using this MOP as a prefabricated cavity enabled us to replicate the structure of HKUST-1, thereby forming the isoreticular three-component RhCu-btc-HKUST-1 comprising COOH-RhMOPs, Cu(II)-paddlewheel clusters, and btc.

Using COOH-RhMOP as a prefabricated cavity in the synthesis of RhCu-btc-HKUST-1 requires the stoichiometric addition of the three MBBs: COOH-RhMOP, the Cu(II)-paddlewheel cluster, and btc. To determine this stoichiometry, we studied the connectivity of the three MBBs in the targeted structure (Figure 2). To mimic this structure, each COOH-RhMOP must be connected to six neighboring COOH-RhMOPs through 24 Cu(II)-paddlewheel clusters. In this connectivity, each COOH-RhMOP is bridged to a neighboring COOH-RhMOP via four Cu(II)-paddlewheel clusters (Figure 2, yellow inset). Each Cu(II)-paddlewheel cluster must then be connected to four other Cu(II) clusters, via coordination of two btc linkers to their two remaining adjacent positions (Figure 2, violet inset). Overall, this connectivity defines a Cu(II)-cluster/btc/COOH-RhMOP ratio of 12:8:1. This connectivity also defines the relative position of each metal ion within the HKUST-1 network. Thus, RhCu-btc-HKUST-1 would present two types of cuboctahedral cavities in its structure: the Rh(II)-based cavity that derives from the prefabricated cavity, and a mixed-metal cavity containing Cu(II) and Rh(II) ions generated upon the self-assembly reaction. These cavities alternate throughout the structure (Figure S1). This degree of control over the relative position of cavities that contain different functionalities within porous frameworks has only been demonstrated for mixed-cage porous solids, in which different MOPs are co-precipitated.[28−30]

We began the synthesis of RhCu-btc-HKUST-1, whose formula is [COOH-RhMOP(Cu)$_{24}$(btc)$_8$], by heating a mixture of COOH-RhMOP with 24 mol equiv of Cu(NO$_3$)$_2$·3H$_2$O and 8 mol equiv of btc in *N*,*N*-dimethylformamide (DMF) at 85 °C for 1 day. The solvothermal reaction yielded a colloidal green dispersion. A green crystalline solid (yield: 78%; Figure 3a) was then isolated through centrifugation, washed with DMF, methanol, water, and acetone, and then dried at room temperature. Field emission scanning electron microscopy (FESEM) analysis of the green

https://doi.org/10.1021/jacs.2c06131
J. Am. Chem. Soc. 2022, 144, 15745−15753

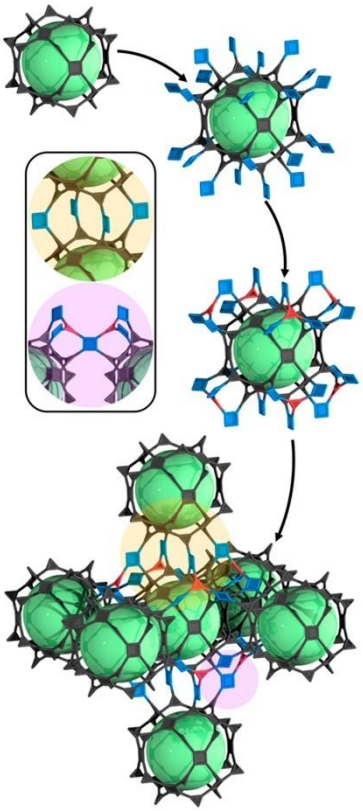

Figure 2. Schematic of the connectivity of COOH-RhMOPs (dark gray cages), Cu(II)-paddlewheel clusters (blue squares), and btc linkers (red triangles) to form RhCu-btc-HKUST-1. The inset details the connectivity between two COOH-RhMOPs.

solid revealed the formation of a uniform sample comprising particles having an average size of 22 ± 3 nm (Figure S2). Energy-dispersive X-ray spectroscopy performed on these single particles using high-resolution transmission electron microscopy corroborated the presence of both Rh and Cu in each tested particle (Figure S3). Moreover, the oxidation states of both Rh and Cu were found to be +2 through X-ray photoelectron spectroscopy (Figure S4). Inductively coupled

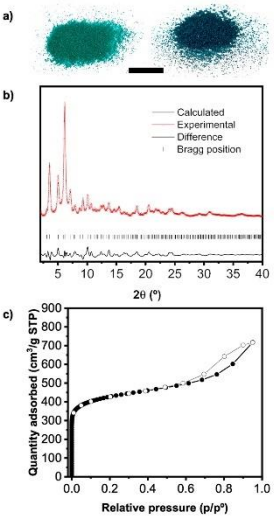

Figure 3. (a) Photographs of as-made (left) and activated (right) RhCu-btc-HKUST-1 powder. Scale bar: 1 cm. (b) Rietveld analysis of RhCu-btc-HKUST-1. (c) N_2-sorption isotherms for RhCu-btc-HKUST-1.

plasma-mass spectrometry (ICP-MS) measurements performed in acid-digested samples revealed that the Cu/Rh ratio was 1.02 ± 0.02, in agreement with the expected ratio in RhCu-btc-HKUST-1.

Synchrotron powder X-ray diffraction (PXRD) data collected on RhCu-btc-HKUST-1 revealed a pattern nearly coincidental with that of the parent Cu(II)-based HKUST-1 (Figure S5), with only slight shifts in the position of the peaks attributable to small differences in lattice parameters. Starting with the reported HKUST-1 atomic positions in the cubic $Fmm\bar{3}m$ space group, a satisfactory Rietveld refinement was reached (Rp = 3.32%, Rwp = 4.68%), corresponding to a structure in which Rh(II) and Cu(II) atoms each occupy 50% of the crystallographic metal site in the paddlewheel clusters (Figure 3b and Table S1). This refinement demonstrated that RhCu-btc-HKUST-1 is isoreticular to HKUST-1, having the same network type. While the metal atoms in RhCu-btc-HKUST-1 are located at topologically and symmetrically equivalent positions, their framework distribution in the MBBs is directed by using COOH-RhMOP. In addition, pair distribution function analyses of synchrotron X-ray scattering data showed the uniquely occurrence of Cu···Cu and Rh···Rh distances, thereby demonstrating the lack of hetero-bimetallic paddlewheel clusters in RhCu-btc-HKUST-1 (Figures S6 and S7).

https://doi.org/10.1021/jacs.2c06131
J. Am. Chem. Soc. 2022, 144, 15745−15753

To further confirm the MOP-guided assembly of RhCu-btc-HKUST-1, we ran a series of control experiments (see the Supporting Information (SI)). Initially, we corroborated the stability of COOH-RhMOP under the reaction conditions (DMF, 85 °C, 1 day) by ^{1}H NMR, UV−vis, and mass spectrometry (Figures S9−S11). Then, we ran three blank reactions under the above conditions but lacking one of the three MBBs. As expected, we did not observe the formation of RhCu-btc-HKUST-1 in any of those reactions. Specifically, the reaction of Cu(II) and btc yielded microcrystals of the expected parent, Cu(II)-HKUST-1. The reaction of COOH-RhMOP with btc produced a clear green solution without any precipitate. This result further confirms that there is no leaching of Rh(II) ions from COOH-RhMOP; as these eventual leached Rh(II) ions would react with btc to yield an extended coordination polymer.[26] Finally, the reaction of COOH-RhMOP with Cu(II) yielded an amorphous coordination polymer. Additionally, we reacted preformed Cu(II)-HKUST-1 crystals with COOH-RhMOP in a mixture containing the same molar ratio of Cu(II)-cluster/btc/COOH-RhMOP as that (12:8:1) used for the synthesis of RhCu-btc-HKUST-1. Under these conditions, we did not observe the formation of RhCu-btc-HKUST-1 crystals (Figure S12). This experiment demonstrates that the reaction mechanism cannot proceed through an initial formation of Cu(II)-HKUST-1 crystals that evolve through solubilization−recrystallization toward the formation of RhCu-btc-HKUST-1. We reasoned that, conversely, the most plausible scenario is that the presence of the COOH-RhMOP rapidly nucleates the formation of RhCu-btc-HKUST-1, thereby suppressing the formation of Cu(II)-HKUST-1.

We confirmed the presence of COOH-RhMOP cavities and btc linkers within the structure of RhCu-btc-HKUST-1 through solid-state cross-polarized/magic angle spinning (CP/MAS) ^{13}C NMR (Figure S13). To quantify the molar ratio between the prefab cavities and the added btc linkers, we developed a methodology to revert the assembly process into its initial components, which we identified and then quantified (Figures S14−S17). This was based on the high chemical stability of COOH-RhMOP. Upon exposing a DMF dispersion of RhCu-btc-HKUST-1 crystals to acidic conditions (see SI), we found that they become fully redissolved. ^{1}H NMR (DMF-d_7) of the resulting solution revealed a btc/COOH-RhMOP ratio of 8:1, in agreement with the ratio expected in RhCu-btc-HKUST-1 (Figure S16). We were able to quantify the amount of liberated COOH-RhMOP by UV−vis spectroscopy. From this experiment, we calculated a concentration of 93.3 μmol COOH-RhMOP/g of RhCu-btc-HKUST-1, which is very close to the theoretical value (94.2) (Figure S17 and Table S2). Altogether, our results confirmed the formation of RhCu-btc-HKUST-1 without significant defects and that COOH-RhMOP remains intact during its synthesis.

Next, we performed N_2-sorption measurements on activated RhCu-btc-HKUST-1 at 77 K, finding that it is microporous to N_2, with a BET surface area (S_{BET}) of 1606 m^2/g (Figure 3c, Figure S18). Furthermore, pore-size distribution analysis revealed the presence of the three characteristic cavities of the HKUST-1 structure together with some mesoporosity, which we ascribed to the interparticle voids (Figure S20). This extrinsic porosity is also responsible for the increased uptake at high pressure ($P/P_0 \approx 0.6$) and the observed hysteresis loop, as previously observed for other nanoscopic MOFs.[31] PXRD diffractogram recorded after these sorption studies confirmed that the RhCu-btc-HKUST-1 had retained its crystallinity (Figure S21).

Hydrolytic Stability of RhCu-btc-HKUST-1. We reasoned that the presence of the water-stable COOH-RhMOP cavity within RhCu-btc-HKUST-1 could confer the overall structure with greater hydrolytic stability relative to the parent Cu(II)-HKUST-1. To test this hypothesis, we incubated RhCu-btc-HKUST-1 and the parent Cu(II)-HKUST-1 in liquid water at room temperature from 1 to 31 days. The water-incubated samples were then characterized through FESEM, PXRD, and N_2 sorption. To our surprise, RhCu-btc-HKUST-1 had retained its morphology, crystallinity, composition, and porosity, even after 1 month of incubation in liquid water (Figure 4a,b, Figures S23 and S30−S35). Conversely, upon exposure to water, the parent Cu(II)-HKUST-1 had undergone the well-reported phase change, with a corresponding loss of porosity from 1888 to 502 m^2/g within the first day (Figures S24−S29).[32]

The hydrolytic stability that we observed for RhCu-btc-HKUST-1 implies that not only the COOH-RhMOP cavities,

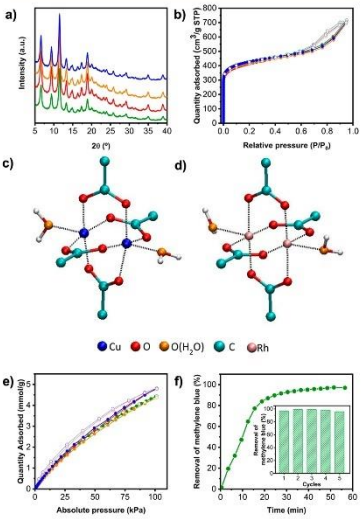

Figure 4. (a) PXRD diffractogram and (b) N_2-sorption isotherms for RhCu-btc-HKUST-1 initially (green) and after incubation in water for 3 (red), 14 (orange), and 31 days (blue). Snapshots (orthographic views) of the optimized DFT structures of (c) Cu(II)- and (d) Rh(II)-paddlewheel clusters in water. (e) CO_2-sorption isotherms at 298 K for RhCu-btc-HKUST-1 initially (green) and after incubation in water for 3 days (red), 14 days (orange), and 31 days (blue). (f) Removal of MB in water by RhCu-btc-HKUST-1 as a function of time. Inset: five consecutive MB-removal/regeneration cycles using RhCu-btc-HKUST-1.

https://doi.org/10.1021/jacs.2c06131
J. Am. Chem. Soc. 2022, 144, 15745−15753

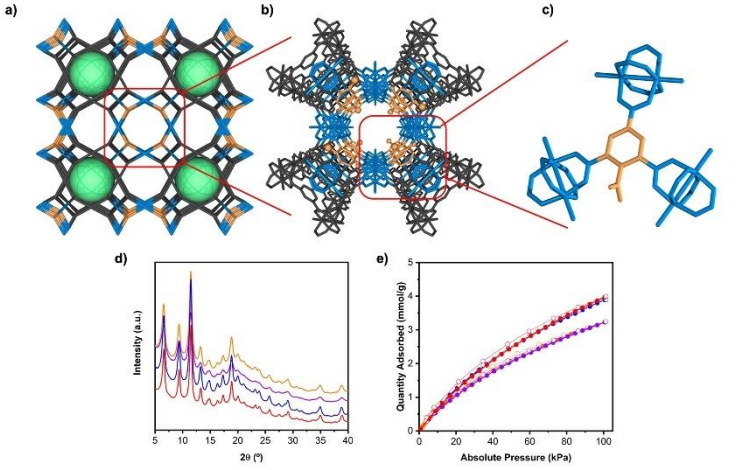

Figure 5. (a) Schematic of the four-component HKUST-1 analogues, showing the three types of channels that are generated when the COOH-RhMOP (structure depicted in gray and cavity depicted in green) is co-assembled with Cu(II) paddlewheels (blue) and (functionalized) btc linkers (orange). (b) Highlight of the chemical structure of the 1D channel decorated exclusively with functionalized btc linkers. (c) Highlight of the coordination environment of the (COOH)btc linker within the channels of RhCu-(COOH)btc-HKUST-1. (d) PXRD diffractogram of RhCu-(NH_2)btc-HKUST-1 (blue), RhCu-(NO_2)btc-HKUST-1 (orange), RhCu-(Br)btc-HKUST-1 (purple), and RhCu-(COOH)btc-HKUST-1 (red). (e) CO_2-adsorption isotherms at 298 K for RhCu-(NH_2)btc-HKUST-1 (blue), RhCu-(NO_2)btc-HKUST-1 (orange), RhCu-(Br)btc-HKUST-1 (purple), and RhCu-(COOH)btc-HKUST-1 (red).

but also the Cu(II)-carboxylate bonds that link them, withstand the incubation in water. Thus, in an effort to rationalize the higher hydrolytic stability of RhCu-btc-HKUST-1, we performed electronic structure calculations in water of both Cu(II)- and Rh(II)-paddlewheel clusters (Figure 4c,d). For this, we employed Gaussian 16[33] at the M06-L/SDD level of theory[34] in the presence of implicit water solvent modeled with the IEFPCM formalism, as described in the SI.[35] Our implicit solvent calculations showed that the Cu(II)-paddlewheel undergoes a significant torsion when exposed to water, whereas the Rh(II)-paddlewheel remains stable (Figures S36–S38). This torsion is enhanced after coordination of a water molecule to the axial position of Cu(II) (Figure 4c, Figures S39–S41), disrupting the original symmetrical bidentate binding with carboxylate ligands (Figure S42). We propose that Cu(II)-paddlewheels are hydrolyzed through this mechanical distortion as pivotal step, provoking the instability of the parent Cu(II)-HKUST-1. In the case of RhCu-btc-HKUST-1, each Cu(II)-paddlewheel is connected to two Rh(II)-paddlewheel clusters, which are not altered by water. The inertness of the Rh(II)-paddlewheel blocks the mechanical instability of the neighboring Cu(II)-paddlewheel, thereby inhibiting the hydrolysis process.

We envisioned that the stability of RhCu-btc-HKUST-1 could enable its use as an adsorbent in aqueous environments or after aqueous exposure. As a proof of concept, we evaluated the CO_2 adsorption capacity of RhCu-btc-HKUST-1 after being incubated in water for up to 31 days. As observed in Figure 4e, CO_2 uptake capacity did not decrease after the incubation. Additionally, we tested the adsorption capabilities of RhCu-btc-HKUST-1 in liquid water. To this end, we incubated RhCu-btc-HKUST-1 in an aqueous solution of methylene blue (MB) at 20 ppm (pH = 7) and then monitored the decrease of MB over 1 h. We found that, after 51 min, 97% of the MB had been removed by the RhCu-btc-HKUST-1 (Figure 4f). Moreover, after the MB-adsorption, the RhCu-btc-HKUST-1 fully retained its crystallinity (Figure S44). This contrasts sharply to the case of its parent, Cu(II)-HKUST-1, which, in the same amount of time, could adsorb 62% of the MB, due to its degradation and amorphization in water (Figures S43 and S45). To explore the MB-removal performance of each analogue after reutilization, we tested them over five consecutive removal/regeneration cycles. The removal step was identical to the one followed above. The regeneration step entailed the recovery of the adsorbent through centrifugation, followed by successive washings with water and acetone. Finally, the adsorbent was activated at 85 °C under vacuum for 1 h. The results showed that uptakes of RhCu-btc-HKUST-1 were similar among the five cycles (Figure 4f, inset), meaning that it had remained stable and that the regeneration was sufficient to maintain its removal capacity. Contrariwise, under these conditions, the MB-

https://doi.org/10.1021/jacs.2c06131
J. Am. Chem. Soc. 2022, 144, 15745−15753

removal capacity of Cu(II)-HKUST-1 dropped from 62% to ~10% (from the second to third cycles), and then to ~3−4% (for the fourth and fifth cycles) (Figure S43). Thus, the difference in MB-removal performance between RhCu-btc-HKUST-1 and Cu(II)-HKUST-1 only widened after reutilization, suggesting a new mechanism for stabilization of Cu(II) paddlewheel clusters based on the mechanical interlock between Rh(II) and Cu(II) paddlewheels, which results in water-resistant adsorbents.

Reticulation of Varied Linkers into the HKUST-1 Structure via Prefabricated Cavity-Directed Synthesis. We envisaged that our prefabricated cavity strategy would provide access to four-component HKUST-1 analogues, given the possibility to differentiate the btc linkers that form the COOH-RhMOP from those that bridge the Cu(II)-paddlewheel clusters, during the synthesis. However, we reasoned that such four-component analogues would require a functionalized btc linker, rather than the previously used btc linker. In this new configuration, the connectivity of the prefabricated COOH-RhMOP cavity dictates that the added functionalized btc linkers will be located on top of the triangular windows that connect three Cu(II) paddlewheels. These positions align into 1D channels, thus generating four-component HKUST-1 analogues in which alternating functionalized and non-functionalized 1D channels coexist (Figure 5a). This scenario differs from the outcome obtained when linkers with the same connectivity but different side functionalities are combined to generate isoreticular frameworks. In this latter case, one generally obtains structures in which the different linkers are randomly distributed or are organized into a non-atomically precise pattern.[36]

Based on the prefab cavity-induced desymmetrization of the organic linkers within the HKUST-1 network, we attempted the synthesis of four-component HKUST-1 analogues, using btc linkers having a pendant functional group [(Br)btc, (NO_2)btc and (NH_2)btc] at the second position of the phenylic ring as one of the reagents. Thus, we followed a synthetic strategy identical to the one that we had used for RhCu-btc-HKUST-1, except that we substituted the non-functionalized btc linker with either (Br)btc, (NO_2)btc or (NH_2)btc to generate RhCu-(Br)btc-HKUST-1, RhCu-(NO_2)btc-HKUST-1, and RhCu-(NH_2)btc-HKUST-1, respectively. The three reactions afforded green crystalline samples composed of particles with an average size of 24 ± 2 nm, for RhCu-(Br)btc-HKUST-1 (yield: 82%); 23 ± 2 nm, for RhCu-(NO_2)btc-HKUST-1 (yield: 78%); and 21 ± 3 nm, for RhCu-(NH_2)btc-HKUST-1 (yield: 74%) (Figures S46, S53, and S60).

Next, we characterized RhCu-(Br)btc-HKUST-1, RhCu-(NO_2)btc-HKUST-1, and RhCu-(NH_2)btc-HKUST-1 by PXRD, finding that their patterns matched the one that we had previously obtained for RhCu-btc-HKUST-1 (Figure 5d). ICP-MS on fully digested RhCu-(Br)btc-HKUST-1, RhCu-(NO_2)btc-HKUST-1, and RhCu-(NH_2)btc-HKUST-1 gave Cu/Rh molar ratios of 1.16 ± 0.01, 1.10 ± 0.01, and 1.09 ± 0.02, respectively. These values are in good agreement with the value (1) expected for their molecular formula. Moreover, ^{1}H NMR signals of the digested materials showed btc/(Br)btc, btc/(NO_2)btc, and btc/(NH_2)btc ratios of 8:1, also in perfect agreement with the expected ratio according to their formula (Figures S48, S55, and S62).

We measured the porosity of RhCu-(Br)btc-HKUST-1, RhCu-(NO_2)btc-HKUST-1, and RhCu-(NH_2)btc-HKUST-1 in N_2-sorption experiments, finding S_{BET} values of 1215, 1133, and 1212 m^2/g, respectively (Figures S49, S56, and S63). In all cases, PXRD diagrams collected after the sorption studies also confirmed their stability (Figures S51, S58, and S65). All these S_{BET} values are lower than the S_{BET} value for RhCu-btc-HKUST-1. We ascribed their inferior porosity to steric hindrance of the side groups located within the pores—a feature common to many other MOFs, such as those of the UiO-66 family.[37] Whereas N_2-sorption isotherms at 77 K accounted for the steric hindrance of the functional groups introduced into these four-component HKUST-1 analogues, CO_2-adsorption measured at 298 K highlighted their different affinities toward CO_2. Thus, the presence of free amine groups in RhCu-(NH_2)btc-HKUST-1 made it a better adsorbent for CO_2 than its Br or NO_2 analogues (Figure 5e).

COOH-Functionalized HKUST-1 Analogue. Having observed the structure-directing properties of the COOH-RhMOP prefabricated cavity on the synthesis of multicomponent HKUST-1 analogues, we envisaged that it could be employed to reticulate tetracarboxylate linkers to functionalize the HKUST-1 architecture with free carboxylic acid groups. Thus, we employed 1,2,3,5-benzenetetracarboxylic acid (hereafter named (COOH)btc) as the organic MBB in the co-assembly of COOH-RhMOP with Cu(II) paddlewheels to yield RhCu-(COOH)btc-HKUST-1 (Figure 5b,c). The solvothermal reaction between COOH-RhMOP, $Cu(NO_3)_2 \cdot 3H_2O$, and (COOH)btc afforded a green crystalline sample made of particles of an average size of 20 ± 3 nm (yield: 65%) (Figure S67). PXRD analysis of RhCu-(COOH)btc-HKUST-1 revealed a pattern consistent with RhCu-btc-HKUST-1 (Figure 5d). The successful reticulation of (COOH)btc within the HKUST-1 network was confirmed by the ^{1}H NMR spectrum of the acid-digested sample, which showed a btc/(COOH)btc ratio of 8:1 (Figure S69). The thermally activated sample retained its crystallinity (Figure S72), which enabled measurement of its gas sorption, for which an S_{BET} of 1380 m^2/g (Figure S70) and a CO_2 uptake (at 298 K and 1 bar) of 4.0 mmol/g were found (Figure 5e).

To further confirm that RhCu-(COOH)btc-HKUST-1 contained free carboxylic acid groups within its channels, we performed a series of spectroscopic characterizations. First, ICP measurements performed on the acid-digested sample revealed that the Cu:Rh molar ratio was 0.94. The fact that there is no excess of Cu(II) ions in the HKUST-1 structure suggests that only three of the four COOH groups of the (COOH)btc are coordinated to Cu(II) ions. Next, infrared spectroscopy performed on RhCu-(COOH)btc-HKUST-1 showed a clear vibration band at 1702 cm^{-1}, which we ascribed to the stretching band of C═O, which indicates the presence of uncoordinated carboxylic acid groups (Figure S73). Altogether, our results illustrate that our prefabricated-cavity approach can be employed to restrict the connectivity of polycarboxylate linkers to introduce free carboxylic acid groups into multicomponent isoreticular structures. Accordingly, this approach enabled the synthesis of a COOH-functionalized HKUST-1 analogue without generation of any defective structures.[38,39]

Finally, as a proof-of-concept, we aimed to demonstrate that the carboxylic acid groups located within the RhCu-(COOH)-btc-HKUST-1 structure are functional and accessible. To this end, we evaluated the behavior of RhCu-(COOH)btc-HKUST-1 as catalyst in a model acid-catalyzed reaction: the conversion of benzaldehyde dimethyl acetal to benzalde-

https://doi.org/10.1021/jacs.2c06131
J. Am. Chem. Soc. 2022, 144, 15745−15753

hyde.[40,41] We observed that, under identical conditions, RhCu-(COOH)btc-HKUST-1 could convert up to 64% of benzaldehyde dimethyl acetal into benzaldehyde, whereas non-functionalized RhCu-btc-HKUST-1 only afforded 32% conversion (Figure S74). Considering that the acidic groups of RhCu-btc-HKUST-1 can only be located at its surface, we ascribed the superior conversion obtained with RhCu-(COOH)btc-HKUST-1 to the activity of the inner carboxylic acid groups, which would confirm their accessibility. Importantly, both RhCu-btc-HKUST-1 and RhCu-(COOH)-btc-HKUST-1 fully retained their crystallinity after the acid catalysis (Figure S75).

■ CONCLUSIONS

We have presented an alternative methodology to synthesize multicomponent MOFs, which is based on the co-assembly of prefabricated cavities (in the form of carboxylic acid-functionalized MOPs) and small MBBs. The methodology benefits from the structure-directing influence of the MOP to organize varied organic and metallic MBBs through the crystal lattice of the targeted MOF, thus providing a greater degree of control over the synthesis of atomically precise multicomponent MOFs.

■ ASSOCIATED CONTENT

Supporting Information

The Supporting Information is available free of charge at https://pubs.acs.org/doi/10.1021/jacs.2c06131.

Detailed syntheses, FESEM data and images, PXRD diffractogram, XPS, UV−vis, and NMR, as well as porosity measurements, including Figures S1−S75 and Tables S1−S3 (PDF)

■ AUTHOR INFORMATION

Corresponding Authors

Arnau Carné-Sánchez − *Catalan Institute of Nanoscience and Nanotechnology (ICN2), CSIC, Barcelona Institute of Science and Technology, 08193 Bellaterra, Barcelona, Spain; Departament de Química, Facultat de Ciències, Universitat Autònoma de Barcelona, 08193 Bellaterra, Spain;* orcid.org/0000-0002-8569-6208; Email: arnau.carne@icn2.cat

Daniel Maspoch − *Catalan Institute of Nanoscience and Nanotechnology (ICN2), CSIC, Barcelona Institute of Science and Technology, 08193 Bellaterra, Barcelona, Spain; Departament de Química, Facultat de Ciències, Universitat Autònoma de Barcelona, 08193 Bellaterra, Spain; ICREA, 08010 Barcelona, Spain;* orcid.org/0000-0003-1325-9161; Email: daniel.maspoch@icn2.cat

Authors

Akim Khobotov-Bakishev − *Catalan Institute of Nanoscience and Nanotechnology (ICN2), CSIC, Barcelona Institute of Science and Technology, 08193 Bellaterra, Barcelona, Spain; Departament de Química, Facultat de Ciències, Universitat Autònoma de Barcelona, 08193 Bellaterra, Spain*

Cornelia von Baeckmann − *Catalan Institute of Nanoscience and Nanotechnology (ICN2), CSIC, Barcelona Institute of Science and Technology, 08193 Bellaterra, Barcelona, Spain; Departament de Química, Facultat de Ciències, Universitat Autònoma de Barcelona, 08193 Bellaterra, Spain*

Borja Ortín-Rubio − *Catalan Institute of Nanoscience and Nanotechnology (ICN2), CSIC, Barcelona Institute of Science and Technology, 08193 Bellaterra, Barcelona, Spain; Departament de Química, Facultat de Ciències, Universitat Autònoma de Barcelona, 08193 Bellaterra, Spain;* orcid.org/0000-0002-0533-3635

Laura Hernández-López − *Catalan Institute of Nanoscience and Nanotechnology (ICN2), CSIC, Barcelona Institute of Science and Technology, 08193 Bellaterra, Barcelona, Spain; Departament de Química, Facultat de Ciències, Universitat Autònoma de Barcelona, 08193 Bellaterra, Spain*

Alba Cortés-Martínez − *Catalan Institute of Nanoscience and Nanotechnology (ICN2), CSIC, Barcelona Institute of Science and Technology, 08193 Bellaterra, Barcelona, Spain; Departament de Química, Facultat de Ciències, Universitat Autònoma de Barcelona, 08193 Bellaterra, Spain*

Jordi Martínez-Esaín − *Catalan Institute of Nanoscience and Nanotechnology (ICN2), CSIC, Barcelona Institute of Science and Technology, 08193 Bellaterra, Barcelona, Spain;* orcid.org/0000-0002-8420-8559

Felipe Gándara − *Consejo Superior de Investigaciones Científicas (CSIC), Materials Science Institute of Madrid (ICMM), 28049 Madrid, Spain;* orcid.org/0000-0002-1671-6260

Judith Juanhuix − *ALBA Synchrotron, 08290 Cerdanyola del Valles, Barcelona, Spain;* orcid.org/0000-0003-3728-8215

Ana E. Platero-Prats − *Departamento de Química Inorgánica, Facultad de Ciencias, Universidad Autónoma de Madrid, 28049 Madrid, Spain; Condensed Matter Physics Center (IFIMAC), Universidad Autónoma de Madrid, 28049 Madrid, Spain;* orcid.org/0000-0002-2248-2739

Jordi Faraudo − *Institut de Ciència de Materials de Barcelona (ICMAB-CSIC), 08193 Bellaterra, Spain;* orcid.org/0000-0002-6315-4993

Complete contact information is available at: https://pubs.acs.org/10.1021/jacs.2c06131

Notes

The authors declare no competing financial interest.

■ ACKNOWLEDGMENTS

This work was supported by the Spanish MINECO (project RTI2018-095622-B-I00), the Catalan AGAUR (project 2017 SGR 238), the CERCA Program/Generalitat de Catalunya, and the MCIN/AEI/10.13039/501100011033 and by the European Union "NextGenerationEU"/PRTR (EUR2020-112294). We also thank CESGA Supercomputing center for technical support and computer time at the supercomputer Finisterrae III. ICN2 and ICMAB are supported by the Severo Ochoa program from the Spanish MINECO (grants SEV-2017-0706 and CEX2019-000917-S). The project that gave rise to these results received the support of a fellowship (LCF/BQ/PR20/11770011) from "la Caixa" Foundation (ID 100010434). A.E.P.-P. acknowledges a Ramón y Cajal fellowship (RYC2018-024328-I). We acknowledge the Diamond Light Source, U.K., for the provision of synchrotron access to the beamline I15-1 (CY28079) and thank Dr. Philip Chater for his assistance with data collection.

REFERENCES

(1) Jiang, J.; Furukawa, H.; Zhang, Y.-B.; Yaghi, O. M. High Methane Storage Working Capacity in Metal-Organic Frameworks with Acrylate Links. *J. Am. Chem. Soc.* **2016**, *138*, 10244−10251.

(2) Hanikel, N.; Pei, X.; Chheda, S.; Lyu, H.; Jeong, W.; Sauer, J.; Gagliardi, L.; Yaghi, O. M. Evolution of water structures in metal-organic frameworks for improved atmospheric water harvesting. *Science* **2021**, *374*, 454−459.

(3) Liu, Q.; Cong, H.; Deng, H. Deciphering the Spatial Arrangement of Metals and Correlation to Reactivity in Multivariate Metal-Organic Frameworks. *J. Am. Chem. Soc.* **2016**, *138*, 13822−13825.

(4) Feng, L.; Wang, K.-Y.; Day, G. S.; Zhou, H.-C. The Chemistry of Multi-Component and Hierarchical Framework Compounds. *Chem. Soc. Rev.* **2019**, *48*, 4823−4853.

(5) Deng, H.; Doonan, C. J.; Furukawa, H.; Ferreira, R. B.; Towne, J.; Knobler, C. B.; Wang, B.; Yaghi, O. M. Multiple Functional Groups of Varying Ratios in Metal-Organic Frameworks. *Science* **2010**, *327*, 846−850.

(6) Ji, Z.; Li, T.; Yaghi, O. M. Sequencing of Metals in Multivariate Metal-Organic Frameworks. *Science* **2020**, *369*, 674−680.

(7) Liu, L.; Konstas, K.; Hill, M. R.; Telfer, S. G. Programmed Pore Architectures in Modular Quaternary Metal-Organic Frameworks. *J. Am. Chem. Soc.* **2013**, *135*, 17731−17734.

(8) Muldoon, P. F.; Liu, C.; Miller, C. C.; Koby, S. B.; Gamble Jarvi, A.; Luo, T.-Y.; Saxena, S.; O'Keeffe, M.; Rosi, N. L. Programmable Topology in New Families of Heterobimetallic Metal-Organic Frameworks. *J. Am. Chem. Soc.* **2018**, *140*, 6194−6198.

(9) Matsunaga, S.; Hasada, K.; Sugiura, K.; Kitamura, N.; Kudo, Y.; Endo, N.; Mori, W. Hetero Bi-Paddle-Wheel Coordination Networks: A New Synthetic Route to Rh-Containing Metal-Organic Frameworks. *Bull. Chem. Soc. Jpn.* **2012**, *85*, 433−438.

(10) Gao, W.-Y.; Sur, A.; Wang, C.-H.; Lorzing, G. R.; Antonio, A. M.; Taggart, G. A.; Ezazi, A. A.; Bhuvanesh, N.; Bloch, E. D.; Powers, D. C. Atomically Precise Crystalline Materials Based on Kinetically Inert Metal Ions via Reticular Mechanopolymerization. *Angew. Chem. Int. Ed.* **2020**, *59*, 10878−10883.

(11) Fracaroli, A. M.; Siman, P.; Nagib, D. A.; Suzuki, M.; Furukawa, H.; Toste, F. D.; Yaghi, O. M. Seven Post-Synthetic Covalent Reactions in Tandem Leading to Enzyme-like Complexity within Metal-Organic Framework Crystals. *J. Am. Chem. Soc.* **2016**, *138*, 8352−8355.

(12) Yuan, S.; Qin, J.-S.; Li, J.; Huang, L.; Feng, L.; Fang, Y.; Lollar, C.; Pang, J.; Zhang, L.; Sun, D.; Alsalme, A.; Cagin, T.; Zhou, H.-C. Retrosynthesis of Multi-Component Metal-organic Frameworks. *Nat. Commun.* **2018**, *9*, 808.

(13) Yuan, S.; Lu, W.; Chen, Y.-P.; Zhang, Q.; Liu, T.-F.; Feng, D.; Wang, X.; Qin, J.; Zhou, H.-C. Sequential Linker Installation: Precise Placement of Functional Groups in Multivariate Metal-Organic Frameworks. *J. Am. Chem. Soc.* **2015**, *137*, 3177−3180.

(14) Kim, M.; Cahill, J. F.; Fei, H.; Prather, K. A.; Cohen, S. M. Postsynthetic Ligand and Cation Exchange in Robust Metal-Organic Frameworks. *J. Am. Chem. Soc.* **2012**, *134*, 18082−18088.

(15) Yaghi, O. M.; Kalmutzki, M. J.; Diercks, C. S. *Introduction to Reticular Chemistry: Metal-Organic Frameworks and Covalent Organic Frameworks*; John Wiley and Sons, 2019; pp 1−27.

(16) Eddaoudi, M.; Moler, D. B.; Li, H.; Chen, B.; Reineke, T. M.; O'Keeffe, M.; Yaghi, O. M. Modular Chemistry: Secondary Building Units as a Basis for the Design of Highly Porous and Robust Metal-Organic Carboxylate Frameworks. *Acc. Chem. Res.* **2001**, *34*, 319−330.

(17) Chui, S. S.-Y.; Lo, S. M.-F.; Charmant, J. P. H.; Orpen, A. G.; Williams, I. D. A Chemically Functionalizable Nanoporous Material $[Cu_3(TMA)_2(H_2O)_3]n$. *Science* **1999**, *283*, 1148−1150.

(18) Eubank, J. F.; Mouttaki, H.; Cairns, A. J.; Belmabkhout, Y.; Wojtas, L.; Luebke, R.; Alkordi, M.; Eddaoudi, M. The Quest for Modular Nanocages: Tbo -MOF as an Archetype for Mutual Substitution, Functionalization, and Expansion of Quadrangular Pillar Building Blocks. *J. Am. Chem. Soc.* **2011**, *133*, 14204−14207.

(19) Belmabkhout, Y.; Mouttaki, H.; Eubank, J. F.; Guillerm, V.; Eddaoudi, M. Effect of Pendant Isophthalic Acid Moieties on the Adsorption Properties of Light Hydrocarbons in HKUST-1-like Tbo-MOFs: Application to Methane Purification and Storage. *RSC Adv.* **2014**, *4*, 63855−63859.

(20) Eddaoudi, M.; Kim, J.; Wachter, J. B.; Chae, H. K.; O'Keeffe, M.; Yaghi, O. M. Porous Metal-Organic Polyhedra: 25 Å Cuboctahedron Constructed from 12 $Cu_2(CO_2)_4$ Paddle-Wheel Building Blocks. *J. Am. Chem. Soc.* **2001**, *123*, 4368−4369.

(21) Kim, D.; Liu, X.; Lah, M. S. Topology Analysis of Metal-Organic Frameworks Based on Metal-Organic Polyhedra as Secondary or Tertiary Building Units. *Inorg. Chem. Front.* **2015**, *2*, 336−360.

(22) Perry, J. J., IV; Perman, J. A.; Zaworotko, M. J. Design and Synthesis of Metal-Organic Frameworks Using Metal-Organic Polyhedra as Supermolecular Building Blocks. *Chem. Soc. Rev.* **2009**, *38*, 1400−1417.

(23) Nouar, F.; Eubank, J. F.; Bousquet, T.; Wojtas, L.; Zaworotko, M. J.; Eddaoudi, M. Supermolecular Building Blocks (SBBs) for the Design and Synthesis of Highly Porous Metal-Organic Frameworks. *J. Am. Chem. Soc.* **2008**, *130*, 1833−1835.

(24) Guillerm, V.; Kim, D.; Eubank, J. F.; Luebke, R.; Liu, X.; Adil, K.; Lah, M. S.; Eddaoudi, M. A Supermolecular Building Approach for the Design and Construction of Metal-Organic Frameworks. *Chem. Soc. Rev.* **2014**, *43*, 6141−6172.

(25) Grancha, T.; Carné-Sánchez, A.; Zarekarizi, F.; Hernández-López, L.; Albalad, J.; Khobotov, A.; Guillerm, V.; Morsali, A.; Juanhuix, J.; Gándara, F.; Imaz, I.; Maspoch, D. Synthesis of polycarboxylate rhodium(II) metal-organic polyhedra (MOPs) and their use as building blocks for highly connected Metal-Organic Frameworks (MOFs). *Angew. Chem., Int. Ed.* **2021**, *60*, 5729−5733.

(26) Albalad, J.; Carné-Sánchez, A.; Grancha, T.; Hernández-López, L.; Maspoch, D. Protection Strategies for Directionally-Controlled Synthesis of Previously Inaccessible Metal-Organic Polyhedra (MOPs): The Cases of Carboxylate- and Amino-Functionalised Rh(II)-MOPs. *Chem. Commun.* **2019**, *55*, 12785−12788.

(27) Furukawa, S.; Horike, N.; Kondo, M.; Hijikata, Y.; Carné-Sánchez, A.; Larpent, P.; Louvain, N.; Diring, S.; Sato, H.; Matsuda, R.; Kawano, R.; Kitagawa, S. Rhodium-Organic Cuboctahedra as Porous Solids with Strong Binding Sites. *Inorg. Chem.* **2016**, *55*, 10843−10846.

(28) Gosselin, A. J.; Decker, G. E.; Antonio, A. M.; Lorzing, G. R.; Yap, G. P. A.; Bloch, E. D. A Charged Coordination Cage-Based Porous Salt. *J. Am. Chem. Soc.* **2020**, *142*, 9594−9598.

(29) Markwell-Heys, A. W.; Roemelt, M.; Slattery, A. D.; Linder-Patton, O. M.; Bloch, W. M. Linking metal−organic cages pairwise as a design approach for assembling multivariate crystalline materials. *Chem. Sci.* **2021**, *13*, 68−73.

(30) Nam, D.; Kim, J.; Hwang, E.; Nam, J.; Jeong, H.; Kwon, T.-H.; Choe, W. Multivariate Porous Platform Based on Metal-Organic Polyhedra with Controllable Functionality Assembly. *Matter* **2021**, *4*, 2460−2473.

(31) Liu, X.; Shen, Z.-Q.; Xiong, H.-H.; Chen, Y.; Wang, X.-N.; Li, H.-Q.; Li, Y.-T.; Cui, K.-H.; Tian, Y.-Q. Hierarchical porous materials based on nanoscale metal-organic frameworks dominated with permanent interparticle porosity. *Microporous Mesoporous Mater.* **2015**, *204*, 25−33.

(32) Majano, G.; Martin, O.; Hammes, M.; Smeets, S.; Baerlocher, C.; Pérez-Ramírez, J. Solvent-Mediated Reconstruction of the Metal-Organic Framework HKUST-1 ($Cu_3(BTC)_2$). *Adv. Funct. Mater.* **2014**, *24*, 3855−3865.

(33) Frisch, M. J.; Trucks, G. W.; Schlegel, H. B.; Scuseria, G. E.; Robb, M. A.; Cheeseman, J. R.; Scalmani, G.; Barone, V.; Petersson, G. A.; Nakatsuji, H.; Li, X.; Caricato, M.; Marenich, A. V.; Bloino, J.; Janesko, B. G.; Gomperts, R.; Mennucci, B.; Hratchian, H. P.; Ortiz, J. V.; Izmaylov, A. F.; Sonnenberg, J. L.; Williams-Young, D.; Ding, F.; Lipparini, F.; Egidi, F.; Goings, J.; Peng, B.; Petrone, A.; Henderson, T.; Ranasinghe, D.; Zakrzewski, V. G.; Gao, J.; Rega, N.; Zheng, G.; Liang, W.; Hada, M.; Ehara, M.; Toyota, K.; Fukuda, R.; Hasegawa, J.;

https://doi.org/10.1021/jacs.2c06131
J. Am. Chem. Soc. 2022, 144, 15745−15753

Ishida, M.; Nakajima, T.; Honda, Y.; Kitao, O.; Nakai, H.; Vreven, T.; Throssell, K.; Montgomery, J. A., Jr.; Peralta, J. E.; Ogliaro, F.; Bearpark, M. J.; Heyd, J. J.; Brothers, E. N.; Kudin, K. N.; Staroverov, V. N.; Keith, T. A.; Kobayashi, R.; Normand, J.; Raghavachari, K.; Rendell, A. P.; Burant, J. C.; Ivengar, S. S.; Tomasi, J.; Cossi, M.; Millam, J. M.; Klene, M.; Adamo, C.; Cammi, R.; Ochterski, J. W.; Martin, R. L.; Morokuma, K.; Farkas, O.; Foresman, J. B.; Fox, D. J. *Gaussian 16*, Revision B.01; Gaussian, Inc., Wallingford, CT, 2016.

(34) Zhao, Y.; Truhlar, D. G. The M06 Suite of Density Functionals for Main Group Thermochemistry, Thermochemical Kinetics, Noncovalent Interactions, Excited States, and Transition Elements: Two New Functionals and Systematic Testing of Four M06-Class Functionals and 12 Other Functionals. *Theor. Chem. Acc.* **2008**, *120*, 215−241.

(35) Tomasi, J.; Mennucci, B.; Cammi, R. Quantum Mechanical Continuum Solvation Models. *Chem. Rev.* **2005**, *105*, 2999−3094.

(36) Kong, X.; Deng, H.; Yan, F.; Kim, J.; Swisher, J. A.; Smit, B.; Yaghi, O. M.; Reimer, J. A. Mapping of Functional Groups in Metal-Organic Frameworks. *Science* **2013**, *341*, 882−885.

(37) Garibay, S. J.; Cohen, S. M. Isoreticular Synthesis and Modification of Frameworks with the UiO-66 Topology. *Chem. Commun.* **2010**, *46*, 7700−7702.

(38) Zhang, W.; Kauer, M.; Guo, P.; Kunze, S.; Cwik, S.; Muhler, M.; Wang, Y.; Epp, K.; Kieslich, G.; Fischer, R. A. Impact of Synthesis Parameters on the Formation of Defects in HKUST-1. *Eur. J. Inorg. Chem.* **2017**, *5*, 925−931.

(39) Steenhaut, T.; Grégoire, N.; Barozzino-Consiglio, G.; Filinchuk, Y.; Hermans, S. Mechanochemical Defect Engineering of HKUST-1 and Impact of the Resulting Defects on Carbon Dioxide Sorption and Catalytic Cyclopropanation. *RSC Adv.* **2020**, *10*, 19822−19831.

(40) Li, J.; Yang, X.; Ma, J.; Yuan, C.; Ren, Y.; Cheng, X.; Deng, Y. Controllable Multicomponent Co-Assembly Approach to Ordered Mesoporous Zirconia Supported with Well-Dispersed Tungsten Oxide Clusters as High-Performance Catalysts. *ChemCatChem* **2021**, *13*, 2863−2872.

(41) Robinson, M. W. C.; Graham, A. E. Mesoporous Aluminosilicate Promoted Protection and Deprotection of Carbonyl Compounds. *Tetrahedron Lett.* **2007**, *48*, 4727−4731.

https://doi.org/10.1021/jacs.2c06131
J. Am. Chem. Soc. 2022, 144, 15745−15753

Check for updates

Chemistry–A European Journal

Research Article
doi.org/10.1002/chem.202301945

Chemistry Europe
European Chemical Societies Publishing

www.chemeurj.org

Hot Paper

(Bio)Functionalisation of Metal–Organic Polyhedra by Using Click Chemistry

Laura Hernández-López,[a, b] Cornelia von Baeckmann,[a, b] Jordi Martínez-Esaín,[a] Alba Cortés-Martínez,[a, b] Jordi Faraudo,[c] Caterina Caules,[a, b] Teodor Parella,[d] Daniel Maspoch,*[a, b, e] and Arnau Carné-Sánchez*[a, b]

The surface chemistry of Metal–Organic Polyhedra (MOPs) is crucial to their physicochemical properties because it governs how they interact with external substances such as solvents, synthetic organic molecules, metal ions, and even biomolecules. Consequently, the advancement of synthetic methods that facilitate the incorporation of diverse functional groups onto MOP surfaces will significantly broaden the range of properties and potential applications for MOPs. This study describes the use of copper(I)-catalysed, azide–alkyne cycloaddition (CuAAC) click reactions to post-synthetically modify the surface of alkyne-functionalised cuboctahedral MOPs. To this end, a novel Rh(II)-based MOP with 24 available surface alkyne groups was synthesised. Each of the 24 alkyne groups on the surface of the "clickable" Rh-MOP can react with azide-containing molecules at room temperature, without compromising the integrity of the MOP. The wide substrate catalogue and orthogonal nature of CuAAC click chemistry was exploited to densely functionalise MOPs with diverse functional groups, including polymers, carboxylic and phosphonic acids, and even biotin moieties, which retained their recognition capabilities once anchored onto the surface of the MOP.

Introduction

As a subclass of molecular cages assembled from metal-ions and organic linkers, Metal–Organic Polyhedra (MOPs) exhibit unique porosity capabilities: for example, they can host molecules in solution and are permanently porous in the solid state. Importantly, most of these materials fall within the nanoscale regime, having outer diameters of ~2 nm to 5 nm. This is especially true for the archetypical cuboctahedral $[M_2(m\text{-bdc})_2]_{12}$ MOP (where *m*-bdc is isophthalate), which resembles a spherical ~2.5 nm-in-diameter molecular nanoparticle.[1] As such, as in inorganic nanoparticles, most of its physicochemical properties (e.g. solubility, recognition, and assembly) rely on its surface chemistry.[2–11] For instance, on its outer surface this cuboctahedral MOP contains up to 84 potential sites that can be used to introduce new functionalities: 72 that stem from positions 4, 5, and 6 of the aromatic organic linkers, and 12 that belong to the axial metal sites.

Among the existing functionalisation strategies, copper(I)-catalysed azide–alkyne cycloaddition (CuAAC), commonly known as click chemistry, is probably the most popular, powerful, and versatile chemical tool to post-synthetically modify molecules and materials.[12–14] This is mainly due to its quantitative and orthogonal reactivity, which makes it compatible with myriad functional groups and even biomolecules.[15,16] However, the straightforward use of CuAAC for the post-synthetic modification of MOPs presents several challenges due to the instability of coordination bonds to common click chemistry reagents (e.g., reducing agents and metal salts).[17] Therefore, researchers have developed alternative reaction conditions for the CuAAC reaction to avoid the use of reducing agents. These conditions involve the use of Cu(I) complexes as catalysts,[6] or of the strain-promoted version of the azide–alkyne cycloaddition, the latter of which has been employed for most partial modifications of parent cages.[18,19] Only very recently did Bloch and co-workers show that robust rectangular prismatic MOPs assembled from Co(II) calixarene-capped clusters and 5-azido isophthalic acid (5-N_3-bdc) or 5-propargyl isophthalic acid can withstand the reaction conditions of the classical CuAAC reaction.[20] Indeed, they reported the quantita-

[a] L. Hernández-López, Dr. C. von Baeckmann, Dr. J. Martínez-Esaín, A. Cortés-Martínez, C. Caules, Prof. Dr. D. Maspoch, Dr. A. Carné-Sánchez
Catalan Institute of Nanoscience and Nanotechnology (ICN2)
CSIC and The Barcelona Institute of Science and Technology
Campus UAB, Bellaterra, 08193 Barcelona (Spain)
E-mail: arnau.carne@icn2.cat
daniel.maspoch@icn2.cat

[b] L. Hernández-López, Dr. C. von Baeckmann, A. Cortés-Martínez, C. Caules, Prof. Dr. D. Maspoch, Dr. A. Carné-Sánchez
Departament de Química, Facultat de Ciencies
Universitat Autonoma de Barcelona, 08193 Bellaterra (Spain)

[c] Dr. J. Faraudo
Institut de Ciència de Materials de Barcelona (ICMAB-CSIC)
08193 Bellaterra (Spain)

[d] Dr. T. Parella
Servei de Ressonància Magnètica Nuclear
Universitat Autònoma de Barcelona
Campus UAB, Bellaterra, 08193 Barcelona (Spain)

[e] Prof. Dr. D. Maspoch
ICREA
Pg. Lluís Companys 23, 08010 Barcelona (Spain)

Supporting information for this article is available on the WWW under https://doi.org/10.1002/chem.202301945

tive conversion of 4 pendant alkyne or azide groups of the MOP through this reaction run at high temperature.

Herein we have adapted and optimised CuAAC to enable covalent functionalisation of up to 24 positions of cuboctahedral Rh-MOPs[21] with a diverse repertoire of molecules. To this end, we initially introduced an alkynyl group onto position 5 of the aromatic organic linker of a 24-functionalized cuboctahedral Rh-MOP through a protection/deprotection method,[22] forming a "clickable" Rh-MOP with formula $[Rh_{24}(ethynyl\text{-}bdc)_{24}]$ (hereafter named BCN-23; where ethynyl-bdc is 5-ethynyl-1,3-benzenedicarboxylate). Afterwards, we demonstrated that each of the 24 alkyne groups located on the outer surface of the cuboctahedron could be reacted at room temperature with azide-containing molecules without compromising the integrity of the MOP. Thus, we used click chemistry to quantitively and densely functionalise the surface of BCN-23 with a wide range of functionalities that could not otherwise be easily introduced (e.g. by direct synthesis or current post-synthetic approaches). These functionalities include polymers, free carboxylic acid groups, free phosphonic acid groups, and bioactive biotin molecules. Furthermore, we proved that addition of these functionalities modulates the properties (e.g. solubility) of BCN-23, and that the biorecognition capabilities of biotin moieties grafted onto the surface of BCN-23 to avidin are preserved.

Results and Discussion

Synthesis of the "clickable" alkyne-terminated Rh-MOP

Traditionally, cuboctahedral Rh-MOPs are synthesised through a solvothermal reaction between Rh_2Ac_4 and the corresponding linker. However, BCN-23 cannot be synthesised this way because the linker ethynyl-bdc is not stable at high temperatures or under basic conditions. Thus, we developed a protection-deprotection strategy that entailed the synthesis of the alkyne-protected Rh-MOP and its subsequent deprotection to finally yield the targeted clickable MOP (Figure 1). Triisopropylsilyl was selected as a protecting group because of its compatibility with the linker and the synthetic conditions required to make Rh-MOPs, including the use of high temperatures and basic conditions. Thus, after reacting dimethyl 5-iodoisophtalate with (triisopropylsilyl)acetylene and subsequently deprotecting the carboxylic groups, the protected version of ethynyl-bdc, 5-((triisopropylsilyl)ethynyl))isophthalic acid (TIPS-bdc), was obtained. Next, TIPS-bdc was reacted with Rh_2Ac_4 in DMA at 100 °C in the presence of Na_2CO_3 for 48 h to yield a MOP with formula $[Rh_{24}(TIPS\text{-}bdc)_{24}]$ (yield: 80%) (Figure 1a). The formation of the alkyne-protected Rh-MOP was confirmed by matrix-assisted laser desorption/ionisation-time-of-flight (MALDI-TOF) spectroscopy, which showed a signal at 11024.5 m/z, which closely agrees with the targeted cuboctahedral Rh(II)-MOP ($[Rh_{24}(TIPS\text{-}bdc)_{24}+H^+]^+ \cdot 2DMA \cdot 2MeOH$, expected m/z = 11024.9) (Figure S4). The ^1H NMR spectrum of the alkyne-protected MOP in $CDCl_3$-d_1 further confirmed the synthesis of a discrete metal–organic assembly with 24 triisopropylsilyl protecting groups on its surface ($\delta = 1.05$ ppm; Figure S1). Furthermore, diffusion-ordered spectroscopy (DOSY) NMR analysis showed the same diffusion coefficient of $3.7 \cdot 10^{-10}$ $m^2 s^{-1}$ for the aromatic and protecting group protons, which further corroborated that both moieties belong to the same metal–organic structure (Figure S2). The integrity of the Rh–Rh paddlewheel was confirmed through UV-Vis spectroscopy in chloroform, which showed the characteristic band centred at 630 nm, which corresponds to Band I of the Rh–Rh paddlewheel (Figure S4).

The alkyne-available Rh-MOP (BCN-23) was synthesised by treating a THF solution of the alkyne-protected MOP with 36 mol. equiv. of tetrabutylammonium fluoride (TBAF) solution (1.0 M in THF) (Figure 1b). Upon addition of the TBAF solution, a blue precipitate was immediately formed. This solid was collected by centrifugation, washed with THF and finally, dissolved in DMSO for further analysis (yield: > 95%). The ^1H NMR spectrum of BCN-23 in DMSO-d_6 confirmed the quantitative fading of the peaks ascribed to the TIPS protecting group, together with the appearance of a new signal at 4.3 ppm (Figure S5), which corresponds to the alkyne proton. The aromatic and alkyne protons showed the same diffusion coefficient of $6.5 \cdot 10^{-11}$ $m^2 s^{-1}$ in the DOSY ^1H NMR data (Figure S6). The hydrodynamic radius of BCN-23 was calculated to

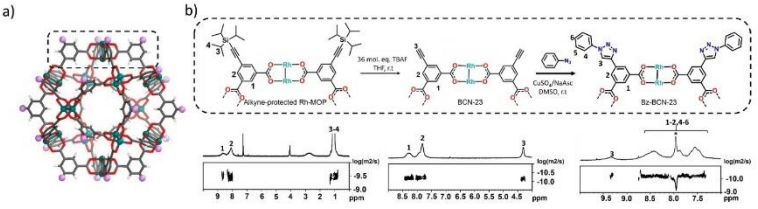

Figure 1. (a) Schematic of the cuboctahedral Rh-MOP, highlighting the positions at which the CuAAC click reaction is performed. (b) Schematic showing the synthesis of the "clickable" BCN-23 MOP, and its subsequent post-synthetic modification with azidobenzene through a CuAAC (top), with the corresponding ^1H-NMR spectra and DOSY NMR representation for each synthetic step (bottom). NMR data for the alkyne-protected Rh-MOP was obtained in $CDCl_3$-d_1 whereas the DMSO-d_6 was used for BCN-23 and Bz-BCN-23.

be approximately 1.7 nm, which agrees with the value obtained from the computer simulation of this structure (Figure S7).[18] MALDI-TOF analysis of BCN-23 was characterised by a single broad peak centred at 7061.6 m/z, which closely agrees with the expected mass of 7064.1 m/z for the targeted formula $[Rh_{24}(ethynyl\text{-}bdc)_{24}+H^+]^+\cdot DMSO$ (Figure S9). Additionally, the integrity of the Rh–Rh paddlewheel after the deprotection reaction was further confirmed by UV-Vis spectroscopy in DMF, which showed the characteristic band centred at 589 nm that corresponds to Band I of the Rh–Rh paddlewheel (Figure S9). Altogether, these results corroborate the successful synthesis of BCN-23 as a cuboctahedral Rh-MOP functionalised with 24 available alkyne groups on its outer surface.

CuAAC click reactions on BCN-23: functionalisation with small and polymeric azide molecules as model substrates

We initially assessed the reactivity and functionalisation of BCN-23 through CuAAC click chemistry using azidobenzene as our model azide compound. To this end, 36 mol. equiv. of azidobenzene per MOP unit (i.e. 1.5 mol. equiv. of azidobenzene per alkyne group) were added to a DMSO solution of BCN-23 followed by the stepwise addition of $CuSO_4$ (1.5 mol. equiv. per alkynyl group) and sodium ascorbate (4.5 mol. equiv. per alkynyl group, 3 mol. equiv. per Cu(II)). The reaction mixture was left to react overnight at room temperature. The reaction proceeded under homogenous conditions: no precipitate was observed throughout the reaction. The product of the reaction (hereafter named Bz-BCN-23) was precipitated out by adding ethyl acetate as counter solvent, and further purified through successive washing with 1:2 mixtures of DMF/HCl (0.3 M) and of DMF/water (yield: 95%).

The UV-Vis spectrum of Bz-BCN-23 in DMF showed a $\lambda_{max}=$ 590 nm, which confirmed the integrity of the Rh(II) paddlewheel unit through the catalytic reaction (Figure S19). This result corroborated that Rh(II) is not reduced upon addition of ascorbic acid or exchanged in the presence of Cu(II). Furthermore, UV-Vis spectrum of Bz-BCN-23 also confirmed that the newly formed triazole ring does not coordinate to the exposed Rh(II) axial sites due to the strong steric hindrance around the coordinating N atoms of the triazole ring.[24] MALDI-TOF analysis revealed a single broad peak centred at 10045 m/z, which closely agrees with the expected molecular mass for $[Rh_{24}(5\text{-}(1\text{-}phenyl\text{-}1H\text{-}1,2,3\text{-}triazol\text{-}4\text{-}yl)\text{-}bdc)_{24}+H^+]^+\cdot DMF\cdot 3H_2O$ (expected = 10045 g/mol) (Figure S19). ^1H NMR analysis of a DMSO-d_6 solution of Bz-BCN-23 showed a downfield shift of the aromatic protons of the BDC moiety, and the appearance of a new broad aromatic signal at $\delta=7.55$ ppm, which corresponds to the incorporated phenyl moiety on the surface of the MOP (Figure S11). Furthermore, the formation of the triazole ring linking the MOP unit to the phenyl ring was first evidenced by the appearance of a signal at $\delta=9.35$ ppm, which corresponds to the olefinic proton of the triazole ring, and by the quantitative fading of the signals of the alkyne protons groups ($\delta=4.30$ ppm, Figure S10). Supporting this later observation, the Fourier transform infrared spectroscopy (FTIR) spectrum of Bz-BCN-23 revealed complete disappearance of the stretching band corresponding to the alkyne group at 3284 cm^{-1} (Figure S20). DOSY NMR data of Bz-BCN-23 showed the same diffusion coefficient ($5.3\cdot10^{-11}$ $m^2\,s^{-1}$) for all aromatic protons (Figure 1b and S12). The calculated hydrodynamic radius was found to be 2.1 nm, in agreement with the equilibrium configuration of the simulated structure (Figure S21).

Further evidence of the quantitative conversion of the alkyne groups was provided by the ^1H NMR analysis of the acid-digested Bz-BCN-23. The spectrum of the digested Bz-BCN-23 showed only the signals corresponding to 5-(1-phenyl-1H-1,2,3-triazol-4-yl)-bdc, which is the linker expected to be created upon coupling of the initial 5-ethynyl-bdc linker of BCN-23 to azidobenzene via CuAAC (Figure S13). Finally, as expected for this type of click reaction, only the 1,4-substituted triazole ring was formed, as confirmed by the ROESY NMR data of the digested Bz-BCN-23 (Figure S18).

From the above model reaction, we corroborated that all 24 alkyne groups on the outer surface of BCN-23 can be reacted through CuAAC click chemistry with an azide group without compromising the integrity of the Rh-MOP. To further confirm this quantitative functionalisation, we next targeted the functionalisation of BCN-23 with a polymer, to form a polymer grafted Rh-MOP.[6,7,25,26] To this end, BCN-23 was reacted with 36 mol. equiv. (i.e. 1.5 mol. equiv. per alkynyl group) of an azide terminated polyethylene glycol polymer ($mPEG_{42}$-N_3) with 42 repeating units (average molecular weight = 2000 ± 300 g/mol) overnight at room temperature. As for the previous click reaction, this reaction also proceeded homogenously in DMSO. The resulting PEGylated Rh-MOP (hereafter named $mPEG_{42}$-BCN-23) was isolated by precipitation from the reaction mixture with diethyl ether, collected by centrifugation, and then purified (yield: > 95%).

The ^1H NMR spectrum of the PEGylated Rh-MOP in MeOD-d_4 showed a broad signal in the aromatic region at *ca.* $\delta=$ 8.54 ppm, which corresponds to the bdc and to the triazole moieties (Figure S22). Additionally, it showed peaks at $\delta=$ 3.64 ppm, corresponding to the aliphatic ethylene glycol units. Both sets of signals belong to the same molecule, as confirmed by DOSY experiments on $mPEG_{42}$-BCN-23 that revealed a diffusion coefficient of $8.1\cdot10^{-11}$ $m^2\,s^{-1}$ (Figure S23). The calculated hydrodynamic size of $mPEG_{42}$-BCN-23 was 4.9 nm. These results reflected a considerable increase in the hydrodynamic radius relative to the previously found values, supporting the notion that the PEG chains were indeed attached to the surface of BCN-23.

Next, to elucidate the degree of PEGylation, we analysed the digested $mPEG_{42}$-BCN-23 by ^1H NMR. The spectrum of the digested $mPEG_{42}$-BCN-23 in DMSO-d_6 revealed that all 24 5-ethynyl-bdc linkers of the parent BCN-23 had been clicked with the polymer chains (Figure S24). The quantitative PEGylation of BCN-23 was further confirmed by MALDI-TOF analysis of $mPEG_{42}$-BCN-23, which showed a broad peak at *ca.* 53470.5 g/mol, which corresponds to a PEGylated Rh-MOP with formula $([Rh_{24}(5\text{-}(mPEG_{42}\text{-}1H\text{-}1,2,3\text{-}triazol\text{-}4\text{-}yl)\text{-}bdc)_{24}+H^+]^+\cdot 20MeOH$ (expected m/z = 53468.4) (Figure 2 and Figure S28). Also, FTIR analysis of $mPEG_{42}$-BCN-23 revealed the complete disappear-

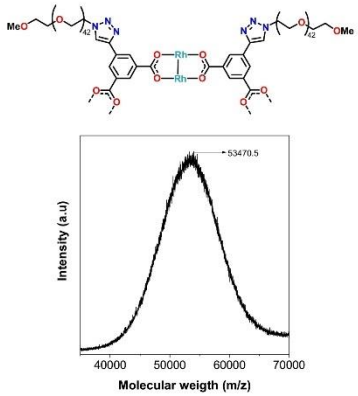

Figure 2. Schematic showing the structure of $mPEG_{42}$-BCN-23 (top) and the corresponding MALDI-TOF spectrum (bottom). The molecular weight corresponding to the formula $([Rh_{24}(5\text{-}(mPEG_{42}\text{-}1H\text{-}1,2,3\text{-triazol-4-yl})\text{-}bdc)_{24} + H^+]^-\cdot 20MeOH$ has been highlighted: expected m/z = 53468.4; found m/z = 53470.5.

ance of the stretching band at 3284 cm^{-1}, further confirming that all the alkyne groups on the surface of the MOP had been reacted (Figure S29). Importantly, due to the quantitative PEGylation, the physicochemical properties of the product were drastically different from those of the initial BCN-23. For example, whereas the initial BCN-23 is only soluble in DMSO and DMF, the densely PEGylated $mPEG_{42}$-BCN-23 exhibits a broad solubility profile, covering most organic solvents such as methanol, chloroform, DMF and DMSO and water in a wide range of pH values (Figure S27).

Functionalisation of BCN-23 with carboxylic and phosphonic acid groups

Having demonstrated the regioselective and quantitative nature of click chemistry on the alkyne surface groups of BCN-23, we next sought to take advantage of the orthogonal reactivity of this chemistry to decorate the surface of BCN-23 with coordinating groups such as carboxylic or phosphonic acid groups. The formation of MOPs with surface-available carboxylic or phosphonic acid groups is very challenging, as these groups tend to react with metal ions, thus precluding formation of the desired MOP. Indeed, there is only one reported example of a covalent COOH-functionalised MOP, which was prepared through a post-synthetic protection/deprotection strategy, and there are no reports of any phosphonic acid-functionalised MOPs.[122] To prove that the CuAAC reaction could be used to post-synthetically functionalise MOPs with available carboxylic or phosphonic acid groups, we ran experiments with four azide substrates: three terminated with carboxylic acid groups (azidobenzoic acid, 6-azidohexanoic acid, and COOH-PEG_3-N_3) and one terminated with a phosphonic acid group (H_2PO_3-PEG_3-N_3). The reaction of BCN-23 with azidobenzoic acid (36 mol. equiv.), 6-azidohexanoic acid (36 mol. equiv.) or COOH-PEG_3-N_3 (36 mol. equiv.) in the presence of $CuSO_4$ (1.5 mol. equiv.), sodium ascorbate (2.25 mol. equiv.) and HCl (0.0031 mol. equiv.) in DMSO yielded three new COOH-functionalised MOPs: COOH–Bz-BCN-23 (yield: >95%), COOH–C_5-BCN-23 (yield: >95%), and COOH-PEG_3-BCN-23 (yield: >95%) (Figure 3). It is important to note here that the addition of HCl to the catalytic reaction was required to prevent coordination of the free carboxylic acid groups to the copper catalyst. In all cases, the click reaction was quantitative, as evidenced by the ^1H NMR spectra of the corresponding acid-digested samples (Figur-

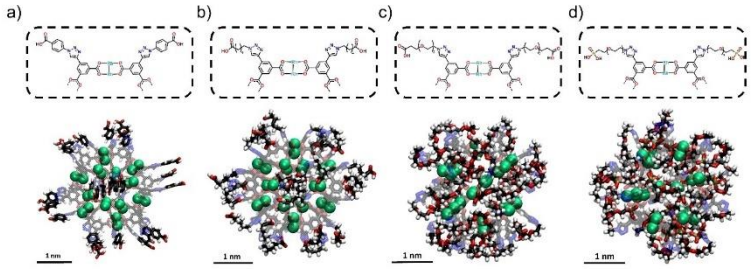

Figure 3. Schematic composition (top) and simulated structure (bottom) of COOH–Bz-BCN-23 (a), COOH-C_5-BCN-23 (b), COOH-PEG_3-BCN-23 (c) and H_2PO_3-PEG_3-BCN-23 (d). The structure shown corresponds to snapshots of the equilibrium configuration obtained in the computer simulations (snapshots made with VMD).[123] Color code: Rhodium (green); carbon (black); hydrogen (white); oxygen (red); nitrogen (blue); phosphor (gold). Rh atoms are shown in their Van der Waals size while linker is represented with Licorice drawing method. For simplicity, the MOP core is displayed as translucent.

es S32, S39, and S46, respectively). Moreover, DOSY NMR analysis of the three COOH-functionalised MOPs in DMSO-d_6 corroborated the successful coupling of the COOH moiety onto the surface of the BCN-23 unit (Figures S31, S38, and S45 respectively). The estimated hydrodynamic radii values derived from the DOSY NMR representation were found to be 2.2 nm (COOH–Bz-BCN-23), 1.9 nm (COOH-C_5-BCN-23), and 2.5 nm (COOH-PEG_3-BCN-23). These values are in agreement with the simulated structures (Figure 3a, 3b and 3c). Furthermore, the simulations also revealed the orientation of the three types of carboxylic acids on the surface of the MOP core. Whereas the carboxylic acids of COOH–Bz-BCN-23 and COOH–C5-BCN-23 are stretched out from the MOP core, the PEG chains of the COOH-PEG_3-BCN-23 are wrapped around the MOP core, in what is called "mushroom" configuration in nanoparticles.[27]

MALDI-TOF analysis also proved that, upon reaction of BCN-23 with each of the three types of carboxylic acid substrates separately, each functionalised product has a higher molecular weight than the starting MOP. In all cases, a broad signal containing the expected molecular formula for each acid derivative of BCN-23 was observed (Figures S33, S40, and S47, respectively). Free carboxylic acid groups were also evident in the FTIR spectrum of all three COOH-functionalised MOPs, which showed a new stretching C=O band centred at *ca.* 1728 cm^{-1} that corresponds to the presence of free carboxylic acid groups (Figures S35, S42, and S49). Therefore, CuAACs enable not only the synthesis of COOH-functionalised MOPs but also enable control over the type (i.e. aliphatic or aromatic) and length of the spacer between the MOP core and the surface carboxylic acid groups.

Next, we challenged our approach by attempting the synthesis of the first ever MOP functionalised with available phosphonic acid groups. Free phosphonic acids are highly coordinating groups that are generally incompatible with metal–organic structures, although they have been used to build up extended structures as an alternative to the metal-carboxylate bond.[28,29] However, we found BCN-23 to be stable against free phosphonic acids such as phenylphosphonic acid, which encouraged us to pursue its post-synthetic functionalisation with pendant phosphonic acid groups (Figure S56). The click reaction between BCN-23 and H_2PO_3-PEG_3-N_3 (36 mol. equiv.) was performed in the presence of the previously employed catalytic mixture comprising $CuSO_4$ (0.25 mol. equiv. per alkynyl group) and sodium ascorbate (7.5 mol. equiv. per alkynyl group, 30 mol. equiv. per Cu(II) ion). Moreover, in this case, we also added the chelating agent tris-hydroxypropyltriazolylmethylamine (THPTA) to the mixture to prevent coordination of the phosphonate groups to the copper catalyst. After 1 h of reaction at room temperature, a precipitate (hereafter named H_2PO_3-PEG_3-BCN-23) was obtained, isolated by centrifugation, and subsequently washed with 0.3 M HCl and water (yield: 87%). The integrity of the Rh(II) paddlewheel in H_2PO_3-PEG_3-BCN-23 was first confirmed by the presence of the characteristic λ_{max} = 582 nm in the UV-Vis spectrum (Figure S54). Furthermore, the ^{1}H NMR spectrum of H_2PO_3-PEG_3-BCN-23 in D_2O revealed the disappearance of the alkyne protons and the appearance of broad PEG and aromatic signals, which had the same diffusion coefficient of $7.2 \cdot 10^{-11}$ m^2 s^{-1}, as determined by DOSY NMR (Figures S51 and S52, respectively). The calculated hydrodynamic radius was 2.6 nm, in agreement with the simulated structure. As in the case of COOH-PEG_3-BCN-23 the PEG chains are wrapped around the MOP core (Figure 3d).

The MALDI-TOF spectrum of COOH-PEG_3-BCN-23 revealed a broad peak with a centred m/z value of 13855.5 g/mol, in good agreement with a Rh-MOP of formula $[Rh_{24}$(5-phosphono-PEG_3-(−1H-1,2,3-triazol-4-yl)-bdc$)_{24} + H^+]^+ \cdot 4H_2O$ (expected m/z for this formula = 13855.0) (Figure S54). The presence of the free phosphonic acid group on H_2PO_3-PEG_3-BCN-23 was further confirmed by FTIR, which exhibited the characteristic band centred at 1044–1046 cm^{-1} (Figure S57). Altogether, these results demonstrate that BCN-23 is stable under homogenous conditions in the presence of free phosphonic acids and chelating agents. This outstanding stability enabled quantitative functionalisation of the surface of BCN-23 with 24 available phosphonic acid groups.

The porosity of the new carboxylic or phosphonic acid-functionalised MOPs was assessed in CO_2-adsorption experiments at 200 K, which revealed that all the tested MOPs were porous to CO_2. Specifically, the maximum CO_2-uptake capacities at 1 bar were: 2.13 mmol/g (COOH–Bz-BCN-23); 1.61 mmol/g (COOH-C_5-BCN-23); 3.53 mmol/g (COOH-PEG_3-BCN-23); and 2.23 mmol/g (H_2PO_3-PEG_3-BCN-23) (Figure S64). Therefore, synthesised carboxylic or phosphonic acid-functionalised MOPs combine permanent porosity with on-surface coordination and covalent reactivity, making them ideal candidates as porous monomers in subsequent self-assembly processes.

Finally, we studied the pH-dependent solubility of all the synthesised carboxylic or phosphonic-acid functionalised MOPs. As expected, both types of MOPs were soluble in aqueous solution upon the stoichiometric deprotonation of the peripheral carboxylic or phosphonic acids, to obtain the corresponding carboxylate or phosphonate groups, respectively, affording negatively charged MOPs (Figure S36, S43, S50 and S58). However, the pH range in which each MOP was found to be water-soluble varied accordingly to its respective functionalisation (Figures S34, S41, S48 and S55). Thus, whereas carboxylic acid-functionalised MOPs precipitated out at pH 4.5 to 5.5, due to protonation of the surface COOH group, the phosphonic acid-functionalised one was soluble in water up to pH 2.7, which reflects the higher pK_a of carboxylic acids relative to phosphonic acid.

Synthesis and bio-recognition capabilities of biotinylated MOPs

Biotinylation of organic or inorganic nanoparticles, which involves attaching biotin molecules to their surface, has proven to be an effective method for enhancing their ability to interact with biological systems through the widely known biotin-streptavidin/avidin interaction.[30] For example, biotinylated nanoparticles have proven invaluable in the development of innovative biosensors and targeted delivery systems.[31,32] Consequently, as a first step towards the development of MOP-

based bioconjugates, we employed CuAAC for the biotinylation of MOPs, and then studied the resultant products for their interactions with avidin.

BCN-23 was biotinylated by reacting it with biotin-PEG_5-azide under the same standardised click conditions previously used for the model compounds. The structure of the product, hereafter named biotin-PEG_5-BCN-23, was confirmed by ^{1}H NMR in DMSO-d_6, which showed new broad signals that correspond to PEGylated biotin (Figure S59 and S60). DOSY NMR revealed the same diffusion coefficient ($D = 7.6 \cdot 10^{-11}$ m^2 s^{-1}) for these signals and for the aromatic peaks assigned to the MOP core (Figure S61). The calculated hydrodynamic radius was 2.5 nm in agreement with equilibrium configuration of the simulated structure (Figure 4a and S63). The incorporation of the PEG-biotin moiety onto the surface of BCN-23 was further confirmed by mass spectrometry, which revealed a broad peak that included the expected mass for $[Rh_{24}(5\text{-biotin-}PEG_5\text{-}(-1H\text{-}1,2,3\text{-triazol-}4\text{-yl})\text{-bdc})_{24} + H^+]^+$ of 19770 g/mol (Figure S62).

Next, we aimed to test the biorecognition capabilities of biotin-PEG_5-BCN-23. To this end, we employed the competitive HABA-avidin binding assay. In this assay, 2-(4-hydroxyphenylazo)benzoic acid (HABA) initially occupies the four possible binding sites of avidin (Figure 4b). When this interaction occurs, λ_{max} is centred at 500 nm, in contrast to the free form of HABA, whose λ_{max} is at 350 nm. The addition of free biotin to this complex induces the quantitative replacement of HABA due to the greater affinity of avidin for biotin ($K_d = 10^{-15}$) than for HABA ($K_d = 10^{-6}$). Therefore, the stoichiometric exchange between HABA and biotin can be followed through UV-Vis spectroscopy, by monitoring the changes in absorbance of the band centred at 500 nm (Figure S65). Thus, to study the biorecognition capabilities of MOP-bounded biotin moieties, we performed a competitive test in which increasing amounts of biotin-PEG_5-BCN-23 were added to separated aliquots of HABA-avidin at a constant concentration. The reaction mixture was maintained in solution up to the addition of one biotin-PEG_5-BCN-23 per avidin (i.e. 24 biotin molecules per avidin), after which partial precipitation was observed. The analysis of the aliquots that remained in solution revealed that biotin-PEG_5-BCN-23 does indeed recognise avidin. Furthermore, the molecular nature of the biotin-PEG_5-BCN-23 enabled calculation of the stoichiometry of these interactions. Thus, the average number of avidin groups attached to the MOP was found to be 1, irrespective of the excess amount of avidin in solution (Figure 4c and Figure S66-S68). This result implies that, once one avidin protein has attached to the MOP surface, there is strong steric hindrance that inhibits the recognition by the remaining 23 available biotin moieties on the surface. This steric hindrance might arise from the relative size of avidin (maximum cross section of ca. 8 nm) relative to the biotin-PEG_5-BCN-23 (diameter of ca. 5 nm), and/or to the mutual steric hindrance of surface-bound biotin groups, given their high surface density (*ca.* 0.5 biotin molecules per nm^2).

Conclusions

We have reported the synthesis of a novel alkyne-functionalised MOP that can be post-synthetically modified through CuAAC reactions. The CuAAC reaction proceeds quantitatively without compromising the structure of the parent MOP structure, which enables the synthesis of densely functionalised MOPs. We validated the scope of our approach by decorating the MOP surface with a wide range of chemically diverse substrates. For example, we synthesised novel MOPs with unprecedented functionalities, including carboxylic or phosphonic acid groups, or bioactive biotins. We envisage the use of CuAACs on "clickable" MOPs to further expand the repertoire of functional MOPs to guide the development of novel catalysts, sensors, and building blocks for hierarchical bio-mediated self-assembly processes.

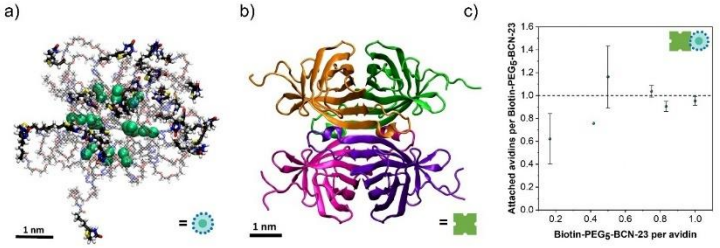

Figure 4. (a) Snapshot of the equilibrium structure of biotin-PEG_5-BCN-23 as obtained from molecular dynamics simulations in water solvent. Snapshots made with VMD.[171] Color code: Rhodium (green); carbon (black); hydrogen (white); oxygen (red); nitrogen (blue); Sulphur (yellow). Rh atoms are shown in their van der Waals size while linker is represented with Licorice drawing method. For simplicity, the MOP core is displayed as translucent. (b) Structure of avidin. (c) Plot of the average number of avidin proteins interacting with biotin-PEG_5-BCN-23 at different molar ratios of biotin-BCN-23/avidin.

Experimental Section

Synthesis of alkyne-protected Rh(II)-MOP: Rh_2Ac_4·2MeOH (20 mg, 0.04 mmol), H_2bdc-TIPS (74.4 mg 0.2 mmol) and Na_2CO_3 (25 mg, 0.2 mmol) were dispersed in 4 mL of DMA. The mixture was then transferred to a scintillation vial and heated at 100 °C for 48 h. A deep green solution was obtained and separated from the residual solids by centrifugation. The crude product was obtained by precipitation with water (20 mL) and then, separated by centrifugation. The solid was washed with water and dried by lyophilization. The resulting green solid was washed two times with methanol (20 mL) for further purification and dried in a vacuum oven at 85 °C overnight (93.9 mg, yield: 80%).

Synthesis of BCN-23: The alkyne-protected Rh(II)-MOP (10 mg, 0.96 μmol) was dissolved in THF (1 mL). Then, tetrabutylammonium fluoride (34.7 μL, 34.7 μmol, 1 M solution in THF) was added to this solution under stirring, from which a blue precipitate appeared. This solid was rapidly centrifuged and subsequently washed three times with THF (2 mL) and dried under air.

General procedure to perform CuAAC reactions on BCN-23: BCN-23 (6.72 mg, 0.96 μmol) and the desired azide-functionalized ligand (34.56 μmol) were dissolved in DMSO (10 mL). Then, two aqueous solutions of sodium ascorbate (1.04 M) and $CuSO_4$ (0.7 M) were prepared. The addition of the required amount of catalyst (100 μL of $CuSO_4$ and 200 μL of sodium ascorbate) to complete the reaction was added stepwise in five additions over a period of 1.25 h under stirring. Once the additions were completed, the mixture was reacted at room temperature overnight. Finally, the obtained reaction products were separated and purified according to their solubility.

Synthesis of acid-functionalized Rh(II)-MOPs through CuAAC post-synthetic reactions: BCN-23 (6.72 mg, 0.96 μmol) and 34.56 μmol of 5-azidohexanoic acid (5.1 μL), 4-azidobenzoic acid (172.8 μL from a 0.2 M solution in tert-butyl ether) or COOH-PEG_3-N_3 (8.6 mg) were dissolved in DMSO (10 mL). The presence of free carboxylic acids in the reaction required the addition of acid to avoid precipitation during the reaction (20 μL, HCl 0.3 M). The CuAAC reaction were performed following the above-described general procedure. After the reaction, ethyl acetate (40 mL) was used to precipitate the product obtaining an orange coloured solid. These solids were washed once with a mixture of DMF: 0.3 M HCl (40 mL, 1:2) and twice with a DMF/H2O mixture (40 mL, 1:2). The final blue solids were dried in a vacuum oven at 85 °C for 2 h.

Synthesis of phosphonic acid-functionalized Rh(II)-MOPs through CuAAC post-synthetic reactions: BCN-23 (6.72 mg, 0.96 μmol) and H_2PO_3-PEG_3-N_3 (9.82 mg 34.56 μmol) were dissolved in DMSO (10 mL). Then, an aqueous solution (160 μL) containing THPTA (15.1 mg, 34.7 μmol) and $CuSO_4$ (10 μL from a 0.7 M solution, 6.94 μmol) was added to the mixture. Afterwards, sodium ascorbate (41.24 mg, 0.83 M) was added, and the mixture was reacted at room temperature overnight. Ethyl acetate (40 mL) was used to precipitate the product obtaining an orange-coloured solid that was subsequently washed once with 0.3 M HCl (40 mL) and twice with water (40 mL). Then, this purple coloured solid was dissolved in water (1 mL) using an aqueous solution of NaOH (46.24 μL, 1 M). The resulting purple solution was further purified using a dialysis procedure for 2 days. After that, a green solid was precipitated from the aqueous solution by treating it with a 3 M HCl until pH 1 was reached. Finally, the solid was lyophilized.

NMR adquisition. All 1D and 2D NMR experiments were acquired and processed under standard conditions. In particular, 2D DOSY experiments used a 150ms diffusion time and 2D ROESY experiments used a 400ms adiabatic mixing time. Other details can be found in the supporting information.

Acknowledgements

This work was supported by the Spanish MINECO (project RTI2018-095622-B–I00) and the Catalan AGAUR (project 2021 SGR 00458). It was also funded by the CERCA Programme /Generalitat de Catalunya and through a fellowship (LCF/BQ/PR20/11770011) from the "la Caixa" Foundation (ID 100010434). ICN2 is supported by the Severo Ochoa Centres of Excellence programme, Grant CEX2021-001214-S, funded by MCIN/AEI/10.13039.501100011033. A.C.S. is indebted to the Ramón y Cajal Program (RYC2020-029749-I Fellowship) and the Europa Excelencia grant (EUR2021-121997) L.H.L acknowledges the support from the Spanish State Research Agency (PRE2019-088056). C.v.B. thanks the Austrian Science Fund (FWF), Erwin Schrödinger fellowship for supporting the project J 4637. J. F acknowledges the financial support from MCIN/AEI/10.13039/501100011033 agency through Grant PID2021-124297NB-C33 and the "Severo Ochoa" Programme for Centres of Excellence in R\&D (CEX2019-000917-S) awarded to ICMAB. We also thank the Government of Catalonia (AGAUR) for Grant 2021SGR01519.

Conflict of Interests

The authors declare no conflict of interest.

Data Availability Statement

The data that support the findings of this study are available from the corresponding author upon reasonable request.

Keywords: biofunctionalization · click chemistry · metal–organic polyhedra · recognition · surface functionalisation

[1] M. Eddaoudi, J. Kim, J. B. Wachter, H. K. Chae, M. O'Keeffe, O. M. Yaghi, *J. Am. Chem. Soc.* **2001**, *123*, 4368–4369.
[2] A. Carné-Sánchez, J. Albalad, T. Grancha, I. Imaz, J. Juanhuix, P. Larpent, S. Furukawa, D. Maspoch, *J. Am. Chem. Soc.* **2019**, *141*, 4094–4102.
[3] T. Grancha, A. Carné-Sánchez, L. Hernández-López, J. Albalad, I. Imaz, J. Juanhuix, D. Maspoch, *J. Am. Chem. Soc.* **2019**, *141*, 18349–18355.
[4] J. Albalad, L. Hernández-López, A. Carné-Sánchez, D. Maspoch, *Chem. Commun.* **2022**, *58*, 2443–2454.
[5] G. A. Taggart, A. M. Antonio, G. R. Lorzing, G. P. A. Yap, E. D. Bloch, *ACS Appl. Mater. Interfaces* **2020**, *22*, 24913–24919.
[6] D. Zhao, S. Tan, D. Yuan, W. Lu, Y. H. Rezenom, H. Jiang, L.-Q. Wang, H.-C. Zhou, *Adv. Mater.* **2011**, *23*, 90–93.
[7] N. Hosono, M. Gochomori, R. Matsuda, H. Sato, S. Kitagawa, *J. Am. Chem. Soc.* **2016**, *138*, 6525–6531.
[8] G. Liu, Y. D. Yuan, J. Wang, Y. Cheng, S. B. Peh, Y. Wang, Y. Qian, J. Dong, D. Yuan, D. Zhao, *J. Am. Chem. Soc.* **2018**, *140*, 6231–6234.
[9] Y. Yang, T. K. Ronson, J. Zheng, N. Mihara, J. R. Nitschke, *Chem.* **2023**, *9*, 1–9.
[10] D. Luo, Z. J. Yuan, L. J. Ping, X. W. Zhu, J. Zheng, C. W. Zhou, X. C. Zhou, X. P. Zhou, D. Li, *Angew. Chem. Int. Ed.* **2023**, *62*, e202216977.
[11] V. J. Pastore, M. G. Sullivan, H. K. Welgama, M. R. Crawley, A. E. Friedman, C. Rumsey, M. Trebbin, J. Rzayev, T. R. Cook, *Chem. Mater.* **2023**, *35*, 1651–1658.
[12] J.-F. Lutz, Z. Zarafshani, *Adv. Drug Delivery Rev.* **2008**, *60*, 958–970.
[13] B. Gui, X. Liu, Y. Cheng, Y. Zhang, P. Chen, M. He, J. Sun, C. Wang, *Angew. Chem. Int. Ed.* **2022**, e202113852.
[14] M. Li, P. De, S. R. Gondi, B. S. Sumerlin, *Macromol. Rapid Commun.* **2008**, 1172–1176.

[15] P. M. E. Gramlich, S. Warncke, J. Gierlich, T. Carell, *Angew. Chem. Int. Ed.* **2008**, *47*, 3442–3444.
[16] P. M. E. Gramlich, C. T. Wirges, A. Manetto, T. Carell, *Angew. Chem. Int. Ed.* **2008**, 8350–8358.
[17] D. A. Roberts, B. S. Pilgrim, J. R. Nitschke, *Chem. Soc. Rev.* **2018**, *47*, 626–644.
[18] R. Chakrabarty, P. J. Stang, *J. Am. Chem. Soc.* **2012**, *134*, 14738–14741.
[19] T. Nakajo, S. Kusaka, H. Hiraoka, K. Nomura, N. Matsubara, R. Baba, Y. Yoshida, K. Nakamoto, M. Honma, H. Iguchi, T. Uchihashi, H. Abe, R. Matsuda, *Chem. Commun.* **2023**, *59*, 4974–4977.
[20] M. R. Dworzak, C. M. Montone, N. I. Haladzynski, G. P. A. Yap, M. O. Kloxin, E. D. Bloch, *Chem. Commun.* **2023**, *59*, 8977–8980.
[21] S. Furukawa, N. Horike, M. Kondo, Y. Hijikata, A. Carné-Sánchez, P. Larpent, N. Louvain, S. Diring, H. Sato, R. Matsuda, R. Kawano, S. Kitagawa, *Inorg. Chem.* **2016**, *55*, 10843–10846.
[22] J. Albalad, A. Carné-Sánchez, T. Grancha, L. Hernández-López, D. Maspoch, *Chem. Commun.* **2019**, *55*, 12785–12788.
[23] W. Humphrey, A. Dalke, K. Schulten, *J. Mol. Graphics* **1996**, *14*, 33–38.
[24] L. Hernández-López, J. Martínez-Esaín, A. Carné-Sánchez, T. Grancha, J. Faraudo, D. Maspoch, *Angew. Chem. Int. Ed.* **2021**, *60*, 11406–11413.
[25] Y. Lai, M. Li, M. Zhang, X. Li, J. Yuan, W. Wang, Q. Zhou, M. Huang, P. Yin, *Macromolecules* **2020**, *53*, 7178–7186.
[26] K. Omoto, N. Hosono, M. Gochomori, S. Kitagawa, *Chem. Commun.* **2018**, *54*, 7290–7293.
[27] M. Li, S. Jiang, J. Simon, D. Paßlick, M.-L. Frey, M. Wagner, V. Mailänder, D. Crespy, K. Landfester, *Nano Lett.* **2021**, *21*, 1591–1598.
[28] F. Steinke, L. Gemmrich Hernandéz, S. J. I. Shearan, M. Pohlmann, M. Taddei, U. Kolb, N. Stock, *Inorg. Chem.* **2023**, *62*, 35–42.
[29] S. Ondrušová, M. Kloda, J. Rohlíček, M. Taddei, J. K. Zaręba, J. Demel, *Inorg. Chem.* **2022**, *61*, 18990–18997.
[30] W. R. Algar, D. E. Prasuhn, M. H. Stewart, T. L. Jennings, J. B. Blanco-Canosa, P. E. Dawson, I. L. Medintz, *Bioconjugate Chem.* **2011**, *22*, 825–858.
[31] N. Nath, A. Chilkoti, *Anal. Chem.* **2002**, *74*, 504–509.
[32] K. Saha, S. S. Agasti, C. Kim, X. Li, V. M. Rotello, *Chem. Rev.* **2012**, *112*, 2739–2779.

Manuscript received: June 19, 2023
Accepted manuscript online: July 31, 2023
Version of record online: September 19, 2023

Chemical Science

ROYAL SOCIETY OF CHEMISTRY

EDGE ARTICLE

View Article Online
View Journal | View Issue

Cite this: *Chem. Sci.*, 2024, **15**, 7992

All publication charges for this article have been paid for by the Royal Society of Chemistry

Received 25th March 2024
Accepted 29th April 2024

DOI: 10.1039/d4sc01974a

rsc.li/chemical-science

Giant oligomeric porous cage-based molecules†

Alba Cortés-Martínez,[ab] Cornelia von Baeckmann,[ab] Laura Hernández-López,[ab] Arnau Carné-Sánchez *[ab] and Daniel Maspoch *[abc]

Most reported porous materials are either extended networks or monomeric discrete cavities; indeed, porous structures of intermediate size have scarcely been explored. Herein, we present the stepwise linkage of discrete porous metal–organic cages or polyhedra (MOPs) into oligomeric structures with a finite number of MOP units. The synthesis of these new oligomeric porous molecules entails the preparation of 1-connected (1-c) MOPs with only one available azide reactive site on their surface. The azide-terminated 1-c MOP is linked through copper(I)-catalysed azide–alkyne cycloaddition click chemistry with additional alkyne-terminated 1-c MOPs, 4-c clusters, or 24-c MOPs to yield three classes of giant oligomeric molecules: dimeric, tetrameric, or satellite-like, respectively. Importantly, all the giant molecules that we synthesised are soluble in water and permanently porous in the solid state.

Introduction

The overwhelming majority of known porous materials are either small (<5 nm) discrete cages (*i.e.* coordination and covalent cages),[1–5] or infinite networks (*i.e.* metal- and covalent-organic frameworks).[6–9] The chemical and dimensional (between 5 nm and 20 nm) space between these two classes has not been largely explored, due to the inherent synthetic and analytical challenges (Scheme 1).[10–12] Specifically, using bottom-up approaches to assemble large porous discrete cages is not trivial.[13] Another challenge lies in stopping the polymerisation reaction of extended networks at the oligomeric regime, which is not thermodynamically favoured, thus leading to polydisperse and metastable materials.[14,15] Moreover, the downsizing of crystalline porous networks below the 20 nm threshold often entails the accumulation of defects that are detrimental to their characterisation and function.[16,17]

To overcome these challenges, one can take inspiration from the stepwise synthesis of giant organic[18–22] and metal–organic[23–25] molecules, in which each growing step proceeds through thermodynamic control. In the case of porous materials, this strategy entails the oligomerization of single pore units into giant multi-pore molecules. Pioneer studies have shown the viability of the pore oligomerization approach by either interlocking[26–29] or linking a defined number of cages[30–32]

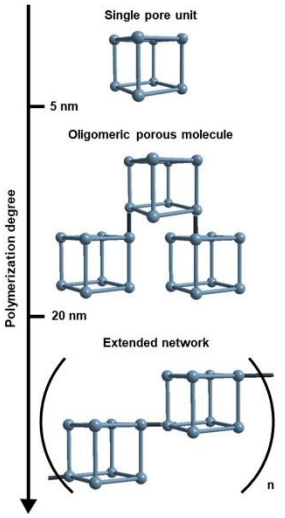

Scheme 1 Illustrated scale of the regimes of reported porous materials.

[a]Catalan Institute of Nanoscience and Nanotechnology (ICN2), CSIC and The Barcelona Institute of Science and Technology, Campus UAB, Bellaterra, 08193 Barcelona, Spain. E-mail: arnau.carne@icn2.cat; daniel.maspoch@icn2.cat
[b]Departament de Química, Facultat de Ciències, Universitat Autònoma de Barcelona (UAB), Cerdanyola del Vallès, 08193 Barcelona, Spain
[c]ICREA, Pg. Lluís Companys 23, 08010 Barcelona, Spain

† Electronic supplementary information (ESI) available. See DOI: https://doi.org/10.1039/d4sc01974a

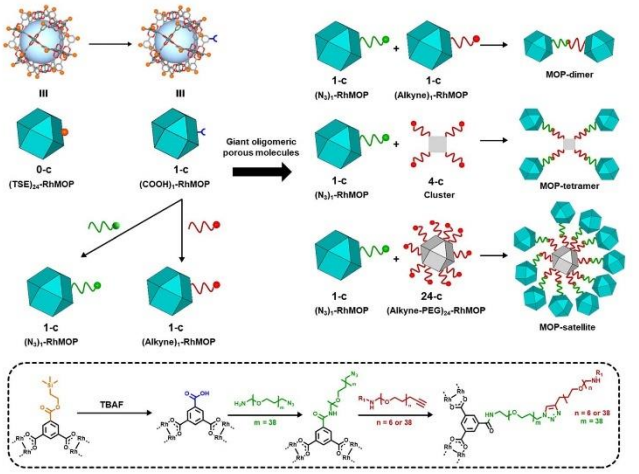

Fig. 1 (Top) Schematic of the synthesis of 1-c MOPs terminated with azide or alkyne groups, and their subsequent linkage to other MOPs or clusters through click chemistry to form oligomeric porous dimeric, tetrameric or satellite-like molecules. (Bottom) Representative reaction schematic for the synthesis of giant, oligomeric, MOP-based molecules.

into multi-cage molecules. However, to the best of our knowledge, the permanent porosity of this giant molecules has not yet been demonstrated.

Herein we report the stepwise synthesis of permanently porous oligomeric molecules by the concatenation of a defined, finite number of metal–organic cages or polyhedra (MOPs). The resultant giant oligomeric porous molecules merge the properties that arise from linking pore-units (*i.e.* extrinsic porosity and inter-cavity cooperativity)[33,34] to the those typically observed in molecules, such as defined molecular weight, stoichiometric reactivity, and solubility in liquids, including water.[21–23,35]

In our synthetic route to oligomeric porous molecules, the building blocks are robust Rh(II)-based MOPs (Rh-MOPs).[36] Rh-MOPs can have up to 24 covalent reactive sites on their external surfaces, stemming from the 5-position of the 1,3-benzendicarboxylate (BDC) derivative used in their synthesis.[37] Consequently, the high connectivity of Rh-MOPs complicates the control of their polymerisation into well-defined oligomeric structures rather than extended networks.[38–41] To address this challenge, we aimed to create Rh-MOPs with only one reactive site on their surface. By employing protecting groups, we selectively masked the reactivity of 23 of the 24 reactive sites to yield 1-connected (1-c) Rh-MOPs.[42] Next, using orthogonal chemistry, we assembled these 1-c MOPs with other 1-c MOPs or with 4-c clusters or 24-c Rh-MOPs to yield giant oligomeric molecules of three types: dimeric, tetrameric, or satellite-like (Fig. 1).

Results and discussion

Synthesis of 1-connected Rh-MOPs

We began the synthesis of 1-c Rh-MOP from a Rh-MOP in which all of its 24 peripheral carboxylic acid groups were protected with 2-(trimethylsilyl)ethyl (TSE) groups. One of the 24 TSE groups was selectively cleaved by treating the fully protected Rh-MOP with 1.5 mol eq. (per MOP) of the deprotecting agent tetrabutylammonium fluoride (TBAF). This reaction afforded a new Rh-MOP having only one available surface carboxylic group with the formula $(COOTSE\text{-}BDC)_{23}(BTC)_1Rh_{24}$ (where BTC = 1,3,5-benzenetricarboxylate; and COOTSE-BDC_{24} = 5-[(2-(trimethylsilyl)ethoxy)carbonyl)-1,3-benzendicarboxylate). The integrity and formula of the 1-c Rh-MOP (hereafter, $(COOH)_1$-RhMOP) was confirmed by Matrix-Assisted Laser Desorption/Ionisation-Time-Of-Flight (MALDI-TOF) mass spectroscopy, which showed a peak centered at 9770 *m/z* that corresponds to the expected molecular formula of $[(COOTSE\text{-}BDC)_{23}(BTC)_1Rh_{24} + H^+]^+ \cdot 2H_2O$ (expected mass of 9776 g mol^{-1}) (Fig. 2a and S4†). Analysis of the ^{1}H-NMR spectrum of the acid digested $(COOH)_1$-RhMOP confirmed the expected ratio between the aromatic and the aliphatic protons of the protected ligand, thus confirming the removal of one protecting group (Fig. S3†). Furthermore, Diffusion-Ordered Spectroscopy (DOSY) NMR analysis of the $(COOH)_1$-RhMOP in $CDCl_3$ revealed the same diffusion coefficient of 1.9×10^{-10} m^2 s^{-1} for both aliphatic and aromatic

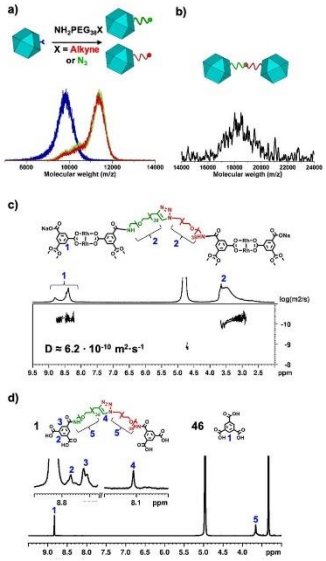

Fig. 2 (a) Comparison of the MALDI-TOF spectra of $(COOH)_1$-RhMOP (blue), $(N_3)_1$-RhMOP (green) and $(alkyne)_1$-RhMOP (red) which evidences an increase in mass due to the attachment of a chain of $NH_2PEG_{38}X$ to the MOP (where X = N_3 or alkyne). (b) MALDI-TOF spectrum of the MOP-dimer, showing the single broad peak centered at 18 538 *m/z*. (c) DOSY-NMR spectrum of the MOP-dimer. (d) ^{1}H-NMR spectrum of the acid-digested MOP-dimer.

signals, which further corroborated that the product had retained 23 of its original 24 TSE groups (Fig. S2†).

Next, to confer $(COOH)_1$-RhMOP with the orthogonal reactivity required to oligomerise it with additional MOPs, we functionalised its surface with a single polyethylene glycol (PEG) chain terminated with either alkyne or azide group. Thus, $(COOH)_1$-RhMOP was reacted with a PEG chain terminated at one end with a primary amine (for coupling to the surface carboxylic acid), and at the other end, with either an alkyne or azide moiety (for the oligomerisation). The coupling reactions between $(COOH)_1$-RhMOP and either NH_2-PEG_{38}-N_3 or NH_2-PEG_{38}-alkyne proceeded homogenously in *N*,*N*-dimethylformamide (DMF), using 1-hydroxybenzotriazole (HOBt), 2-(1*H*-benzotriazole-1-yl)-1,1,3,3-tetramethyluronium hexafluorophosphate (HBTU), and *N*,*N*-diisopropylethylamine (DIPEA) as coupling agents. They yielded two distinct MOPs, each with only one PEG chain attached at its surface: an azide-terminated one, having the formula $(COOTSE\text{-}BDC)_{23}(N_3\text{-}PEG_{38}\text{-}BDC)Rh_{24}$ (hereafter, $(N_3)_1$-RhMOP); and an alkyne-terminated one, having the formula $(COOTSE\text{-}BDC)_{23}(alkyne\text{-}PEG_{38}\text{-}BDC)Rh_{24}$ (hereafter, $(alkyne)_1$-RhMOP). The coupling of a single functionalised PEG chain on the surface of $(COOH)_1$-RhMOP was first demonstrated by MALDI-TOF mass spectroscopy, which showed the expected mass for each product: 11 540 *m/z* for $(N_3)_1$-RhMOP and 11 521 *m/z* for $(alkyne)_1$-RhMOP (Fig. 2a, S10 and S16† respectively). Both values agree with the respective calculated molecular weights for the corresponding expected molecular formulae of the 1-c Rh-MOPs: 11 544 ± 480 g mol^{-1} for $[(COOTSE\text{-}BDC)_{23}(N_3\text{-}PEG_{38}\text{-}BDC)Rh_{24} + H^+]^+$ and 11 521 ± 370 g mol^{-1} for $[(COOTSE\text{-}BDC)_{23}(N_3\text{-}PEG_{38}\text{-}BDC)Rh_{24} + H^+]^+$. The formation of a single amide bond on the surface of the MOP was further supported by the ^{1}H-NMR analysis of the corresponding acid-digested samples: the spectra revealed the quantitative transformation of the initial BTC linker into a PEG functionalised BDC linker *via* amide-bond formation (Fig. S9 and S15†). The ratio between the PEG-functionalised BDC and COOTSE-BDC was found to be the expected value of 1 : 23 in both $(N_3)_1$-RhMOP and $(alkyne)_1$-RhMOP (Fig. S7 and S13†). The DOSY analysis of $(N_3)_1$-RhMOP and $(alkyne)_1$-RhMOP revealed a single diffusion-coefficient for the MOP core and the PEG chain in both products: 1.8 × 10^{-10} m^2 s^{-1} and 1.7 × 10^{-10} m^2 s^{-1} respectively (Fig. S8 and S14†). Interestingly, the remaining 23 protected carboxylic acid groups on the surface of $(N_3)_1$-RhMOP and $(alkyne)_1$-RhMOP could be removed by treating both 1-c RhMOPs with excess of TBAF. Under these conditions, both deprotected $(N_3)_1$-RhMOP and $(alkyne)_1$-RhMOP were functionalized with 23 carboxylic acid groups (Fig. S19–S30†).

Finally, to corroborate the synthesis of pure $(COOH)_1$-RhMOP and derived mono-PEGylated compounds, we performed a control experiment consisting of reacting $(COOH)_1$-RhMOP (obtained by treating a TSE-protected Rh-MOP with 1.5 mol eq. of TBAF) with an excess amount of NH_2-PEG_{38}-N_3 (5 mol eq. per Rh-MOP). The product obtained from this reaction was analysed through MALDI-TOF mass spectrometry, showing only the peak corresponding to $(N_3)_1$-RhMOP that contains one attached PEG chain on the MOP surface (Fig. S31†). Conversely, when NH_2-PEG_{38}-N_3 was reacted with Rh-MOPs containing a higher percentage of free carboxylic acid groups on their surface, a distribution of multi-PEGylated Rh-MOPs was obtained as a product. Specifically, PEGylated Rh-MOPs with 2 and 3 PEG chains on their surface were obtained when 5 mol eq. of NH_2-PEG_{38}-N_3 was reacted with TSE-protected Rh-MOPs treated with 3 and 5 mol eq. of TBAF, respectively (Fig. S32†). These experiments confirm the successful synthesis of pure $(COOH)_1$-RhMOP as the presence of Rh-MOPs with a higher number of available carboxylic acids on their surface would yield a distribution of PEGylated Rh-MOPs in the presence of excess of NH_2-PEG_{38}-N_3.

Synthesis of the oligomeric dimeric MOP-based molecule

Next, we synthesised a dimeric MOP-based molecule (hereafter, MOP-dimer), by coupling $(N_3)_1$-RhMOP to $(alkyne)_1$-RhMOP through a copper(I)-catalysed, azide–alkyne cycloaddition

(CuAAC) click reaction.[43] To this end, both MOPs were reacted under homogenous conditions in a mixture of CH_2Cl_2/DMF (1 : 1), using copper sulphate and sodium acetate as catalysts, to afford the corresponding crude products as a green solid. To facilitate the purification of the MOP-dimer, all surface TSE protecting groups were cleaved, which yielded a dimeric MOP in which each MOP unit had 23 available carboxylic acid groups. Next, the MOP-dimer was purified through successive washing with 0.3 M HCl and basic MeOH, in which the dimer is insoluble, but the catalyst and unreacted precursors are soluble. The obtained purified product exhibited pH-dependent aqueous solubility, which we ascribed to the presence of up to 46 available carboxylic groups. Once deprotonated, the carboxylate groups imparted negative charge to the resulting MOP-dimer, as confirmed by ζ-potential measurements performed in basic water, which revealed a value of -48.5 ± 6.9 mV for the MOP-dimer (Fig. S41†). The successful dimerization of two different MOPs was first evidenced by MALDI-TOF. The spectrum exhibited a single broad peak centred at 18 538 m/z, in good agreement with the expected mass (18 539 $\pm$ 850 g mol^{-1}) for the MOP-dimer having a molecular formula of [(COOH-BDC)$_{46}$(BDC-PEG$_{3k}$-1*H*-1,2,3-triazol-4-yl-PEG$_{3k}$-BDC)$_1$Rh$_{4k}$-H$^+$] $\cdot$DMF (Fig. 2b and S38†). DOSY NMR spectroscopy in basic D_2O revealed a decrease in the diffusion coefficient from the deprotected 1-c MOP precursors (6.6×10^{-10} m^2 s^{-1} and 6.9×10^{-10} m^2 s^{-1}) to the MOP-dimer (6.2×10^{-10} m^2 s^{-1}) (Fig. 2c, S20, S26 and S34†).[44] Analogously, Dynamic Light Scattering (DLS) measurements revealed that the molecule size in solution had increased from that of the deprotected $(N_3)_1$-RhMOP (2.6 ± 0.2 nm) or the deprotected $(alkyne)_1$-RhMOP (2.3 ± 0.3 nm), to that of the MOP-dimer (6.3 ± 1.1 nm) (Fig. 3a, S24, S30 and S40†).

To confirm that the two MOPs in MOP-dimer were linked through a covalent bond (*i.e.* the triazole ring formed upon the CuAAC reaction) and not simply entangled through supramolecular PEG-MOP interactions, we submitted it to acid digestion and then, analysed the resultant ligands through ^{1}H-NMR (Fig. 2d). The spectrum of the isolated PEG linker clearly showed a peak at 8.11 ppm, which can be ascribed to the proton of the expected triazole ring (Fig. S35–S37†). Further analysis of the relative integration of the triazole ring and the aromatic core belonging to the Rh-MOP confirmed that every 1-c Rh-MOP was linked through a triazole ring. Together, these data confirmed that the two MOPs had indeed been assembled into one new dimer, thus corroborating our original idea that this could be accomplished by strategically controlling the number of reactive sites on the surface of the MOP precursors, and then subjecting them to orthogonal click chemistry.

Increasing the connectivity in the synthesis of oligomeric MOP-based molecules: a MOP-tetramer and a MOP-satellite

Having confirmed the viability of the MOP oligomerisation, we next targeted oligomeric structures having a higher number of MOP units. We began by synthesising a tetrameric structure in which four 1-c MOPs are linked to a single 4-c node that comprises a dirhodium paddlewheel unit (Fig. 1). The starting point was the $Rh_2(bdc)_4$ cluster, which has four available

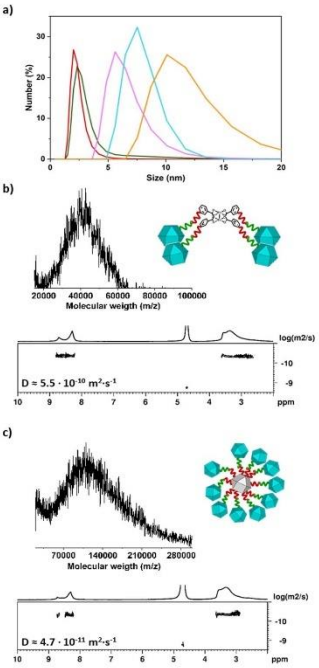

Fig. 3 (a) DLS spectra illustrating the differences in particle size (hydrodynamic-diameter) among the deprotected $(N_3)_1$-RhMOP (green), the deprotected $(alkyne)_1$-RhMOP (red), the MOP-dimer (violet), the MOP-tetramer (cyan) and the MOP-satellite (orange). (b and c) MALDI-TOF spectra (top) and DOSY-NMR spectra (bottom) of MOP-tetramer (b) and MOP-satellite (c).

carboxylic acid groups,[45] which were used to attach, *via* amide coupling, four alkyne-terminated NH_2-PEG$_b$-alkyne chains (Fig. S42–S45†). Next, $(N_3)_1$-RhMOP (10 mol eq.) was reacted with the synthesised alkyne-functionalised 4-c cluster in a mixture of CH_2Cl_2/DMF (1 : 1), using copper sulfate and sodium ascorbate as CuAAC catalysts. The reaction proceeded homogenously and, after 48 hours, it was quenched by extracting the crude reaction with 0.3 M HCl and water to remove the catalysts. The remaining organic solvent was removed *in vacuo*, and the resultant crude product was treated with TBAF to deprotect all the carboxylic acid groups present in the mixture. To purify the carboxylic acid-functionalised tetramer (hereafter, MOP-tetramer) from any unreacted 4-c

cluster or $(N_3)_1$-RhMOP, the crude product was dissolved in basic water, and then filtered using a centrifugal filter with a molecular weight cut-off of 30 kDa. The MOP-tetramer was retained, whereas the (smaller) 4-c cluster and $(N_3)_1$-RhMOP passed through the filter. The purified MOP-tetramer was characterised by MALDI-TOF, which confirmed the successful attachment of four MOPs to the 4-c cluster, as evidenced by a broad peak centred at 39 027 *m/z*, in agreement with the expected mass of a MOP-tetramer having a molecular formula of $[[(COOH\text{-}BDC)_{23}(BDC\text{-}PEG_{38}\text{-}1H\text{-}1,2,3\text{-}triazol\text{-}4\text{-}yl\text{-}PEG_6\text{-}BDC)_1\text{-}Rh_{24}]_4Rh_2 + H^-]^+$ (39 047 ± 1480 g mol^{-1}) (Fig. 3b and S48†). Moreover, the ^{1}H-NMR spectrum of MOP-tetramer in basic D_2O confirmed the expected ratio of aliphatic PEG protons to aromatic protons in the 1-c MOP and the 4-c cluster, which had the same diffusion coefficient of 5.5×10^{-10} m^2 s^{-1} (Fig. 3b, S46 and S47†). Importantly, the higher oligomeric degree of MOP-tetramer compared to MOP-dimer was corroborated analytically by its lower diffusion coefficient (5.5×10^{-10} m^2 s^{-1} *vs.* 6.2×10^{-10} m^2 s^{-1}) and by its greater particle-size (7.2 ± 0.6 nm *vs.* 6.3 ± 1.1 nm), as revealed by DLS (Fig. 3a and S50†).

Finally, to further extend the oligomeric degree of this family of MOP-based giant molecules, we sought to prepare a highly connected node. We reasoned that such a node could be synthesised from a cuboctahedral Rh-MOP, which can contain up to 24 reactive sites on its surface. Thus, a 24-c node was synthesised using a Rh-MOP with all its carboxylic acid groups available (hereafter, $COOH_{24}$-RhMOP). This entailed attaching 24 NH_2-PEG_6-alkyne chains, *via* amide-coupling chemistry, onto the surface of the $COOH_{24}$-RhMOP to afford a 24-c node (hereafter, $(alkyne)_{24}$-RhMOP). MALDI-TOF and ^{1}H-NMR spectroscopy confirmed the quantitative functionalisation of $COOH_{24}$-RhMOP into $(alkyne)_{24}$Rh-MOP (Fig. S52–S55†). Next, 24-c $(alkyne)_{24}$Rh-MOP was reacted with an excess of 1-c $(N_3)_1$-RhMOP (240 mol eq. per $(alkyne)_{24}$-RhMOP) in a CuAAC click reaction to yield a satellite-like, MOP-based, giant molecule. The reaction proceeded homogenously in a mixture of CH_2Cl_2/DMF (1 : 1), using the same CuAAC catalysts as above with the addition of tris(hydroxypropyltriazolylmethyl)amine (THPTA), for up to 14 days. Note that the chelating agent THPTA was used to further accelerate the reaction.[46,47] The solvent was removed *in vacuo* to afford the crude product, which was then treated with TBAF to yield a deprotected, satellite-like molecule (hereafter, MOP-satellite) in which all the peripheral MOPs contained 23 surface carboxylic-acid groups available for further reactions. MOP-satellite is soluble in basic water and could be separated from unreacted $(N_3)_1$-RhMOPs using a centrifugal filter with a molecular weight cut-off of 50 kDa. The isolated, purified MOP-satellite was first analysed through mass spectrometry, which revealed a peak centred at 107 346 *m/z*, which we ascribed to a satellite structure having 10 peripheral MOPs and a molecular formula of $[[((COOH\text{-}BDC)_{23}(BDC\text{-}PEG_{38}\text{-}1H\text{-}1,2,3\text{-}triazol\text{-}4\text{-}yl\text{-}PEG_6\text{-}BDC)_1\text{-}Rh_{24})_{10}(alkyne\text{-}PEG_6\text{-}BDC)_{14}Rh_{24}] + H^-]^+$ (expected molecular weight: 107 678 ± 3700 g mol^{-1}; Fig. 3c and S59†). This molecular composition was further supported by the ^{1}H-NMR spectrum of the MOP-satellite in basic D_2O, in which the ratio of aromatic protons to aliphatic PEG protons was 0.39; in agreement with the expected value for a satellite with 10 peripheral MOPs (0.41) (Fig. S57†). The aromatic and aliphatic signals displayed the same diffusion coefficient of 4.7×10^{-11} m^2 s^{-1} (Fig. 3c and S58†), which is the smallest value among those of the synthesised oligomeric MOP-based molecules, consistent with the MOP-satellite having the highest oligomeric degree and the largest molecule size (calculated: 8.6 nm; DLS value: 9.6 ± 0.8 nm (Fig. 3a and S61†). Finally, we also analysed the Na(I) to Rh(II) ratio of the fully deprotonated MOP-satellite salt through inductively coupled plasma mass spectrometry (ICP-MS). The experimentally observed ratio of Na : Rh molar ratio was 1.19, which agrees with the expected value (1.15) (Table S1†).

Study of the adsorption capabilities

Having prepared a family of giant oligomeric MOP-based molecules of increasing oligomeric degree, we next endeavoured to explore the functionality of the intrinsic voids stemming from their respective MOP cavities. We had envisioned that their oligomerisation would give rise to the first set of intrinsically porous oligomeric molecules. To demonstrate the permanent porosity of the three oligomeric MOP-based molecules, we subjected them to CO_2-adsorption/desorption experiments at 195 K (Fig. S63–S68†). The measurements confirmed that each giant molecule had retained the microporosity of its parent MOP, as evidenced by the corresponding isotherms, all of which exhibit a type-1 shape (Fig. 4). These isotherms were characterized by a sharp increase in the low-pressure range, followed by a plateau in the middle-to-high pressure range. This shape of the isotherm is consistent with the type-1 adsorption characteristic of microporous materials. The total CO_2-uptakes at 1 bar were: 54.4 mol mol^{-1} MOP unit (MOP-dimer), 30.8 mol mol^{-1} MOP unit (MOP-tetramer), and 35.1 mol mol^{-1} MOP unit

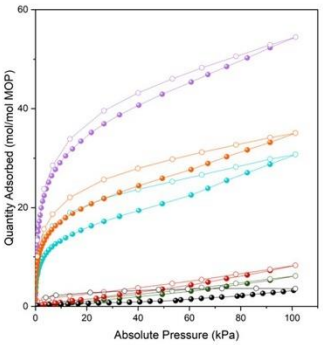

Fig. 4 Isotherms of CO_2-adsorption at 195 K for the deprotected $(N_3)_1$-RhMOP (green), the deprotected $(alkyne)_1$-RhMOP (red), the $(alkyne)_{24}$-RhMOP (black), the MOP-dimer (purple), the MOP-tetramer (blue), and the MOP-satellite (orange).

(MOP-satellite). We ascribed the higher uptake of MOP-dimer to its lack of dangling free PEG chains, which can block porosity; indeed, such chains are found in MOP-satellite. It can also be attributed to its absence of non-porous structuring units (*i.e.* cluster); for example, these units are found in the MOP-tetramer. Interestingly, CO_2-uptake was markedly higher for all the giant oligomeric molecules than for the deprotected 1-c $(N_3)_1$-RhMOP (6.1 mol mol^{-1} MOP unit), the deprotected 1-c $(alkyne)_1$-RhMOP (8.3 mol mol^{-1} MOP unit) and the 24-c $(alkyne)_{24}$-RhMOP (3.6 mol mol^{-1} MOP unit) precursors. We ascribed the greater porosity of the oligomeric molecules relative to their precursors to fact that the PEG chains are less mobile when they act as linkers in the former, than when they are dangling from the surface of the latter.

Conclusions

In summary, we have synthesised, characterised, and functionally validated a new class of giant oligomeric porous cage-based molecules. Namely, we developed a new method for the stepwise assembly of individual MOP cavities into oligomeric molecules, based on two factors that enable oligomerisation, rather than polymerisation. Firstly, the use of 1-c MOPs as building blocks enables termination of the linkage reaction at the oligomeric regime. Secondly, the use of an orthogonal reaction (in our case, CuAAC click chemistry) to link these blocks with other 1-c MOPs or with 4-c nodes or 24-c MOPs to yield molecules of increasing oligomeric degrees, precluding self-condensation between the precursors. Furthermore, gas-sorption experiments revealed that the giant oligomeric molecules retain the intrinsic porosity of the cavities of their parent MOP. We are confident that our results should inform the future design of new porous materials that will occupy the chemical and dimensional space between purely monomeric cavities and extended networks.

Author contributions

A. C. M.: conceptualization, methodology, investigation, and writing-original draft. C. v. B.: methodology and investigation. L. H. L.: validation and investigation. A. C. S: funding acquisition, conceptualization, supervision and writing-review and editing. D. M.: funding acquisition, conceptualization, supervision and writing-review and editing.

Conflicts of interest

There are no conflicts to declare.

Acknowledgements

This work has received funding from the Europa Excelencia grant (EUR2021-121997) and the Catalan AGAUR (project 2017 SGR 238). It was also funded by the CERCA Programme/Generalitat de Catalunya. ICN2 is supported by the Severo Ochoa Centres of Excellence programme, Grant CEX2021-001214-S, funded by MCIN/AEI/10.13039.501100011033. A. C. S. is indebted to the Ramón y Cajal Program (RYC2020-029749-I Fellowship). C. v. B. thanks the Austrian Science Fund (FWF), Erwin Schrödinger fellowship for supporting the project J 4637.

Notes and references

1 S. Lee, H. Jeong, D. Nam, M. S. Lah and W. Choe, *Chem. Soc. Rev.*, 2021, **50**, 528.
2 D. Zhang, T. K. Ronson, Y. Q. Zou and J. R. Nitschke, *Nat. Rev. Chem.*, 2021, **5**, 168.
3 T. Hasell and A. I. Cooper, *Nat. Rev. Mater.*, 2016, **1**, 16053.
4 G. Zhang and M. Mastalerz, *Chem. Soc. Rev.*, 2014, **43**, 1934.
5 A. J. Gosselin, C. A. Rowland and E. D. Bloch, *Chem. Rev.*, 2020, **120**, 8987.
6 O. K. Farha, I. Eryazici, N. C. Jeong, B. G. Hauser, C. E. Wilmer, A. A. Sarjeant, R. Q. Snurr, S. T. Nguyen, A. Ö. Yazaydin and J. T. Hupp, *J. Am. Chem. Soc.*, 2012, **134**, 15016.
7 N. Huang, P. Wang and D. Jiang, *Nat. Rev. Mater.*, 2016, **1**, 16068.
8 K. Geng, T. He, R. Liu, S. Dalapati, K. T. Tan, Z. Li, S. Tao, Y. Gong, Q. Jiang and D. Jiang, *Chem. Rev.*, 2020, **120**, 8814.
9 G. Maurin, C. Serre, A. Cooper and G. Férey, *Chem. Soc. Rev.*, 2017, **46**, 3104.
10 A. V. Virovets, E. Peresypkina and M. Scheer, *Chem. Rev.*, 2021, **121**, 14485.
11 J. V. Rival, P. Mymoona, K. M. Lakshmi, Nonappa, T. Pradeep and E. S. Shibu, *Small*, 2021, **17**, 1.
12 H. Wang, Y. Li, N. Li, A. Filosa and X. Li, *Nat. Rev. Mater.*, 2021, **6**, 145.
13 D. Fujita, Y. Ueda, S. Sato, N. Mizuno, T. Kumasaka and M. Fujita, *Nature*, 2016, **540**, 563.
14 X. G. Wang, Q. Cheng, Y. Yu and X. Z. Zhang, *Angew. Chem., Int. Ed.*, 2018, **57**, 7836.
15 F. Caddeo, R. Vogt, D. Weil, W. Sigle, M. E. Toimil-Molares and A. W. Maijenburg, *ACS Appl. Mater. Interfaces*, 2019, **11**, 25378.
16 X. Cai, Z. Xie, D. Li, M. Kassymova, S.-Q. Zang and H.-L. Jiang, *Coord. Chem. Rev.*, 2020, **417**, 213366.
17 J. Andreo, R. Ettlinger, O. Zaremba, Q. Peña, U. Lächelt, R. F. de Luis, R. Freund, S. Canossa, E. Ploetz, W. Zhu, C. S. Diercks, H. Gröger and S. Wuttke, *J. Am. Chem. Soc.*, 2022, **144**, 7531.
18 D. T. S. Rijkers, G. W. Van Esse, R. Merkx, A. J. Brouwer, H. J. F. Jacobs, R. J. Pieters and R. M. J. Liskamp, *Chem. Commun.*, 2005, **13**, 4581.
19 C. N. Urban, C. A. Bell, M. R. Whittaker and M. J. Monteiro, *Macromolecules*, 2008, **41**, 1057.
20 Z. Liu, S. Wang, G. Li, Z. Yang, Z. Gan and X. H. Dong, *Macromolecules*, 2022, **55**, 5954.
21 Y. Li, R. Biswas, W. P. Kopcha, T. Dubroca, L. Abella, Y. Sun, R. A. Crichton, C. Rathnam, L. Yang, Y. Yeh, K. Kundu, A. Rodriguez-Fortea, J. M. Poblet, K. Lee, S. Hill and J. Zhang, *Angew. Chem., Int. Ed.*, 2023, **62**, e202211704.
22 A. Muñoz, D. Sigwalt, B. M. Illescas, J. Luczkowiak, L. Rodriguez-Pérez, I. Nierengarten, M. Holler, J. S. Remy, K. Buffet, S. P. Vincent, J. Rojo, R. Delgado, J. F. Nierengarten and N. Martín, *Nat. Chem.*, 2016, **8**, 50.

23 A. Macdonell, N. A. B. Johnson, A. J. Surman and L. Cronin, *J. Am. Chem. Soc.*, 2015, **137**, 5662.
24 Z. Zhang, Y. Li, B. Song, Y. Zhang, X. Jiang, M. Wang, R. Tumbleson, C. Liu, P. Wang, X.-Q. Hao, T. Rojas, A. T. Ngo, J. L. Sessler, G. R. Newkome, S. W. Hla and X. Li, *Nat. Chem.*, 2020, **12**, 468.
25 G. F. S. Whitehead, F. Moro, G. A. Timco, W. Wernsdorfer, S. J. Teat and R. E. P. Winpenny, *Angew. Chem., Int. Ed.*, 2013, **52**, 9932.
26 T. Hasell, X. Wu, J. T. A. Jones, J. Bacsa, A. Steiner, T. Mitra, A. Trewin, D. J. Adams and A. I. Cooper, *Nat. Chem.*, 2010, **2**, 750.
27 M. Frank, M. D. Johnstone and G. H. Clever, *Chem.–Eur. J.*, 2016, **22**, 14104.
28 R. Zhu, I. Regeni, J. J. Holstein, B. Dittrich, M. Simon, S. Prévost, M. Gradzielski and G. H. Clever, *Angew. Chem., Int. Ed.*, 2018, **57**, 13652.
29 B. P. Benke, T. Kirschbaum, J. Graf, J. H. Gross and M. Mastalerz, *Nat. Chem.*, 2023, **15**, 413.
30 C. Yu, P. Yang, X. Zhu and Y. Wang, *Sci. China: Chem.*, 2022, **65**, 858.
31 C. Yu, Y. Yang and Y. Wang, *New J. Chem.*, 2021, **45**, 22049.
32 R. L. Greenaway, V. Santolini, F. T. Szczypiński, M. J. Bennison, M. A. Little, A. Marsh, K. E. Jelfs and A. I. Cooper, *Chem.–Eur. J.*, 2020, **26**, 3718.
33 A. Khobotov-Bakishev, L. Hernández-López, C. von Baeckmann, J. Albalad, A. Carné-Sánchez and D. Maspoch, *Adv. Sci.*, 2022, **9**, e2104753.
34 E. Sánchez-González, M. Y. Tsang, J. Troyano, G. A. Craig and S. Furukawa, *Chem. Soc. Rev.*, 2022, **51**, 4876–4889.
35 A. Fernandez, J. Ferrando-Soria, E. M. Pineda, F. Tuna, I. J. Vitorica-Yrezabal, C. Knappke, J. Ujma, C. A. Muryn, G. A. Timco, P. E. Barran, A. Ardavan and R. E. P. Winpenny, *Nat. Commun.*, 2016, **7**, 1.
36 S. Furukawa, N. Horike, M. Kondo, Y. Hijikata, A. Carné-Sánchez, P. Larpent, N. Louvain, S. Diring, H. Sato, R. Matsuda, R. Kawano and S. Kitagawa, *Inorg. Chem.*, 2016, **55**, 10843.
37 J. Albalad, L. Hernández-López, A. Carné-Sánchez and D. Maspoch, *Chem. Commun.*, 2022, **58**, 2443.
38 T. Grancha, A. Carné-Sánchez, F. Zarekarizi, L. Hernández-López, J. Albalad, A. Khobotov, V. Guillerm, A. Morsali, J. Juanhuix, F. Gándara, I. Imaz and D. Maspoch, *Angew. Chem.*, 2021, **133**, 5793.
39 J. Troyano, S. Horike and S. Furukawa, *J. Am. Chem. Soc.*, 2022, **144**, 19475.
40 A. Khobotov-Bakishev, C. von Baeckmann, B. Ortín-Rubio, L. Hernández-López, A. Cortés-Martínez, J. Martínez-Esaín, F. Gándara, J. Juanhuix, A. E. Platero-Prats, J. Faraudo, A. Carné-Sánchez and D. Maspoch, *J. Am. Chem. Soc.*, 2022, **144**, 15745.
41 A. J. Gosselin, G. E. Decker, A. M. Antonio, G. R. Lorzing, G. P. A. Yap and E. D. Bloch, *J. Am. Chem. Soc.*, 2020, **142**, 9594.
42 J. Albalad, A. Carné-Sánchez, T. Grancha, L. Hernández-López and D. Maspoch, *Chem. Commun.*, 2019, **55**, 12785.
43 L. Hernández-López, C. von Baeckmann, J. Martínez-Esaín, A. Cortés-Martínez, J. Faraudo, C. Caules, T. Parella, D. Maspoch and A. Carné-Sánchez, *Chem.–Eur. J.*, 2023, **29**, e202301945.
44 L. Avram and Y. Cohen, *Chem. Soc. Rev.*, 2015, **44**, 586.
45 C. von Baeckmann, S. Ruiz-Relaño, I. Imaz, M. Handke, J. Juanhuix, F. Gándara, A. Carné-Sanchez and D. Maspoch, *Chem. Commun.*, 2023, **59**, 3423.
46 V. Hong, S. I. Presolski, C. Ma and M. G. Finn, *Angew. Chem., Int. Ed.*, 2009, **48**, 9879.
47 C. Uttamapinant, A. Tangpeerachaikul, S. Grecian, S. Clarke, U. Singh, P. Slade, K. R. Gee and A. Y. Ting, *Angew. Chem., Int. Ed.*, 2012, **51**, 5852.

JACS
JOURNAL OF THE AMERICAN CHEMICAL SOCIETY
pubs.acs.org/JACS

Communication

Synthesis of Metal−Organic Cages via Orthogonal Bond Cleavage in 3D Metal−Organic Frameworks

Sara Ruiz-Relaño, Dongsik Nam, Jorge Albalad,* Alba Cortés-Martínez, Judith Juanhuix, Inhar Imaz,* and Daniel Maspoch*

Cite This: J. Am. Chem. Soc. 2024, 146, 26603−26608

ABSTRACT: Herein we address the question of whether a supramolecular finite metal−organic structure such as a cage or metal−organic polyhedron (MOP) can be synthesized via controlled cleavage of a three-dimensional (3D) metal−organic structure. To demonstrate this, we report the synthesis of a Cu(II)-based cuboctahedral MOP through orthogonal olefinic bond cleavage of the cavities of a 3D, Cu(II)-based, metal−organic framework (MOF). Additionally, we demonstrate that controlling the ozonolysis conditions used for the cleavage enables Clip-off Chemistry synthesis of two cuboctahedral MOPs that differ by their external functionalization: one in which all 24 external groups represent a mixture of aldehydes, carboxylic acids, acetals and esters, and one in which all are aldehydes.

Bond formation and bond breaking are fundamental chemical processes. Although bond formation has traditionally driven most chemical syntheses and technologies,[1−6] control of bond breaking at the molecular scale begun to garner interest due to its growing importance in emerging technologies and chemical strategies.[7−13] For example, controlling bond cleavage in organic polymers has become essential for improving their recyclability and for developing new closed-loop recycling processes.[14−17] Similarly, controlling bioorthogonal cleavage reactions has become crucial for liberating and activating prodrugs,[18] reactivating proteins,[19] and releasing bioconjugates.[20] In this context, we recently introduced the concept of Clip-off Chemistry, whereby we design and synthesize novel molecules and materials with well-defined structures through orthogonal bond cleavage within molecular structures.[21−23]

Among the various types of molecular structures, reticular materials stand out as particularly appealing precursors for Clip-off Chemistry.[24,25] Reticular materials can be viewed as the linkage of repetitive units or fragments that form when basic inorganic and/or organic building blocks are connected.[26−32] These units or fragments, which can include clusters, cages, macrocycles, chains and layers, among others, can exhibit new properties and functions on their own. Therefore, they hold promise as a new source of molecules or materials if isolated from the reticular precursor. We devised Clip-off Chemistry to isolate these units or fragments via cleavage of the bonds (*e.g.* olefinic bonds by ozonolysis)[33] that link them within reticular materials.

Herein, we report the first example of Clip-off Chemistry being applied to three-dimensional (3D) metal−organic frameworks (MOFs) to synthesize 0D metal−organic cages or polyhedra (MOPs).[29,34−42] This work entails the quantitative orthogonal bond cleavage within a 3D structure, followed by isolation and characterization of the unconnected, "released" MOPs (Figure 1).

To demonstrate the feasibility of this synthesis, we initially selected the 3D MOF **PCN-61** as our reticular precursor.[43] Within this **rht**-Cu-MOF, cuboctahedral $Cu_{24}bdc_{24}$ cavities (where bdc= 1,3-benzenedicarboxylate)[44] spontaneously form during the assembly of Cu(II) ions and the hexacarboxylate linker 5,5′,5″-benzene-1,3,5-triyltris(1-ethylnyl-2-isophthalate) (btei); a linker composed of three bdc moieties connected by a central phenyl ring at its 1, 3, and 5 positions via alkyne bonds. Each bdc moiety of btei contributes to the formation of a distinct cuboctahedral cavity, resulting in the 3D interconnection of different cavities in **PCN-61** through the central alkyne-benzene unit of this linker, which acts as a trigonal (3-c) symmetric node. Based on this structure, we reasoned that cleavage of the three alkyne bonds of btei through ozonolysis would release the cavities in the form of cuboctahedral Cu(II)-based MOPs (Figure 1). However, despite subjecting **PCN-61** to various ozonolysis conditions, we were unable to quantitatively cleave those alkyne bonds, which precluded us from synthesizing the isolated MOPs (Figure S1). Moreover, ozonolysis of alkynes requires the presence of water in the media,[45] which, as we observed, also promotes partial hydrolysis of the labile Cu-COO bonds.[46]

To enhance bond cleavage within this 3D structure using ozone, we chose to substitute all alkyne bonds in **PCN-61** with alkene bonds. This modification ensured that the cuboctahedral $Cu_{24}bdc_{24}$ cavities in the new structure would now be linked through alkene bonds, a type of bond that requires less aggressive conditions than alkynes to be ozonized and that we

Received: July 11, 2024
Revised: September 17, 2024
Accepted: September 17, 2024
Published: September 23, 2024

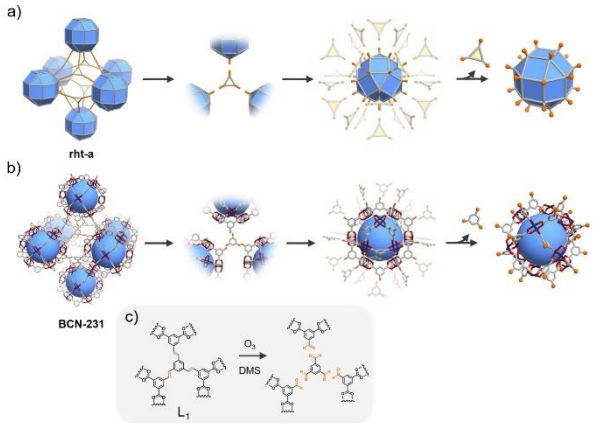

Figure 1. (a) Schematic of the synthesis and isolation of a cuboctahedral metal−organic polyhedron (MOP) via orthogonal bond cleavage of a 3D **rht** MOF. (b) Schematic of how the 3D **rht BCN-231** can be orthogonally cleaved on its alkene bonds to synthesize cuboctahedral MOPs with different external functionalities. (c) Cleavage, by ozonolysis, of the three olefinic bonds of L_1 needed to release the MOPs from the 3D framework. When the ozonolysis is performed using reductive workup (DMS = dimethyl sulfide, as reducing agent), all the olefinic bonds of the framework are selectively cleaved into aldehyde groups.

recently demonstrated could be quantitatively cleaved in reticular materials using ozone (Figure 1).[21−24] Additionally, controlling the workup steps after ozonolysis at low temperature can lead to the homolytic cleavage of alkene bonds.[17] Consequently, this control could facilitate the Clip-off synthesis of $Cu_{24}bdc_{24}$ cages or MOPs featuring only one type of functional group on the outer surface: for example, we envisioned that using reductive workup conditions would afford 24 aldehyde groups (Figure S2).

To this end, we initially synthesized the new hexacarboxylate linker 1,3,5-tris[5-(*E*)-vinylisophthalic acid]benzene (referred to as H_6L_1; Figure 1 and Figures S3−S5). Subsequently, crystals of the isoreticular **rht**-Cu-MOF (hereafter denoted as **BCN-231**) were obtained by reacting the new linker with $Cu(NO_3)_2{\cdot}2.5H_2O$ in *N*,*N*-dimethylformamide (DMF) at 70 °C for 48 h (Figure 2a, left). Single-crystal X-ray diffraction (SCXRD) confirmed the formation of the expected Cu-MOF exhibiting an underlying **rht**-topology. Within it, the assembled cuboctahedral cavities, reminiscent of cuboctahedral $Cu_{24}bdc_{24}$ MOPs, were periodically spaced through alkene-benzene units (Figure 1). Powder X-ray diffraction (PXRD) and N_2 sorption measurements validated the phase purity of **BCN-231** and revealed a remarkably high Brunauer−Emmett−Teller surface area (S_{BET}) of 3139 $m^2\ g^{-1}$ (Figures S6−S11).

Having prepared **BCN-231**, we next proceeded with cleavage of its olefinic bonds. To this end, it was dispersed in methanol, and the resultant solution was treated with ozone at a constant flux (30 g Nm^{-3}) at room temperature. The disconnection and formation of MOP species became evident to the naked eye, as the solid suspension transitioned into a transparent blue solution within 10 min (Figure 2a). The ozonolysis reaction was monitored using ultraviolet−visible spectroscopy (UV−vis) and matrix-assisted laser desorption/ionization-time-of-flight mass spectrometry (MALDI-ToF-MS), with periodic analysis of the supernatant at t = 1, 5, and 10 min (Figures S12 and S13). UV−vis analysis of the solution revealed the presence of a broad band centered at 700 nm, characteristic of Cu(II) paddlewheel clusters, indicating that these clusters were not disassembled during the reaction.[18] Moreover, the MALDI-ToF-MS spectrum contained a broad peak ranging from approximately 5440 to 6856 m/z, consistent with the formation of a cuboctahedral Cu(II)-based MOP within the first minute of the reaction. Then, after ozonolysis, a blue solid was rapidly precipitated from the supernatant by the addition of ether and characterized by proton nuclear magnetic resonance (^{1}H NMR). ^{1}H NMR spectrum revealed the complete disappearance of alkene signals from **BCN-231** (δ = 7.66, 7.63, 7.49, and 7.46 ppm, Figure S14). It also revealed the emergence of new signals, which we attributed to a mixture of different ozonolysis products, including 5-formylisophthalic acid, 5-(dimethoxymethyl)isophthalic acid, benzene-1,3,5-tricarboxylic acid, and 5-(methoxycarbonyl)isophthalic acid, resulting from the uncontrolled oxidative cleavage of L_1 in methanol (Figures S2 and S14). Altogether, these results confirmed the selective cleavage of the alkene bonds, the release of the MOP from the framework, and the stability of the "released" MOP in solution.

Next, we attempted to crystallize the product by slowly evaporating off the solvent from the above ozonolysis product under ambient conditions, which afforded blue crystals (yield = 79%) suitable for SCXRD (Figure 2a, right). The SCXRD data confirmed formation of a multivariate cuboctahedral $Cu_{24}bdc_{24}$

https://doi.org/10.1021/jacs.4c09431
J. Am. Chem. Soc. 2024, 146, 26603−26608

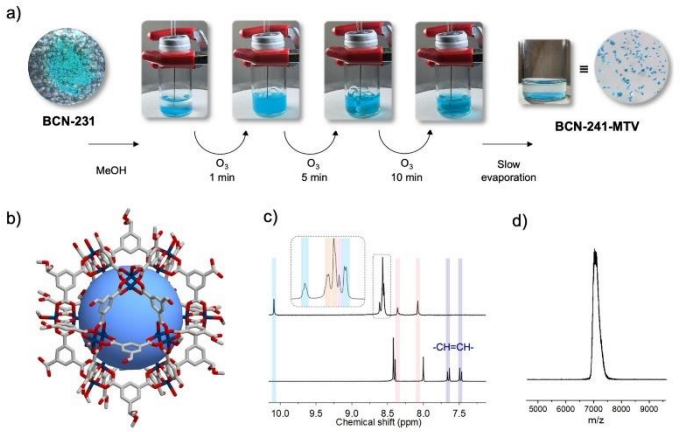

Figure 2. (a) Photographs of the synthesis of **BCN-241-MTV** via Clip-off Chemistry. From left to right: starting with a crystalline sample of **BCN-231**; introduction of these crystals into methanol; bubbling ozone into the methanolic dispersion, causing the cleavage of L_{ij} "dissolution" of **BCN-231** and release of the cuboctahedral MOPs; and finally, crystallization of cuboctahedral MOPs (Video S1). (b) SCXRD structure of **BCN-241-MTV**. Hydrogen atoms have been omitted for clarity. Cu(II): blue, O: red, C: gray. (c) ^{1}H NMR spectra (DMSO-d_6/DCl) of digested **BCN-241-MTV** (top) and **BCN-231** (bottom). Note the lack of alkene bond (violet) from initial **BCN-231**, and the displacement of bdc signals owing to the formation of **BCN-241-MTV** functionalized with aldehyde (coming from 5-formylisophthalic acid, blue), acetal (coming from 5-(dimethoxymethyl)isophthalic acid, red), carboxylic acid (coming from benzene-1,3,5-tricarboxylic acid, purple), and ester groups (coming from 5-(methoxycarbonyl)isophthalic acid, orange). (d) MALDI-ToF-MS spectrum of **BCN-241-MTV**.

MOP (hereafter denoted as **BCN-241-MTV**), comprising 12 Cu−Cu paddlewheel clusters connected through 24 5-substituted bdc linkers (Figure 2b). The external surface of each cage was decorated with a mixture of the aforementioned functional groups (aldehydes, acetals, carboxylic acids and esters) at the 5-position of the linker. According to SCXRD data, potentially disordered groups at the 5-position were approximated as follows: 10 aldehydes, 4 acetals, 2 carboxylic acids, and 8 esters. To further investigate the composition of the external surface of these cages, we analyzed the crystals of **BCN-241-MTV** by NMR. To this end, the crystals were digested in DMSO-d_6/DCl, and the products from three independent reactions were studied by ^{1}H NMR (Figure 2c, Figure S14). The average values for the external functional group distribution for **BCN-241-MTV** were: 9.6 ± 1.8 aldehydes, 4.1 ± 1.7 acetals, 1.4 ± 1.2 carboxylic acids, and 9.0 ± 2.8 esters (Table S3), a ratio similar to that observed in the single-crystal structure. MALDI-ToF-MS analysis of **BCN-241-MTV** revealed a broad peak ranging from 6860.3 to 7374.3 m/z (Figure 2d, Figure S15), which includes the mass of the single MOP cage with the average functional group composition and six DMF solvent molecules (expected: 7052.6 m/z). Interestingly, nitrogen-sorption measurements on **BCN-241-MTV** demonstrated its microporosity, revealing a N_2 uptake of 133 $cm^3\ g^{-1}$ at $P/P_0 = 0.95$ and a S_{BET} of up to 425 $m^2\ g^{-1}$. (Figure 3d, Figures S16−S20).

Having demonstrated our ability to orthogonally cleave bonds in **BCN-231** and subsequently isolate the unconnected cuboctahedral MOPs, we next endeavored to control the synthesis of the cuboctahedral MOPs whose 24 external functional groups were exclusively aldehydes (hereafter denoted as **BCN-241-CHO**), using reductive conditions. For this, we dispersed **BCN-231** in methanol and exposed the resulting dispersion to a constant ozone flux (30 g Nm^{-3}) for 10 min at −78 °C. This yielded a blue solution, into which was added dimethyl sulfide (DMS) as reducing agent. UV−vis analysis of the solution confirmed no degradation of the paddlewheel clusters upon DMS addition (Figure S21). Afterward, diethyl ether was added, and after 12 h, the resultant solution afforded blue crystals (yield = 62%).

SCXRD analysis of these crystals revealed the successful synthesis of the cuboctahedron-shaped Cu(II)-based cage functionalized with 24 aldehyde groups (Figure 3a). The exclusive presence of aldehyde groups on the surface of the MOP synthesized via Clip-off Chemistry was further confirmed by ^{1}H NMR of the acid-digested (DMSO-d_6/DCl) MOP product. In addition to the expected disappearance of olefinic protons of **BCN-231** at δ = 7.66, 7.63, 7.49, and 7.46 ppm, characteristic signals for 5-formylisophthalic acid (δ = 10.16, 8.68, and 8.62 ppm) were clearly identifiable (Figure 3b and Figure S22). Formation of **BCN-241-CHO** was also corroborated by MALDI-ToF-MS, where a sharp peak at 6200.7 m/z was observed, consistent with the expected molecular weight of $[Cu_{24}(CHO\text{-}bdc)_{24}+H^+]^+ \cdot 2$ MeOH (m/z= 6200.6) (Figure 3c, Figure S23). Furthermore, the phase purity of the sample was confirmed by the close match

https://doi.org/10.1021/jacs.4c09431
J. Am. Chem. Soc. 2024, 146, 26603−26608

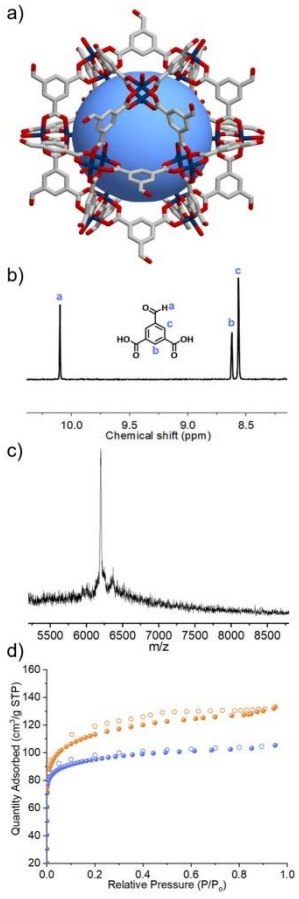

Figure 3. (a) SCXRD structure of **BCN-241-CHO**, showing the 24 aldehyde groups on the external surface of the MOP. Hydrogen atoms have been omitted for clarity. Cu(II): blue, O: red, C: gray. (b) ^{1}H NMR spectrum (DMSO-d_6/DCl) of digested **BCN-241-CHO**, showing exclusively the peaks corresponding to 5-formylisophthalic acid. (c) MALDI-ToF-MS spectrum of **BCN-241-CHO**. (d) N_2 isotherms (77 K) for **BCN-241-MTV** (orange) and **BCN-241-CHO** (blue).

between the experimental and simulated PXRD patterns for **BCN-241-CHO** (Figure S24). Finally, N_2-sorption measurements also showed this MOP to be porous, with a N_2 uptake of 105.4 cm^3 g^{-1} at P/P$_o$ = 0.95 and a S_{BET} of 368 m^2 g^{-1} (Figure 3d, Figures S25–S29).

In summary, we have reported the first-ever controlled synthesis and isolation of a metal–organic finite structure, such as a cage or MOP, through selective cleavage of olefinic bonds within a 3D MOF. By employing orthogonal olefinic bond cleavage, and optimizing the required ozonolysis, we successfully synthesized, via Clip-off Chemistry, two distinctly functionalized cuboctahedral cages. These findings underscore the versatility and potential applications of Clip-off Chemistry in synthesizing novel finite complex supramolecular architectures (*e.g.*, cages, catenanes, etc.) that can be derived from the structures found within the vast array of reported 2 and 3D MOFs.

■ ASSOCIATED CONTENT

Supporting Information

The Supporting Information is available free of charge at https://pubs.acs.org/doi/10.1021/jacs.4c09431.

Detailed synthesis and methods, NMR spectra, UV–vis spectra, mass spectrometry analysis, crystallographic data, FT-IR spectra, FE-SEM images, TGA analysis, PXRD diffractograms, and nitrogen adsorption–desorption isotherms (PDF)

Video showing the ozonolysis reaction for the clip-off synthesis of the cuboctahedral Cu(II)-based MOP (MP4)

Accession Codes

CCDC 2366265–2366266 and 2367002 contain the supplementary crystallographic data for this paper. These data can be obtained free of charge via www.ccdc.cam.ac.uk/data_request/cif, or by emailing data_request@ccdc.cam.ac.uk, or by contacting The Cambridge Crystallographic Data Centre, 12 Union Road, Cambridge CB2 1EZ, UK; fax: +44 1223 336033.

■ AUTHOR INFORMATION

Corresponding Authors

Jorge Albalad – *Catalan Institute of Nanoscience and Nanotechnology (ICN2), CSIC and Barcelona Institute of Science and Technology, 08193 Barcelona, Spain; Departament de Química, Facultat de Ciències, Universitat Autònoma de Barcelona, 08193 Barcelona, Spain;* orcid.org/0000-0001-5850-6723; Email: jorge.albalad@icn2.cat

Inhar Imaz – *Catalan Institute of Nanoscience and Nanotechnology (ICN2), CSIC and Barcelona Institute of Science and Technology, 08193 Barcelona, Spain; Departament de Química, Facultat de Ciències, Universitat Autònoma de Barcelona, 08193 Barcelona, Spain;* orcid.org/0000-0002-0278-1141; Email: inhar.imaz@icn2.cat

Daniel Maspoch – *Catalan Institute of Nanoscience and Nanotechnology (ICN2), CSIC and Barcelona Institute of Science and Technology, 08193 Barcelona, Spain; Departament de Química, Facultat de Ciències, Universitat Autònoma de Barcelona, 08193 Barcelona, Spain; ICREA, 08010 Barcelona, Spain;* orcid.org/0000-0003-1325-9161; Email: daniel.maspoch@icn2.cat

https://doi.org/10.1021/jacs.4c09431
J. Am. Chem. Soc. 2024, 146, 26603–26608

Authors

Sara Ruiz-Relaño – *Catalan Institute of Nanoscience and Nanotechnology (ICN2), CSIC and Barcelona Institute of Science and Technology, 08193 Barcelona, Spain; Departament de Química, Facultat de Ciències, Universitat Autònoma de Barcelona, 08193 Barcelona, Spain;* orcid.org/0009-0006-5681-8962

Dongsik Nam – *Catalan Institute of Nanoscience and Nanotechnology (ICN2), CSIC and Barcelona Institute of Science and Technology, 08193 Barcelona, Spain; Departament de Química, Facultat de Ciències, Universitat Autònoma de Barcelona, 08193 Barcelona, Spain;* orcid.org/0000-0002-9941-3504

Alba Cortés-Martínez – *Catalan Institute of Nanoscience and Nanotechnology (ICN2), CSIC and Barcelona Institute of Science and Technology, 08193 Barcelona, Spain; Departament de Química, Facultat de Ciències, Universitat Autònoma de Barcelona, 08193 Barcelona, Spain*

Judith Juanhuix – *Alba Synchrotron Light Facility, 08290 Barcelona, Spain;* orcid.org/0000-0003-3728-8215

Complete contact information is available at: https://pubs.acs.org/10.1021/jacs.4c09431

Notes

The authors declare no competing financial interest.

■ ACKNOWLEDGMENTS

This work has received funding from the European Union's Horizon 2020 research and innovation program under grant agreement No. 101019003, Grant ref. PID2021-124804NB-I00 funded by MCIN/AEI/10.13039/501100011033/and by "ERDF A way of making Europe", and the Catalan AGAUR (project 2021 SGR 00458). It was also funded by the CERCA program/Generalitat de Catalunya. ICN2 is supported by the Ochoa Centres of Excellence programme, Grant CEX2021-001214-S, funded by MCIN/AEI/10.13039.501100011033. D.N. acknowledges the Juan de la Cierva fellowship from Spanish Ministerio de Ciencia e Innovación.

■ REFERENCES

(1) Zhu, X.; Schmidt, R. R. New Principles for Glycoside-Bond Formation. *Angew. Chem., Int. Ed.* **2009**, *48*, 1900−1934.
(2) Blaser, H. U. Enantioselective Catalysis in Fine Chemicals Production. *Chem. Commun.* **2003**, 3 (3), 293−296.
(3) Brovetto, M.; Gamenara, D.; Saenz Méndez, P.; Seoane, G. A. C-C Bond-Forming Lyases in Organic Synthesis. *Chem. Rev.* **2011**, *111* (7), 4346−4403.
(4) Fritch, B.; Kosolapov, A.; Hudson, P.; Nissley, D. A.; Woodcock, H. L.; Deutsch, C.; O'Brien, E. P. Origins of the Mechanochemical Coupling of Peptide Bond Formation to Protein Synthesis. *J. Am. Chem. Soc.* **2018**, *140* (15), 5077−5087.
(5) Hili, R.; Yudin, A. K. Making Carbon-Nitrogen Bonds in Biological and Chemical Synthesis. *Nat. Chem. Biol.* **2006**, *2* (6), 284−287.
(6) Visco, M. D.; Wieting, J. M.; Mattson, A. E. Carbon-Silicon Bond Formation in the Synthesis of Benzylic Silanes. *Org. Lett.* **2016**, *18* (12), 2883−2885.
(7) Schmidt, S. W.; Kersch, A.; Beyer, M. K.; Clausen-Schaumann, H. Mechanically Activated Rupture of Single Covalent Bonds: Evidence of Force Induced Bond Hydrolysis. *Phys. Chem. Chem. Phys.* **2011**, *13* (13), 5994−5999.
(8) Xiao, Y.; Longo, J. M.; Hieshima, G. B.; Hill, R. J. Understanding the Kinetics and Mechanisms of Hydrocarbon Thermal Cracking: An Ab Initio Approach. *Ind. Eng. Chem. Res.* **1997**, *36* (10), 4033−4040.
(9) Gao, E.; Lin, S. Z.; Qin, Z.; Buehler, M. J.; Feng, X. Q.; Xu, Z. Mechanical Exfoliation of Two-Dimensional Materials. *J. Mech. Phys. Solids* **2018**, *115*, 248−262.
(10) Kanarik, K. J.; Tan, S.; Gottscho, R. A. Atomic Layer Etching: Rethinking the Art of Etch. *J. Phys. Chem. Lett.* **2018**, *9* (16), 4814−4821.
(11) Wang, J.; Wang, X.; Fan, X.; Chen, P. R. Unleashing the Power of Bond Cleavage Chemistry in Living Systems. *ACS Cent. Sci.* **2021**, *7* (6), 929−943.
(12) Shieh, P.; Hill, M. R.; Zhang, W.; Kristufek, S. L.; Johnson, J. A. Clip Chemistry: Diverse (Bio)(Macro)Molecular and Material Function through Breaking Covalent Bonds. *Chem. Rev.* **2021**, *121* (12), 7059−7121.
(13) Klán, P.; Šolomek, T.; Bochet, C. G.; Blanc, A.; Givens, R.; Rubina, M.; Popik, V.; Kostikov, A.; Wirz, J. Photoremovable Protecting Groups in Chemistry and Biology: Reaction Mechanisms and Efficacy. *Chem. Rev.* **2013**, *113* (1), 119−191.
(14) Lefay, C.; Guillaneuf, Y. Recyclable/Degradable Materials via the Insertion of Labile/Cleavable Bonds Using a Comonomer Approach. *Prog. Polym. Sci.* **2023**, *147*, 101764.
(15) Ko, K.; Lundberg, D. J.; Johnson, A. M.; Johnson, J. A. Mechanism-Guided Discovery of Cleavable Comonomers for Backbone Deconstructable Poly(Methyl Methacrylate). *J. Am. Chem. Soc.* **2024**, *146* (13), 9142−9154.
(16) Hu, Y.; Wang, L.; Kevlishvili, I.; Wang, S.; Chiou, C. Y.; Shieh, P.; Lin, Y.; Kulik, H. J.; Johnson, J. A.; Craig, S. L. Self-Amplified HF Release and Polymer Deconstruction Cascades Triggered by Mechanical Force. *J. Am. Chem. Soc.* **2024**, *146* (14), 10115−10123.
(17) Delplace, V.; Nicolas, J. Degradable Vinyl Polymers for Biomedical Applications. *Nat. Chem.* **2015**, *7* (10), 771−784.
(18) Li, J.; Jia, S.; Chen, P. R. Diels-Alder Reaction-Triggered Bioorthogonal Protein Decaging in Living Cells. *Nat. Chem. Biol.* **2014**, *10* (12), 1003−1005.
(19) Wang, X.; Liu, Y.; Fan, X.; Wang, J.; Ngai, W. S. C.; Zhang, H.; Li, J.; Zhang, G.; Lin, J.; Chen, P. R. Copper-Triggered Bioorthogonal Cleavage Reactions for Reversible Protein and Cell Surface Modifications. *J. Am. Chem. Soc.* **2019**, *141* (43), 17133−17141.
(20) Van Onzen, A. H. A. M.; Versteegen, R. M.; Hoeben, F. J. M.; Filot, I. A. W.; Rossin, R.; Zhu, T.; Wu, J.; Hudson, P. J.; Janssen, H. M.; Ten Hoeve, W.; Robillard, M. S. Bioorthogonal Tetrazine Carbamate Cleavage by Highly Reactive Trans-Cyclooctene. *J. Am. Chem. Soc.* **2020**, *142* (25), 10955−10963.
(21) Yang, Y.; Broto-Ribas, A.; Ortín-Rubio, B.; Imaz, I.; Gándara, F.; Carné-Sánchez, A.; Guillerm, V.; Jurado, S.; Busqué, F.; Juanhuix, J.; Maspoch, D. Clip-off Chemistry: Synthesis by Programmed Disassembly of Reticular Materials. *Angew. Chem., Int. Ed.* **2022**, *61*, e202111228.
(22) Broto-Ribas, A.; Ruiz-Relaño, S.; Albalad, J.; Yang, Y.; Gándara, F.; Juanhuix, J.; Imaz, I.; Maspoch, D. Retrosynthetic Analysis Applied to Clip-off Chemistry: Synthesis of Four Rh(II)-Based Complexes as Proof-of-Concept. *Angew. Chem., Int. Ed.* **2023**, *62*, e202310354.
(23) Yang, Y.; Fernández-Seriñán, P.; Imaz, I.; Gándara, F.; Handke, M.; Ortín-Rubio, B.; Juanhuix, J.; Maspoch, D. Isoreticular Contraction of Metal-Organic Frameworks Induced by Cleavage of Covalent Bonds. *J. Am. Chem. Soc.* **2023**, *145* (31), 17398−17405.
(24) Albalad, J.; Xu, H.; Gándara, F.; Haouas, M.; Martineau-Corcos, C.; Mas-Ballesté, R.; Barnett, S. A.; Juanhuix, J.; Imaz, I.; Maspoch, D. Single-Crystal-to-Single-Crystal Postsynthetic Modification of a Metal-Organic Framework via Ozonolysis. *J. Am. Chem. Soc.* **2018**, *140* (6), 2028−2031.
(25) Guillerm, V.; Xu, H.; Albalad, J.; Imaz, I.; Maspoch, D. Postsynthetic Selective Ligand Cleavage by Solid-Gas Phase Ozonolysis Fuses Micropores into Mesopores in Metal-Organic Frameworks. *J. Am. Chem. Soc.* **2018**, *140* (44), 15022−15030.
(26) Yaghi, O. M.; O'Keeffe, M.; Ockwig, N. W.; Chae, H. K.; Eddaoudi, M.; Kim, J. Reticular Synthesis and the Design of New Materials. *Nature* **2003**, *423* (6941), 705−714.

(27) Kitagawa, S.; Kitaura, R.; Noro, S. I. Functional Porous Coordination Polymers. *Angew. Chem., Int. Ed.* **2004**, *43* (18), 2334−2375.
(28) Tranchemontagne, D. J.; Mendoza-Cortes, J. L.; O'Keeffe, M.; Yaghi, O. M. Secondary Building Units, Nets and Bonding in the Chemistry of Metal−Organic Frameworks. *Chem. Soc. Rev.* **2009**, *38* (5), 1257−1283.
(29) Tranchemontagne, D. J.; Ni, Z.; O'Keeffe, M.; Yaghi, O. M. Reticular Chemistry of Metal-Organic Polyhedra. *Angew. Chem., Int. Ed.* **2008**, *47* (28), 5136−5147.
(30) Su, K.; Wang, W.; Du, S.; Ji, C.; Zhou, M.; Yuan, D. Reticular Chemistry in the Construction of Porous Organic Cages. *J. Am. Chem. Soc.* **2020**, *142* (42), 18060−18072.
(31) Ding, S. Y.; Wang, W. Covalent Organic Frameworks (COFs): From Design to Applications. *Chem. Soc. Rev.* **2013**, *42* (2), 548−568.
(32) Feng, X.; Ding, X.; Jiang, D. Covalent Organic Frameworks. *Chem. Soc. Rev.* **2012**, *41* (18), 6010−6022.
(33) Criegee, R. Mechanism of Ozonolysis. *Angew. Chem., Int. Ed.* **1975**, *14* (11), 745−752.
(34) Lee, S.; Jeong, H.; Nam, D.; Lah, M. S.; Choe, W. The Rise of Metal-Organic Polyhedra. *Chem. Soc. Rev.* **2021**, *50* (1), 528−555.
(35) Gosselin, A. J.; Rowland, C. A.; Bloch, E. D. Permanently Microporous Metal-Organic Polyhedra. *Chem. Rev.* **2020**, *120* (16), 8987−9014.
(36) Mollick, S.; Fajal, S.; Mukherjee, S.; Ghosh, S. K. Stabilizing Metal−Organic Polyhedra (MOP): Issues and Strategies. *Chem. Asian J.* **2019**, *14* (18), 3096−3108.
(37) Li, J. R.; Zhou, H. C. Bridging-Ligand-Substitution Strategy for the Preparation of Metal-Organic Polyhedra. *Nat. Chem.* **2010**, *2* (10), 893−898.
(38) Tateishi, T.; Yoshimura, M.; Tokuda, S.; Matsuda, F.; Fujita, D.; Furukawa, S. Coordination/Metal−Organic Cages inside Out. *Coord. Chem. Rev.* **2022**, *467*, 214612.
(39) Zarra, S.; Wood, D. M.; Roberts, D. A.; Nitschke, J. R. Molecular Containers in Complex Chemical Systems. *Chem. Soc. Rev.* **2015**, *44* (2), 419−432.
(40) Fujita, D.; Ueda, Y.; Sato, S.; Mizuno, N.; Kumasaka, T.; Fujita, M. Self-Assembly of Tetravalent Goldberg Polyhedra from 144 Small Components. *Nature* **2016**, *540* (7634), 563−566.
(41) Cook, T. R.; Stang, P. J. Recent Developments in the Preparation and Chemistry of Metallacycles and Metallacages via Coordination. *Chem. Rev.* **2015**, *115* (15), 7001−7045.
(42) Prakash, M. J.; Lah, M. S. Metal-Organic Macrocycles, Metal-Organic Polyhedra and Metal-Organic Frameworks. *Chem. Commun.* **2009**, 3326−3341.
(43) Zhao, D.; Yuan, D.; Sun, D.; Zhou, H. C. Stabilization of Metal-Organic Frameworks with High Surface Areas by the Incorporation of Mesocavities with Microwindows. *J. Am. Chem. Soc.* **2009**, *131* (26), 9186−9188.
(44) Eddaoudi, M.; Kim, J.; Wachter, J. B.; Chae, H. K.; O'Keeffe, M.; Yaghi, O. M. Porous Metal-Organic Polyhedra: 25 Å Cuboctahedron Constructed from 12 $Cu_2(CO_2)_4$ Paddle-Wheel Building Blocks. *J. Am. Chem. Soc.* **2001**, *123* (18), 4368−4369.
(45) Silbert, L. S.; Foglia, T. A. Analysis of Alkynes and Alkynoic Esters by Ozonolysis. *Anal. Chem.* **1985**, *57* (7), 1404−1407.
(46) Low, J. J.; Benin, A. I.; Jakubczak, P.; Abrahamian, J. F.; Faheem, S. A.; Willis, R. R. Virtual High Throughput Screening Confirmed Experimentally: Porous Coordination Polymer Hydration. *J. Am. Chem. Soc.* **2009**, *131* (43), 15834−15842.
(47) Appell, R. B.; Tomlinson, I. A.; Hill, I. New Reagents for the Reductive Quenching of Ozonolysis Reactions. *Synth. Commun.* **1995**, *25* (22), 3589−3595.
(48) Mosae Selvakumar, P.; Nadella, S.; Sahoo, J.; Suresh, E.; Subramanian, P.S. Copper(II) Bis-Chelate Paddle Wheel Complex and Its Bipyridine/ Phenanthroline Adducts. *J. Coord. Chem.* **2013**, *66* (2), 287−299.

https://doi.org/10.1021/jacs.4c09431
J. Am. Chem. Soc. 2024, 146, 26603−26608

JACS
JOURNAL OF THE AMERICAN CHEMICAL SOCIETY
pubs.acs.org/JACS

Communication

Isolation of the Secondary Building Unit of a 3D Metal−Organic Framework through Clip-Off Chemistry, and Its Reuse To Synthesize New Frameworks by Dynamic Covalent Chemistry

Dongsik Nam, Jorge Albalad, Roberto Sánchez-Naya, Sara Ruiz-Relaño, Alba Cortés-Martínez, Yunhui Yang, Judith Juanhuix, Inhar Imaz,* and Daniel Maspoch*

Cite This: J. Am. Chem. Soc. 2024, 146, 27255−27261

Read Online

ACCESS | Metrics & More | Article Recommendations | Supporting Information

ABSTRACT: Herein, we present a novel methodology for synthesizing metal clusters or secondary building units (SBUs) that are subsequently employed to construct innovative metal−organic frameworks (MOFs) via dynamic covalent chemistry. Our approach entails extraction of SBUs from preformed MOFs through complete disassembly by clip-off chemistry. The initial MOF precursor is designed to incorporate the desired SBU, connected exclusively by cleavable linkers (in this study, with olefinic bonds). Cleavage of all the organic linkers (in this study, via ozonolysis under reductive conditions) liberates the SBUs functionalized with aldehyde groups. Once synthesized, these SBUs can be further reacted with amines in dynamic covalent chemistry to build new, rationally designed MOFs.

Metal−organic frameworks (MOFs) are crystalline porous materials composed of metal ions or clusters connected by organic linkers. The design approach for MOFs has gradually shifted from serendipity to rational methods.[1,2] Among synthetic strategies, the use of secondary building units (SBUs) has been pivotal in the systematic design and construction of MOFs.[1] These SBUs, which are formed by coordinating metal ions or clusters with organic linkers, determine the overall topology and properties of the resulting MOF, including its porosity and chemical reactivity. Today, myriad SBUs with diverse compositions, geometries, sizes and connectivities are well-documented.[3] Thus, predicting their formation by combination of the basic metal and organic building blocks is essential for the rational design of MOFs. However, chemical reactions involving metal ions remain complex and sensitive to experimental conditions,[4,5] often necessitating synthetic optimization for target SBUs, which relies heavily on trial and error.

One strategy to reduce uncertainty in this chemistry involves the use of presynthesized SBUs for constructing MOFs.[6−11] Early efforts included synthesizing discrete Zr_6-based SBUs and subsequently forming extended Zr-based MOFs through linker exchange. For example, Guillerm et al. synthesized a Zr_6-based cluster with monocarboxylate ligands and assembled UiO-66-type MOFs by introducing additional dicarboxylate linkers.[7] Subsequently, Zr_{12} and Zr_{16} clusters were also utilized to create Zr-based MOFs via linker exchange, as demonstrated by Bezrukov et al. and Hou et al.[9,10] However, in these studies, while the Zr clusters were incorporated into the resulting MOFs, the linker exchange processes could alter the coordination environment and final connectivity of the clusters, thereby introducing uncertainty into predicting formation of the resultant MOFs.

Different approaches involving preformed SBUs have been demonstrated using dynamic covalent chemistry, commonly employed in the synthesis of covalent-organic frameworks (COFs).[12−22] Nguyen et al. synthesized Ti-based MOFs composed of Ti_6 SBUs linked via imine condensation.[23,24] Although these MOFs were formed through a one-pot reaction, this study showed promise by combining the chemistry of MOFs and COFs. Alternatively, stepwise synthesis using preformed SBUs was explored.[12−18] In 2019, Xu et al. synthesized a MOF by connecting ditopic amino-functionalized polyoxometalate with 4-connected aldehyde-based linkers.[12] In 2020, Wei et al. and Li et al. utilized Cu(I)-based trimeric SBUs featuring three terminal aldehyde groups to connect with ditopic amine linkers.[16,17] Despite these recent advances, the use of preformed SBUs to synthesize extended MOFs remains in its early stages, limited to only a few types of metal clusters. This limitation largely stems from the challenge of synthesizing metal clusters with the available functional linkers required for their use as extendable SBUs in constructing the desired MOFs.

Herein, we report a new approach for synthesizing metal clusters or SBUs, which involves extracting them from preformed MOFs through complete disassembly via clip-off chemistry (Figure 1a).[25−27] To achieve this, the initial MOF precursor must incorporate the targeted SBU, connected exclusively via linkers containing cleavable bonds (in this

Received: July 4, 2024
Revised: September 17, 2024
Accepted: September 24, 2024
Published: September 30, 2024

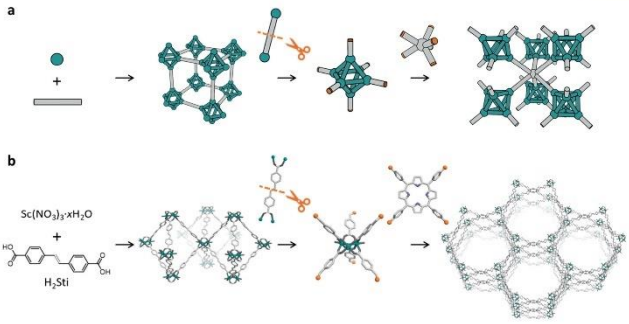

Figure 1. (a) Schematic illustrating our synthetic approach that entails isolating a SBU from a 3D MOF using clip-off chemistry. This SBU can then be reused to construct an extended framework. (b) Schematic illustrating application of our strategy to synthesize a 6-connected trimeric Sc^{3+} cluster terminated with aldehyde groups, and its subsequent extension through a 4-connected amine linker to form a 3D **stp** MOF.

study, olefinic bonds) (Figure 1b). Cleavage of all organic linkers via reductive ozonolysis releases the SBUs functionalized with terminal aldehyde groups. Thanks to these functional groups, these presynthesized SBUs can then undergo dynamic imine condensation to form novel MOFs with predictable topologies.

As a proof-of-concept to demonstrate our approach, we targeted the clip-off synthesis of the typical trimeric metal cluster with the general formula $M_3(\mu_3\text{-}O)(-COO)_6$ (M = Fe^{3+}, Sc^{3+}, Al^{3+}, In^{3+}, Cr^{3+}, V^{3+}, Mg^{2+}, $Co^{2+/3+}$, Ni^{2+}, $Mn^{2+/3+}$, Ga^{3+}), which has been among the most explored and versatile SBUs since this field began.[28−38] This SBU adopts a triangular prismatic geometry, establishing six connections to organic linkers. Among all metal ions, we selected the trimeric cluster, composed of Sc^{3+}, given the absence of similar clusters with available functional groups. In fact, to date, only one example using amino acids has been reported in the Cambridge Structural Database (No. CCDC-103179).[39]

When these 6-connected trimeric clusters are connected via six ditopic linkers, various archetypal MOFs and topologies can be formed, such as MIL-101 (**mtn** topology) or MIL-88 (**acs** topology).[6,34] Among these, we chose to synthesize a MOF precursor isoreticular to MIL-88, as it is known that the latter can be assembled using ditopic linkers of varying lengths.[37] One of these isoreticular MIL-88 analogs comprising long ditopic linkers is MIL-126, which contains two interpenetrated **acs** nets built up by connecting the Sc^{3+} clusters through biphenyl-4,4′-dicarboxylate linkers (Figure S1).[40−42] Accordingly, we attempted to synthesize a MIL-126 analog using the targeted Sc^{3+} clusters through a ditopic cleavable linker of similar length, 4,4′-stilbenedicarboxylic acid (H_2Sti). The reaction of scandium nitrate hydrate and H_2Sti in *N*,*N*-dimethylformamide (DMF) and concentrated HCl afforded a white crystalline material that was characterized to confirm its isoreticular relationship with MIL-126. To verify this, we used Materials Studio[43] to construct a model framework based on the structure of the two-interpenetrated MIL-126 with the $P4_12_12$ space group.[40] Geometric energy minimization of the model was performed with the Forcite module. The simulated powder X-ray diffraction (PXRD) pattern of the model closely matched the experimental pattern of the MIL-126 analog (Figure S2). A full-profile Pawley fitting was conducted, yielding final unit-cell parameters of a = 24.993(2) Å and c = 42.414(6) Å, with good agreement factors (R_p = 1.4% and R_{wp} = 3.5%), confirming the formation of the anticipated framework.

Once we had synthesized our MOF precursor, we then explored using clip-off chemistry to fully disconnect the MIL-88/MIL-126 type framework. We reasoned that this would enable synthesis of the trimeric Sc^{3+} oxocluster with molecular formula $[Sc_3O(COOC_6H_4CHO)_6(H_2O)_2(OH)]$, formed by six 4-formylbenzoate linkers. To this end, our MOF precursor was dispersed in methanol and exposed to a constant ozone flux (20 g Nm^{-3}) for 5 min at −10 °C (Figure 2a). The suspension was stirred for further 2 min with dimethyl sulfide (DMS) as the reducing agent.[44] The mixture was stirred for another hour at room temperature. Next, a clear supernatant was filtered from the suspension, and then concentrated in vacuo to afford a white solid (yield = 80%). Proton nuclear magnetic resonance (^{1}H NMR) spectrum of the solid showed a peak at 10.04 ppm, characteristic of aldehyde groups, and broad peaks at 8.54−7.65 ppm, attributed to the aromatic signals of 4-formylbenzoate linkers, resulting from the cleavage of Sti (Figures 2a and 2b). Moreover, we attributed this peak broadening to the presence of metal−organic Sc^{3+} complexes, as typically observed in metal−organic cages.[45] To further confirm the presence of 4-formylbenzoate in the solid, we digested it with a cesium fluoride solution in DMSO-d_6/D_2O, from which the ^{1}H NMR spectrum unambiguously confirmed the exclusive presence of free 4-formylbenzoic acid (Figure 2c). Finally, the formation and isolation of the expected Sc^{3+} cluster was corroborated by matrix-assisted laser desorption/ionization mass spectrometry (MALDI-MS). The spectrum exhibited two main peaks, at m/z = 1045.0 and 1123.0, corresponding to the theoretical values (m/z = 1045.0 and 1123.0) of the expected Sc^{3+} cluster with the molecular formula $[Sc_3O(COOC_6H_4CHO)_6]^+$ and $[Sc_3O(COOC_6H_4CHO)_6]^+$·DMSO (Figures 2d and S3).

https://doi.org/10.1021/jacs.4c09077
J. Am. Chem. Soc. 2024, 146, 27255−27261

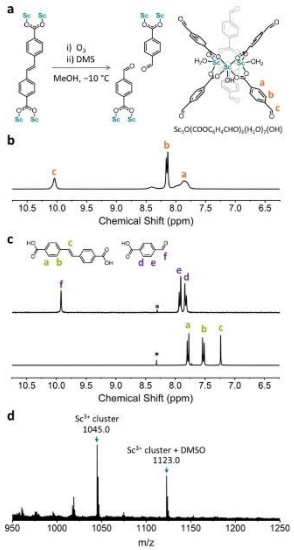

Figure 2. (a) Cleavage of the Sti linker under reductive conditions (left), and illustration of the Sc^{3+} cluster with terminal aldehyde groups (right). (b) ^{1}H NMR spectrum of the Sc^{3+} cluster in DMSO-d_6. (c) ^{1}H NMR spectra of the digested MOF precursor (bottom) and the Sc^{3+} cluster (top). Asterisks indicate formic acid. (d) MALDI-MS for the Sc^{3+} cluster.

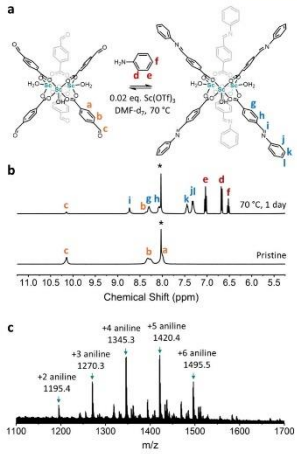

Figure 3. (a) Imine condensation between the Sc^{3+} cluster and aniline, using $Sc(OTf)_3$. (b) ^{1}H NMR spectra of pristine Sc^{3+} cluster (bottom), and the reaction (70 °C, 1 day) with aniline in DMF-d_7 (top). Asterisks indicate DMF. (c) MALDI-MS after reacting the Sc^{3+} cluster, aniline and $Sc(OTf)_3$.

We next sought to demonstrate the utility of this synthesized Sc^{3+} cluster by using it as a 6-connected building unit, given its six terminal aldehyde groups. To achieve this, we aimed to extend its functionality with amine-based linkers through imine condensation to create novel MOFs. A critical consideration in this process is the stability of the Sc^{3+} cluster during imine condensation reactions, which often require acetic acid as a catalyst for imine-bond formation.[46−48] Indeed, exposure of the synthesized cluster to 6 M acetic acid in DMF-d_7 led to its complete decomposition, resulting in peaks corresponding only to free 4-formylbenzoic acid (Figure S4). Alternatively, we chose $Sc(OTf)_3$ as a Lewis acid catalyst, renowned for its ability to facilitate the formation of imine-based COFs under milder conditions.[49] Under these modified conditions, the Sc^{3+} cluster exhibited stability, as confirmed by ^{1}H NMR spectroscopy (Figure S4). Following this approach, we investigated the feasibility of imine-bond formation by combining the Sc^{3+} cluster, featuring six terminal aldehyde groups, with aniline (Figure 3a). The reaction was run with 0.02 equiv. of $Sc(OTf)_3$ in DMF-d_7 at 70 °C for 3 days. After 1 day, the formation of *N*-(4-carboxybenzylidene)aniline via imine bond formation was evidenced by peaks at 8.74, 8.30, 8.10, 7.45, and 7.33 ppm in the ^{1}H NMR spectrum (Figure 3b). Over the next 2 days, similar ^{1}H NMR spectra were obtained, showing a total conversion of 80% (Figure S5). Additionally, peak broadening in these spectra suggested no degradation of the cluster species. Imine bond formation, and stability of the Sc^{3+} cluster, during this process were each confirmed by MALDI-MS, revealing peaks corresponding to the Sc^{3+} cluster having reacted with six, five, four, three, or two aniline molecules at m/z = 1495.5, 1420.4, 1345.3, 1270.3, and 1195.4, respectively (Figure 3c and Table S1). These values closely matched the theoretical values of m/z = 1495.3, 1420.2, 1345.2, 1270.1, and 1195.1. Formation of *N*-(4-carboxybenzylidene)aniline was confirmed by ^{1}H NMR analysis of a digested sample (Figure S6). Overall, these findings confirmed that our aldehyde-terminated Sc^{3+} cluster could undergo Schiff-base condensations with amines.

Next, we aimed to extend the 6-connected Sc^{3+} cluster with a 4-connected amine linker such as 5,10,15,20-tetrakis(4-aminophenyl)porphyrin (TAPP), which we envisioned would lead to a new 3D MOF with large pores and an underlying **stp** topology. However, our initial attempts to reproduce the above-mentioned conditions (using 0.02 equiv. $Sc(OTf)_3$, as typically employed in the synthesis of 2D-COFs) were unsuccessful, yielding only amorphous solids. At this point, we hypothesized that forming a crystalline 3D framework from highly connected aldehyde and amine building units would require greater reversibility in the imine chemistry to avoid any kinetic trapping that would lead to amorphous polymers. Interestingly, to the best of our knowledge, the synthesis of 3D

https://doi.org/10.1021/jacs.4c09077
J. Am. Chem. Soc. 2024, 146, 27255−27261

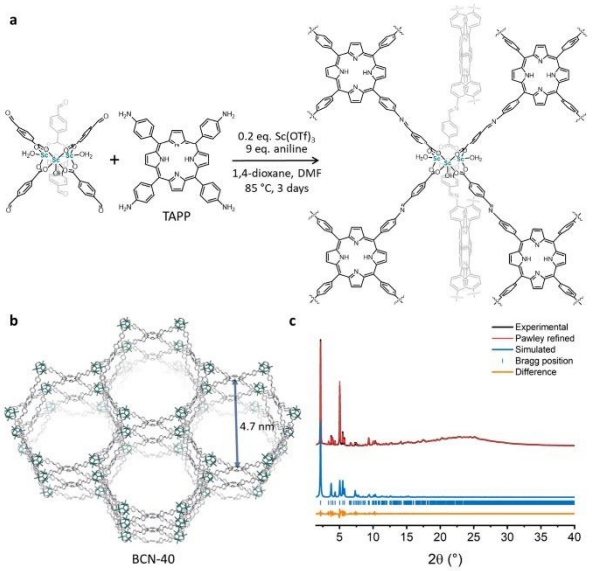

Figure 4. (a) Schematic for synthesis of BCN-40. (b) Proposed structure of BCN-40, featuring 4.7 nm-sized hexagonal channels. (c) PXRD pattern of BCN-40 in methanol, and the refined Pawley fitting.

COFs using $Sc(OTf)_3$ and both building blocks having a connectivity higher than 2 has never been demonstrated.[50,51] To this end, we increased the amount of $Sc(OTf)_3$ to accelerate the forward reaction, and incorporated aniline as a modulator competing with TAPP. We tested different stoichiometries and conditions, eventually obtaining a highly crystalline powder by using aldehyde-terminated Sc^{3+} cluster; TAPP; 0.2 equiv. $Sc(OTf)_3$; 9 equiv. aniline; dioxane/DMF (7:1 v/v) as solvent; 85 °C as the temperature; and 3 days as the time (Figure 4a). Field-emission scanning electron microscopy (FESEM), energy-dispersive X-ray (EDX) mapping, and X-ray photoelectron spectroscopy (XPS) of this solid revealed the formation of rodlike crystals (size: ~1 μm × 4 μm) with a homogeneous distribution of scandium, oxygen, and carbon, where the Sc ions retain the same oxidation state as in the original cluster (Figures S7 and S8). XPS also confirmed the presence of porphyrin moieties in the crystals. Additionally, characterization of this solid using ^{13}C cross-polarization magic angle spinning (CP-MAS) solid-state NMR confirmed the formation of imine bonds, with a characteristic imine carbon signal at ~161 ppm (Figure S9).[52]

To confirm the structural identity of the solid, we used Materials Studio to build and geometrically optimize a model of the target structure.[43] The proposed structure, named BCN-40, was built up from the 6-connected Sc^{3+} clusters linked by 4-connected planar TAPP, forming 1D hexagonal channels as large as 4.7 nm (Figure 4b). Remarkably, this theoretical pore width is the largest reported for **stp** MOFs since that of 3.1 nm had been observed in PCN-600 (Table S2).[53] A full profile Pawley fitting based on the model revealed final unit-cell parameters of a = 47.06(21) Å and c = 26.21(12) Å with good agreement factors (R_p = 1.6% and R_{wp} = 4.4%) (Figure 4c). The simulated PXRD pattern with these cell parameters matched well with the experimental pattern of the non-interpenetrated structure (Figure S10), confirming the successful synthesis of the expected **stp** 3D BCN-40. Porosity measurements after supercritical CO_2 activation revealed an N_2 uptake of 120 $cm^3\ g^{-1}$ at 77 K (Figure S11), indicating poor porosity, a common issue in mesoporous MOFs due to their weak mechanical stability after solvent removal.[54] However, in solution, mesopore accessibility in BCN-40 was confirmed through the adsorption of Vitamin B_{12}, a model molecule (dimensions: 1.41 nm × 1.83 nm × 1.14 nm) often used to evaluate pore accessibility in mesoporous MOFs (Figure S12).[55,56] A total uptake of 0.24 mg of Vitamin B_{12} per mg of BCN-40 was observed after 16 h of incubation.[53]

In summary, our results demonstrate that preformed SBUs or metal clusters within MOFs can be synthesized using clip-off chemistry and subsequently employed as building units for novel MOFs via dynamic covalent chemistry. Given the large

https://doi.org/10.1021/jacs.4c09077
J. Am. Chem. Soc. 2024, 146, 27255−27261

variety of SBUs and clusters in MOFs, some of which only exist in those frameworks, our approach will provide access to isolated, previously inaccessible clusters and more-complex building units at the molecular level.

■ ASSOCIATED CONTENT

Data Availability Statement

Supporting structure modeling of MIL-126 analog, BCN-40 and interpenetrated BCN-40 are available (for comparison purposes).

Supporting Information

The Supporting Information is available free of charge at https://pubs.acs.org/doi/10.1021/jacs.4c09077.

Detailed experimental section and characterization including PXRD diffractograms, ^{1}H NMR spectra, MALDI-ToF data, FESEM images, EDX elemental maps, XPS spectra, ^{13}C CP-MAS solid-state NMR spectrum, N_2 isotherm, and UV−vis spectrum (PDF)

■ AUTHOR INFORMATION

Corresponding Authors

Inhar Imaz − *Catalan Institute of Nanoscience and Nanotechnology (ICN2), CSIC and The Barcelona Institute of Science and Technology, Bellaterra 08193 Barcelona, Spain; Department of Chemistry, Autonomous University of Barcelona (UAB), Bellaterra 08193 Barcelona, Spain;* orcid.org/0000-0002-0278-1141; Email: inhar.imaz@icn2.cat

Daniel Maspoch − *Catalan Institute of Nanoscience and Nanotechnology (ICN2), CSIC and The Barcelona Institute of Science and Technology, Bellaterra 08193 Barcelona, Spain; Department of Chemistry, Autonomous University of Barcelona (UAB), Bellaterra 08193 Barcelona, Spain; ICREA, 08010 Barcelona, Spain;* orcid.org/0000-0003-1325-9161; Email: daniel.maspoch@icn2.cat

Authors

Dongsik Nam − *Catalan Institute of Nanoscience and Nanotechnology (ICN2), CSIC and The Barcelona Institute of Science and Technology, Bellaterra 08193 Barcelona, Spain; Department of Chemistry, Autonomous University of Barcelona (UAB), Bellaterra 08193 Barcelona, Spain;* orcid.org/0000-0002-9941-3504

Jorge Albalad − *Catalan Institute of Nanoscience and Nanotechnology (ICN2), CSIC and The Barcelona Institute of Science and Technology, Bellaterra 08193 Barcelona, Spain; Department of Chemistry, Autonomous University of Barcelona (UAB), Bellaterra 08193 Barcelona, Spain;* orcid.org/0000-0001-5850-6723

Roberto Sánchez-Naya − *Catalan Institute of Nanoscience and Nanotechnology (ICN2), CSIC and The Barcelona Institute of Science and Technology, Bellaterra 08193 Barcelona, Spain; Department of Chemistry, Autonomous University of Barcelona (UAB), Bellaterra 08193 Barcelona, Spain*

Sara Ruiz-Relaño − *Catalan Institute of Nanoscience and Nanotechnology (ICN2), CSIC and The Barcelona Institute of Science and Technology, Bellaterra 08193 Barcelona, Spain; Department of Chemistry, Autonomous University of Barcelona (UAB), Bellaterra 08193 Barcelona, Spain;* orcid.org/0009-0006-5681-8962

Alba Cortés-Martínez − *Catalan Institute of Nanoscience and Nanotechnology (ICN2), CSIC and The Barcelona Institute of Science and Technology, Bellaterra 08193 Barcelona, Spain; Department of Chemistry, Autonomous University of Barcelona (UAB), Bellaterra 08193 Barcelona, Spain*

Yunhui Yang − *Catalan Institute of Nanoscience and Nanotechnology (ICN2), CSIC and The Barcelona Institute of Science and Technology, Bellaterra 08193 Barcelona, Spain; Department of Chemistry, Autonomous University of Barcelona (UAB), Bellaterra 08193 Barcelona, Spain*

Judith Juanhuix − *Alba Synchrotron Light Facility, Cerdanyola del Vallès 08290 Barcelona, Spain;* orcid.org/0000-0003-3728-8215

Complete contact information is available at: https://pubs.acs.org/10.1021/jacs.4c09077

Notes

The authors declare no competing financial interest.

■ ACKNOWLEDGMENTS

This work was supported by the European Union's Horizon 2020 Research and Innovation Program, under Grant Agreement No. 101019003, Grant Ref. Nos. PID2021-124804NB-I00 and PID2021-123287OB-I00 funded by MCIN/AEI/10.13039/501100011033/ and by "ERDF A Way of Making Europe", and the Catalan AGAUR (Project No. 2021 SGR 00458). It was also funded by the CERCA program/Generalitat de Catalunya. ICN2 is supported by the Ochoa Centres of Excellence programme, Grant No. CEX2021-001214-S, funded by MCIN/AEI/10.13039.501100011033. D.N. acknowledges the Juan de la Cierva fellowship from Spanish Ministerio de Ciencia e Innovación. Y.Y. acknowledges the China Scholarship Council for scholarship support.

■ REFERENCES

(1) Kalmutzki, M. J.; Hanikel, N.; Yaghi, O. M. Secondary Building Units as the Turning Point in the Development of the Reticular Chemistry of MOFs. *Sci. Adv.* **2018**, *4* (10), eaat9180.

(2) Jiang, H.; Alezi, D.; Eddaoudi, M. A Reticular Chemistry Guide for the Design of Periodic Solids. *Nat. Rev. Mater.* **2021**, *6* (6), 466−487.

(3) Guillerm, V.; Eddaoudi, M. The Importance of Highly Connected Building Units in Reticular Chemistry: Thoughtful Design of Metal-Organic Frameworks. *Acc. Chem. Res.* **2021**, *54* (17), 3298−3312.

(4) Angeli, G. K.; Batzavali, D.; Mavronasou, K.; Tsangarakis, C.; Stuerzer, T.; Ott, H.; Trikalitis, P. N. Remarkable Structural Diversity between Zr/Hf and Rare-Earth MOFs via Ligand Functionalization and the Discovery of Unique (4, 8)-c and (4, 12)-Connected Frameworks. *J. Am. Chem. Soc.* **2020**, *142* (37), 15986−15994.

(5) Zou, L.; Feng, D.; Liu, T.-F.; Chen, Y.-P.; Yuan, S.; Wang, K.; Wang, X.; Fordham, S.; Zhou, H.-C. A Versatile Synthetic Route for the Preparation of Titanium Metal-Organic Frameworks. *Chem. Sci.* **2016**, *7* (2), 1063−1069.

(6) Serre, C.; Millange, F.; Surblé, S.; Férey, G. A Route to the Synthesis of Trivalent Transition-Metal Porous Carboxylates with Trimeric Secondary Building Units. *Angew. Chem., Int. Ed.* **2004**, *43* (46), 6285−6289.

(7) Guillerm, V.; Gross, S.; Serre, C.; Devic, T.; Bauer, M.; Férey, G. A Zirconium Methacrylate Oxocluster as Precursor for the Low-Temperature Synthesis of Porous Zirconium(IV) Dicarboxylates. *Chem. Commun.* **2010**, *46* (5), 767−769.

(8) Peng, L.; Asgari, M.; Mieville, P.; Schouwink, P.; Bulut, S.; Sun, D. T.; Zhou, Z.; Pattison, P.; van Beek, W.; Queen, W. L. Using Predefined $M_3(M_3$-O) Clusters as Building Blocks for an Isostructural

Series of Metal-Organic Frameworks. *ACS Appl. Mater. Interfaces* **2017**, *9* (28), 23957−23966.
(9) Bezrukov, A. A.; Törnroos, K. W.; Roux, E. L.; Dietzel, P. D. C. Incorporation of an Intact Dimeric Zr_{12} Oxo Cluster from a Molecular Precursor in a New Zirconium Metal-Organic Framework. *Chem. Commun.* **2018**, *54* (22), 2735−2738.
(10) Hou, B.; Qin, C.; Sun, C.; Wang, X.; Su, Z. Stepwise Construction of Multivariate Metal-Organic Frameworks from a Predesigned Zr_{16} Cluster. *CCS Chem.* **2021**, *3* (12), 287−293.
(11) Yuan, S.; Qin, J.-S.; Xu, H.-Q.; Su, J.; Rossi, D.; Chen, Y.; Zhang, L.; Lollar, C.; Wang, Q.; Jiang, H.-L.; Son, D. H.; Xu, H.; Huang, Z.; Zou, X.; Zhou, H.-C. $[Ti_8Zr_2O_{12}(COO)_{16}]$ Cluster: An Ideal Inorganic Building Unit for Photoactive Metal-Organic Frameworks. *ACS Cent. Sci.* **2018**, *4* (1), 105−111.
(12) Xu, W.; Pei, X.; Diercks, C. S.; Lyu, H.; Ji, Z.; Yaghi, O. M. A Metal-Organic Framework of Organic Vertices and Polyoxometalate Linkers as a Solid-State Electrolyte. *J. Am. Chem. Soc.* **2019**, *141* (44), 17522−17526.
(13) Yu, X.; Li, C.; Ma, Y.; Li, D.; Li, H.; Guan, X.; Yan, Y.; Valtchev, V.; Qiu, S.; Fang, Q. Crystalline, Porous, Covalent Polyoxometalate-Organic Frameworks for Lithium-Ion Batteries. *Microporous Mesoporous Mater.* **2020**, *299*, 110105.
(14) Ma, R.; Liu, N.; Lin, T.-T.; Zhao, T.; Huang, S.-L.; Yang, G.-Y. Anderson Polyoxometalate Built-in Covalent Organic Frameworks for Enhancing Catalytic Performances. *J. Mater. Chem. A* **2020**, *8* (17), 8548−8553.
(15) Zhao, Y.; Wang, Z.; Gao, J.; Zhao, Z.; Li, X.; Wang, T.; Cheng, P.; Ma, S.; Chen, Y.; Zhang, Z. COF-Inspired Fabrication of Two-Dimensional Polyoxometalate Based Open Frameworks for Biomimetic Catalysis. *Nanoscale* **2020**, *12* (41), 21218−21224.
(16) Wei, R.-J.; Zhou, H.-G.; Zhang, Z.-Y.; Ning, G.-H.; Li, D. Copper (I)-Organic Frameworks for Catalysis: Networking Metal Clusters with Dynamic Covalent Chemistry. *CCS Chem.* **2021**, *3* (7), 2045−2053.
(17) Li, X.; Wang, J.; Xue, F.; Wu, Y.; Xu, H.; Yi, T.; Li, Q. An Imine-Linked Metal-Organic Framework as a Reactive Oxygen Species Generator. *Angew. Chem., Int. Ed.* **2021**, *60* (5), 2534−2540.
(18) Zhou, J.; Li, J.; Kan, L.; Zhang, L.; Huang, Q.; Yan, Y.; Chen, Y.; Liu, J.; Li, S.-L.; Lan, Y.-Q. Linking Oxidative and Reductive Clusters to Prepare Crystalline Porous Catalysts for Photocatalytic CO_2 Reduction with H_2O. *Nat. Commun.* **2022**, *13* (1), 4681.
(19) Han, W.-K.; Liu, Y.; Yan, X.; Jiang, Y.; Zhang, J.; Gu, Z.-G. Integrating Light-Harvesting Ruthenium(II)-Based Units into Three-Dimensional Metal Covalent Organic Frameworks for Photocatalytic Hydrogen Evolution. *Angew. Chem., Int. Ed.* **2022**, *61* (40), e202208791.
(20) Chang, J.-N.; Li, Q.; Yan, Y.; Shi, J.-W.; Zhou, J.; Lu, M.; Zhang, M.; Ding, H.-M.; Chen, Y.; Li, S.-L.; Lan, Y.-Q. Covalent-Bonding Oxidation Group and Titanium Cluster to Synthesize a Porous Crystalline Catalyst for Selective Photo-Oxidation Biomass Valorization. *Angew. Chem., Int. Ed.* **2022**, *61* (37), e202209289.
(21) Li, Y.; Karimi, M.; Gong, Y.-N.; Dai, N.; Safarifard, V.; Jiang, H.-L. Integration of Metal-Organic Frameworks and Covalent Organic Frameworks: Design, Synthesis, and Applications. *Matter* **2021**, *4* (7), 2230−2265.
(22) Xiong, C.; Shao, Z.; Hong, J.; Bi, K.; Huang, Q.; Liu, C. Structural Survey of Metal-Covalent Organic Frameworks and Covalent Metal-Organic Frameworks. *Int. J. Miner. Metall. Mater.* **2023**, *30* (12), 2297−2309.
(23) Nguyen, H. L.; Gándara, F.; Furukawa, H.; Doan, T. L. H.; Cordova, K. E.; Yaghi, O. M. A Titanium-Organic Framework as an Exemplar of Combining the Chemistry of Metal- and Covalent-Organic Frameworks. *J. Am. Chem. Soc.* **2016**, *138* (13), 4330−4333.
(24) Nguyen, H. L.; Vu, T. T.; Le, D.; Doan, T. L. H.; Nguyen, V. Q.; Phan, N. T. S. A Titanium-Organic Framework: Engineering of the Band-Gap Energy for Photocatalytic Property Enhancement. *ACS Catal.* **2017**, *7* (1), 338−342.
(25) Yang, Y.; Broto-Ribas, A.; Ortín-Rubio, B.; Imaz, I.; Gándara, F.; Carné-Sánchez, A.; Guillerm, V.; Jurado, S.; Busqué, F.; Juanhuix, J.; Maspoch, D. Clip-off Chemistry: Synthesis by Programmed Disassembly of Reticular Materials. *Angew. Chem., Int. Ed.* **2022**, *61* (4), e202111228.
(26) Broto-Ribas, A.; Ruiz-Relaño, S.; Albalad, J.; Yang, Y.; Gándara, F.; Juanhuix, J.; Imaz, I.; Maspoch, D. Retrosynthetic Analysis Applied to Clip-off Chemistry: Synthesis of Four Rh(II)-Based Complexes as Proof-of-Concept. *Angew. Chem., Int. Ed.* **2023**, *62* (48), e202310354.
(27) Yang, Y.; Fernández-Seriñán, P.; Imaz, I.; Gándara, F.; Handke, M.; Ortín-Rubio, B.; Juanhuix, J.; Maspoch, D. Isoreticular Contraction of Metal-Organic Frameworks Induced by Cleavage of Covalent Bonds. *J. Am. Chem. Soc.* **2023**, *145* (31), 17398−17405.
(28) Mian, M. R.; Afrin, U.; Fataftah, M. S.; Idrees, K. B.; Islamoglu, T.; Freedman, D. E.; Farha, O. K. Control of the Porosity in Manganese Trimer-Based Metal-Organic Frameworks by Linker Functionalization. *Inorg. Chem.* **2020**, *59* (12), 8444−8450.
(29) Zhang, Y.-B.; Zhang, W.-X.; Feng, F.-Y.; Zhang, J.-P.; Chen, X.-M. A Highly Connected Porous Coordination Polymer with Unusual Channel Structure and Sorption Properties. *Angew. Chem., Int. Ed.* **2009**, *48* (29), 5287−5290.
(30) Zhang, X.-M.; Zheng, Y.-Z.; Li, C.-R.; Zhang, W.-X.; Chen, X.-M. Unprecedented (3,9)-Connected $(4^2.6)_3(4^6.6^{21}.8^9)$ Net Constructed by Trinuclear Mixed-Valence Cobalt Clusters. *Cryst. Growth Des.* **2007**, *7* (5), 980−983.
(31) Liu, Y.; Eubank, J. F.; Cairns, A. J.; Eckert, J.; Kravtsov, V. Ch.; Luebke, R.; Eddaoudi, M. Assembly of Metal-Organic Frameworks (MOFs) Based on Indium-Trimer Building Blocks: A Porous MOF with soc Topology and High Hydrogen Storage. *Angew. Chem., Int. Ed.* **2007**, *46* (18), 3278−3283.
(32) Loiseau, T.; Lecroq, L.; Volkringer, C.; Marrot, J.; Férey, G.; Haouas, M.; Taulelle, F.; Bourrelly, S.; Llewellyn, P. L.; Latroche, M. MIL-96, a Porous Aluminum Trimesate 3D Structure Constructed from a Hexagonal Network of 18-Membered Rings and M_3-Oxo-Centered Trinuclear Units. *J. Am. Chem. Soc.* **2006**, *128* (31), 10223−10230.
(33) Dietzel, P. D. C.; Blom, R.; Fjellvåg, H. A Scandium Coordination Polymer Constructed from Trimeric Octahedral Building Blocks and 2,5-Dihydroxyterephthalate. *Dalton Trans.* **2006**, *17*, 2055−2057.
(34) Férey, G.; Mellot-Draznieks, C.; Serre, C.; Millange, F.; Dutour, J.; Surblé, S.; Margiolaki, I. A Chromium Terephthalate-Based Solid with Unusually Large Pore Volumes and Surface Area. *Science* **2005**, *309* (5743), 2040−2042.
(35) Zhai, Q.-G.; Bu, X.; Mao, C.; Zhao, X.; Daemen, L.; Cheng, Y.; Ramirez-Cuesta, A. J.; Feng, P. An Ultra-Tunable Platform for Molecular Engineering of High-Performance Crystalline Porous Materials. *Nat. Commun.* **2016**, *7* (1), 13645.
(36) Barthelet, K.; Riou, D.; Férey, G. $[V^{III}(H_2O)]_3O(O_2CC_6H_4CO_2)_3\cdot(Cl, 9H_2O)$ (MIL-59): A Rare Example of Vanadocarboxylate with a Magnetically Frustrated Three-Dimensional Hybrid Framework. *Chem. Commun.* **2002**, *14*, 1492−1493.
(37) Serre, C.; Mellot-Draznieks, C.; Surblé, S.; Audebrand, N.; Filinchuk, Y.; Férey, G. Role of Solvent-Host Interactions That Lead to Very Large Swelling of Hybrid Frameworks. *Science* **2007**, *315* (5820), 1828−1831.
(38) Pang, M.; Cairns, A. J.; Liu, Y.; Belmabkhout, Y.; Zeng, H. C.; Eddaoudi, M. Highly Monodisperse M^{III}-Based soc-MOFs (M = In and Ga) with Cubic and Truncated Cubic Morphologies. *J. Am. Chem. Soc.* **2012**, *134* (32), 13176−13179.
(39) Yan, C.; Lu, Z.; Wang, Z.; Liao, C. CCDC 103179: Experimental Crystal Structure Determination. *CSD Commun.* **2001**, DOI: 10.5517/cc3gcc8.
(40) Dan-Hardi, M.; Chevreau, H.; Devic, T.; Horcajada, P.; Maurin, G.; Férey, G.; Popov, D.; Riekel, C.; Wuttke, S.; Lavalley, J.-C.; Vimont, A.; Boudewijns, T.; de Vos, D.; Serre, C. How Interpenetration Ensures Rigidity and Permanent Porosity in a Highly Flexible Hybrid Solid. *Chem. Mater.* **2012**, *24* (13), 2486−2492.
(41) Bara, D.; Wilson, C.; Mörtel, M.; Khusniyarov, M. M.; Ling, S.; Slater, B.; Sproules, S.; Forgan, R. S. Kinetic Control of Inter-

https://doi.org/10.1021/jacs.4c09077
J. Am. Chem. Soc. 2024, 146, 27255−27261

penetration in Fe-Biphenyl-4,4′-Dicarboxylate Metal-Organic Frameworks by Coordination and Oxidation Modulation. *J. Am. Chem. Soc.* **2019**, *141* (20), 8346−8357.
(42) Marshall, R. J.; Lennon, C. T.; Tao, A.; Senn, H. M.; Wilson, C.; Fairen-Jimenez, D.; Forgan, R. S. Controlling Interpenetration through Linker Conformation in the Modulated Synthesis of Sc Metal-Organic Frameworks. *J. Mater. Chem. A* **2018**, *6* (3), 1181−1187.
(43) *Materials Studio 7.0*; Dassault Systèmes BIOVIA: San Diego, CA, 2017.
(44) Van Ornum, S. G.; Champeau, R. M.; Pariza, R. Ozonolysis Applications in Drug Synthesis. *Chem. Rev.* **2006**, *106* (7), 2990−3001.
(45) Nam, D.; Kim, J.; Hwang, E.; Nam, J.; Jeong, H.; Kwon, T.-H.; Choe, W. Multivariate Porous Platform Based on Metal-Organic Polyhedra with Controllable Functionality Assembly. *Matter* **2021**, *4* (7), 2460−2473.
(46) Smith, B. J.; Overholts, A. C.; Hwang, N.; Dichtel, W. R. Insight into the Crystallization of Amorphous Imine-Linked Polymer Networks to 2D Covalent Organic Frameworks. *Chem. Commun.* **2016**, *52* (18), 3690−3693.
(47) Haase, F.; Lotsch, B. V. Solving the COF Trilemma: Towards Crystalline, Stable and Functional Covalent Organic Frameworks. *Chem. Soc. Rev.* **2020**, *49* (23), 8469−8500.
(48) Uribe-Romo, F. J.; Hunt, J. R.; Furukawa, H.; Klöck, C.; O'Keeffe, M.; Yaghi, O. M. A Crystalline Imine-Linked 3-D Porous Covalent Organic Framework. *J. Am. Chem. Soc.* **2009**, *131* (13), 4570−4571.
(49) Matsumoto, M.; Dasari, R. R.; Ji, W.; Feriante, C. H.; Parker, T. C.; Marder, S. R.; Dichtel, W. R. Rapid, Low Temperature Formation of Imine-Linked Covalent Organic Frameworks Catalyzed by Metal Triflates. *J. Am. Chem. Soc.* **2017**, *139* (14), 4999−5002.
(50) Zhu, Q.; Wang, X.; Clowes, R.; Cui, P.; Chen, L.; Little, M. A.; Cooper, A. I. 3D Cage COFs: A Dynamic Three-Dimensional Covalent Organic Framework with High-Connectivity Organic Cage Nodes. *J. Am. Chem. Soc.* **2020**, *142* (39), 16842−16848.
(51) Ma, X. Synthesis and Functionalization of Three-Dimensional Covalent Organic Frameworks. Thesis, 2019. http://deepblue.lib.umich.edu/handle/2027.42/153364, accessed July 2, 2024).
(52) Gong, C.; Yang, X.; Wei, X.; Dai, F.; Zhang, T.; Wang, D.; Li, M.; Jia, J.; She, Y.; Xu, G.; Peng, Y. Three-Dimensional Porphyrin-Based Covalent Organic Frameworks with stp Topology for an Efficient Electrocatalytic Oxygen Evolution Reaction. *Mater. Chem. Front.* **2023**, *7* (2), 230−237.
(53) Wang, K.; Feng, D.; Liu, T.-F.; Su, J.; Yuan, S.; Chen, Y.-P.; Bosch, M.; Zou, X.; Zhou, H.-C. A Series of Highly Stable Mesoporous Metalloporphyrin Fe-MOFs. *J. Am. Chem. Soc.* **2014**, *136* (40), 13983−13986.
(54) Peng, L.; Yang, S.; Jawahery, S.; Moosavi, S. M.; Huckaba, A. J.; Asgari, M.; Oveisi, E.; Nazeeruddin, M. K.; Smit, B.; Queen, W. L. Preserving Porosity of Mesoporous Metal-Organic Frameworks through the Introduction of Polymer Guests. *J. Am. Chem. Soc.* **2019**, *141* (31), 12397−12405.
(55) Chen, Y.; Hong, S.; Fu, C.-W.; Hoang, T.; Li, X.; Valencia, V.; Zhang, Z.; Perman, J. A.; Ma, S. Investigation of the Mesoporous Metal-Organic Framework as a New Platform to Study the Transport Phenomena of Biomolecules. *ACS Appl. Mater. Interfaces* **2017**, *9* (12), 10874−10881.
(56) Deng, H.; Grunder, S.; Cordova, K. E.; Valente, C.; Furukawa, H.; Hmadeh, M.; Gándara, F.; Whalley, A. C.; Liu, Z.; Asahina, S.; Kazumori, H.; O'Keeffe, M.; Terasaki, O.; Stoddart, J. F.; Yaghi, O. M. Large-Pore Apertures in a Series of Metal-Organic Frameworks. *Science* **2012**, *336* (6084), 1018−1023.

https://doi.org/10.1021/jacs.4c09077
J. Am. Chem. Soc. 2024, 146, 27255−27261

JACS
JOURNAL OF THE AMERICAN CHEMICAL SOCIETY
pubs.acs.org/JACS

Article

DNA-Based Networks Formed by Coordination Cross-Linking of DNA with Metal–Organic Polyhedra: From Gels to Aerogels to Hydrogels

Laura Hernández-López,[#] Akim Khobotov-Bakishev,[#] Alba Cortés-Martínez, Eduard Garrido-Ribó, Partha Samanta, Sergio Royuela, Félix Zamora, Daniel Maspoch,* and Arnau Carné-Sánchez*

Cite This: J. Am. Chem. Soc. 2025, 147, 16560−16567

ABSTRACT: Herein, we introduce a supramolecular method to form DNA-based networks by cross-linking DNA with Rh(II)-based metal−organic polyhedra (MOPs), which entails coordination of DNA to the exohedral Rh(II) axial sites of the MOP. The resultant highly connected networks can then be processed into gels, porous aerogels, or hydrogels, exhibiting properties suitable for pollutant removal and drug release.

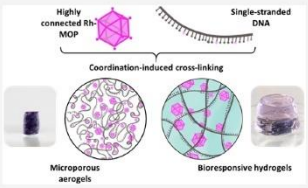

INTRODUCTION

DNA is an appealing natural polymer due to its unique capability to encode biological and chemical information on a biocompatible polymeric matrix, and to its high environmental responsiveness.[1−3] These features can be harnessed to develop functional materials for applications such as molecular delivery,[4] biorecognition and environmental protection.[5] The synthesis of DNA-based materials involves the cross-linkage of DNA into networks, which can be shaped into macroscopic functional objects, such as hydrogels and aerogels.[6,7] A common strategy for cross-linking DNA into purely DNA-based networks relies on the base pairing of complementary strands.[8] The reversible nature of this interaction yields responsive materials whose physicochemical and mechanical properties can be further enhanced when the network includes self-assembled structures of DNA[9] such as i-motifs,[10] G-quadruplexes,[11] DNA triplex structures[12] or aptamers.[13] Alternatively, the diversity of functional groups in DNA confers it with rich latent reactivity, allowing for the cross-linking of DNA strands with other materials through covalent bonding (between nucleobases),[14] hydrophobic interactions,[15] H-bonding,[16] physical entanglement,[17] coordinative bonds[18] and electrostatic interactions.[19]

Despite these advances, current synthetic strategies for DNA networks rely on cross-linkers with low connectivity (e.g., DNA junctions or end-functionalized linear polymers) or multivalent nodes with undefined connectivity due to their inherent polydispersity (e.g., polycationic polymers and inorganic nanoparticles). These limitations hinder the controlled synthesis of highly connected DNA networks with enhanced mechanical properties and stability. In contrast, the field of reticular materials has addressed this challenge through the supermolecular building block (SBB) approach,[20] which enables the design and construction of highly connected porous networks by incorporating in situ-formed or preassembled metal−organic (or organic) polyhedra (MOPs) as highly connected structural nodes.[21,22]

Herein, we introduce the SBB concept to the synthesis of DNA networks by using MOPs as molecularly precise, nanoscopic nodes with high connectivity. Specifically, we employ the robust, anionic, and water-soluble Rh(II)-based cuboctahedral MOP with the formula $Na_{24}[Rh_{24}O\text{-}BDC_{24}]$ (hereafter referred to as ONa-RhMOP, where O-BDC is 5-oxido-1,3-benzendicarboxylate) to facilitate the three-dimensional cross-linking of DNA into gels, aerogels, and hydrogels.[23] This MOP exhibits 24 sodium phenoxide groups on its external surface, conferring it with water solubility, and 12 Rh(II) axial sites that are suitable for coordinatively interacting with other species. In fact, this type of MOP has recently been employed as a 3D, 12-connected building block to construct amorphous and crystalline coordinative networks through connection with organic linkers or molecular clusters via the 12 Rh(II) axial sites.[24,25] Here, we propose that the high connectivity and molecular precision of ONa-RhMOP can be exploited to create highly cross-linked DNA networks,

Received: March 5, 2025
Revised: April 15, 2025
Accepted: April 22, 2025
Published: May 1, 2025

https://doi.org/10.1021/jacs.5c03934
J. Am. Chem. Soc. 2025, 147, 16560−16567

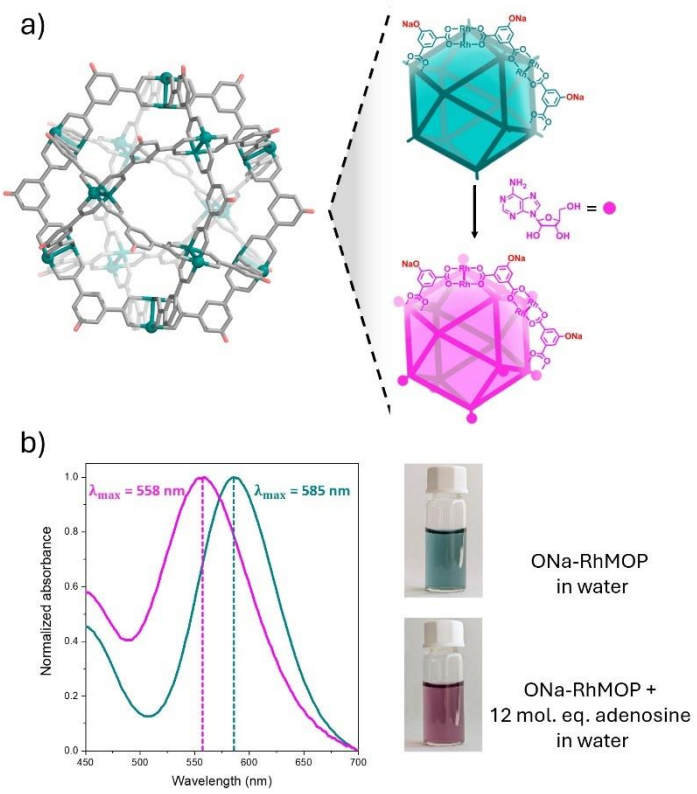

Figure 1. (a) Structure of ONa-RhMOP (left), and schematics of its coordination with adenosine (right). (b) UV−vis spectra and photographs of ONa-RhMOP before (green) and after (pink) its coordination to adenosine.

facilitating the transition from gels to robust aerogels and hydrogels. Accordingly, we selected genomic salmon sperm DNA with over 9000 bp (Figure S1), a surrogate of biomass-derived DNA,[26] as a sustainable, renewable and abundant source of DNA. The DNA-MOP networks displayed excellent mechanical properties in both the gel (storage modulus >10 KPa) and aerogel (Young's modulus >45 MPa) forms, which can be attributed to the high connectivity of the network. Additionally, the incorporation of MOP into the DNA network induced permanent microporosity in the aerogel, making it the first DNA network to exhibit this property. Furthermore, the hydrogel form demonstrated adsorptive capacity and triggered release for guest molecules, expanding the potential of DNA-based materials as robust adsorbents for both solid-state and liquid-phase applications.

RESULTS AND DISCUSSION

Synthesis and Formation Mechanism of DNA-MOP Gel Networks. We began by analyzing the coordinative interactions of the exposed Rh(II) axial sites of ONa-RhMOP with the N-donor atoms of the four nucleosides present in

https://doi.org/10.1021/jacs.5c03934
J. Am. Chem. Soc. 2025, 147, 16560−16567

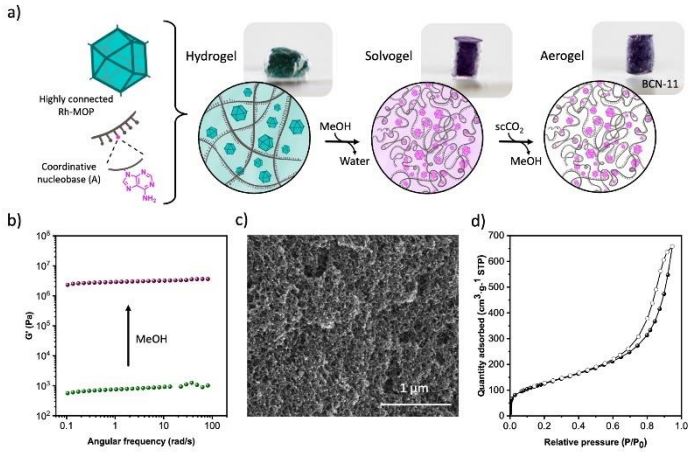

Figure 2. (a) Schematic of the formation mechanism of BCN-11. (b) Rheology measurements of DNA-MOP networks before (green) and after (purple) methanol exchange. (c) FE-SEM image of BCN-11_42. (d) N_2-sorption isotherm for BCN-11_42.

DNA. To this end, ONa-RhMOP was separately combined with 12 mol equivalents (mol eq.) of each of the nucleosides in basic water. UV−vis spectroscopy revealed that only adenosine coordinates to ONa-RhMOP through its N-donor atoms, as evidenced by a shift in the $\pi^* \rightarrow \sigma^*$ transition of Rh−Rh bonds (λ_{max}) from 585 to 558 nm (Figure 1).[27] Steric hindrance around the N-donor atoms of the other three nucleosides precludes their coordinative interaction with ONa-RhMOP (Figure S2).[28] These results align with previous reports showing the Rh(II) paddlewheel cluster's preference for adenine over other nucleobases, as demonstrated by computational modeling and experimental studies. In all cases, the preferred coordination involves the axial Rh(II) site binding to basic nitrogen atoms.[29−31]

Once we had confirmed adenosine as a potential coordinative binding site, we then reacted ONa-RhMOP with DNA in an aqueous solution containing NaOH. Basic conditions were selected to form single-stranded DNA with all adenosine moieties available to react with the MOP. Mixing the two components immediately afforded a green gel with a frequency-independent storage modulus (G') of 0.76 kPa, as determined by rheological analysis (Figure 2b). However, solid-state UV−vis analysis of the DNA-MOP hydrogel showed that λ_{max} remained constant at 586 nm throughout the gel formation reaction, indicating the absence of coordinative interactions between the DNA and the MOP (Figure S3). We reasoned that H-bonding between ONa-RhMOP and DNA caused gelification. FT-IR spectrum of the lyophilized gel supported this, showing a 12−14 cm^{-1} decrease in carbonyl and phosphate peaks, indicating that these moieties participate in H-bonding interactions, such as carboxylate-amine or phosphonate-hydroxyl interactions (Figure S4).[16,32] FE-SEM analysis of the lyophilized gel revealed a macroporous network in which DNA and ONa-RhMOP are homogeneously dispersed, as confirmed by EDX analysis (Figure S5).

We ascribed the lack of coordinative interactions in the DNA-MOP hydrogel to the electrostatic repulsion between the two negatively charged constituents of the gel. One strategy to screen electrostatic repulsion is the use of solvents with low dielectric constant. Thus, the DNA-MOP hydrogel was incubated in methanol to leverage the latent coordination potential of DNA. Upon immersion in methanol for 24 h, the DNA-MOP hydrogel changed color, from green to purple, which indicated the coordinative interaction between the DNA and the Rh(II) axial sites of ONa-RhMOP. Solid-state UV−vis of the methanol exchanged solvogel confirmed the coordination of DNA to the ONa-RhMOP through N-donor groups as λ_{max} shifted from 586 to 566 nm (Figure S6). Furthermore, the methanol exchange process also induced densification of the network by decreasing the volume of the gel by 65% due to the alcohol-induced condensation of DNA (Figure S7).[33] These changes in the network induced an increase of the mechanical properties of the gel, as G' increased from 0.76 to 2880 kPa upon incubation in methanol (Figure 2b). An increase of G' by a factor of 3790 can not only be ascribed to the densification of DNA in apolar solvents but also to the strong DNA-MOP coordination interaction.[34]

Therefore, we propose that the coordinative DNA-MOP network forms in two steps (Figure 2a). In the first step, ONa-RhMOP establishes hydrogen-bonding interactions with DNA, generating a network in which mutual electrostatic repulsion inhibits adenosine coordination to the Rh(II) axial sites. In the second step, methanol addition to the H-bonded network induces simultaneous DNA condensation and coordination to

https://doi.org/10.1021/jacs.5c03934
J. Am. Chem. Soc. 2025, 147, 16560−16567

the ONa-RhMOP surface. To validate this hypothesis, we replicated this two-step process using adenosine monophosphate as a model compound. Similar to DNA, adenosine monophosphate does not coordinate to ONa-RhMOP through its N atoms in basic water, as confirmed by UV−vis spectroscopy, which showed no shift in λ_{max}. However, after exposing the reaction mixture to methanol, λ_{max} shifted from 590 to 570 nm indicating that the exohedral Rh(II) axial sites are coordinated to N atoms, as the O-donor groups present in the molecule (e.g., phosphate groups) do not induce a blue shift in the λ_{max} of the Rh(II) paddlewheel (Figure S8).[35−37] Therefore, once the Rh−N coordination between adenosine monophosphate and Rh(II) is established in methanol, it remains stable even upon re-exposing the mixture to basic water, as evidenced by UV−vis and NMR spectra (Figures S29−S31). Thus, the initial electrostatic repulsion acts as an energy barrier to coordination, but once overcome, the interaction is preserved in water.

Remarkably, the above-described two-step mechanism was independent of the initial amount of ONa-RhMOP. Indeed, we synthesized a series of solvogels by systematically varying the mass percentage (% w/w, defined as $(w_{ONa\text{-}RhMOP}/w_{(ONa\text{-}RhMOP+DNA)}) \times 100$) of ONa-RhMOP in the reaction mixture from 50% to 14% (w/w). Conversely, when the same reaction was performed with a simple Rh(II) acetate cluster, immediate precipitation of ill-defined, mechanically weak amorphous solids was observed, which could not be further processed or characterized in terms of mechanical properties. These results highlight the importance of the high connectivity and surface negative charge of the MOP in the two-step gelation process described above.

Synthesis and Characterization of BCN-11 Aerogels. We transformed all DNA-MOP solvogels into aerogels by drying them with supercritical CO_2. The composition of each of these aerogels was determined by quantifying the amount of Rh and P through inductively coupled plasma-optical emission spectroscopy of the acid-digested samples (Table S1). Thus, the reaction mixtures containing ONa-RhMOP at 14%, 25%, 40% and 50% (w/w) afforded aerogels containing ONa-RhMOP at final concentrations of 13%, 21%, 35%, and 42% (w/w), respectively. This discrepancy is directly proportional to the amount of MOP used in the synthesis, due to the progressive saturation of the networks by MOPs, which leads to leaching of unbound MOP during washing. The coordinative DNA-MOP interactions were preserved in all aerogel networks (hereafter named as BCN-11_XX, where XX denotes the % w/w in the aerogel), as confirmed through solid-state UV−vis (Figure S9). The mechanical properties of all BCN-11 aerogels were measured through uniaxial quasi-static compression tests, which revealed that the amount of MOP in the network modulates the stiffness of the obtained aerogel. Thus, BCN-11_13 and BCN-11_21 are plastic materials with Young's modulus values of 14.8 and 30.5 MPa, respectively. Conversely, BCN-11_35 and BCN-11_42 are stiffer brittle monoliths with Young's modulus values of 40.9 and 46.3 MPa, respectively, an order of magnitude higher than current DNA-based aerogels (Figure S10).[38−40]

Next, we characterized the microstructure of the BCN-11 series by FE-SEM, which revealed a colloidal network of fused nanoparticles of sizes of ca. 25 nm (Figures 2c and S11−S14). This network was thermally stable up to ca. 225 °C, enabling thermal activation before the gas-sorption experiments (Figure S15). Measurements of N_2 sorption at 77 K revealed that all aerogels are porous to N_2, exhibiting a type IV isotherm characteristic of aerogels having a broad range of pore sizes (Figures 2d and S16). The BET surface area of BCN-11 aerogels increased with the concentration of MOP in the network, ranging from 177 $m^2 \cdot g^{-1}$ for BCN-11_13 to 452 $m^2 \cdot g^{-1}$ for BCN-11_42 (Figures S17−24). The micropore (V_μ) and total pore volumes (V_t) of the four aerogels were as follows: BCN-11_13 (0.085 and 0.52 cm^3/g), BCN-11_21 (0.19 and 1.24 cm^3/g), BCN-11_35 (0.21 and 1.14 cm^3/g), and BCN-11_42 (0.22 and 1.02 cm^3/g). Pore-size distribution (PSD) analysis consistently revealed the presence of micropores (pore sizes: 1.4 and 1.7 nm) and mesopores (pore size: *ca.* 4 nm) in the colloidal network (Figure S25). The micropore size determined by PSD is larger than the inner MOP cavity (0.6 nm),[41] indicating that N_2 cannot access it due to the steric hindrance from the DNA attached to the MOP surface. However, the MOP cross-linking unit structures DNA into a microporous network that also generates mesopores through hierarchical organization of the colloidal particles, becoming the first example of a permanently porous DNA network. The porosity of BCN-11 was also confirmed through CO_2 gas-sorption measurements at 298 K, which, for BCN-11_42, revealed a maximum uptake of 1.13 $mmol \cdot g^{-1}$ at 1 bar (Figure S26).

Synthesis, Mechanical Properties and Stability Against DNAse I of BCN-11 Derived Hydrogels. A common feature of polymeric networks is their ease of conversion from xerogels or aerogels to hydrogels upon immersion in water.[42,43] However, this phenomenon is much less common for permanently porous aerogels, which are brittle and decompose or maintain their solid-like behavior upon incubation in water, as they are generally assembled from low molecular weight linkers.[44] Thus, considering the polymeric nature of DNA, we aimed to investigate the behavior of BCN-11 aerogels upon incubation in water. All four BCN-11 aerogels transformed into stable hydrogels upon incubation in water for 24 h, without any leaching of ONa-RhMOP or DNA (Figures 3a, S27 and Table S2). Furthermore, the coordinative DNA-MOP interaction was preserved in all cases, as evidenced by solid-state UV−vis (Figure S28). This behavior is consistent with the experiments performed with model nucleotides, in which the selective N−Rh coordinative interaction established by adenosine monophosphate in methanol was preserved in water, as evidenced by UV−vis spectroscopy and Diffusion-Ordered Spectroscopy (DOSY) NMR analysis (Figures S29−S37). The swelling ratio (g/g) of the hydrogels was strongly dependent on the % w/w, increasing from 22 for BCN-11_42 to 968 for BCN-11_13 (Figure 3b). Conversely, the robustness of the hydrogels followed the inverse trend, as G' decreased from 10.1 kPa for BCN-11_42 to 2.1 KPa for BCN-11_13 (Figures 3b and S38). These values of storage modulus are significantly higher than most hydrogels made with synthetic DNA that rarely reach 1 KPa.[45] Notably, BCN-11 derived hydrogels also show superior stiffness when compared to hydrogels made from long genomic DNA that display values of G' in the range of 0.01 KPa−1 KPa (Table S3).[46,47] We ascribe the excellent mechanical properties of the BCN-11 hydrogel network to the high connectivity of the ONa-RhMOP and the strength of the Rh−N coordination.

The rheology and swelling measurements indicate that the ONa-RhMOP node controls the density and entanglement of DNA within the network. We envisioned that the response of BCN-11-derived hydrogels to DNase I could be modulated

https://doi.org/10.1021/jacs.5c03934
J. Am. Chem. Soc. 2025, 147, 16560−16567

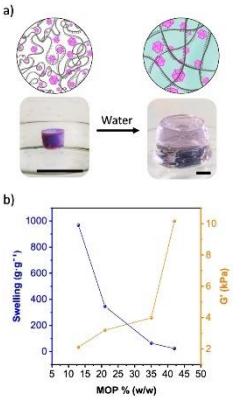

Figure 3. (a) Photographs and schematic of the hydration of BCN-11. Scale bars: 1 cm. (b) Swelling and storage moduli of hydrogels derived from BCN-11.

since these two parameters are crucial for recognition of DNA by DNase I.[48] Therefore, the stability of all four BCN-11-derived hydrogels against DNase I was assessed by incubating the hydrogels in a solution containing the enzyme for 24 h. We found that BCN-11_35 and BCN-11_42 hydrogels remained stable upon incubation in DNase I, whereas hydrogels with a lower content of MOP degraded into noncytotoxic byproducts under the same conditions (Figures S27 and S39). We attribute the stability of BCN-11_35 and BCN-11_42 hydrogels against DNase I to the coordinative linkages between DNA and the 3D MOP cross-linking units, which entangle DNA into dense conformations, effectively shielding it from enzymatic degradation. As the number of MOP nodes increases, the protected regions within the DNA network expand, reaching a threshold at 35% w/w, beyond which the entire network becomes resistant to DNase I. We compared this behavior to that of histones, DNA-binding proteins that are crucial for gene regulation and operate principally by electrostatic interactions. Therefore, the DNA-MOP coordinative cross-linking strategy enables the modulation of the biochemical and mechanical properties of DNA hydrogels.

BCN-11 Derived Hydrogels as Dual Site Adsorbents for Pollutant Removal. We hypothesize that the MOP nodes' control over the DNA network could be leveraged to tailor DNA hydrogels for specific applications, such as pollutant removal from water, which requires hydrogels with adsorptive sites, good mechanical properties, and high stability.[49,50] To test this hypothesis, we employed the dense, mechanically robust hydrogels derived from BCN-11_42 as adsorbents for Acridine Yellow, as a model of a DNA-intercalating pollutant.[51] Time-dependent experiments showed that BCN-11_42 hydrogel adsorbed over 90% of pollutant at initial concentrations in the range of 4−10 ppm after 24 h (Figures 4a and S49−S4). This adsorption process is best described by the Freundlich model, which implies a multilayer adsorption mechanism and heterogeneous distribution of adsorptive sites (Figure S40 and Table S4). The obtained correction factor was found to be less than 1 (n = 0.68), which is characteristic of a favorable process. Time-dependent removal data were fitted against the pseudo-second-order kinetic model with good correlation (R^2 > 0.97), indicating strong chemical interaction between the absorbent and adsorbate molecules, which we ascribed to the high density of DNA adsorptive sites in the network (Figures S41−44). This hypothesis was further supported by the fitting of the kinetic data to the Elovich model, which showed a good correlation (R^2 > 0.87). The strong agreement with the Elovich model indicates that the adsorption process involves significant chemical interactions (chemisorption) on heterogeneous surfaces (Figures S4S−S48).

Once we confirmed that DNA in the BCN-11_42 network is an efficient adsorptive site for planar, intercalating molecules, we next studied the potential of the MOP nodes as adsorptive sites. To this end, we selected the Bisphenol A (BPA), a widely used industrial chemical of concern due to its severe toxicological and adverse health effects that cannot be trapped by DNA.[52,53] We begun by studying the interaction of BPA

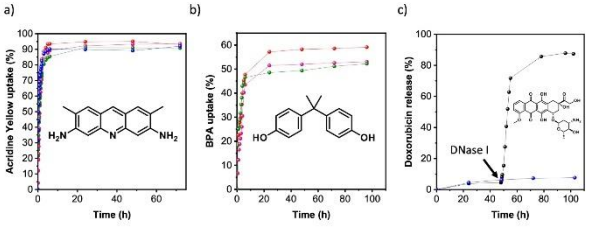

Figure 4. (a) Time-dependent removal of acridine yellow (initial concentration: 10 (red), 7 (pink), 6 (green) and 4 ppm (blue)) in the presence of BCN-11_42 in aqueous medium. (b) Time-dependent removal of BPA (initial concentration: 200 (green), 80 (pink), and 40 ppm (red)) in the presence of BCN-11_42. (c) Release profile of doxorubicin encapsulated in BCN-11_13 (black) and BCN-11_42 (blue) in the absence and presence of DNase I, added 48 h after the start of the experiment.

https://doi.org/10.1021/jacs.5c03934
J. Am. Chem. Soc. 2025, 147, 16560−16567

with ONa-RhMOP in solution through NMR spectroscopy. The ^{1}H NMR spectrum of a solution containing ONa-RhMOP and 6 mol. eq. of BPA revealed that the aromatic and aliphatic signals of BPA were shifted upfield, indicative of shielding (Figure S55). Additionally, the NMR signals attributed to BPA appeared broadened compared to the free molecule. Furthermore, the DOSY-NMR spectra showed that the diffusion coefficient of BPA decreased from $5.31 \cdot 10^{-10}$ m^2/s to $2.6 \cdot 10^{-10}$ m^2/s upon the addition of ONa-RhMOP (Figure S56). These results indicate that BPA interacts with the MOP through a slow exchange rate, operating on the NMR time scale, via supramolecular forces on the surface of the MOP.[54]

After confirming the interaction between the MOP and BPA in solution, we evaluated the performance of ONa-RhMOP as adsorptive sites in the DNA-MOP network. To this end, we first performed time-dependent removal experiments at different concentrations (40, 80, and 200 ppm) of BPA with BCN-11_42 hydrogel (Figures S57−S62). These experiments revealed BPA uptakes of 48% (200 ppm), 51% (80 ppm), and 57% (40 ppm) after 24 h of incubation (Figure 4b). In each case, the kinetics of the capture process followed the pseudo-second-order model with good correlation ($R^2 > 0.95$; Figures S63−S65) and also fit well to the Elovich model (Figures S66−S68). These results signify that the BPA molecules exhibit strong interactions with the adsorptive sites. Moreover, we found that the adsorption isotherm of this BPA removal study is well fitted with the Freundlich adsorption isotherm model with good correlation ($R^2 = 0.99$) (Figure S69). This result indicates a multilayer adsorption mechanism and heterogeneous distribution of adsorptive sites, similar to the previous pollutant. Therefore, these experiments confirm that the MOP cavities are accessible in the swollen BCN-11_42 hydrogel network, thereby designating these hydrogels as dual-site adsorbents, with performance comparable to that of state-of-the-art materials (Table S5).

Enzyme-Triggered Release from BCN-11 Derived Hydrogels. Once the guest uptake was confirmed for BCN-11 derived hydrogels, we aimed to demonstrate enzyme-triggered release of active compounds, taking doxorubicin as a model molecule. Thus, the DNase I-degradable BCN-11_13 hydrogel was loaded with doxorubicin (drug loading of 105 mg/g) and incubated in water in the presence of the nuclease. This experiment revealed that the passive release of doxorubicin from the hydrogel in the absence of enzyme was less than 10%, which we attributed to the strong interaction between DNA and doxorubicin.[55] However, after 24 h incubation of the drug-loaded hydrogel in a solution containing DNase I, 90% of the doxorubicin had been released. In contrast, for drug-loaded hydrogels derived from BCN-11_42 (drug loading of 24 mg/g) and studied under identical conditions, only 8% of the doxorubicin had been released (Figures 4c and S74).

CONCLUSIONS

In conclusion, we have demonstrated the use of MOPs as molecular nodes for synthesizing highly connected DNA networks, which can be processed into mechanically robust aerogels and hydrogels capable of capturing and storing molecules from air and water, respectively. These findings not only pave the way for integrating molecular cage chemistry[56,57] with the (bio)chemical properties of DNA but also provide synthetic guidelines for upcycling biomass-derived DNA into functional materials.

ASSOCIATED CONTENT

Supporting Information

The Supporting Information is available free of charge at https://pubs.acs.org/doi/10.1021/jacs.5c03934.

Detailed synthesis and methods, UV−vis spectra, FT-IR spectra, ^{1}H NMR spectra, DOSY-NMR spectra, composition analysis, FE-SEM images, TGA analysis, rheology measurements, uniaxial compression tests, and gas adsorption−desorption isotherms (PDF)

AUTHOR INFORMATION

Corresponding Authors

Arnau Carné-Sánchez − *Catalan Institute of Nanoscience and Nanotechnology (ICN2), CSIC, and The Barcelona Institute of Science and Technology, Bellaterra 08193, Spain; Departament de Química, Facultat de Ciències, Universitat Autònoma de Barcelona, Bellaterra 08193, Spain;* orcid.org/0000-0002-8569-6208; Email: arnau.carne@uab.cat

Daniel Maspoch − *Catalan Institute of Nanoscience and Nanotechnology (ICN2), CSIC, and The Barcelona Institute of Science and Technology, Bellaterra 08193, Spain; Departament de Química, Facultat de Ciències, Universitat Autònoma de Barcelona, Bellaterra 08193, Spain; ICREA, Barcelona 08010, Spain;* orcid.org/0000-0003-1325-9161; Email: daniel.maspoch@icn2.cat

Authors

Laura Hernández-López − *Catalan Institute of Nanoscience and Nanotechnology (ICN2), CSIC, and The Barcelona Institute of Science and Technology, Bellaterra 08193, Spain; Departament de Química, Facultat de Ciències, Universitat Autònoma de Barcelona, Bellaterra 08193, Spain*

Akim Khobotov-Bakishev − *Catalan Institute of Nanoscience and Nanotechnology (ICN2), CSIC, and The Barcelona Institute of Science and Technology, Bellaterra 08193, Spain; Departament de Química, Facultat de Ciències, Universitat Autònoma de Barcelona, Bellaterra 08193, Spain*

Alba Cortés-Martínez − *Catalan Institute of Nanoscience and Nanotechnology (ICN2), CSIC, and The Barcelona Institute of Science and Technology, Bellaterra 08193, Spain; Departament de Química, Facultat de Ciències, Universitat Autònoma de Barcelona, Bellaterra 08193, Spain*

Eduard Garrido-Ribó − *Catalan Institute of Nanoscience and Nanotechnology (ICN2), CSIC, and The Barcelona Institute of Science and Technology, Bellaterra 08193, Spain; Departament de Química, Facultat de Ciències, Universitat Autònoma de Barcelona, Bellaterra 08193, Spain*

Partha Samanta − *Catalan Institute of Nanoscience and Nanotechnology (ICN2), CSIC, and The Barcelona Institute of Science and Technology, Bellaterra 08193, Spain; Departament de Química, Facultat de Ciències, Universitat Autònoma de Barcelona, Bellaterra 08193, Spain*

Sergio Royuela − *Departamento de Química Inorgánica, Universidad Autónoma de Madrid, Ciudad Universitaria de Cantoblanco, Madrid 28049, Spain;* orcid.org/0000-0003-3113-1831

Félix Zamora − *Departamento de Química Inorgánica, Universidad Autónoma de Madrid, Ciudad Universitaria de Cantoblanco, Madrid 28049, Spain*

Complete contact information is available at: https://pubs.acs.org/10.1021/jacs.5c03934

https://doi.org/10.1021/jacs.5c03934
J. Am. Chem. Soc. 2025, 147, 16560−16567

Author Contributions

*L.H.-L. and A.K.-B. contributed equally to this study.

Notes

The authors declare no competing financial interest.

■ ACKNOWLEDGMENTS

This work was supported by the Spanish MINECO (project RTI2018-095622-B-I00), the Catalan AGAUR (project 2021 SGR 00458), the CERCA Program/Generalitat de Catalunya, the MCIN/AEI/10.13039/501100011033, and by the European Union "NextGenerationEU"/PRTR (EUR2020-112294). ICN2 is supported by the Severo Ochoa program (grant CEX2021-001214-S) funded by MCIN/AEI/10.13039.501100011033. The project that gave rise to these results received the support of a fellowship (LCF/BQ/PR20/11770011) from "la Caixa" Foundation (ID 100010434). A.C.-S. is indebted to the Ramón y Cajal Program (RYC2020-029749-I Fellowship) and the Europa Excelencia grant (EUR2021-121997). P.S. thanks the Generalitat de Catalunya for a Beatriu de Pinós fellowship (2022 BP 00085) (Co-funded by EU under the Marie Skłodowska-Curie Actions grant agreement).

■ REFERENCES

(1) Pinheiro, A. V.; Han, D.; Shih, W. M.; Yan, H. Challenges and Opportunities for Structural DNA Nanotechnology. *Nat. Nanotechnol.* **2011**, *6* (12), 763−772.

(2) Wang, D.; Hu, Y.; Liu, P.; Luo, D. Bioresponsive DNA Hydrogels: Beyond the Conventional Stimuli Responsiveness. *Acc. Chem. Res.* **2017**, *50* (4), 733−739.

(3) Peng, S.; Derrien, T. L.; Cui, J.; Xu, C.; Luo, D. From Cells to DNA Materials. *Mater. Today* **2012**, *15* (5), 190−194.

(4) Um, S. H.; Lee, J. B.; Park, N.; Kwon, S. Y.; Umbach, C. C.; Luo, D. Enzyme-Catalysed Assembly of DNA Hydrogel. *Nat. Mater.* **2006**, *5* (10), 797−801.

(5) Dave, N.; Chan, M. Y.; Huang, P.-J.-J.; Smith, B. D.; Liu, J. Regenerable DNA-Functionalized Hydrogels for Ultrasensitive, Instrument-Free Mercury(II) Detection and Removal in Water. *J. Am. Chem. Soc.* **2010**, *132* (36), 12668−12673.

(6) Shao, Y.; Jia, H.; Cao, T.; Liu, D. Supramolecular Hydrogels Based on DNA Self-Assembly. *Acc. Chem. Res.* **2017**, *50* (4), 659−668.

(7) Wang, D.; Liu, P.; Luo, D. Putting DNA to Work as Generic Polymeric Materials. *Angew. Chem., Int. Ed.* **2022**, *61* (4), No. e202110666.

(8) Nöll, T.; Schönherr, H.; Wesner, D.; Schopferer, M.; Paululat, T.; Nöll, G. Construction of Three-Dimensional DNA Hydrogels from Linear Building Blocks. *Angew. Chem., Int. Ed.* **2014**, *53* (32), 8328−8332.

(9) Lachance-Brais, C.; Rammal, M.; Asohan, J.; Katolik, A.; Luo, X.; Saliba, D.; Jonderian, A.; Damha, M. J.; Harrington, M. J.; Sleiman, H. F. Small Molecule-Templated DNA Hydrogel with Record Stiffness Integrates and Releases DNA Nanostructures and Gene Silencing Nucleic Acids. *Adv. Sci.* **2023**, *10* (12), 2205713.

(10) Hu, Y.; Gao, S.; Lu, H.; Ying, J. Y. Acid-Resistant and Physiological pH-Responsive DNA Hydrogel Composed of A-Motif and i-Motif toward Oral Insulin Delivery. *J. Am. Chem. Soc.* **2022**, *144* (12), 5461−5470.

(11) Lu, C.-H.; Qi, X.-J.; Orbach, R.; Yang, H.-H.; Mironi-Harpaz, I.; Seliktar, D.; Willner, I. Switchable Catalytic Acrylamide Hydrogels Cross-Linked by Hemin/G-Quadruplexes. *Nano Lett.* **2013**, *13* (3), 1298−1302.

(12) Ren, J.; Hu, Y.; Lu, C.-H.; Guo, W.; Aleman-Garcia, M. A.; Ricci, F.; Willner, I. pH-Responsive and Switchable Triplex-Based DNA Hydrogels. *Chem. Sci.* **2015**, *6* (7), 4190−4195.

(13) Song, P.; Ye, D.; Zuo, X.; Li, J.; Wang, J.; Liu, H.; Hwang, M. T.; Chao, J.; Su, S.; Wang, L.; Shi, J.; Wang, L.; Huang, W.; Lal, R.; Fan, C. DNA Hydrogel with Aptamer-Toehold-Based Recognition, Cloaking, and Decloaking of Circulating Tumor Cells for Live Cell Analysis. *Nano Lett.* **2017**, *17* (9), 5193−5198.

(14) Wang, D.; Cui, J.; Gan, M.; Xue, Z.; Wang, J.; Liu, P.; Hu, Y.; Pardo, Y.; Hamada, S.; Yang, D.; Luo, D. Transformation of Biomass DNA into Biodegradable Materials from Gels to Plastics for Reducing Petrochemical Consumption. *J. Am. Chem. Soc.* **2020**, *142* (22), 10114−10124.

(15) Xu, Y.; Wu, Q.; Sun, Y.; Bai, H.; Shi, G. Three-Dimensional Self-Assembly of Graphene Oxide and DNA into Multifunctional Hydrogels. *ACS Nano* **2010**, *4* (12), 7358−7362.

(16) Shin, M.; Ryu, J. H.; Park, J. P.; Kim, K.; Yang, J. W.; Lee, H. DNA/Tannic Acid Hybrid Gel Exhibiting Biodegradability, Extensibility, Tissue Adhesiveness, and Hemostatic Ability. *Adv. Funct. Mater.* **2015**, *25* (8), 1270−1278.

(17) Lee, C. K.; Shin, S. R.; Lee, S. H.; Jeon, J.-H.; So, I.; Kang, T. M.; Kim, S. I.; Mun, J. Y.; Han, S.-S.; Spinks, G. M.; Wallace, G. G.; Kim, S. J. DNA Hydrogel Fiber with Self-Entanglement Prepared by Using an Ionic Liquid. *Angew. Chem., Int. Ed.* **2008**, *47* (13), 2470−2474.

(18) Tang, J.; Ou, J.; Zhu, C.; Yao, C.; Yang, D. Flash Synthesis of DNA Hydrogel via Supramacromolecular Assembly of DNA Chains and Upconversion Nanoparticles for Cell Engineering. *Adv. Funct. Mater.* **2022**, *32* (12), 2107267.

(19) Han, J.; Guo, Y.; Wang, H.; Zhang, K.; Yang, D. Sustainable Bioplastic Made from Biomass DNA and Ionomers. *J. Am. Chem. Soc.* **2021**, *143* (46), 19486−19497.

(20) Guillerm, V.; Kim, D.; Eubank, J. F.; Luebke, R.; Liu, X.; Adil, K.; Lah, M. S.; Eddaoudi, M. A Supermolecular Building Approach for the Design and Construction of Metal−Organic Frameworks. *Chem. Soc. Rev.* **2014**, *43* (16), 6141−6172.

(21) Nouar, F.; Eubank, J. F.; Bousquet, T.; Wojtas, L.; Zaworotko, M. J.; Eddaoudi, M. Supermolecular Building Blocks (SBBs) for the Design and Synthesis of Highly Porous Metal-Organic Frameworks. *J. Am. Chem. Soc.* **2008**, *130* (6), 1833−1835.

(22) Zhu, Q.; Wang, X.; Clowes, R.; Cui, P.; Chen, L.; Little, M. A.; Cooper, A. I. 3D Cage COFs: A Dynamic Three-Dimensional Covalent Organic Framework with High-Connectivity Organic Cage Nodes. *J. Am. Chem. Soc.* **2020**, *142* (39), 16842−16848.

(23) Carné-Sánchez, A.; Albalad, J.; Grancha, T.; Imaz, I.; Juanhuix, J.; Larpent, P.; Furukawa, S.; Maspoch, D. Postsynthetic Covalent and Coordination Functionalization of Rhodium(II)-Based Metal−Organic Polyhedra. *J. Am. Chem. Soc.* **2019**, *141* (9), 4094−4102.

(24) Carné-Sánchez, A.; Craig, G. A.; Larpent, P.; Hirose, T.; Higuchi, M.; Kitagawa, S.; Matsuda, K.; Urayama, K.; Furukawa, S. Self-assembly of metal-organic polyhedra into supramolecular polymers with intrinsic microporosity. *Nat. Commun.* **2018**, *9* (1), 2506.

(25) Grancha, T.; Carné-Sánchez, A.; Zarekarizi, F.; Hernández-López, L.; Albalad, J.; Khobotov, A.; Guillerm, V.; Morsali, A.; Juanhuix, J.; Gándara, F.; Imaz, I.; Maspoch, D. Synthesis of Polycarboxylate Rhodium(II) Metal−Organic Polyhedra (MOPs) and Their Use as Building Blocks for Highly Connected Metal−Organic Frameworks (MOFs). *Angew. Chem., Int. Ed.* **2021**, *60* (11), 5729−5733.

(26) Yamada, M.; Kawamura, M.; Yamada, T. Preparation of Bioplastic Consisting of Salmon Milt DNA. *Sci. Rep.* **2022**, *12* (1), 7423.

(27) Boyar, E. B.; Robinson, S. D. Robinson, S. D. Rhodium(II) Carboxylates. *Coord. Chem. Rev.* **1983**, *50* (1), 109−208.

(28) Hernández-López, L.; Martínez-Esaín, J.; Carné-Sánchez, A.; Grancha, T.; Faraudo, J.; Maspoch, D. Steric Hindrance in Metal Coordination Drives the Separation of Pyridine Regioisomers Using Rhodium(II)-Based Metal−Organic Polyhedra. *Angew. Chem., Int. Ed.* **2021**, *60* (20), 11406−11413.

(29) Tolbatov, I.; Umari, P.; Marrone, A. The Binding of Diruthenium (II,III) and Dirhodium (II,II) Paddlewheel Complexes

https://doi.org/10.1021/jacs.5c03934
J. Am. Chem. Soc. 2025, 147, 16560−16567

at DNA/RNA Nucleobases: Computational Evidences of an Appreciable Selectivity toward the AU Base Pairs. *J. Mol. Graphics* **2024**, *131*, 108806.
(30) Rainen, L.; Howard, R. A.; Kimball, A. P.; Bear, J. L. Complexes of Rhodium(II) Carboxylates with Adenosine 5′-Mono-, 5′-Di-, and 5′-Triphosphates. *Inorg. Chem.* **1975**, *14* (11), 2752−2754.
(31) Chifotides, H. T.; Koomen, J. M.; Kang, M.; Tichy, S. E.; Dunbar, K. R.; Russell, D. H. Binding of DNA Purine Sites to Dirhodium Compounds Probed by Mass Spectrometry. *Inorg. Chem.* **2004**, *43* (20), 6177−6187.
(32) Carné-Sánchez, A.; Martínez-Esaín, J.; Rookard, T.; Flood, C. J.; Faraudo, J.; Stylianou, K. C.; Maspoch, D. Ammonia Capture in Rhodium(II)-Based Metal−Organic Polyhedra via Synergistic Coordinative and H-Bonding Interactions. *ACS Appl. Mater. Interfaces* **2023**, *15* (5), 6747−6754.
(33) Xiong, Q.; Lee, O.-S.; Mirkin, C. A.; Schatz, G. Ethanol-Induced Condensation and Decondensation in DNA-Linked Nanoparticles: A Nucleosome-like Model for the Condensed State. *J. Am. Chem. Soc.* **2023**, *145* (1), 706−716.
(34) Han, J.; Cui, Y.; Han, X.; Liang, C.; Liu, W.; Luo, D.; Yang, D. Super-Soft DNA/Dopamine-Grafted-Dextran Hydrogel as Dynamic Wire for Electric Circuits Switched by a Microbial Metabolism Process. *Adv. Sci.* **2020**, *7* (13), 2000684.
(35) Warzecha, E.; Berto, T. C.; Wilkinson, C. C.; Berry, J. F. Rhodium Rainbow: A Colorful Laboratory Experiment Highlighting Ligand Field Effects of Dirhodium Tetraacetate. *J. Chem. Educ.* **2019**, *96* (3), 571−576.
(36) Fussell, E. D.; Kline, N. D.; Bennin, E.; Hirschbeck, S. S.; Darko, A. Chromogenic Detection of the Organophosphorus Nerve Agent Simulant DCP Mediated by Rhodium(II,II) Paddlewheel Complexes. *ACS Sens.* **2024**, *9* (5), 2325−2333.
(37) Hernández-López, L.; von Baeckmann, C.; Martínez-Esaín, J.; Cortés-Martínez, A.; Faraudo, J.; Caules, C.; Parella, T.; Maspoch, D.; Carné-Sánchez, A. (Bio)Functionalisation of Metal−Organic Polyhedra by Using Click Chemistry. *Chem. - Eur. J.* **2023**, *29* (60), No. e202301945.
(38) Postnova, I.; Sarin, S.; Zinchenko, A.; Shchipunov, Y. DNA−Chitosan Aerogels and Regenerated Hydrogels with Extraordinary Mechanical Properties. *ACS Appl. Polym. Mater.* **2022**, *4* (1), 663−671.
(39) Ma, J.-W.; Zeng, F.-R.; Lin, X.-C.; Wang, Y.-Q.; Ma, Y.-H.; Jia, X.-X.; Zhang, J.-C.; Liu, B.-W.; Wang, Y.-Z.; Zhao, H.-B. A Photoluminescent Hydrogen-Bonded Biomass Aerogel for Sustainable Radiative Cooling. *Science* **2024**, *385* (6704), 68−74.
(40) Basu, S.; Johl, R.; Pacelli, S.; Gehrke, S.; Paul, A. Fabricating Tough Interpenetrating Network Cryogels with DNA as the Primary Network for Biomedical Applications. *ACS Macro Lett.* **2020**, *9* (9), 1230−1236.
(41) Wang, Z.; Villa Santos, C.; Legrand, A.; Haase, F.; Hara, Y.; Kanamori, K.; Aoyama, T.; Urayama, K.; Doherty, C. M.; Smales, G. J.; Pauw, B. R.; Colón, Y. J.; Furukawa, S. Multiscale Structural Control of Linked Metal−Organic Polyhedra Gel by Aging-Induced Linkage-Reorganization. *Chem. Sci.* **2021**, *12* (38), 12556−12563.
(42) Nayak, A. K.; Das, B. 1 - Introduction to Polymeric Gels. In *Polymeric Gels*. Pal, K.; Banerjee, I. Eds.; Woodhead Publishing, 2018, pp. 3−27.
(43) Zhang, X.; Zhang, D.; Wei, C.; Wang, D.; Lavendomme, R.; Qi, S.; Zhu, Y.; Zhang, J.; Zhang, Y.; Wang, J.; et al. Coordination Cages Integrated into Swelling Poly(Ionic Liquid)s for Guest Encapsulation and Separation. *Nat. Commun.* **2024**, *15* (1), 3766.
(44) Khobotov-Bakishev, A.; Samanta, P.; Roztocki, K.; Albalad, J.; Royuela, S.; Furukawa, S.; Zamora, F.; Carné-Sánchez, A.; Maspoch, D. Post-Synthetic Modification of Aerogels Made of Covalent Cross-Linked Metal-Organic Polyhedra. *Adv. Funct. Mater.* **2024**, *34* (8), 2312166.
(45) Cao, D.; Xie, Y.; Song, J. DNA Hydrogels in the Perspective of Mechanical Properties. *Macromol. Rapid Commun.* **2022**, *43* (19), 2200281.
(46) Sarma, S.; Thakur, N.; Varshney, N.; Jha, H. C.; Sarma, T. K. Chromatin Inspired Bio-Condensation between Biomass DNA and Guanosine Monophosphate Produces All-Nucleic Hydrogel as a Hydrotropic Drug Carrier. *Commun. Chem.* **2024**, *7* (1), 261.
(47) Nayak, S.; Kumar, P.; Shankar, R.; Mukhopadhyay, A. K.; Mandal, D.; Das, P. Biomass Derived Self-Assembled DNA-Dot Hydrogels for Enhanced Bacterial Annihilation. *Nanoscale* **2022**, *14* (43), 16097−16109.
(48) Jeon, K.; Lee, C.; Lee, J. Y.; Kim, D.-N. DNA Hydrogels with Programmable Condensation, Expansion, and Degradation for Molecular Carriers. *ACS Appl. Mater. Interfaces* **2024**, *16* (19), 24162−24171.
(49) Kumar, N.; Gusain, R.; Pandey, S.; Ray, S. S. Hydrogel Nanocomposite Adsorbents and Photocatalysts for Sustainable Water Purification. *Adv. Mater. Interfaces* **2023**, *10* (2), 2201375.
(50) Fan, J.; Shi, Z.; Lian, M.; Li, H.; Yin, J. Mechanically Strong Graphene Oxide/Sodium Alginate/Polyacrylamide Nanocomposite Hydrogel with Improved Dye Adsorption Capacity. *J. Mater. Chem. A* **2013**, *1* (25), 7433−7443.
(51) Narita, Y.; Sakti, S. C. W.; Akemoto, Y.; Tanaka, S. Ultra-Rapid Removal of Cationic Organic Dyes by Novel Single- and Double-Stranded DNA Immobilized on Quaternary Ammonium Magnetic Chitosan. *J. Environ. Chem. Eng.* **2019**, *7* (5), 103308.
(52) Wang, B.; Lu, L.; Zhang, Y.; Fang, K.; An, D.; Li, H. Removal of Bisphenol A by Waste Zero-Valent Iron Regulating Microbial Community in Sequencing Batch Biofilm Reactor. *Sci. Total Environ.* **2021**, *753*, 142073.
(53) Yamada, M.; Inoue, M.; Yamada, T. Synthesis of DNA Intercalator−Immobilized Cyclodextrin and Interaction with Double-Stranded DNA: Utilization of DNA−Cyclodextrin Conjugated Material as an Environmental Remediation Material. *Polym. Chem.* **2012**, *3* (5), 1291−1299.
(54) Yang, D.; Hartman, M. R.; Derrien, T. L.; Hamada, S.; An, D.; Yancey, K. G.; Cheng, R.; Ma, M.; Luo, D. DNA Materials: Bridging Nanotechnology and Biotechnology. *Acc. Chem. Res.* **2014**, *47* (6), 1902−1911.
(55) Blumenfeld, C. M.; Schulz, M. D.; Aboian, M. S.; Wilson, M. W.; Moore, T.; Hetts, S. W.; Grubbs, R. H. Drug Capture Materials Based on Genomic DNA-Functionalized Magnetic Nanoparticles. *Nat. Commun.* **2018**, *9* (1), 2870.
(56) Albalad, J.; Hernández-López, L.; Carné-Sánchez, A.; Maspoch, D. Surface Chemistry of Metal−Organic Polyhedra. *Chem. Commun.* **2022**, *58* (15), 2443−2454.
(57) Zhang, D.; Ronson, T. K.; Zou, Y.-Q.; Nitschke, J. R. Metal−Organic Cages for Molecular Separations. *Nat. Rev. Chem.* **2021**, *5* (3), 168−182.

https://doi.org/10.1021/jacs.5c03934
J. Am. Chem. Soc. 2025, 147, 16560−16567

GDCh Research Article Angewandte International Edition Chemie www.angewandte.org

Check for updates

How to cite: *Angew. Chem. Int. Ed.* **2025**, e202505682
doi.org/10.1002/anie.202505682

Metal-Organic Polyhedra Hot Paper

Isoreticular Synthesis of Mesoporous Metal-Organic Polyhedra with Permanent Porosity to Gas and Water

Alba Cortés-Martínez, Pilar Fernández-Seriñán, Cornelia von Baeckmann, Caterina Caules, Laura Hernández-López, María Susana Gutiérrez Gómez, Yunhui Yang, Roberto Sánchez-Naya, José A. Suárez del Pino, Judith Juanhuix, Inhar Imaz, Arnau Carné-Sánchez, and Daniel Maspoch**

Abstract: Synthesis of mesoporous metal-organic cages or polyhedra (MOCs or MOPs) that retain their porous functionality in the solid-state remains challenging, given their tendency to collapse upon desolvation. Herein, we report the use of the isoreticular expansion approach to synthesize two permanently porous Rh(II)-based octahedral MOPs within the mesoporous regime. Our mesoporous MOPs, featuring internal cavities of up to 12.5 nm^3, withstand the activation process, enabling their use as solid-state adsorbents for gases and water. In particular, the largest mesoporous MOP, named BCN-17, captures up to 0.47 $g_{water} \cdot g_{MOP}^{-1}$ and exhibits an S-shaped water-sorption isotherm with a hysteresis loop, characteristic of mesoporous materials.

Introduction

Synthetic chemists have long been inspired by Nature's unparalleled ability to create large, well-defined and functional molecular architectures. Seeking to replicate these remarkable structures,[1,2] chemists have turned to supramolecular chemistry, the assembly of molecular building blocks into large molecules.[3,4] Among the different types of large molecular architectures,[5] metal-organic cages (MOCs) in the mesoporous regime (cavity diameter > 2 nm) stand out due to their (macro)molecular host–guest chemistry. Mesoporous MOCs have typically been assembled either through the controlled assembly of numerous building blocks or the use of organic ligands with increasing sizes. In the first approach, the bent angle of the organic ligand is carefully adjusted to achieve topologies with numerous building blocks, such as the Goldberg polyhedron, which is assembled from 144 components and has a diameter of 5.9 nm.[6] In the second approach, known as isoreticular expansion and commonly employed for metal-organic frameworks,[7,8] the size of a parent cage is enlarged by using ligands of increasing size but having the same bent angle, such that the final structure retains the initial geometry.[9–11] Large MOCs assembled from either of these approaches are typically used in solution, in applications such as biomolecular storage, catalysis or separation.[12–17] However, fabricating robust, large MOCs that are permanently mesoporous in the solid state remains a challenge, given their tendency to collapse upon desolvation.[18] To overcome this challenge, the robustness of the cage backbone must be enhanced to withstand the capillary forces during desolvation and maintain the integrity of the empty cavity formed upon solvent removal. This principle is exemplified by permanently mesoporous organic cages, which, owing to strong covalent bonding, resist collapse.[19,20]

Herein, we demonstrate the synthesis of permanently porous MOCs with mesoporous cavities, highlighting that coordination bonds can stabilize large internal voids in discrete cages in the solid-state. To this end, we applied the isoreticular expansion approach to metal-organic polyhedra (MOPs) constructed from Rh(II) paddlewheel clusters (Figure 1). We hypothesized that the exceptional chemical

[*] A. Cortés-Martínez, P. Fernández-Seriñán, Dr. C. von Baeckmann, C. Caules, Dr. L. Hernández-López, Dr. M. S. Gutiérrez Gómez, Dr. Y. Yang, Dr. R. Sánchez-Naya, Dr. J. A. Suárez del Pino, Dr. I. Imaz, Dr. A. Carné-Sánchez, Prof. Dr. D. Maspoch
Catalan Institute of Nanoscience and Nanotechnology (ICN2), CSIC and The Barcelona Institute of Science and Technology, Campus UAB, Bellaterra, Barcelona 08193, Spain
E-mail: arnau.carne@icn2.cat
daniel.maspoch@icn2.cat

A. Cortés-Martínez, P. Fernández-Seriñán, Dr. C. von Baeckmann, C. Caules, Dr. L. Hernández-López, Dr. M. S. Gutiérrez Gómez, Dr. Y. Yang, Dr. R. Sánchez-Naya, Dr. J. A. Suárez del Pino, Dr. I. Imaz, Dr. A. Carné-Sánchez, Prof. Dr. D. Maspoch
Departament de Química, Facultat de Ciències, Universitat Autònoma de Barcelona (UAB), Cerdanyola del Vallès, Barcelona 08193, Spain

Dr. J. Juanhuix
Alba Synchrotron Light Facility, Cerdanyola del Vallès, Barcelona 08290, Spain

Prof. Dr. D. Maspoch
ICREA, Pg. Lluís Companys 23, Barcelona 08010, Spain

Additional supporting information can be found online in the Supporting Information section

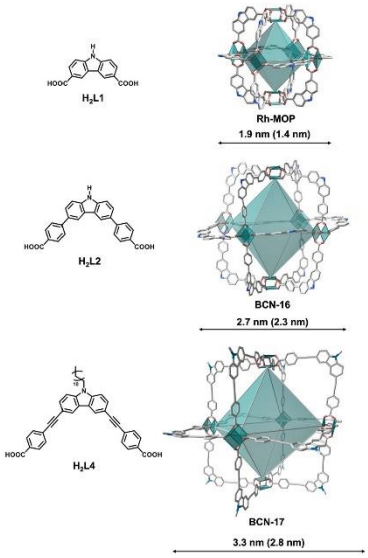

Figure 1. Representation of the ligands (left) used in the isoreticular expansion of octahedral Rh-MOPs (right), indicating their external size, measured as the distance between their two opposing Rh(II) paddlewheels vertices. The value in parentheses is the internal cavity size, as measured between identical paddlewheels. Note that, for clarity, only the first carbon atom of the C_{12} chains in BCN-17 has been shown.

and structural stability of these cluster units would enable the isoreticular expansion of the archetypal parent octahedral Rh(II)-based MOP, having the formula $Rh_{12}(L1)_{12}$ (where L1 is 9*H*-carbazole-3,6-dicarboxylate), while preserving its structural integrity upon desolvation.[21–23] This octahedral MOP, initially reported by Furukawa and coworkers and denoted as **oct** according to the Reticular Chemistry Structure Resource (RCSR) database,[24] features two opposite Rh(II) paddlewheel vertices separated by distance of 1.9 nm, and a microporous internal cavity of 1.4 nm^3 (Figures S1–S10, Table S1).[25,26] Building upon this octahedral MOP, we envisioned a double expansion of the carbazole ligand L1 to synthesize two new mesoporous isoreticular Rh(II)-based MOPs (hereafter named BCN-16 and BCN-17), featuring two opposite Rh(II) paddlewheel vertices separated by respective internal distances of 2.3 nm (BCN-16) or 2.8 nm (BCN-17), and respective internal cavities of 6.5 nm^3 (BCN-16) or 12.5 nm^3 (BCN-17) (Figure 1). We observed that, beyond control over the bite angle of the coordinating carboxylate groups in the carbazole ligands, precise tuning of the ligand twist-angle is also critical for synthesis of these MOPs. As we had hypothesized, the expanded MOPs retained their structural integrity upon desolvation, enabling their characterization as solid-state gas- and water-adsorbents. Interestingly, the largest mesoporous MOP, BCN-17, exhibited a stepwise water-adsorption isotherm characteristic of mesoporous materials and achieved a total water uptake of 0.47 g g^{-1} (584.8 cm^3 g^{-1}), the highest reported for discrete cages to date.

Results and Discussion

First Isoreticular Expansion of the Rh(II)-Based Octahedral MOP

To tackle the first isoreticular expansion of the parent $Rh_{12}(L1)_{12}$ MOP, we began with the synthesis of 4,4′-(9*H*-carbazole-3,6-diyl)dibenzoic acid (H_2L2), an expanded version of L1 that adds a benzene ring between the carbazole core and the adjacent carboxylic acid group (Figures S11–S20). Once synthesized, H_2L2 was reacted with Rh(II) acetate under solvothermal conditions. The complexation reaction yielded a green solution. The crude product was precipitated out with diethyl ether (Et_2O), which afforded a green solid that was further washed with methanol (MeOH) to remove unreacted reagents and then, dried. Proton nuclear magnetic resonance (^{1}H-NMR) analysis of the redissolved crude product in DMSO-d_6 confirmed the success of the complexation reaction, as the aromatic signals appeared broad and shifted relative to the free ligand (Figure S21). Diffusion-ordered spectroscopy (DOSY) NMR analysis of the crude product revealed a diffusion coefficient of $5.1 \cdot 10^{-11}$ m^2 s^{-1}, consistent with the synthesis of a large, discrete metal-organic assembly (Figure S22). Matrix-Assisted Laser Desorption/Ionization-Time-of-Flight (MALDI-TOF) mass spectroscopy of the crude product revealed that it contains at least two different metal-organic compounds, having the formulae $[Rh_{10}(L2)_{10} + H^+]^+$ (found mass 5079.5, expected mass 5084.0 g mol^{-1}) and $[Rh_{12}(L2)_{12} + H^+]^+$ (found mass 6100.6, expected mass 6100.6 g mol^{-1}) (Figure S23).

Isolation of supramolecular compounds through conventional separation techniques such as chromatography is difficult, due to their similar affinity to the stationary phase. Accordingly, we aimed to purify the crude mixture by recrystallization (Figure 2). To this end, we exposed a solution of the crude product in *N*,*N*-dimethylacetamide (DMA) to MeOH vapor, which yielded a microcrystalline material (**A**) and an amorphous solid (**B**). The crystalline material could be separated from the amorphous portion by sedimentation in MeOH, with the crystalline material **A** settling faster than did the amorphous fraction **B**. The crystalline product **A** was redissolved in DMA and recrystallized in the presence of 12 molecular equivalents of 4-*tert*-butylpyiridine and acetonitrile vapor. This crystallization yielded single crystals of sufficient quality for single-crystal X-ray diffraction (SCXRD) analysis (yield based on Rh(II): 2%). Note that subjecting the crude mixture to these crystallization conditions did not yield a

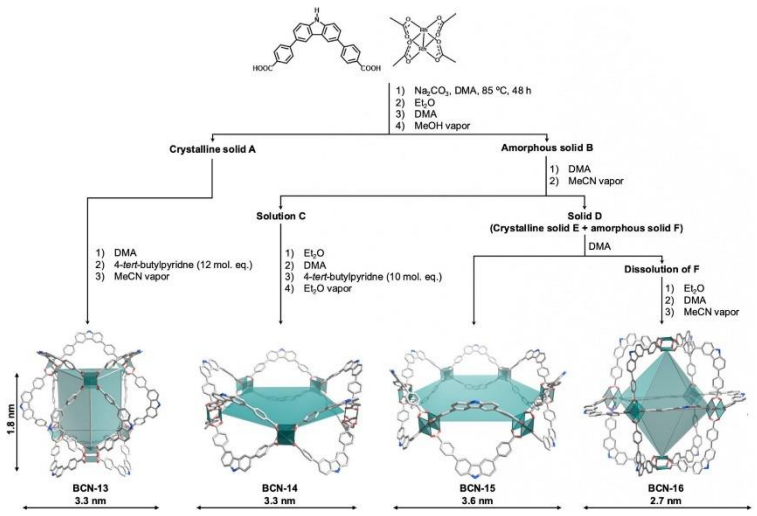

Figure 2. Schematic illustrating the synthesis of the four different MOPs and polygons (named BCN-13, BCN-14, BCN-15, and BCN-16) formed by reacting H_2L2 with Rh(II) acetate. Note that the size indicated for BCN-13 is calculated between Rh(II) paddlewheels at opposite vertices and from the N atoms of opposite ligands. For BCN-14, the size was calculated from the Rh(II) paddlewheel to the center of the opposite edge, whereas for BCN-15 and BCN-16, it was measured between the Rh(II) paddlewheels at opposite vertices.

crystalline material, indicating that the first purification step is required to obtain good quality single crystals. SCXRD analysis revealed formation of a peculiar trigonal prismatic MOP, which crystallizes in the orthorhombic space group *Ibam* with corresponding cell parameters $a = 93.4627(6)$, $b = 37.2998(4)$, $c = 52.7312(3)$ Å (Table S2). This MOP (hereafter named BCN-13), which is denoted as **trp** according to the RCSR database, comprises six Rh(II) paddlewheel units and 12 L2 ligands (formula: $[Rh_{12}(L2)_{12}]$). Although a few examples of this type of structure have been reported,[27,28] to the best of our knowledge, this is the first-ever report of one with metal-paddlewheel clusters. ^{1}H-NMR, DOSY-NMR and Ultraviolet-visible (UV–vis) spectroscopy all confirmed the purity of BCN-13 and notably, the absence of free ligand (Figures S24–S26).

After obtaining pure BCN-13 from the microcrystalline **A**, we purified the amorphous portion **B**. Firstly, it was redissolved in DMA and then, exposed to acetonitrile vapor. This yielded a purple solution (**C**) and a solid (**D**). Addition of Et_2O to **C** caused a solid to precipitate out, which was redissolved in *N,N*-dimethylformamide (DMF) and then, crystallized in the presence of 4-*tert*-butylpyridine and Et_2O vapor to yield single crystals (yield based on Rh(II): 36%). SCXRD analysis revealed the formation of an unprecedented metal-organic polygon (hereafter named BCN-14), comprising a five-membered ring that crystallizes in the monoclinic space group $P2_1/n$ with corresponding cell parameters $a = 34.4336(3)$, $b = 28.8627(3)$, $c = 58.0490(3)$ Å, and $\alpha = \gamma = 90°$, $\beta = 93.1923(7)°$ (Table S3). BCN-14 comprises five Rh(II) paddlewheel clusters and 10 L2 ligands in a double-walled configuration (formula: $[Rh_{10}(L2)_{10}]$). Its purity was confirmed by ^{1}H-NMR, DOSY-NMR, Fourier-transform infrared spectroscopy (FTIR), UV–vis, MALDI-TOF, thermogravimetric analysis (TGA) and powder X-ray diffraction (PXRD) (Figures S28–S34).

Having obtained crystalline BCN-14 from **B**, we next aimed to characterize **D**. Closer observation of **D** under optical microscope revealed that it comprises rectangular single crystals (**E**) and amorphous spheres (**F**) (Figure S36). When DMA was added to the solid, **F** dissolved but **E** remained (yield based on Rh(II): 20%). SCXRD analysis of the rectangular crystals **E** revealed formation of a second metal-organic polygon (hereafter named BCN-15), comprising a six-membered ring built up from six Rh(II) paddlewheel units and 12 double-walled L2 ligands (formula: $[Rh_{12}(L2)_{12}]$), which crystallizes in the monoclinic space group $P2_1/c$ with

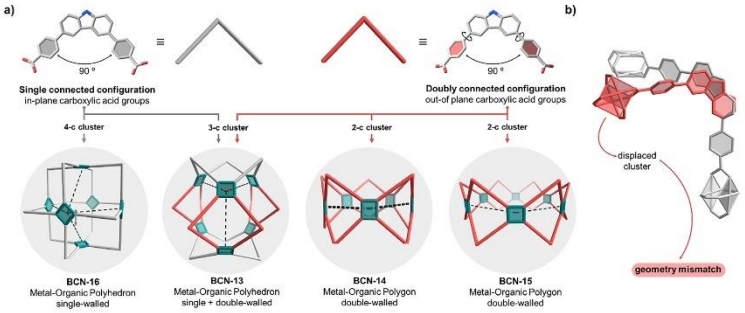

Figure 3. a) Representation of L2 showing its two possible conformations: planar (left, grey) and twisted (right, red), along with their positions in the different polygons and MOPs, which force different cluster connectivities. b) Schematic illustrating how the configuration of L2 (single- or double-walled) changes the positions of the clusters.

corresponding cell parameters $a = 31.4498(3)$, $b = 39.6841(5)$, $c = 40.5297(4)$ Å, and $\alpha = \gamma = 90°$, $\beta = 90.4263(8)°$ (Table S4). The purity of BCN-15 was confirmed by MALDI-TOF, FTIR, TGA, and PXRD (Figures S37–S40).

Finally, the DMA solution containing **F** was exposed to acetonitrile, which afforded rhombic single crystals (hereafter named BCN-16; yield based on Rh(II): 32%). Note that BCN-16 could only be crystallized in the presence of acetonitrile after all the other compounds had already been isolated. SCXRD analysis corroborated formation of the initially expected octahedral isoreticular MOP, having molecular formula of $Rh_{12}(L2)_{12}$. Structure analysis revealed that BCN-16 is isostructural to the parent microporous octahedral $Rh_{12}(L1)_{12}$ MOP, crystallizing in the triclinic space group *P*-1 with corresponding cell parameters $a = 27.2945(8)$, $b = 28.0465(6)$, $c = 29.7602(6)$ Å, and $\alpha = 111.087(2)°$, $\beta = 112.027(2)°$ and $\gamma = 101.813(2)°$ (Table S5). BCN-16 exhibits internal and external diameters of 2.3 and 2.7 nm (calculated from opposite paddlewheel units in the octahedron), and an internal cavity of 6.5 nm^3 (Figure S51). The purity of BCN-16 was further confirmed by ^{1}H-NMR, DOSY-NMR, FTIR, UV-vis, MALDI-TOF, TGA and PXRD (Figures S42–S48).

Geometry Mismatch in Discrete Metal-Organic Assemblies

Interestingly, the structures of BCN-13, BCN-15, and BCN-16 are isomers: each one comprises six rhodium paddlewheel units and 12 L2 ligands. However, they differ vastly by geometry, chiefly by the connectivity of their respective Rh(II) paddlewheel clusters. Paddlewheel metal centers are commonly understood to be 4-connected (4-c) clusters; therefore, we had expected this connectivity and indeed observed it in the octahedral cage BCN-16. In this structure, the L2 ligand is planar, yielding what it has been denoted as the "single-walled configuration" of the ligand (Figure 3a).[29,30] Consequently, BCN-16 can be considered as the default structure for the L2 ligand in combination with a paddlewheel metal cluster. Conversely, BCN-15 adopts a geometrically mismatched structure, influenced by the twist of the phenyl groups surrounding the carbazole core, which renders the ligand non-planar (Figure 3b). In this arrangement, each paddlewheel behaves as a 2-connected (2-c) cluster due to the double-walled configuration of the ligands (Figure 3a). Although not isomeric to BCN-15, BCN-14 exhibits an analogous non-planar double-walled ligand configuration, forming a pentagonal metal-organic polygon with 2-c Rh(II) paddlewheel clusters. The Rh(II) paddlewheel cluster remains undistorted in both polygons, with the only difference being the twist angle of the L2 ligand, measured at 56.3 ± 5.8° for BCN-14 and 58.2 ± 6.5° for BCN-15 (Figures S35 and S41). Therefore, we attributed the formation of both polygons to slight variations in the twist angle of the L2 ligand. These small differences in ligand conformation are likely close in energy, allowing both polygons to form under the tested reaction conditions.

The structure of BCN-13 arises from the combination of planar and non-planar arrangements of L2, leading to the uncommon 3-connected (3-c) Rh(II) paddlewheel cluster (Figure 3a). Specifically, the 3-c Rh(II) paddlewheel clusters result from the double-walled configuration of the ligands, which account for the edges of each lateral rectangular face, whereas only single-walled ligands compose both triangular bases of the structure.[31–33] As with the structures analyzed above, the Rh(II) paddlewheel cluster in this case remains undistorted, with the final structure being attributed to the twist of the ligand, which is 55.1 ± 9.2° for the ligands with double-walled configuration and 14.4 ± 6.2° for those with single-walled configuration (Figure S27). Overall, these results highlight that the twist angle between the carbazole and the adjacent benzene ring is as important as their bite

angle in determining the structural outcome of the assembly reaction, in line with previous reports showing that subtle variations in ligand conformation -particularly twist angles- can direct the formation of distinct cage topologies.[13]

Second Isoreticular Expansion of the Rh(II)-Based Octahedral MOP

Geometrical analysis of the structures formed with H_2L2 revealed that the final structure depends not only on the ligand's bite angle but also on the twist of the linker. Notably, the octahedral cage formed only when the ligand had adopted a planar conformation. Guided by this observation, we designed the ligand for the second isoreticular expansion to induce planarity between the carbazole core, the benzene ring, and the carboxylic acid groups. To this end, an alkyne bond was introduced between the phenyl and carbazole moieties to enable synthesis of 4,4′-((9*H*-carbazole-3,6-diyl)bis(ethyne-2,1-diyl))dibenzoic acid (H_2L3) (Figures S53–S62). However, all solvothermal reactions performed with H_2L3 and Rh(II) acetate under solvothermal conditions resulted in insoluble amorphous precipitates that could not be characterized.

We then explored strategies to increase the solubility of the ligand and avoid early kinetic traps in the form of amorphous solids during the complexation reaction. To this end, an alkane chain was added to the carbazole core of the ligand to enable synthesis of 4,4′-((9-dodecyl-carbazole-3,6-diyl)bis(ethyne-2,1-diyl))dibenzoic acid (H_2L4) (Figures S63–S72), which was then reacted with Rh(II) acetate under solvothermal conditions to yield green rectangular crystals in good yield (68%). These crystallize in the triclinic space group *P*-1 with corresponding cell parameters a = 30.8769(2), b = 33.8701(3), c = 36.1112(2) Å, and α = 107.5252(6)°, β = 100.1424(6)° and γ = 114.2237(6)° (Table S6). SCXRD analysis corroborated formation of the expected octahedral cage (hereafter named BCN-17), isostructural to the parent microporous octahedral Rh-MOP and BCN-16. Remarkably, BCN-17 possesses internal and external diameters of 2.8 and 3.3 nm (calculated from opposite paddlewheel units in the octahedron), and an internal cavity of 12.5 nm^3 (Figure S79), which represents the biggest cavity reported for a paddlewheel-based MOP (Table S7). The purity of BCN-17 was confirmed by MALDI-TOF, FTIR, TGA, and PXRD (Figures S73–S76).

Solid-State Sorption Properties of Isoreticular Octahedral Rh-MOPs

To evaluate the solid-state adsorption properties of the synthesized octahedral MOPs, we conducted gas- and vapor-adsorption studies on BCN-16, BCN-17 and their parent microporous octahedral Rh-MOP, and compared their respective values. To this end, all three MOPs were initially fully evacuated by first exchanging them with MeOH and then, drying them with supercritical CO_2. This resulted in the amorphization of BCN-16 and BCN-17, and a partial loss of crystallinity in the parent microporous octahedral Rh-MOP (Figures S8, S49 and S77). However, the molecular structure of all tested MOPs was preserved in all cases, as confirmed by MALDI-TOF analysis of the activated samples (Figures S9, S50 and S78).

Next, we ran N_2-sorption experiments at 77 K on all three MOPs, which demonstrated their permanent porosity, as evidenced by their corresponding Brunauer–Emmett–Teller (BET) surface areas: 812 m^2 g^{-1} for the parent Rh-MOP; 780 m^2 g^{-1} for BCN-16; and 121 m^2 g^{-1} for BCN-17 (Figure 4a,b). The parent microporous octahedral Rh-MOP exhibited the expected type I isotherm, whereas BCN-16 and BCN-17 exhibited type IV isotherms, as typically observed in mesoporous materials (Figures S81–S89).[34] We attributed the slight decrease in the BET surface area after the first isoreticular expansion to the higher molecular weight of BCN-16 than of the parent microporous Rh-MOP. However, when the isotherm is normalized per mol of MOP, BCN-16 outperforms the parent microporous Rh-MOP (87.2 mol N_2 mol^{-1} BCN-16 versus 49.5 mol N_2 mol^{-1} Rh-MOP at 1 bar). In contrast, we attributed the lower BET surface area and maximum uptake (36.4 mol N_2 mol^{-1} MOP at 1 bar) of BCN-17 to its large cavity-volume-to-surface ratio and to the presence of its surface alkane chains, which can block gas diffusion pathways to the inner pore. The detrimental effect of bulky surface groups on the solid-state adsorption properties of MOPs has been previously reported.[35,36] The permanent porosity of all synthesized Rh-MOPs was further confirmed through CO_2-adsorption measurements run at 200 K, which revealed a similar trend to the N_2-adsorption experiments. BCN-16 exhibited the greatest adsorption, with an uptake of 80 mol CO_2 mol^{-1} MOP at 1 bar, which we attributed to its large, accessible cavity (Figure 4c, Figures S90–S92).

Next, we investigated the water-adsorption properties of the three Rh-MOPs. To this end, we ran water-adsorption isotherms at 298 K, in which the final water uptake at 90% relative humidity increased with cavity size, reaching 0.08 g g^{-1} (98.2 cm^3 g^{-1}, 18.7 mol H_2O mol^{-1} MOP) for the parent Rh-MOP; 0.24 g g^{-1} (304.4 cm^3 g^{-1}, 82.9 mol H_2O mol^{-1} MOP) for BCN-16; and 0.47 g g^{-1} (584.8 cm^3 g^{-1}, 225.7 mol H_2O mol^{-1} MOP) for BCN-17 (Figure 4d, Figures S93–S95). The water uptake value for BCN-17 represents the highest value reported for a cage[37] and is comparable to values for other absorbent materials such as metal-organic frameworks or covalent-organic frameworks.[38,39] A deeper analysis of the water-adsorption isotherms revealed that the parent microporous octahedral Rh-MOP exhibits a reversible isotherm without a step and a moderate final uptake, consistent with the pore-filling mechanism observed in microporous hydrophilic materials, such as zeolites and MOFs.[40] Conversely, the isotherms (type V) for both mesoporous BCN-16 and BCN-17 feature a step that indicates the occurrence of capillary condensation, characteristic of adsorbents with pore sizes exceeding 2 nm.[41,42] For BCN-16, the step of the "S"-shaped isotherm occurs at α = 0.45 (where α is the relative humidity at 50% uptake). More remarkably, in the case of BCN-17, the water adsorption is entirely dominated by capillary condensation exhibiting an "S"-shaped isotherm that resembles that of mesoporous materials such as MCM-41

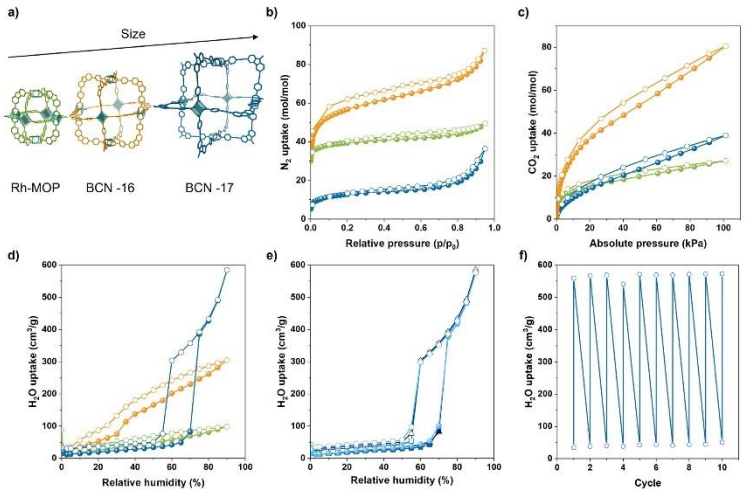

Figure 4. a) Representation of the isoreticular octahedral Rh-MOPs. b) N_2 adsorption isotherm at 77 K. c) CO_2 adsorption isotherm at 200K. d) Water vapor uptake isotherms. e) Three consecutive water vapor uptake isotherms of BCN-17. The sample was activated under vacuum prior each uptake isotherm. f) Water uptake of BCN-17 at high (90%) and low (20%) RH over 10 consecutive cycles.

and MIL-101.[43,44] We ascribed the high relative humidity at which the step occurs in the isotherm of BCN-17 ($\alpha = 0.57$) to the hydrophobicity of BCN-17, imparted by its surface alkyl chains. The hydrophobic character of BCN-17 was further confirmed by contact-angle measurements, which revealed a value of 88.83 ± 0.71° (Figure S80), in contrast to BCN-16, which showed complete wetting with a contact angle of 0° (Figure S52). These findings are consistent with observations in mesoporous MOFs, where total uptake is mainly governed by the mesopore size, while the position of the adsorption step is primarily dictated by the hydrophilic or hydrophobic nature of the framework.[45,46]

Finally, we sought to evaluate the potential of BCN-17 as a water adsorbent. In addition to high water-uptake and stepwise adsorption at ambient pressure, a good water adsorbent must also exhibit cyclability and facile regeneration.[39] Thus, we subjected BCN-17 to three consecutive adsorption–desorption water isotherms, which did not reveal any significant differences between cycles (Figure 4e). Moreover, to assess its regeneration and recyclability, BCN-17 was exposed to alternating high (90%) and low (20%) relative humidity (Figure 4f), which confirmed that it can maintain its performance over 10 cycles. Overall, the performance of BCN-17, characterized by high water-uptake, an S-shaped isotherm, and ease of regeneration and recyclability, meets the key requirements for materials used in humidity control.[47]

Conclusion

In summary, we have synthesized a series of isoreticularly expanded, Rh-based, octahedral MOPs exhibiting internal cavities within the mesoporous regime. We have demonstrated that linker planarity is crucial for developing novel finite structures, as evidenced in the synthesis of the first expanded MOP, BCN-16, in which three additional finite structures – a trigonal prismatic MOP, a hexagonal polygon, and a pentagonal polygon – are simultaneously assembled. We attributed formation of these additional structures to the torsional flexibility of the linker L2. Furthermore, since two of these additional finite structures are isomeric species of BCN-16, our results highlight the importance of characterizing products by PXRD together with MALDI-TOF to confirm the purity of any newly synthesized cage or MOP before its practical use. Finally, gas- and vapor-sorption studies revealed that the enlarged octahedral Rh-MOPs withstand the desolvation process, making them viable mesoporous materials for solid-state adsorption applications. In fact, the larger Rh-MOP, BCN-17, exhibited high water uptake (0.47 $g_{water} \cdot g_{MOP}^{-1}$), accompanied by an "S"-shaped water sorption isotherm with a hysteresis loop. We are confident that our new processable materials will open avenues in water sorption-based applications.

Acknowledgements

This work has received funding from the European Union's Horizon 2020 research and innovation program under grant agreement no. 101019003, grant refs. PID2021-124804NB-I00 funded by MCIN/AEI/10.13039/501100011033/ and by "ERDF A way of making Europe", and the Catalan AGAUR (project 2021 SGR 00458). It was also funded by the CERCA Programme/Generalitat de Catalunya. ICN2 is supported by the Severo Ochoa Centres of Excellence program, Grant CEX2021-001214-S, funded by MCIN/AEI/10.13039.501100011033. A.C.S. is indebted to the Ramón y Cajal Program (RYC2020-029749-I Fellowship). C.v.B. thanks the Austrian Science Fund (FWF), Erwin Schrödinger fellowship for supporting the project J 4637. Y.Y. acknowledges the China Scholarship Council for scholarship support. M.S.G acknowledges the CONACyT for scholarship support.

Conflict of Interests

The authors declare no conflict of interest.

Data Availability Statement

The data that support the findings of this study are available in the Supporting Information of this article.

Keywords: Cages · Mesoporous · Metal-organic polygons · Metal-organic polyhedra · Water adsorption

[1] Y. Hsia, J. B. Bale, S. Gonen, D. Shi, W. Sheffler, K. K. Fong, U. Nattermann, C. Xu, P. S. Huang, R. Ravichandran, S. Yi, T. N. Davis, T. Gonen, N. P. King, D. Baker, *Nature* **2016**, *535*, 136–139.
[2] R. Divine, H. V. Dang, G. Ueda, J. A. Fallas, I. Vulovic, W. Sheffler, S. Saini, Y. T. Zhao, I. X. Raj, P. A. Morawski, M. F. Jennewein, L. J. Homad, Y.-H. Wan, M. R. Tooley, F. Seeger, A. Etemadi, M. L. Fahning, J. Lazarovits, A. Roederer, A. C. Walls, L. Stewart, M. Mazloomi, N. P. King, D. J. Campbell, A. T. McGuire, L. Stamatatos, H. Ruohola-Baker, J. Mathieu, D. Veesler, D. Baker, *Science* **2021**, *372*, eabd9994.
[3] J. A. Davies, T. K. Ronson, J. R. Nitschke, *Chem* **2022**, *8*, 1099–1106.
[4] H. Wu, Y. Wang, L. Đorđević, P. Kundu, S. Bhunia, A. X.-Y. Chen, L. Feng, D. Shen, W. Liu, L. Zhang, B. Song, G. Wu, B.-T. Liu, M. Y. Yang, Y. Yang, C. L. Stern, S. I. Stupp, W. A. Goddard, W. Hu, J. F. Stoddart, *Nature* **2025**, *637*, 347–353.
[5] A. V. Virovets, E. Peresypkina, M. Scheer, *Chem. Rev.* **2021**, *121*, 14485–14554.
[6] D. Fujita, Y. Ueda, S. Sato, N. Mizuno, T. Kumasaka, M. Fujita, *Nature* **2016**, *540*, 563–566.
[7] H. Deng, S. Grunder, K. E. Cordova, C. Valente, H. Furukawa, M. Hmadeh, F. Gándara, A. C. Whalley, Z. Liu, S. Asahina, H. Kazumori, M. O'Keeffe, O. Terasaki, J. F. Stoddart, O. M. Yaghi, *Science* **2012**, *336*, 1018–1023.
[8] M. Eddaoudi, J. Kim, N. Rosi, D. Vodak, J. Wachter, M. O'Keeffe, O. M. Yaghi, *Science* **2002**, *295*, 469–472.
[9] H. Furukawa, J. Kim, N. W. Ockwig, M. O'Keeffe, O. M. Yaghi, *J. Am. Chem. Soc.* **2008**, *130*, 11650–11661.
[10] J.-R. Li, A. A. Yakovenko, W. Lu, D. J. Timmons, W. Zhuang, D. Yuan, H.-C. Zhou, *J. Am. Chem. Soc.* **2010**, *132*, 17599–17610.
[11] M. Tominaga, K. Suzuki, T. Murase, M. Fujita, *J. Am. Chem. Soc.* **2005**, *127*, 11950–11951.
[12] T. Xie, K. Guo, Z. Guo, W. Gao, L. Wojtas, G. Ning, M. Huang, X. Lu, J. Li, S. Liao, Y. Chen, C. N. Moorefield, M. J. Saunders, S. Z. D. Cheng, C. Wesdemiotis, G. R. Newkome, *Angew. Chem. Int. Ed.* **2015**, *54*, 9224–9229.
[13] B. Olenyuk, J. A. Whiteford, A. Fechtenkötter, P. J. Stang, *Nature* **1999**, *398*, 796–799.
[14] K. Harris, D. Fujita, M. Fujita, *Chem. Commun.* **2013**, *49*, 6703.
[15] J. Koo, I. Kim, Y. Kim, D. Cho, I.-C. Hwang, R. D. Mukhopadhyay, H. Song, Y. H. Ko, A. Dhamija, H. Lee, W. Hwang, S. Kim, M.-H. Baik, K. Kim, *Chem* **2020**, *6*, 3374–3384.
[16] D. Fujita, Y. Ueda, S. Sato, H. Yokoyama, N. Mizuno, T. Kumasaka, M. Fujita, *Chem* **2016**, *1*, 91–101.
[17] M.-T. Chen, Q.-F. Xu, M. Aibibula, X.-J. Kong, L.-S. Long, L.-S. Zheng, *J. Am. Chem. Soc.* **2024**, *146*, 22134–22139.
[18] S. Klotzbach, T. Scherpf, F. Beuerle, *Chem. Commun.* **2014**, *50*, 12454–12457.
[19] S. Hong, M. R. Rohman, J. Jia, Y. Kim, D. Moon, Y. Kim, Y. H. Ko, E. Lee, K. Kim, *Angew. Chem. Int. Ed.* **2015**, *54*, 13241–13244.
[20] G. Zhang, O. Presly, F. White, I. M. Oppel, M. Mastalerz, *Angew. Chem. Int. Ed.* **2014**, *53*, 1516–1520.
[21] B. D. Suso, A. Legrand, C. Weetman, A. R. Kennedy, A. J. Fletcher, S. Furukawa, G. A. Craig, *Chem. – A Eur. J.* **2023**, *29*, e202300732.
[22] A. Carné-Sánchez, J. Martínez-Esaín, T. Rookard, C. J. Flood, J. Faraudo, K. C. Stylianou, D. Maspoch, *ACS Appl. Mater. Interfaces* **2023**, *15*, 6747–6754.
[23] S. Furukawa, N. Horike, M. Kondo, Y. Hijikata, A. Carné-Sánchez, P. Larpent, N. Louvain, S. Diring, H. Sato, R. Matsuda, R. Kawano, S. Kitagawa, *Inorg. Chem.* **2016**, *55*, 10843–10846.
[24] T. Tateishi, J. Troyano, S. Tokuda, G. A. Craig, S. Krause, A. López-Olvera, I. A. Ibarra, S. Furukawa, *Inorg. Chem.* **2024**, *63*, 6571–6575.
[25] M. O'Keeffe, M. A. Peskov, S. J. Ramsden, O. M. Yaghi, *Acc. Chem. Res.* **2008**, *41*, 1782–1789.
[26] V. Martí-Centelles, T. K. Piskorz, F. Duarte, *J. Chem. Inf. Model.* **2024**, *64*, 5604–5616.
[27] S. Wang, X. Gao, X. Hang, X. Zhu, H. Han, W. Liao, W. Chen, *J. Am. Chem. Soc.* **2016**, *138*, 16236–16239.
[28] J. P. Carpenter, C. T. McTernan, T. K. Ronson, J. R. Nitschke, *J. Am. Chem. Soc.* **2019**, *141*, 11409–11413.
[29] T.-Y. Liu, X.-L. Qu, Y. Zhang, B. Yan, *Inorg. Chem.* **2021**, *60*, 8613–8620.
[30] X. Sun, X. Li, S. Yao, R. Krishna, J. Gu, G. Li, Y. Liu, *J. Mater. Chem. A* **2020**, *8*, 17106–17112.
[31] F. Haase, G. A. Craig, M. Bonneau, K. Sugimoto, S. Furukawa, *J. Am. Chem. Soc.* **2020**, *142*, 13839–13845.
[32] T. Abe, K. Takeuchi, M. Higashi, H. Sato, S. Hiraoka, *Nat. Commun.* **2024**, *15*, 7630.
[33] V. Guillerm, D. Maspoch, *J. Am. Chem. Soc.* **2019**, *141*, 16517–16538.
[34] L. Peng, J. Zhang, Z. Xue, B. Han, X. Sang, C. Liu, G. Yang, *Nat. Commun.* **2014**, *5*, 4465.
[35] P. S. Reiss, M. A. Little, V. Santolini, S. Y. Chong, T. Hasell, K. E. Jelfs, M. E. Briggs, A. I. Cooper, *Chem. – A Eur. J.* **2016**, *22*, 16547–16553.
[36] T.-H. Chen, L. Wang, J. V. Trueblood, V. H. Grassian, S. M. Cohen, *J. Am. Chem. Soc.* **2016**, *138*, 9646–9654.
[37] J. Troyano, S. Horike, S. Furukawa, *J. Am. Chem. Soc.* **2022**, *144*, 19475–19484.

[38] M. J. Kalmutzki, C. S. Diercks, O. M. Yaghi, *Adv. Mater.* **2018**, *30*, 1704304.
[39] S. M. Towsif Abtab, D. Alezi, P. M. Bhatt, A. Shkurenko, Y. Belmabkhout, H. Aggarwal, Ł. J. Weseliński, N. Alsadun, U. Samin, M. N. Hedhili, M. Eddaoudi, *Chem* **2018**, *4*, 94–105.
[40] F. Jeremias, V. Lozan, S. K. Henninger, C. Janiak, *Dalt. Trans.* **2013**, *42*, 15967.
[41] B. Coasne, A. Galarneau, R. J. M. Pellenq, F. Di Renzo, *Chem. Soc. Rev.* **2013**, *42*, 4141.
[42] J. Canivet, A. Fateeva, Y. Guo, B. Coasne, D. Farrusseng, *Chem. Soc. Rev.* **2014**, *43*, 5594–5617.
[43] G. Akiyama, R. Matsuda, H. Sato, A. Hori, M. Takata, S. Kitagawa, *Microporous Mesoporous Mater.* **2012**, *157*, 89–93.
[44] S. Kittaka, S. Ishimaru, M. Kuranishi, T. Matsuda, T. Yamaguchi, *Phys. Chem. Chem. Phys.* **2006**, *8*, 3223.
[45] B. Li, F.-F. Lu, X.-W. Gu, K. Shao, E. Wu, G. Qian, *Adv. Sci.* **2022**, *9*, 2105556.
[46] B.o Zhang, Z. Zhu, X. Wang, X. Liu, F. Kapteijn, *Adv. Funct. Mater.* **2024**, *34*, 2304788.
[47] R. G. AbdulHalim, P. M. Bhatt, Y. Belmabkhout, A. Shkurenko, K. Adil, L. J. Barbour, M. Eddaoudi, *J. Am. Chem. Soc.* **2017**, *139*, 10715–10722.

Manuscript received: March 11, 2025
Revised manuscript received: May 19, 2025
Accepted manuscript online: May 19, 2025
Version of record online: ■■, ■■

Research Article

Metal-Organic Polyhedra

A. Cortés-Martínez, P. Fernández-Seriñán, C. von Baeckmann, C. Caules, L. Hernández-López, M. S. Gutiérrez Gómez, Y. Yang, R. Sánchez-Naya, J. A. Suárez del Pino, J. Juanhuix, I. Imaz, A. Carné-Sánchez*, D. Maspoch* — **e202505682**

Isoreticular Synthesis of Mesoporous Metal-Organic Polyhedra with Permanent Porosity to Gas and Water

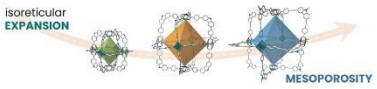

In this work, we report the synthesis of two robust, mesoporous metal-organic cages or polyhedra (MOCs/MOPs) using an isoreticular expansion approach. Among them, the largest mesoporous MOP captures up to 0.47 $g_{water} \cdot g_{MOP}^{-1}$, displaying an S-shaped water sorption isotherm with a hysteresis loop.

ORGANIC SYNTHESIS

Excision of organic macrocycles from covalent organic frameworks

Roberto Sánchez-Naya[1,2], Juan Pablo Cavalieri[1,2,3], Jorge Albalad[1,2,*], Alba Cortés-Martínez[1,2], Kaiyu Wang[4,5], Carles Fuertes-Espinosa[6], Teodor Parella[7], Sara Fiori[1], Esteve Ribas[1], Aitor Mugarza[1,8], Xavi Ribas[6], Jordi Faraudo[9], Omar M. Yaghi[4,5], Inhar Imaz[1,2,*], Daniel Maspoch[1,2,8,*]

Molecules are typically synthesized through stepwise processes involving chemical reactions between simple molecular precursors. Here, we report an advance in the synthesis of new organic molecules based on the approach of clip-off chemistry, in which molecules are excised from ordered, extended organic structures. We synthesized macrocycles by selectively cleaving them out of covalent organic frameworks. The synthesized macrocycles include eight macrocyclic polyamides with 114-, 138-, and 162-atom rings, and one 114-atom ring macrocyclic polyimide. This excision approach expands the scope of chemical organic synthesis to previously inaccessible macromolecules.

The synthesis of new organic molecules is usually approached through stepwise processes that involve reactions between simpler precursors (*1*–*7*). However, a crystalline solid can be viewed as preformed template from which molecules, such as clusters and cages, can be excised through specific cleavage reactions. The original concept of excision in synthesis was first introduced in the isolation of unusual clusters from inorganic solids (*8*). We recently extended this concept and demonstrated its success in molecular structures, enabling the synthesis of metal-organic clusters and cages from metal-organic frameworks through "clip-off chemistry" (*9*–*11*).

We extended this approach to another demanding synthesis: organic macrocyclic molecules. Challenges in the synthesis of these molecules include low selectivity, poor yields given the increasing difficulty of directing the closure of larger rings, and the need for complex purification steps (*12*–*21*), as well as stringent control to avoid side products such as linear oligomers or smaller rings. We show that macrocycles can be synthesized with precision and in high yields through their excision from covalent organic frameworks (COFs) (Fig. 1) (*22*–*25*), which can be disassembled not into their original building blocks but into larger macrocycles (*26*–*29*). Specifically, we synthesized hexagonal polyamide- and polyimide-linked macrocycles. Moreover, we demonstrate that our excision synthesis strategy can be coupled with isoreticular chemistry to rationally tune both the size and functionality of the synthesized macrocycles, enabling the synthesis of macrocycles with progressively larger ring sizes, including 114-, 138- and 162-atom rings, as well as the incorporation of functional groups such as fluorine.

[1]Catalan Institute of Nanoscience and Nanotechnology (ICN2), CSIC and The Barcelona Institute of Science and Technology, Campus UAB, Bellaterra, Barcelona, Spain. [2]Departament de Química, Universitat Autònoma de Barcelona (UAB), Cerdanyola del Vallès, Barcelona, Spain. [3]School of Engineering, Royal Melbourne Institute of Technology (RMIT), Melbourne, Australia. [4]Department of Chemistry and Kavli Energy Nano Sciences Institute, University of California, Berkeley, CA, USA. [5]Bakar Institute of Digital Materials for the Planet, College of Computing, Data Science, and Society, University of California, Berkeley, CA, USA. [6]Institut de Química Computacional i Catàlisi, Universitat de Girona, C/M. Aurèlia Capmany 69, Girona, Spain. [7]Servei de Ressonància Magnètica Nuclear, Universitat Autònoma de Barcelona, Campus UAB, Bellaterra, Barcelona, Spain. [8]ICREA, Pg. Lluis Companys 23, Barcelona, Spain. [9]Institut de Ciència de Materials de Barcelona (ICMAB-CSIC), Bellaterra, Spain. ***Corresponding author. Email: jorge.albalad@icn2.cat (J.A.); inhar.imaz@icn2.cat (I.I.); daniel.maspoch@icn2.cat (D.M.)**

Design and synthesis of COFs for their conversion to unusual macrocycles

The synthesis of organic macrocycles by excision requires an appropriate topology of the COF precursor. A parent framework would need to contain at least two distinct types of pores. One would correspond to our product and should not contain cleavable bonds. Adjacent pores would contain cleavable bonds that would liberate our target macrocycle. In the case that we report here, the cleavable bonds are olefinic bonds and the cleavage method is ozonolysis. This design ensures that, upon exposure to ozone, every cleavable bond breaks, releasing the first targeted pores as discrete macrocycles.

After exploring two-dimensional (2D) COFs that would satisfy our requirements, we chose those with an underlying Kagome (kgm) topology (*30*–*33*). These kgm COFs are typically constructed by combining a planar tetratopic (D_{4h}, D_{2h}, C_{2h}) organic building block with a linear one, resulting in a 2D lattice comprising a periodic arrangement of alternating hexagonal and triangular pores (Fig. 1). Closer analysis of the structure reveals that the hexagonal pores are exclusively extended by the condensation linkages formed during COF synthesis, and these are interconnected by the bisection of the tetratopic building blocks. Thus, we envisioned that by incorporating cleavable olefinic bonds into the central part of this later linker, the cleavable bonds would only be located within the triangular pores and that, once cleaved, the hexagonal pores (our desired macrocycles), would be liberated for isolation.

Following the aforementioned design, we began by synthesizing a 2D iminic kgm COF (hereafter, im-COF-1) by reacting the olefinic-containing (*E*)-3,3′,5,5′-tetrakis(4-aminophenyl)stilbene [(StTA) C_{2h} building block] and terephthalaldehyde [(PDA) linear building block] in a scintillation vial for 3 days at 85°C, using benzoic acid as a catalyst and aniline as a structural modulator [see supplementary materials (SM) for detailed synthetic protocol and fig. S1] (*34*). Powder x-ray diffraction (PXRD) measurements of the resulting powder revealed sharp, intense peaks at 2.21°, 3.75°, 4.29°, 5.67°, and 7.64° (fig. S2). A full-profile Pawley fitting based on this model gave final unit cell parameters of $a = b = 49.33$ Å and $c = 3.53$ Å, with angles of $\alpha = \beta = 90°$ and $\gamma = 120°$, and good agreement factors (Rp = 2.3% and Rwp = 4.3%, figs. S3 and S4). The simulated PXRD pattern using these cell parameters matched well with the experimental pattern of the kgm lattice, confirming the successful synthesis of im-COF-1.

Further evidence of iminic COF formation was provided by Fourier transformance infrared (FTIR) spectroscopy and ^{13}C cross polarization-magic angle spinning (CP-MAS) solid-state nuclear magnetic resonance (NMR). The FTIR spectrum showed the characteristic imine-stretching band at 1620 cm^{-1} (fig. S5), whereas the ^{13}C CP-MAS NMR spectrum exhibited the corresponding imine peak at 157.7 parts per million (ppm) (fig. S6). Finally, porosity was measured using nitrogen-physisorption isotherms at 77 K, yielding an experimental S_{BET} surface area of 1153 m^2 g^{-1} (figs. S7 to S9).

Having confirmed that synthesis of im-COF-1 enabled formation of the targeted precursor framework encoded with cleavable olefinic bonds exclusively at the triangular pores, we next turned to the question of their cleavage. Our group and others have recently demonstrated that imine bonds can be broken in the presence of ozone (fig. S10) (*35*). Accordingly, we anticipated that this side reaction might hinder the orthogonal cleavage of olefinic bonds within the framework, thereby complicating the synthesis of our desired hexagonal macrocycles. Thus, we subjected im-COF-1 to a postsynthetic oxidation that first converted all the imine bonds into amide bonds, leading to a product (hereafter, am-COF-1) (*36*, *37*) that we have demonstrated to be highly resistant to ozone (figs. S11 to S15). The oxidation entailed treating the iminic COF with sodium chlorite and acetic acid in the presence of 2-methyl-2-butene and dioxane (for the detailed synthetic protocol see the SM and fig. S16) (*36*).

The complete disappearance of the imine C=N stretching band (1620 cm^{-1}) and the subsequent appearance of the amide C=O stretching

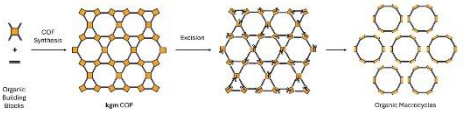

Fig. 1. Schematic of the approach through excision of organic macrocycles from a COF.

band (1656 cm^{-1}) in the FTIR spectrum of am-COF-1 confirmed the successful oxidation of the imine to amide bonds (fig. S17). Additionally, the full conversion from imine to amide bonds was unambiguously confirmed by solid-state ^{13}C CP-MAS NMR analysis (fig. S18), in which the carbon signals associated with imine groups (157.7 ppm) gradually disappeared, as those corresponding to amide groups (166.5 ppm) gradually appeared. Furthermore, the sharp and intense reflection at 2.31° in the PXRD pattern indicated that am-COF-1 retained the crystalline nature of the parent COF, without any appreciable changes to the long-range kgm topology (fig. S19).

Synthesis of the polyamide-linked macrocycles

Having prepared am-COF-1, we next proceeded to cleave its olefinic bonds (Fig. 2A). We dispersed am-COF-1 in a mixture of *N*,*N*-dimethylformamide (DMF), tetrahydrofuran (THF) and methanol (MeOH), and the resulting dispersion was treated with ozone at a constant flow rate (30 g N^{-1} m^{-3}) at −78°C for 10 minutes. The disconnection and liberation of discrete macrocyclic species became visibly apparent as the solid orange suspension transformed into a transparent yellow solution within the first 6 minutes (Fig. 2B). After ozonolysis, dimethyl sulfide (DMS) was added to the solution, which was stirred for 2 hours at room temperature to ensure total reductive ozonolysis—that is, the complete selective cleavage of all the olefinic bonds into aldehyde groups. The reaction mixture was then centrifuged to remove any solid traces, after which both THF and MeOH were removed from the supernatant. The remaining DMF solution was eluted through size-exclusion chromatography (BioBeads SX3, MW > 2000 Da). Addition of ethyl acetate (EtOAc) to the eluent led to precipitation of a crude solid. Finally, the crude product was washed with aqueous Na_2CO_3, water, and acetone, and then dried under high vacuum to obtain the desired macrocycle, comprising MC-1 functionalized with six aldehyde groups on its outer surface (hereafter, MC-1-CHO; yield: 90%; Fig. 2A, left). Notably, when performed on both a 10-mg and 1-g scale, this reaction maintained similar purities and yields (fig. S20). Electrospray mass spectrometry (ESI-MS) analysis of MC-1-CHO revealed a peak at $[m/z]$ = 2531.7466, matching with the simulated isotopic distribution values attributed to the hexagonal macrocyclic species functionalized with six aldehyde groups (formula: $[C_{162}H_{108}N_{12}O_{18} + Na]^+$; Fig. 2E and figs. S21 and S22).

We repeated the above synthetic protocol except under oxidative (rather than reductive) conditions to obtain MC-1 functionalized with six carboxylic acid groups (rather than aldehydes) on its outer surface (hereafter, MC-1-COOH; Fig. 2A, right). For this reaction, a dispersion of am-COF-1 in a mixture of DMF and THF was treated with ozone as described above. After ozonolysis, the reaction mixture was centrifuged to remove any remaining solid traces and the THF was removed from the supernatant. To ensure oxidative ozonolysis, Oxone was then added to the solution, which was stirred for 3 days at room temperature. Addition of water to the reaction mixture led to precipitation of a solid that was then washed with water and dissolved in DMF.

The resulting solution was eluted through size-exclusion chromatography (BioBeads SX3, MW > 2000 Da). Addition of water to the eluent led to precipitation of a crude solid. Finally, the crude product was washed with water and then dried under high vacuum to obtain MC-1-COOH (yield: 96%). Again, this oxidative reaction was successfully performed at both 10-mg and 1-g scales (fig. S23). ESI-MS analysis of MC-1-COOH revealed a peak at $[m/z]$ = 2627.7243, consistent with the simulated isotopic distribution values attributed to the hexagonal macrocyclic species functionalized with six carboxylic acid groups (formula: $[C_{162}H_{108}N_{12}O_{24} + Na]^+$; Fig. 2F and figs. S24 and S25).

Once synthesized, we attempted to crystallize both macrocycles; however, all attempts were unsuccessful. Therefore, to gain further insight into the structures of MC-1-CHO and MC-1-COOH, we performed density functional theory (DFT) calculations to optimize the molecular geometries of both macrocycles (figs. S26 and S27). The DFT-optimized structures revealed that, once excised from the COF, the macrocycles are no longer planar. Instead, they adopt a distorted, twisted boat conformation due to torsional distortions around the amide bonds.

We further validated MC-1-CHO and MC-1-COOH in parallel by NMR spectroscopy, including ^1H NMR, ^{13}C NMR, heteronuclear single quantum coherence (HSQC), heteronuclear multiple bond coherence (HMBC), and diffusion-ordered spectroscopy (DOSY) experiments (DMSO-d_6), as well as by FTIR and elemental analysis (EA) (Fig. 2, C and D, and figs. S28 to S40). To facilitate interpretation of the NMR spectra, which exhibited broad and overlapping peaks, we synthesized three molecular models: Model-COF-1, which is analogous to the asymmetric unit of am-COF-1; and Model-CHO and Model-COOH, which are analogous to the repetitive 1/6th fragment of MC-1-CHO and MC-1-COOH, respectively (Fig. 2, C and D).

Briefly, Model-COF-1 was synthesized by reacting StTA with an excess of benzoyl chloride, yielding a soluble compound with an identical molecular structure to the COF precursor. Model-COF-1 was then subjected to ozonolysis under either reductive or oxidative conditions, affording the expected cleavage products, Model-CHO or Model-COOH, respectively, in quantitative yields (detailed protocol in the SM, and figs. S41 to S53). Comparing the ^1H NMR spectra of the model molecules with those of the corresponding synthesized products corroborated that, upon each ozonolysis reaction, the olefinic bonds in am-COF-1 had been quantitatively cleaved, as evidenced by the complete disappearance of the singlet at 7.73 ppm in both cases (Fig. 2, C and D). Under reductive conditions, a new aldehyde signal emerged at 10.18 ppm (Model-CHO) and 10.22 ppm (MC-1-CHO), integrating at a 1:2 ratio relative to the amide protons, which shift from 10.36 ppm (Model-CHO) to 10.65 ppm (MC-1-CHO). We ascribed these discrepancies to the differences in their respective electron delocalization.

Every aromatic signal in the model molecules was successfully assigned and matched with those observed in the macrocyclic species, except for the expected terminal protons (h,i) in Model-CHO (Fig. 2C), which are absent in the cyclic structure of MC-1-CHO. We observed a similar pattern for the reaction under oxidative conditions, with a broad peak at 13.0 ppm appearing after complete cleavage of the alkene bond, which we attributed to formation of the carboxylic acid groups. Similarly, comparison of the ^{13}C NMR spectra of the model molecules with those of the corresponding synthesized products enabled identification of every expected signal in the symmetric macrocyclic species (from C_2 to C_{12}, fig. S54).

We observed two important differences: First, the spectra for Model-CHO and Model-COOH exhibited two additional signals (C_{13} and C_{14}) that we attributed to terminal carbons and which are absent in the spectra for MC-1-CHO and MC-1-COOH. Second, the peak for the carbon that is alpha to the amide group (C_{11}), located at 136 ppm in the molecular models, shifted downfield (138 ppm) because of the presence of symmetric amide bonds (in the *para*- position) throughout the macrocycle. Moreover, the small number of peaks in the 2D NMR analysis (HSQC, HMBC) of MC-1-CHO and of MC-1-COOH was consistent with highly symmetric closed species, as supported by good correlation between the ^1H-^1H and the ^1H-^{13}C couplings (figs. S30, S31, S36, and S37).

The DOSY analyses of MC-1-CHO and of MC-1-COOH revealed single diffusion-coefficients of *ca.* $5.6{\cdot}10^{-11}$ m^2 s^{-1} and $6.5{\cdot}10^{-11}$ m^2 s^{-1},

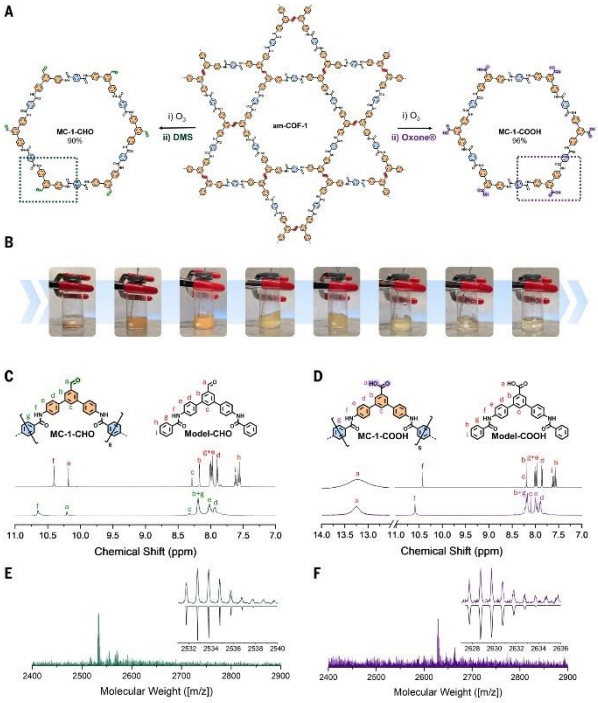

Fig. 2. Overview of syntheses of MC-1-CHO and of MC-1-COOH by selective ozonolytic cleavage of am-COF-1. (**A**) Schematic of the syntheses under either reductive (MC-1-CHO) or oxidative (MC-1-COOH) conditions. The box highlights the repetitive units, which are used for ^{1}H NMR interpretation. (**B**) Photographs of the synthesis of MC-1-CHO through excision. (Left to right) Starting with a crystalline solid sample of am-COF-1 in a mixture of MeOH, DMF, and THF, ozone is bubbled into the dispersion, causing the cleavage of olefinic bonds and "dissolution" of am-COF-1 and release of macrocycles. Each image corresponds to a time lapse of ~1.5 min. (**C** and **D**) ^{1}H NMR spectra of MC-1-CHO (DMSO-d_6, 500 MHz (C) and of MC-1-COOH (DMSO-d_6, 500 MHz (D), as compared with those of Model-CHO and of Model-COOH, respectively. The region from 14.0 to 12.5 ppm is shown with increased intensity to highlight the presence of carboxylic acid protons. (**E** and **F**) ESI-QTOF MS spectra of MC-1-CHO (e, [*m/z*]: calculated for $[C_{152}H_{108}N_{12}O_{18} + Na]^+$ 2531.7797, found 2531.7466) and of MC-1-COOH (f, [*m/z*]: calculated for $[C_{152}H_{108}N_{12}O_{24} + Na]^+$ 2627.7492, found 26277243), with the corresponding comparison between experimental and simulated isotopic distribution.

respectively, corresponding to solvodynamic diameters in the ranges of 32.3 Å to 46.6 Å (MC-1-CHO), or 25.6 Å to 43.5 Å (MC-1-COOH). These values were consistent with the dimensions derived from DFT-optimized molecular structures of each macrocycle (figs. S26, S27, S32, and S38). The ensemble of analytical results unambiguously confirmed the formation of the targeted polyamide-linked macrocycles upon cleavage of olefinic bonds in the COF precursor, with chemoselective control of their peripheral functionality.

Finally, to further confirm the formation of the macrocycles and verify the accessibility of their external functional groups for postsynthetic modification, we covalently attached two different amine-terminated polyethylene glycol (PEG) chains (*ca.* 350 and 750 g mol^{-1}) to each of the six carboxylic acid groups of MC-1-COOH through amide bond formation. We hypothesized that the attachment of six PEG chains would significantly increase the molecular weight of MC-1-COOH, enabling clear detection of the functionalized macrocycles by Matrix-Assisted Laser Desorption/Ionization-Time of Flight (MALDI-TOF) mass spectrometry. Indeed, after postfunctionalization, MALDI-TOF analysis revealed a peak at (m/z) = 4777.9 for PEG_{350} and at (m/z) = 6935.7 for PEG_{750}, both consistent with the expected molecular weights of MC-1 functionalized with six PEG_{350} and six PEG_{750} chains, respectively (figs. S55 and S56).

As expected, the ^{1}H NMR spectra of both postfunctionalized macrocycles showed the disappearance of the broad peak at 13.0 ppm

attributed to the COOH groups, and the appearance of a signal at 8.81 ppm corresponding to the newly formed amides (figs. S55 and S56). PEG-related signals were observed at 3.50 ppm. The quantitative nature of the reaction was confirmed by the correct integration ratios: 90 aromatic protons from the central organic core, 18 amide NH protons, and approximately 192 PEG protons for PEG_{350} or 428 for PEG_{750}, consistent with the incorporation of six chains per macrocycle. Additionally, DOSY-NMR confirmed that all these signals belong to the same molecular species, with a diffusion coefficient of 4.8×10^{-11} m^2 s^{-1} in the case of the smaller PEG_{350} chain and 4.7×10^{-11} m^2 s^{-1} for the larger PEG_{750}-functionalized macrocycle (figs. S55 and S56).

Design and synthesis of functionalized and large macrocycles

An advantage of using reticular materials such as COFs as precursors in this excision approach is that the well-established principles of reticular chemistry can be applied to rationally modify the precursor, thus enabling ready control over synthesis of new macrocycles (Fig. 3) (*38*, *39*). For example, by using the isoreticular principle, we can substitute the linear dialdehyde PDA building block with one functionalized with fluorine groups, such as 2,3,5,6-tetrafluoroterephthalaldehyde (4F-PDA), to form a new COF (hereafter, am-COF-1-4F). Am-COF-1-4F is isostructural to am-COF-1 but has pores functionalized with fluorine atoms. We reasoned that because am-COF-1 ultimately led to MC-1, then am-COF-1-4F should afford fluoro-analogs of the macrocycles MC-1-CHO and MC-1-COOH (hereafter, MC-1-4F-CHO and MC-1-4F-COOH).

We further reasoned that we could apply the isoreticular expansion principle to rationally modify the sizes of the pores in the synthesized COFs. For example, we could substitute the linear dialdehyde PDA building block with larger ones, such as [1,1'-biphenyl]-4,4'-dicarbaldehyde (BPDA) or [1,1':4',1''-terphenyl]-4,4''-dicarboxaldehyde (TPDA), such that the synthesized COFs (hereafter, am-COF-2 and am-COF-3) would exhibit larger pores (inner cavity: 45.2 Å in am-COF-2 and 51.5 Å in am-COF-3 versus 35.3 Å in am-COF-1). This modification enabled synthesis of larger macrocycles, leading to MC-2 (a 138-atom ring macrocycle) and MC-3 (a 162-atom ring macrocycle.)

Following the above strategy, we extended our excision approach to the synthesis of six additional macrocycles (Fig. 3). First, we synthesized am-COF-1-4F and am-COF-2, using a protocol similar to that used for am-COF-1. We confirmed the formation and purity of these COFs by PXRD, FTIR, ^{13}C CP-MAS NMR, and nitrogen physisorption studies (figs. S57 to S74). Next, we ozonized each COF using protocols similar to those used for MC-1-CHO and MC-1-COOH. This step afforded the fluoro-functionalized macrocycles MC-1-4F-CHO (yield: 90%) and MC-1-4F-COOH (yield: 92%), as well as the macrocycles MC-2-CHO (yield: 74%) and MC-2-COOH (yield: 86%), which are larger than their MC-1 counterparts.

We confirmed formation of these macrocycles by mass spectrometry [either ESI-quadrupole time-of-flight (QTOF) or MALDI-TOF], which revealed peaks corresponding to their molecular masses and isotopic distributions consistent with their formulas: $[m/z] = 2963.5050$, for MC-1-4F-CHO ($[C_{162}H_{84}F_{24}N_{12}O_{18} + Na]^+$); $[m/z] = 3059.5208$, for

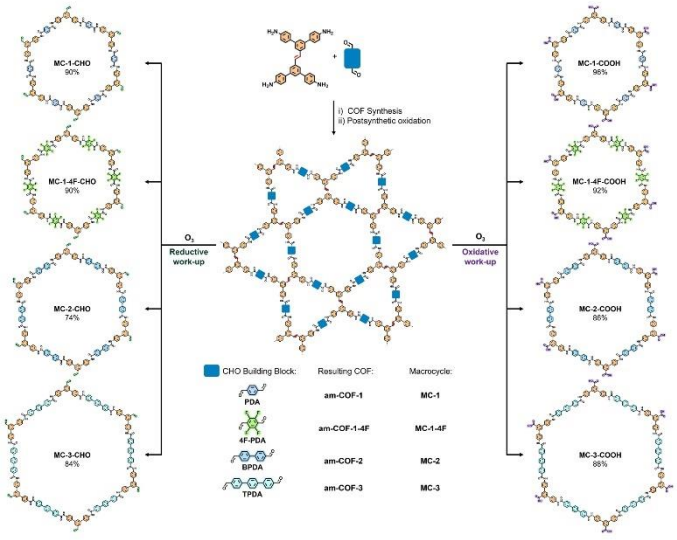

Fig. 3. Isolation of isoreticular organic macrocycles. Schematic showing the selective ozonolytic cleavage of olefinic bonds in each isoreticular COF liberates macrocycles, with precise control over the resultant functionalities, pore dimensions, and chemical environments.

MC-1-4F-COOH ($[C_{162}H_{84}F_{24}N_{12}O_{24} + Na]^+$); [*m/z*]= 2987.9457, for MC-2-CHO ($[C_{108}H_{132}N_{12}O_{18} + Na]^+$); [*m/z*] = 3061.9647 for MC-2-COOH ($[C_{108}H_{132}N_{12}O_{24} + H]^+$) (figs. S75 to S82). Finally, we validated formation of these four macrocycles by NMR spectroscopy, including by ^{1}H NMR, ^{13}C NMR, HSQC, HMBC, and DOSY experiments (DMSO-d_6), as well as by FTIR and EA (figs. S83 to S112).

The synthesis of MC-3-CHO and MC-3-COOH was performed with slightly modified protocols compared with those used for previous macrocycles because of their insolubility after cleavage from am-COF-3. After the synthesis of am-COF-3 (figs. S113 to S121), the product was dispersed in a mixture of DMF and THF (with MeOH also added for MC-3-CHO) and subjected to a constant ozone flow (30 g N^{-1} m^{-3}) at −78°C for 30 minutes. Subsequently, DMS or Oxone was added, and the mixture was stirred at room temperature for 2 hours and 6 days, respectively.

In both cases, the reactions proceeded in a solid-to-solid manner, attributed to the high insolubility of the large macrocycles. During the reaction, the orange-brown precursor gradually transformed into a pale-yellow product upon ozone exposure. The resulting products were washed sequentially with EtOAc, aqueous Na_2CO_3, water, and acetone for MC-3-CHO, and water and acetone for MC-3-COOH, before being dried under vacuum (yield: 84% for MC-3-CHO and 88% for MC-3-COOH). Despite their insolubility, both macrocycles were initially characterized by ^{1}H NMR, using a minimal amount of solid dissolved in hot DMSO-d_6. Notably, the resulting spectrum confirmed the formation of the respective macrocycle, displaying a profile similar to those of MC-1 and MC-2, with the expected 1:2 aldehyde-to-amide or carboxylic acid-to-amide ratios (figs. S122 and S125). Further characterization of both solids by quantitative deconvolution solid-state ^{13}C NMR and FTIR spectroscopies also corroborated the macrocycle formation, consistently showing the same 1:2 aldehyde-to-amide or carboxylic acid-to-amide ratios (figs. S123, S124, S126, and S127).

Synthesis to polyimide-linked macrocycles

Finally, to further demonstrate that our approach could synthesize other types of macrocycles, we applied it to synthesize one of the largest rigid polyimide macrocycles generated to date (*40*, *41*). We began by synthesizing the precursor, which comprised a polyimide kgm COF (hereafter, pi-COF-1), in two steps: First, we synthesized a 2D iminic COF (im-COF-4), by reacting the alkyne-containing tetratopic D_{2h} linker 5′,5′′′-(ethyne-1,2-diyl)*bis*(([1,1′:3′,1′′-terphenyl]-4,4′′-diamine)) (EBTD) with linear 2,5-dihydroxyterephthalaldehyde (2,5-OH-PDA) for 3 days at 120°C, using acetic acid as a catalyst and aniline as a modulator (detailed synthetic protocol in the SM, and figs. S128 to S134). Next, pi-COF-1 was synthesized through postsynthetic linker-exchange on the im-COF-4, using an excess of pyromellitic dianhydride at 250°C for 5 days, followed by an acid wash to remove any residual imine COF (fig. S135) (*42*, *43*).

As confirmed by PXRD (fig. S136), the resulting pi-COF-1 (S_{BET} = 1934 m^2 g^{-1}, figs. S137 to S139) comprised a kgm framework, in which the hexagonal polyimide pores were interconnected by the bisection of the EBTD building block that contained a cleavable alkyne site. We chose alkyne bonds as a different cleavable bond option and one that exclusively yielded carboxylic acid products (*44*, *45*). The complete exchange of imine moieties for imide bonds, forming the polyimide skeleton, was confirmed by FTIR (fig. S140). We observed the quantitative disappearance of the C=N stretching bands characteristic of imines (1613 cm^{-1}), and the appearance of the C=O stretching bands typical for imides (1723 cm^{-1}). Further validation by ^{13}C solid-state NMR corroborated these findings, revealing a loss of the imine-C peak at 159 ppm and the emergence of a new imide-C peak at 165 ppm (fig. S141).

Next, we subjected pi-COF-1 to ozonolysis by first dispersing it in EtOAc and then exposing the resulting dispersion to a constant ozone flow (30 g N^{-1} m^{-3}) with stirring for 40 minutes (Fig. 4A). Subsequently,

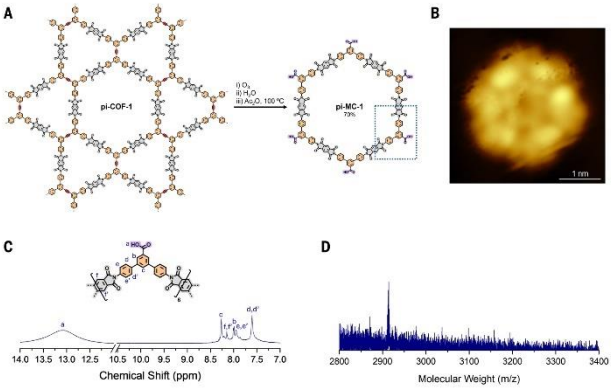

Fig. 4. Overview of the synthesis of pi-MC-1 by selective ozonolytic cleavage of pi-COF-1. (**A**) Schematic of the synthesis. (**B**) A representative STM image of a ring deposited on a Au(111) surface. Image size: 3.8 nm × 3.8 nm; tunneling parameters: I_t= 500 pA, V_{bias}= 1.5 V. Environmental conditions: deposition at T = 300 K, P < 5 × 10^{-9} mbar; acquisition at T = 5 K, P < 1×10^{-11} mbar. (**C**) ^{1}H NMR spectrum of pi-MC-1 (DMSO-d_6, 500 MHz. The region from 14 to 12 ppm is shown with increased intensity to highlight the presence of carboxylic acid protons. (**D**) MALDI-TOF spectrum of pi-MC-1: [*m/z*]: calculated for $[C_{126}H_{84}N_{12}O_{36}]^+$ 2916.5111, found 2914.0335.

2 mL of water were added and the ozone flow was maintained for an additional 20 minutes. The resulting pale-yellow dispersion was filtered and the resultant solid was treated with acetic anhydride at 100°C for 24 hours to prevent imide ring-opening, a reaction that is typically observed in discrete molecular imides (*46*). The product was then collected by centrifugation, dissolved in DMF, and eluted through size-exclusion chromatography (BioBeads MW > 2000 Da). It was precipitated out with EtOAc, isolated, and finally dried under dynamic vacuum to obtain the polyimide macrocycle (pi-MC-1) (yield: 70%) (Fig. 4A).

The formation of pi-MC-1 was first confirmed by MALDI-TOF mass spectrometry, which revealed a peak at $[m/z]$ = 2914.0335, near the expected polyimidic macrocyclic product containing six carboxylic acid groups at its external surface (calculated for $[C_{174}H_{84}N_{12}O_{36}]^-$, $[m/z]$ = 2916.5111, Fig. 4D and fig. S142). Next, the structure of pi-MC-1 was further validated by NMR spectroscopy, including ^{1}H NMR (Fig. 4C), ^{13}C NMR, HSQC, HMBC, and DOSY experiments (in DMSO-d_6), as well as by FTIR and EA (figs. S143 to S149).

Finally, we sublimated pi-MC-1 in ultrahigh vacuum conditions and deposited it on a Au(111) surface, which allowed us to visualize its structure using scanning tunneling microscopy (STM). Figure 4B shows the image of a ring (a larger-scale overview of the deposited rings can be found in fig. S150), further confirming its formation and detachment from the initial COF. The bright lobes and erratic spikes—the latter characteristic of dynamic effects—suggested a nonplanar (as confirmed by the torsional distortions of the DFT-optimized molecular structure of pi-MC-1, fig. S151), labile conformation that hindered atomic structural resolution. Nevertheless, the observed ring displayed the expected sixfold symmetry and a size matching the expected macrocyclic unit.

Summary

In conclusion, we have introduced a synthetic approach for the design and preparation of organic macrocycles through their excision from COFs. This method relies on the spontaneous formation of macrocycles during assembly of COFs, in which some of the pores are delineated by the macrocycles themselves. Initially, reticular chemistry was used to design and construct the COF, incorporating repeated units of the target macrocycle separated by cleavable bonds such as double or triple bonds. Subsequently, the COF was subjected to a cleavage reaction—in the case we have reported here, ozonolysis—to liberate the macrocycles, thus enabling their synthesis with precise selectivity control and high yields. Notably, the choice of reductive or oxidative conditions for the ozonolysis dictated the functional groups, either aldehyde or carboxylic acid groups, that appear at the external surface of the macrocycle. We have demonstrated the versatility of our approach by synthesizing nine macrocycles of distinct skeletal composition (based on polyamide and polyimide linkages), functionalities, and/or sizes. Given the wide variety of repetitive (macro)molecules such as cages, catenanes, and polymers that can be spontaneously formed within the COFs during assembly, we believe that our approach could provide generalized access to previously inaccessible (macro)molecules and polymers at the molecular level, including structurally sophisticated macrocycles, for diverse applications.

REFERENCES AND NOTES

1. K. C. Nicolaou, J. S. Chen, *Chem. Soc. Rev.* **38**, 2993–3009 (2009).
2. J. Li, M. D. Eastgate, *Org. Biomol. Chem.* **13**, 7164–7176 (2015).
3. S. V. Rosokha, J. K. Kochi, *J. Org. Chem.* **67**, 1727–1737 (2002).
4. C. Chen *et al.*, *J. Am. Chem. Soc.* **142**, 1332–1340 (2020).
5. C. C. Chintawar, A. K. Yadav, A. Kumar, S. P. Sancheti, N. T. Patil, *Chem. Rev.* **121**, 8478–8558 (2021).
6. J. F. Lutz, M. Ouchi, D. R. Liu, M. Sawamoto, *Science* **341**, 1238149 (2013).
7. A. Ya-Ting Huang, C. L. Kao, A. Selvaraj, L. Peng, *Mater. Today Chem.* **27**, 101285 (2023).
8. O. M. Yaghi, M. J. Scott, R. H. Holm, *Inorg. Chem.* **31**, 4778–4784 (1992).
9. Y. Yang *et al.*, *Angew. Chem. Int. Ed.* **61**, e202111228 (2022).
10. S. Ruiz-Relaño *et al.*, *J. Am. Chem. Soc.* **146**, 26603–26608 (2024).
11. D. Nam *et al.*, *J. Am. Chem. Soc.* **146**, 27255–27261 (2024).
12. Y. Itoh *et al.*, *Science* **376**, 738–743 (2022).
13. X. N. Han, Y. Han, C. F. Chen, *Chem. Soc. Rev.* **52**, 3265–3298 (2023).
14. V. Marti-Centelles, M. D. Pandey, M. I. Burguete, S. V. Luis, *Chem. Rev.* **115**, 8736–8834 (2015).
15. K. Katagiri, T. Tohaya, H. Masu, M. Tominaga, I. Azumaya, *J. Org. Chem.* **74**, 2804–2810 (2009).
16. H. M. Colquhoun *et al.*, *Chemistry* **16**, 907–918 (2010).
17. Y. Wang, H. Wu, J. F. Stoddart, *Acc. Chem. Res.* **54**, 2027–2039 (2021).
18. D. G. Hamilton, L. Prodi, N. Feeder, J. K. M. Sanders, *J. Chem. Soc., Perkin Trans. 1* **1**, 1057–1066 (1999).
19. F. Zeng, L.-L. Tang, M.-H. Ding, W. Dessie, *Org. Lett.* **25**, 6290–6294 (2023).
20. K. Nakao *et al.*, *J. Am. Chem. Soc.* **128**, 16740–16747 (2006).
21. Y. Y. Zhu, C. Li, G. Y. Li, X. K. Jiang, Z. T. Li, *J. Org. Chem.* **73**, 1745–1751 (2008).
22. A. P. Côté *et al.*, *Science* **310**, 1166–1170 (2005).
23. C. S. Diercks, O. M. Yaghi, *Science* **355**, eaal1585 (2017).
24. K. Geng *et al.*, *Chem. Rev.* **120**, 8814–8933 (2020).
25. F. Haase, B. V. Lotsch, *Chem. Soc. Rev.* **49**, 8469–8500 (2020).
26. T. Prakasam *et al.*, *Chem* **11**, 102307 (2025).
27. Y. Liu *et al.*, *Science* **351**, 365–369 (2016).
28. X. Han *et al.*, *J. Am. Chem. Soc.* **145**, 22885–22889 (2023).
29. F. Chen *et al.*, *Chem. Soc. Rev.* **54**, 484–514 (2025).
30. Y. Tian *et al.*, *CrystEngComm* **19**, 4877–4881 (2017).
31. J. Tu, W. Song, B. Chen, Y. Li, L. Chen, *Chemistry* **29**, e202302380 (2023).
32. J. Li *et al.*, *Chem. Commun.* **59**, 13191–13194 (2023).
33. Y. Wang *et al.*, *ACS Mater. Lett.* **6**, 140–152 (2024).
34. A. Natraj *et al.*, *J. Am. Chem. Soc.* **144**, 19813–19824 (2022).
35. D. Yan, Z. Wang, P. Cheng, Y. Chen, Z. Zhang, *Angew. Chem. Int. Ed.* **60**, 6055–6060 (2021).
36. P. J. Waller *et al.*, *J. Am. Chem. Soc.* **138**, 15519–15522 (2016).
37. Z.-B. Zhou *et al.*, *J. Am. Chem. Soc.* **144**, 1138–1143 (2022).
38. W. Li *et al.*, *Adv. Funct. Mater.* **32**, 2207394 (2022).
39. Z. Mu *et al.*, *J. Am. Chem. Soc.* **144**, 5145–5154 (2022).
40. P. Spenst *et al.*, *J. Am. Chem. Soc.* **139**, 2014–2021 (2017).
41. T. Iwanaga *et al.*, *Angew. Chem. Int. Ed.* **45**, 3643–3647 (2006).
42. J. Maschita, T. Banerjee, B. V. Lotsch, *Chem. Mater.* **34**, 2249–2258 (2022).
43. M. K. Shehab, K. S. Weeraratne, O. M. El-Kadri, V. K. Yadavalli, H. M. El-Kaderi, *Macromol. Rapid Commun.* **44**, e2200782 (2023).
44. D. J. Miller, T. F. Nemo, I. A. Hull, *J. Org. Chem.* **40**, 2675–2678 (1975).
45. N. Havare, *ARKIVOC* **2023**, 202211942 (2023).
46. S. V. Vinogradova *et al.*, *Polymer Sci. USSR* **16**, 584–589 (1974).

ACKNOWLEDGMENTS

We extend our gratitude to L. Gómez and V. Oliveras from the Serveis Tècnics de Recerca at the University of Girona (STR-UdG) and N. Cabello from the High-resolution Mass Spectrometry Unit at the Institut Català d'Investigació Química (ICIQ) for their invaluable insights and continuous support in conducting mass spectrometry measurements throughout the project. We also thank H. Celik, R. Giovine, and the Pines Magnetic Resonance Center's Core NMR Facility (PMRC Core) for spectroscopic assistance. The instrument used in this work is supported by the National Science Foundation under grant 2018784. We thank CESGA Supercomputing Center for technical support and computer time at the supercomputer FinisTerrae III. **Funding:** This work has received funding from the European Union's Horizon 2020 research and innovation program under grant agreement 101019003, grant ref PID2021-124804NB-I00 and PID2022–136970NB–I00 funded by MCIN/AEI/10.13039/501100011033/ and by "ERDF A way of making Europe", and the Catalan AGAUR (project 2021 SGR 00458, project 2021 SGR 01519, and project 2021 SGR 00475). It was also funded by the CERCA program/Generalitat de Catalunya. ICN2 and ICMAB are supported by the Ochoa Centres of Excellence programme, grants CEX2021-001214-S and CEX2023-001263-S, funded by MCIN/AEI/10.13039.501100011033. A.M., S.F., and E.R. acknowledge funding from grant TED2021-132388B-C41, funded by MCIN/AEI/10.13039/ 501100011033 and the European Union NextGenerationEU/PRTR, and grant PID2022-140845OB-C63, funded by MICIU/AEI/10.13039/501100011033 and by FEDER, the European Union (EU). J.P.C. is grateful for his PhD grant, funded from the Marie-Skłodowska Curie grant agreement 101034328. S.F. acknowledges the grant agreement 101149783 - ATOSENSE funded by the European Union. This paper reflects only the authors' views, and the Research Executive Agency is not responsible for any use that may be made of the information it contains. C.F.E. is grateful for a Beatriu de Pinós contract (2022–BP–0078). X.R. is grateful for an ICREA Acadèmia award. **Author contributions:** Conceptualization: J.A., O.M.Y., I.I., and D.M.; Funding acquisition: D.M. Investigation: R.S.N., J.P.C., J.A., A.C.M., K.W., S.F., and E.R. Methodology: R.S.N., J.P.C., J.A., A.C.M., K.W., T.P., C.F.E., X.R., and A.M. DFT calculations: J.F. Supervision: J.A., O.M.Y., I.I., and D.M. Writing – original draft: R.S.N., J.P.C., and J.A. Writing – review & editing: J.A., O.M.Y., I.I., and D.M. **Competing interests:** ICN2, ICREA, and CSIC have applied for a patent on the synthesis of macrocycles via Clip-off Chemistry, on which D.M., I.I., J.A., R.S.N., and J.P.C. are listed as co-inventors. **Data and materials availability:** All data are available in the main text or the supplementary materials. All isotherm data in adsorption information file format (.aif); the XYZ files, including the coordinates of the DFT geometry optimization files, are available as digital files in the supplementary materials.

SUPPLEMENTARY MATERIALS

science.org/doi/10.1126/science.adw4126
Materials and Methods; Figs. S1 to S151; Table S1; References (*47*–*64*)

Submitted 1 February 2025; accepted 16 April 2025
10.1126/science.adw4126

Synthesis and characterization of giant porous molecules

Alba Cortés Martínez

Catalan Institute of Nanoscience and Nanotechnology (ICN2)

Department of Chemistry – Faculty of Science

2025